UNIVERSITEIT VAN PRETORIA
UNIVERSITY OF PRETORIA
YUNIBESITHI YA PRETORIA

Surface influences on falling film boiling and pool boiling of saturated refrigerants

Influences of nanostructures, roughness and material on heat transfer, dryout and critical heat flux of tubes

Bradley D. Bock

Submitted in partial fulfilment of the requirements for the degree

Doctor of Philosophy, Mechanical Engineering

Department of Mechanical and Aeronautical Engineering
University of Pretoria
South Africa

Supervisor: Prof. Josua P. Meyer
Co-supervisor: Prof. John R. Thome

December 2020

Abstract

Title:	Surface influences on falling film boiling and pool boiling of saturated refrigerants: Influences of nanostructures, roughness and material on heat transfer, dryout and critical heat flux of tubes
Supervisor:	Prof. Josua P. Meyer
Co-supervisor:	Prof. John R. Thome
Department:	Mechanical and Aeronautical Engineering
Degree:	PhD (Mechanical Engineering)

Falling film evaporators that operate in the nucleate boiling regime in the refrigeration industry offer a number of advantages over their flooded counterparts such as lower refrigerant charge and at times improved heat transfer. Existing literature has not characterised the influence of surface characteristics on the falling film boiling process, and they are poorly understood for the pool boiling process. The purpose of this study was therefore to experimentally measure the influence of roughness, material and nanostructures on the heat transfer of falling film boiling and pool boiling of saturated refrigerants on the outside of horizontal tubes. The critical heat flux point was measured if it occurred, and the falling film heat transfer enhancement ratio, critical dryout threshold and general dryout characteristics were investigated in the study.

The tubes tested consisted of plain copper, stainless steel and mild steel tubes that were polished and roughened with various grades of sandpaper to achieve a range of roughnesses between 0.1 to 1.9 µm. Furthermore, three types of nanostructured surfaces were applied to polished copper tubes, through a layer-by-layer (LbL) process that deposited silica nanoparticles, a chemical oxidation process where an intertwined mat of sharp copper oxide (CuO) structures were generated and a commercial nanocoating process termed nanoFLUX. The study used refrigerants R-134a at saturation temperatures of 5°C and 25°C and R-245fa at 20°C. All tubes were individually tested in the horizontal position in both pool boiling and falling film boiling conditions and heated by internal water flow with Wilson plots conducted to characterise the internal heat transfer coefficients. Heat fluxes of between 20 to 100 kW/m^2 were tested, followed by a further increase in heat flux in an attempt to reach the critical heat flux point. The falling film boiling studies were conducted across a film Reynolds number range of 0 to approximately 1500 to 2500, depending on the refrigerant.

Both plain and nanostructured tubes had HTCs that increased linearly on a log-log plot as the heat flux was increased under both pool boiling and falling film boiling conditions.

The nanoFLUX and CuO surfaces displayed greater heat flux sensitivity compared with the other surfaces, possibly due to a larger population of small nucleation sites.

Increases in surface roughness were found to increase both pool boiling and falling film boiling heat transfer coefficients. Changes in surface material decreased the heat transfer coefficients in line with the decrease of the material's thermal effusivity. Increases in reduced pressure increased pool boiling and falling film boiling heat transfer coefficients for all surfaces tested.

The nanoFLUX tube had the highest heat transfer coefficients of tubes tested under both pool boiling and falling film conditions, with between 40 and 200% higher heat transfer coefficients than those of a polished copper tube. Of the nanostructured tubes, the LbL tube had the lowest heat transfer coefficients, and the CuO tube had intermediate heat transfer coefficients.

The nanoFLUX surface outperformed the other nanostructured surfaces due to a rougher microstructure and thus higher nucleation site density and outperformed a roughened tube due to a unique heat transfer mechanism, possibly linked to capillary wicking of liquid inside the nanochannels of the porous coating driven by external bubble pumping, which contributed to enhanced single-phase liquid superheating by flow through the nano-sized channels or reduced dryout and increased microlayer evaporation underneath the nucleating bubbles. The falling film heat transfer enhancement ratios for the plain and nanostructured tubes were found to be of a similar order of magnitude, typically between 1.3 and 0.8, suggesting the unique heat transfer mechanisms of the nanostructured tubes were not enhanced under falling film conditions.

The falling film heat transfer enhancement ratios of the nanostructured tubes increased as reduced pressure was increased. The falling film heat transfer enhancement ratio was found to increases as surface roughness was increased on plain tubes, and the falling film heat transfer enhancement ratios of the nanoFLUX tube were higher than those of the CuO tube. These findings all suggested that conditions that increased bubble density were key to increasing falling film enhancement, suggested to be as a result of enhanced microlayer evaporation from the trapped sliding bubbles in the thin flowing film.

Changes in surface roughness and material had no discernible influence on critical dryout threshold for falling film boiling. The refrigerant condition that had the worst falling film boiling dryout performance in terms of film Reynolds number was R-134a at 25°C, followed by R-134a at 5°C and R245fa at 20°C, although the refrigerant condition was a relatively weak influence.

The nanoFLUX and CuO surfaces experienced lower critical heat flux as a result of departure from nucleate boiling under pool boiling and falling film boiling conditions compared with plain surfaces. They also experienced some of the worst critical dryout performance under falling film conditions as the heat fluxes were increased towards 100 kW/m^2. However, the nanoFLUX and CuO tubes had a HTC plateau region under falling film boiling conditions that was the least sensitive to film flow rate changes and performed well in terms of critical dryout at lower heat fluxes. The wicking capabilities of the nanoFLUX and CuO surfaces were thought to be the cause of their improved dryout capabilities at lower heat fluxes, but increased heat fluxes possibly led to dryout of the nanostructures resulting in operation in the Cassie-Baxter state and subsequent reduced wettability.

Publications

The following articles and conference papers were published based on the work contained in this thesis:

Published journal articles

B. D. Bock, J. P. Meyer, and J. R. Thome, "Falling film boiling and pool boiling on plain circular tubes: Influence of surface roughness, surface material and saturation temperature on heat transfer and dryout," Experimental Thermal and Fluid Science, vol. 109, 109870, 2019.

B. D. Bock, M. Bucci, C. N. Markides, J. R. Thome, and J. P. Meyer, "Pool boiling of refrigerants over nanostructured and roughened tubes," *International Journal of Heat and Mass Transfer,* vol. 162, 120387, 2020.

B. D. Bock, M. Bucci, C. N. Markides, J. R. Thome, and J. P. Meyer, "Falling film boiling of refrigerants over nanostructured and roughened tubes: Heat transfer, dryout and critical heat flux," *International Journal of Heat and Mass Transfer,* vol. 163, 120452, 2020.

Conference papers

B. D. Bock, J. P. Meyer, and J. R. Thome, "Surface roughness effect of plain tubes during falling film boiling," presented at the 10th International Conference on Boiling and Condensation Heat Transfer, Nagasaki, Japan, 12th - 15th March 2018.

Acknowledgements

Prof. Josua Meyer and Prof. John Thome for guidance and support throughout the duration of this PhD.

Charles Moon and Koos Mthombeni for assistance in the lab.

Louw Coetzee and Johan van den Berg for company in the lab and serving as a sounding board as I wrestled my equipment into submission.

Prof. Matteo Bucci and Prof. Christos Markides for collaboration and guidance on the nanocoating initiative undertaken in this study.

Dr. Alexander Reip and Tim Bullen of Oxford nanoSystems for assistance with their nanoFLUX coating.

Chi Wang and Dr. Bren Phillips for assistance with the coatings at MIT.

Dr. Dorette Kritzinger and Prof. Jackie Nel at the University of Pretoria for assistance with the surface characterisation.

Marcus Oberlechner of Eriger South Africa for donations of the mild steel tubing used in this study.

This work was, in part, supported by the MIT International Science and Technology Initiatives (MISTI) programme under an MIT-Africa-Imperial College London seed fund grant; by the UK Department for International Development (DFID) through the Royal Society-DFID Africa Capacity Building Initiative and by the European Union's Horizon 2020 Research and Innovation Programme within the ThermaSMART network under the Marie Sklodowska-Curie Grant Agreement No. 778104.

My parents, Denis and Beverley, for everything.

My wife Alice for supporting me throughout this PhD, dutifully listening to me complain about leaks and thermocouples while feigning interest in heat transfer coefficients and sliding bubbles.

Table of Contents

List of Figures

List of Tables

Nomenclature

a	Fitting coefficient
b	Fitting coefficient
C	Wilson plot modifier coefficient
c_p	Specific heat capacity
D	Diameter
e	Thermal effusivity
f	Friction factor
h	Heat transfer coefficient
h^+	Normalised heat transfer coefficient
h_{fg}	Latent heat of vapourisation
K	Heat transfer enhancement ratio
k	Thermal conductivity
L	Length of tube
m	Boiling exponent
$\dot{m}$	Mass flow rate
n	Nucleation site density
P	Pressure
Pr_w	Prandtl number of heating water
p_r	Reduced pressure
q	Heat flux
R_a	ISO 4287 arithmetic mean surface roughness
R_p	ISO 4287 maximum profile height
$R_{p,old}$	DIN 4762:1960 arithmetic mean surface roughness
R	Thermal resistance
Re_f	Film Reynolds number
Re_w	Reynolds number of heating water
T	Temperature
U	Overall heat transfer coefficient
x	Coordinate dimension along the length of the tube

Greek symbols

Δ	Uncertainty/ Difference between
Γ	Film mass flow rate per unit length
ρ	Density
μ	Dynamic viscosity

Subscripts

c	Combined/Condensation
cr	Critical
e	Expanded
ff	Falling film
evap	Evaporative limit
gni	Gnielinski correlation
h	Hydraulic
i	Inner
l	Liquid refrigerant
meas	Experimentally measured
o	Outer
pb	Pool boiling
plain	Plain surface
pol	Polished tube
probe	Heating water temperature probe
r	Refrigerant
sat	Saturated refrigerant
surf	Surface enhancement relative to polished copper tube
t	Tube
w	Water
wp	Wilson plot
ws	Wall superheat
wall	Tube wall

List of Acronyms

AFM	Atomic force microscopy
CHF	Critical heat flux
Cu	Copper
CuO	Copper oxide
DNB	Departure from nucleate boiling
GWP	Global warming potential
HTC	Heat transfer coefficient
LED	Light-emitting diode
LbL	Layer-by-layer
MS	Mild steel
MWR	Minimum wetting rate
NI	National Instruments
PC	Personal computer
SEM	Scanning electron microscope
SiO_2	Silicon dioxide/Silica
SS	Stainless steel
TiO_2	Titanium dioxide

1. Introduction

1.1 Background

Falling film evaporators in the refrigeration industry operating in the nucleate boiling regime have great potential due to a number of advantages over their flooded counterparts such as a lower refrigerant charge and often improved heat transfer at lower heat fluxes [1]. They also have the option of being gravity fed, resulting in a low pressure drop system. This results in lower costs, greater efficiencies and reduced environmental impact [2].

Horizontal falling film evaporators in particular have an advantage over vertical in-tube falling film evaporators as they can make use of tubes with external enhancements that increase the heat transfer performance, although they suffer from the disadvantage that, in certain applications, the corrosive fluid is placed on the shell side of the evaporator [6]. However, refrigerant applications do not suffer this disadvantage because the refrigerant is not corrosive and thus most research works focused on the refrigeration industry have used horizontal falling film evaporators.

Evaporators such as falling film evaporators have safety advantages when poisonous or flammable refrigerants are used due to the lower refrigerant charge required. This has become particularly pertinent with the signing of the Kigali amendment to the Montreal Protocol, which seeks to phase out high global warming potential (GWP) refrigerants [3], with many of the low GWP refrigerants touted to replace the current generation of refrigerants classified as mildly flammable (e.g. hydrofluoro-olefins) [4] or poisonous (e.g. ammonia).

A number of reviews on the topic of falling film boiling in refrigerant evaporators, namely those by Ribatski and Jacobi [1], Thome [5], Fernandez-Seara and Pardiñas [2] and Abed et al. [6], have shown that much research still needs to be conducted to understand falling film boiling. This is because the majority of previous research into falling film evaporators and similar thin film technology focused on applications in desalination and ocean thermal energy conversion in the 1970s and 1980s, where the working fluid was water or ammonia [1], or in other industries, such as food, cosmetics and fine chemicals, where they proved to be a popular concentration process [7].

Therefore, significant work has been done in recent years to better characterise the heat transfer of falling film evaporators in the refrigeration industry so that this promising technology can better compete with its flooded counterpart. A significant portion of the research has focused on enhanced tubes due to their immediate industrial usefulness, while gaps in the fundamental understanding of falling film boiling on plain tubes still remain.

Surface influences of plain tubes in particular have had little attention but should play a significant role in the heat transfer process. Ribatski and Jacobi [1] noted in their review that falling film boiling heat transfer coefficients (HTCs) should be influenced by surface roughness, surface material and surface wettability. However, there is no literature as yet to quantify these fundamental surface influences, as evident in the reviews on the topic [1,2,5,6].

Surface wettability is a particularly important unstudied factor in falling film boiling as dry patches can occur when insufficient liquid is supplied. This dryout can be a concern because of the subsequent reduction in heat transfer under falling film boiling conditions [1,5]. Typically, this falling film dryout occurs in two stages. Firstly, as refrigerant film flow rates are lowered from a high point, a plateau region is seen where HTCs remain relatively insensitive to changes [8-12]. After this, critical dryout is reached where HTCs decrease significantly when flow rates are decreased further [8,9,11,12]. Higher HTCs have been measured for falling film boiling of refrigerants than for pool boiling under identical conditions when boiling refrigerant on plain and microstructured tubes, but as heat fluxes are increased and refrigerant film flow rates are lowered, the HTCs of falling film boiling are lowered below their pool boiling counterparts due to dryout [13-15]. The operational abilities of falling film evaporators are thus practically limited by dryout, both in the plateau region, where lowered HTCs can reduce performance, as well as critical dryout, where the HTCs are sharply reduced and an operational limit is effectively reached.

Surface coatings that improve wettability but are non-porous have been shown to decrease HTCs in pool boiling studies due to the deactivation of nucleation sites by fluid flooding [16]. Wickable porous structures, typically nanostructured, with high wettability have subsequently been investigated in an attempt to increase HTCs in pool boiling [16].

Nanostructured surfaces may thus offer an exciting opportunity for falling film boiling in the battle against dryout. They may be able to extend the operational dryout limits of falling film evaporators because some of these surfaces have been developed to have high wetting capabilities and many are wickable, drawing liquid into the surface through capillary action, while still providing good heat transfer performance through active nucleation sites and unique enhanced heat transfer mechanisms [16,17].

Surface influences are also not particularly well understood for pool boiling, with the influence of surface material perhaps the worst understood of the influences on pool boiling [18], the influence of roughness and roughness distribution not fully characterised yet [19] and a shortage of literature on the influence of pool boiling of refrigerants (or any organic fluids for that matter) on nanostructures, as evident from reviews on the topic [16,17,20].

Understanding the heat transfer mechanisms in pool boiling is important to better understand falling film boiling, as evident by the numerous researchers who have used pool boiling as a useful base line and comparison case for falling film boiling [21-23]. Pool boiling is a far more widely studied phenomenon than falling film boiling and as such, the understanding gained of mechanisms identified in pool boiling can be applied to falling film boiling if also investigated under similar conditions. Pool boiling comparisons also allow for the isolation of mechanisms that are unique to falling film boiling, such as dryout. In the future, the comparison of falling film boiling with pool boiling may also be the basis for an effective modelling strategy to predict falling film boiling HTCs, as was already attempted by Roques and Thome [21], who developed a falling film boiling HTC correlation that was based on the modification of existing pool boiling correlations.

1.2 Problem statement

The heat transfer of falling film boiling is not well understood, particularly concerning the influence of surface factors. Factors such as surface roughness and surface material, which are known to influence pool boiling heat transfer, have not been studied in falling film boiling.

To compound matters, while experimental work has been conducted to understand the influence of surface material and surface roughness on pool boiling, these influences are some of the weakest understood influences on pool boiling.

The influence of the modification of the surface properties through the addition of nanostructures on falling film boiling is also not known as it has not been documented in literature before.

Again to compound matters, most pool boiling heat transfer studies on nanostructured surfaces have been conducted with water on flat plates at atmospheric pressure [16,17,20,24-26]. For highly wetting fluids, such as refrigerants, the mechanisms involved in nanostructured surface pool boiling are thus not well understood. Furthermore, very little work has been done with nanostructures under boiling conditions on the outside surface of circular tubes with dimensions similar to those used in commercial systems such as chillers.

1.3 Aim

The aim of this study was to experimentally investigate the roughness, material and nanostructure surface influences on the heat transfer characteristics of falling film boiling and pool boiling of refrigerants on the outside of horizontal tubes heated by water under a range of refrigerant conditions. The influence of these factors on dryout, critical dryout and where possible critical heat flux (CHF) as a result of departure from nucleate boiling (DNB) was also investigated.

1.4 Objectives

The main objectives of this study were as follows:

- Commission, calibrate and validate an experimental facility that can measure pool boiling and falling film boiling HTCs on the outside of tubes heated internally by water.
- Investigate the influence of surface roughness on the HTCs measured on plain tubes.
- Investigate the influence of surface material on the HTCs measured on plain tubes.
- Investigate the influence of nanostructures on the HTCs measured.
- Determine how these influences vary across a range of heat fluxes.
- Determine how these influences vary under different saturation temperatures and different refrigerants, namely R-134a and R-245fa.
- Determine how these influences on the falling film boiling HTCs vary under a range of refrigerant film flow rates.
- Determine the operational limits of falling film boiling heat transfer due to critical dryout.
- Determine the operational limits of pool boiling and falling film boiling heat transfer on nanostructures due to CHF caused by DNB if possible.
- Use a high-speed video camera to record the falling film boiling and pool boiling processes to better understand the heat transfer mechanisms.

The overriding goal was to experimentally gather data to better understand the influence that the surface characteristics mentioned would have on the pool boiling and falling film boiling heat transfer process and mechanisms involved. This knowledge would improve future falling film evaporator designs both directly from the HTCs measured as well as indirectly from the greater understanding of the mechanisms involved.

1.5 Scope of work

Plain copper tubes of four different roughnesses were tested across a heat flux range of 20 to 100 kW/m^2 under pool boiling and falling film boiling conditions in refrigerant R-134a at saturation temperatures of 5°C and 25°C. The smoothest and roughest plain copper tubes were also tested in R-245fa at a saturation temperature of 20°C.

Two stainless steel and two mild steel tubes, one polished and one roughened each, were also tested in pool boiling and falling film boiling of R-134a at saturation temperatures of 5°C and 25°C across a heat flux range of 20 to 100 kW/m^2.

Lastly, three different nanostructured tubes were manufactured and subsequently tested in pool boiling and falling film boiling conditions of R-134a at saturation temperature of 5°C and 25°C and R-245fa at a saturation temperature of 20°C across heat fluxes of between 20 to 100 kW/m^2.

Heat fluxes were also increased above 100 kW/m^2 to see if the CHF point could be reached with the experimental apparatus under pool boiling and falling film boiling conditions.

Falling film boiling tests were conducted with a refrigerant film flow rate of approximately 0.13 kg/m/s when varying heat fluxes. Thereafter, the heat flux was kept at a constant of 20, 50 and 80 kW/m^2, while the film flow was varied from 0 to 0.13 kg/m/s in order the determine the influence of film flow rate and to find the operational limits in terms of critical dryout and CHF.

A high-speed camera was used to record videos of the tests done throughout.

1.6 Original outcomes

The original outcomes of this thesis were published in three papers, listed under the Publications chapter and referenced as [27-29]. The original outcomes emanating from this thesis, and published in the papers, were as follows:

Chapter **5**. Falling film and pool boiling of plain tubes: Surface roughness and material influence [27]

- Expansion of existing pool boiling literature database of the influence of roughness on the HTCs of copper tubes.
- Expansion of existing pool boiling literature database of the influence of surface material on the HTCs of tubes.
- Expansion of existing pool boiling literature database of the influence of refrigerant conditions on the HTCs of pool boiling of plain tubes of different roughnesses and materials and the sensitivity of the HTCs of those tubes to heat flux changes.
- Influence of surface roughness on falling film boiling heat transfer, falling film heat transfer enhancement and dryout.
- Influence of surface material on falling film boiling heat transfer, falling film heat transfer enhancement and dryout.

- Expansion of existing literature database of the influence of refrigerant conditions on falling film boiling heat transfer, falling film heat transfer enhancement and dryout.

Chapter **6**. Pool boiling over nanostructured and plain tubes [28]

- Three types of nanostructured tubes were tested in refrigerant pool boiling.
- Influence of refrigerant type and conditions on nanostructured tubes.
- Influence of nucleation site density and possible advanced heat transfer mechanisms identified.
- Early onset of CHF recorded for pool boiling of refrigerants on nanostructures.
- Description of mechanisms that may explain the early onset of CHF in pool boiling and falling film boiling seen in this study.

Chapter **7**. Falling film boiling over nanostructured and plain tubes [29]

- Early onset of CHF recorded for falling film boiling of refrigerants on nanostructures due to DNB.
- Images of DNB in falling film boiling on tubes recorded.
- Description of mechanisms that may explain the early onset of CHF due to DNB in falling film boiling seen in this study.
- Influence of nanostructures on dryout of falling film boiling.
- Expansion of existing literature database of the influence of refrigerant conditions on dryout in falling film boiling.
- Operational limits of nanostructured tubes due to critical dryout and CHF recorded
- Influence of nanostructures on falling film boiling heat transfer.
- Mechanisms proposed to explain falling film HTC trends.
- Influence of nanostructures on falling film boiling enhancement.
- Mechanisms proposed to explain falling film boiling enhancement trends.

1.7 Overview of thesis

Chapter **2** reviews relevant literature on topics such as roughness, nanostructures, dryout and CHF and their influence on pool boiling and falling film boiling heat transfer. Chapter **3** details the experimental setup used, the methods of data reduction and the uncertainty of the apparatus, as well as the tubes tested and the surface characterisation of those tubes. Chapter **4** describes the process to validate the experimental setup. Chapter **5** details the pool boiling and falling film boiling heat transfer characteristics of plain tubes of different roughness and material across a range of heat fluxes and refrigerant conditions. The dryout characteristics of the falling film boiling heat transfer as film flow rate is varied is also covered as well as the falling film heat transfer enhancement ratios. Chapter **6** details the pool boiling HTCs measured on nanostructured tubes and details the nucleation site density to help understand the HTCs seen. Cases of pool boiling CHF due to DNB that were recorded on the nanostructured tubes are documented. Chapter **7** focuses on the falling film boiling HTCs measured on nanostructured tubes and details the operational limits due to critical dryout and CHF due to DNB. The HTCs across a range of conditions are investigated, as well as the falling film heat transfer enhancement ratio. Chapter **8** summarizes the key aspects and conclusions of the thesis and provides recommendations for future research work. Appendices **A**, **B** and **C** contain detailed information on the calibration process, uncertainty calculation and Wilson plot investigation respectively and Appendix **D** documents additional results from the study for reference.

2. Literature review

2.1 Introduction

This chapter summarises key concepts as well as the most recent work undertaken in the study of surface and fluid influences on pool boiling and falling film boiling heat transfer with a focus on refrigerants and tubes. The influence of roughness, material, wettability and nanostructures, as well as the fluid influence, is reviewed for pool boiling and falling film boiling heat transfer. The influence of microstructures on heat transfer is discussed, but only with the aim of better understanding nanostructure heat transfer mechanisms, given the relative scarcity of literature on the topic of nanostructure pool boiling and falling film boiling in refrigerants. Falling film heat transfer enhancement mechanisms are discussed, where the heat transfer of falling film boiling is compared with that of pool boiling, because this comparison allows for a greater understanding of falling film boiling based on the more extensively studied and, at times, simpler subject of pool boiling. Lastly, the topics of critical dryout and CHF due to DNB and how they influence and limit pool boiling and falling film boiling heat transfer are reviewed.

2.2 Pool boiling heat transfer

2.2.1 Heat flux

Increases in heat flux increase the heat transfer of pool boiling for plain tubes, with the associated increased wall superheat allowing for smaller nucleation sites to become active, as described by the equilibrium bubble radius. The increased number of active nucleation sites and increased bubble nucleation increase heat transfer through a number of mechanisms such as locally enhanced natural convection through the stripping away of the thermal boundary layer by the departing bubbles and the transport of latent heat away from the surface by the bubbles themselves [30].

2.2.2 Roughness influence

Increases in surface roughness increase the heat transfer in the pool boiling of plain tubes, through an increased number of potential nucleation sites and thus typically, the number of active nucleation sites [31-33].

However, the heat transfer enhancement of increased roughness was found to have a limit, whereafter the HTCs decreased as roughness was further increased [19,34]. Pioro, Rohsenow and Doerffer [34] suggested the reason for this was that once cavities became too large, liquid was able to fill them and they then no longer served as active nucleation sites.

The relative importance of roughness on HTCs has been found to vary depending on fluid factors. Studies showed that the influence of roughness on the boiling curve was stronger at lower reduced pressures than at higher reduced pressures when boiling refrigerants on roughened copper tubes [31,35]. Therefore, as saturation pressure increased, the influence of roughness decreased. The fluid type also played a role in the magnitude of the influence of roughness, as a study by Jones, McHale and Garimella [33] found, namely that water was less sensitive to changes in roughness than the Fluorinert FC-77 when boiling on copper plates.

Jabardo [19] conducted an experimental study of the pool boiling HTCs of R-134a and R-123 on tubes of varying roughnesses and found that as the roughness increased, the sensitivity of the HTCs to changes in heat flux decreased. Jabardo suggested that differences in the population distribution of nucleation sites were the likely cause. Smooth surfaces showed high sensitivity to heat flux because smooth surfaces had a greater number of small cavities, hence the relatively improved performance as heat fluxes were increased because these small cavities were progressively activated. Rougher surfaces showed lower sensitivity to changes in heat flux because they consisted of a greater number of larger cavities that were already activated at lower heat fluxes. As heat fluxes increased, nucleation sites were not activated at the same rate as for smoother surfaces. Jabardo thus suggested that further research into nucleation site distribution should be conducted to better understand this relationship.

Kim et al. [36] found similar results to those of Jabardo, with increased roughness of a copper plate in the pool boiling of water decreasing the sensitivity of the HTCs to heat flux changes. However, in the formulation of an empirical model to predict their measured results, Kim et al. omitted the influence of roughness on the heat flux sensitivity of the HTCs because the omission influenced their model insignificantly, showing the relative coarseness typical of many empirical pool boiling models.

Studies with so-called heterogeneous wetting surfaces further illustrated the importance of the distribution of potential nucleation sites in heat transfer enhancement. Jo et al. [37] conducted a study of pool boiling of water on a heterogeneous wettability surface consisting of hydrophobic dots on a hydrophilic surface. They found that as the number of dots increased, HTCs improved, due to a greater number of active nucleation sites. Bigger dots were better at low heat fluxes, because they were activated easier, while smaller dots were better at high heat fluxes, as the bigger dots (at small pitch diameters) resulted in the vapour bubbles merging and blanketing and insulating the surface. The pitch of the dots also played a role, because at low heat fluxes, the pitch distance dominated the number of dots, while at high heat fluxes, the number of dots dominated and the pitch was less significant.

Yamada et al. [38] also did a study with hydrophobic dots on a hydrophilic surface. Again, larger dots did better at lower heat fluxes, but as heat flux increased, the HTCs of the larger dots increased slower than the small dots, until eventually, their performance was the same at high heat fluxes. This can be interpreted in a similar fashion to the performance of smoother surfaces compared with rougher surfaces discussed already, where the small dots are activated as heat fluxes are increased until they are able to match the heat transfer performance of the larger dot surfaces.

The influence of roughness is typically accounted for through the arithmetical mean roughness, R_a, in a number of correlations [18,31,39]. However, the work reviewed here shows that other factors such as the roughness distribution should also be taken into account when factoring in the influence of surface roughness on heat transfer.

Gorenflo and Kenning [18] and Gogonin [40] all in fact argue that using a single surface roughness parameter such as mean roughness has limitations. Gorenflo and Kenning [18] explain that this is because various types of roughness and surface conditions can produce the same mean roughness while altering the heat transfer process, while Kotthoff and Gorenflo [41] note that a few small rough spots on a smooth surface can influence the overall heat transfer significantly through the motion of sliding bubbles.

However, Gorenflo and co-authors [18,41,42], Jabardo and co-authors [31,32] and Luke [35,43] could not suggest any easily measurable combination of surface parameters that could be used to better quantify the roughness influence on HTCs in pool boiling and thus arithmetical mean roughness still tends to be used by most authors. Therefore, further research or technology development that allows for better quantification of roughness size and distribution influences is still required.

2.2.3 Material influence

In their review of surface influences on pool boiling, Pioro, Rohsenow and Doerffer [34] explain that a key material property that would influence HTCs is the surface conductivity because it would influence the transfer of heat to the nucleation sites. Thus, when nucleation sites are few, the HTCs can be influenced by high thermal conductivities being able to effectively transfer heat to those sites. As heat fluxes increase, higher thermal conductivity materials will outperform their counterparts because they more effectively feed the nucleation sites with heat. At higher surface roughnesses, this influence will be diminished, due to the widespread availability of nucleation sites, and therefore, the reduced reliance on transfer of heat to the sites.

Jabardo, Ribatski and Stelute [32] investigated the influence of surface material of tubes on the pool boiling process using R-134a and R-123. They found that brass and copper had higher HTCs than those of stainless steel, as well as a more rapid increase in HTCs as flux was increased. However, there was no indication of reduced surface material influence at higher roughnesses in their study.

Gorenflo and Kenning [18] captured the influence of surface material in their correlation through the thermal effusivity, e, which is the square root of the product of the material's thermal conductivity, k, and the volumetric heat capacity, ρc_p. Based on data gathered, Gorenflo and Kenning [18] found that the approximate relationship $h \propto e^{0.5}$ fit the data well. However, Gorenflo and Kenning point out that the influence of the surface material (and surface condition) is perhaps the worst understood of the influences on pool boiling.

Bombiardieri and Manfletti [44], for example, found that the thermal effusivity relationship used by Gorenflo and Kenning did not hold for the pool boiling of liquid nitrogen on copper, aluminium and stainless steel polished plates. Higher HTCs were recorded for the stainless steel plates than for the aluminium plates, despite stainless steel having a lower thermal effusivity than that of aluminium.

2.2.4 Wettability influence

Improved wettability has been shown by a number of pool boiling studies to lower HTCs and worsen heat transfer [45-47]. Wang and Dhir [45] conducted an early study where the wettability of polished copper samples was controlled through differences in oxidation. They measured the nucleation site density with an optical microscope and found that increased wettability reduced the nucleation site density and reduced the HTCs measured. The increased wettability was thought to draw liquid into the nucleation sites and thus flood them, reducing the number of active nucleation sites.

However, as heat fluxes increase towards the CHF point, low wettability surfaces create large amounts of vapour which blanket the surface, reducing HTCs and promoting early CHF due to DNB. High wettability surfaces conversely delay the onset of CHF [20].

However, nanostructured surfaces do not always adhere to this relationship. Wu et al. [48] investigated the influence of TiO_2 and SiO_2 nanoparticle coatings on nucleate pool boiling of water and the organic Fluorinert FC-72 on flat surfaces at atmospheric pressure. They found that in water, SiO_2 has similar HTCs to those of the plain surface, while TiO_2 outperformed both, despite having the same roughness and surface structure of the SiO_2 surface. The authors attributed the improved HTCs of the TiO_2 surface to the improved wettability of TiO_2 compared with that of SiO_2, arguing that the improved TiO_2 wettability resulted in enhanced heat transfer mechanisms such as increased liquid-solid interaction and reduced dry patches underneath growing bubbles.

Further testing in FC-72 showed that the TiO_2 surface still had the highest HTCs. The SiO_2 surface now had higher HTCs than those of the plain surface, which the authors argued was due to the roughness of the SiO_2 being utilised because FC-72 fluid properties allowed for a lower active nucleation site diameter threshold than that of water. The TiO_2 surface still had the highest HTCs due to the enhanced heat transfer afforded by its improved wettability while still having a similar roughness to the SiO_2 surface with the associated nucleation site density.

Some studies with nanostructured surfaces with excellent wettability have showed improved heat transfer compared with that of plain surfaces, while some cases showed worsened HTCs compared with those of plain surfaces [17]. Therefore, traditional heat transfer theory may not always apply to nanostructured surfaces due to the novel heat transfer mechanisms at play.

2.2.5 Fluid influence

The boiling of refrigerants on plain surfaces in pool boiling conditions showed increased HTCs as fluid pressure was increased [30] or when fluids with increased saturation pressures were used at the same saturation temperature [49-52]. The influence of saturation pressure is often captured in the form of reduced pressure in a number of correlations [30], and these results show that as reduced pressure is increased, HTCs increase for plain surfaces. Pressure has also been found to influence the sensitivity of HTCs to changes in heat flux. Kotthoff and Gorenflo [41] found that as reduced pressure increased, HTCs became less sensitive to changes in heat flux.

Differences in other properties, such as density and latent heat of vapourisation, at the same reduced pressure are expected to influence the heat transfer through changes in factors such as thermal layer thicknesses and bubble dynamics, as evident by their presence in a number of correlations predicting bubble growth rate and bubble release diameter and frequency [30].

However, Gorenflo et al. [53] argue that the influence of thermophysical properties on pool boiling HTCs are mostly captured through the influence of reduced pressure changes, and that the influences of changes in other properties at constant reduced pressure are significantly smaller. Similar arguments resulted in a number of correlations that used reduced pressure as the key parameter to define the influence of thermophysical properties on pool boiling HTCs [18,30,39].

Studies such as those by Van Rooyen and Thome [52], who found that R-134a outperformed R-236 on Turbo-B5 tubes in pool boiling, and by Christians and Thome [13], who found similar results on Turbo B5 and Gewa B5 tubes, show that the trend of higher HTCs as reduced pressures are increased often applies to microstructured tubes as well.

However, changes in reduced pressure do not always have consistent influences, particularly with refrigerants at high reduced pressures. Webb and Pais [49] conducted pool boiling studies using R-11, R-12, R-22, R-123 and R-134a on single plain tubes as well as microstructured tubes, namely low-finned, Turbo-B, Gewa TX19 and Gewa SE tubes, and found an anomaly in the trend of reduced pressures dictating the refrigerant influence on HTCs. They found that the HTCs increased as fluids with higher saturation pressures and respectively higher reduced pressures were used on most of the tubes, with the HTCs highest for R-22, followed by similar HTCs for R134a and R12, and lastly, similar HTCs for the lowest-pressure refrigerants R-11 and R-123. However, refrigerant R-11 went from having some of the lowest HTCs measured across the conditions to having some of the highest HTCs when tested on the Turbo-B tube. They could not provide a possible explanation for the anomaly, but did repeat the experiments and found the anomaly consistent. It is possible that the Turbo-B tube had the optimal geometry for the bubble dynamics produced by boiling R-11.

A study by Jung, An and Park [50] also illustrated how increased reduced pressure does not always lead to increased HTCs. They tested plain, low-finned, Turbo-B and Thermoexcel-E tubes with R-125, R-32, R-22 and R-134a in pool boiling conditions over fluxes from 10 to 80 kW/m^2 at a saturation temperature of 7°C. Plain and low-finned tube HTCs did not follow the trend of the reduced pressures and instead, the HTCs followed the trend of the saturation pressures, with the highest HTCs measured on R-32, followed closely by R-125, R-22 and R-134a. However, Jung, An and Park [50] noted that these results could also be interpreted as having followed the trend of reduced pressures except for R-125, which may have poorer thermophysical properties than those of R-32 resulting in HTCs that were slightly lower than those of R-32.

The Turbo-B and Thermoexcel-C results of Jung, An and Park [50] also showed the highest HTCs for R-32, followed by R-22 and R-134a, in line with the reduced pressures of these refrigerants. R-125 again bucked the trend, with the second or third highest HTCs on the Turbo-B tube, and the lowest HTCs on the Thermoexcel-C tube. Jung, An and Park [50] ascribe the peculiar behaviour of R-125 to its high reduced pressure, noting that refrigerants at high reduced pressures often do not benefit from the advantage of microstructured surfaces because the high reduced pressures mean that nucleation sites are already activated and do not need the geometric features of the microstructures to create active nucleation sites. The geometric features of the microstructures tested may also not have been suited to the particular bubble mechanics of R-125.

The studies by Webb and Pais [49] and Jung, An and Park [50] highlight that while reduced pressure is often the best indicator of the expected magnitude of HTCs when testing different refrigerants, it is not always the dominant property. The interplay between microstructure geometry and the specific bubble dynamics of the refrigerant used can invalidate this correlation, as well as HTCs measured at high reduced pressures, even on plain surfaces.

Nanostructured surfaces have also showed instances where increases in pressure were not accompanied by increased HTCs, such as reported in the work by Zimmermann et al. [54], who saw no real influence of pressure in the pool boiling of organic fluids on nanostructured surfaces.

2.2.6 Microstructured surfaces

Microstructured surfaces (also known as micro-enhanced or 3D-enhanced surfaces) have surface structures with dimensions in the micrometre range and are widely used in industry to enhance heat transfer, with a wide variety of structures available [55]. Microstructured surfaces were not tested in this study, but a few studies of microstructured pool boiling focusing on the mechanics of microstructure heat transfer enhancement were reviewed due to their relevance to this study and the sparsity of pool boiling studies of nanostructured surfaces with organic fluids.

The presence of microstructures can complicate and invalidate HTC trends seen on plain surface pool boiling, as already discussed under the previous section on the influence of refrigerant conditions. Increases in heat flux on microstructured surfaces lead, for example, to HTCs either increasing [8,9,23,56,57], decreasing [10,11,58] or remaining constant [13,59].

Microstructured surfaces have enhanced HTCs by factors as high as 10 to 15 compared with those of plain surfaces under optimal conditions [5]. Thome [55] identifies six key mechanisms that contribute to the high thermal performance of these surfaces. The first three describe the increased amount of heat leaving the surface via latent heat:

- Nucleation superheat: The re-entrant cavities typical of many microstructured surfaces allow bubble nucleation to occur at lower superheats than for plain tubes with non-re-entrant cavities.
- Thin film evaporation: The complex geometries also allow bubbles that pass through the surface to create thin evaporating films of liquid.
- Capillary evaporation: Capillary pores with a liquid meniscus can promote evaporation as heat is conducted to the liquid at this liquid-vapour interface.

The next three mechanisms describe those that increase the amount of heat leaving the surface as sensible heat:

- External convection: The large quantity of bubbles produced by these surfaces further enhances the external convection adjacent to the surface through liquid agitation and stripping of the thermal boundary layer.
- Internal convection: The departing bubbles induce flow within the often porous surfaces, which can result in high HTCs due to the small radius of these micro-channels

- Wetted surface area: The complex geometries of these microstructured surfaces result in wetted surface areas that are as much as 10 times greater than the respective plain surface.

Visualisation studies by Nakayama et al. [60-62] of pool boiling of R-11 on custom-manufactured microstructured surfaces with controlled pore sizes and interconnected cavities recorded that liquid was pumped through the interconnected cavities induced by the nucleating bubbles. Nakayama et al. highlighted the importance of the heat leaving the surface from latent heat mechanisms, but also showed that under certain conditions, sensible heat mechanisms could become dominant and could contribute as much as 85% of the total heat removed [55,61,62].

2.2.7 Nanostructured surfaces

Nanostructured surfaces can improve or worsen boiling heat transfer compared with plain surfaces. Some of the earliest created nanostructured surfaces were through the surface deposition of nanoparticles during the boiling of nanofluids. At times, this produced improved heat transfer, with increased roughness and thus increased nucleation site densities, or worsened heat transfer with nanoparticles filling the pores of the surface and reducing roughness or adding a low thermal conductivity layer on top of the surface [24]. Subsequently, various nanostructures were created through chemical and mechanical means with varying influences on boiling heat transfer [16,17,20,25,26]. Cases with improved heat transfer were attributed to the increased roughness of the surfaces, capillary pumping of liquid to nucleation sites by wickable surfaces, the positive modification of bubble dynamics and surfaces with lower wettability activating a greater number of nucleation sites [16,17,20]. Deterioration in heat transfer was typically attributed to lower nucleation site densities caused by either lower surface roughness or the flooding of nucleation sites through increased wettability [17,20,26].

Previous studies were conducted on the nanostructured surfaces used in this study, but only with water at atmospheric pressure on flat surfaces or wires. The LbL nanoparticle coating method implemented in this study was used to produce hydrophilic and hydrophobic coatings for the pool boiling of water on nickel wires [46]. Compared with the uncoated wire, the heat transfer improved for the hydrophobic wire and worsened for the hydrophilic wire, despite the coating producing a similar roughness. Images showed that the hydrophobic wire had more nucleation sites and the hydrophilic wire had fewer nucleation sites than those of the uncoated wire. Therefore, the wettability of the surfaces appeared to play a major role in the heat transfer, either flooding or activating cavities.

The CuO surface used in this study was found to produce either lower [63] or equivalent heat transfer [64] to plain surfaces when boiling water at atmospheric pressure. Rahman et al. [64] conducted a water pool boiling study where infrared high-speed thermometry was used to measure the time-dependent heat flux distribution at the bubble footprints. They observed that the bubble base diameters were larger on the CuO surface than on the plain surface. The CuO surface also had a lower bubble departure frequency and lower nucleation site density than those of the plain surface, despite similar HTCs. Dryout was observed to be reduced underneath the growing bubbles on the CuO surface, with the evaporation of liquid underneath the bubbles supplied by capillary wicking put forward as the cause. This provided an additional heat flux pathway compared with the plain surface, increasing heat transfer at nucleation sites.

Studies of the pool boiling of refrigerants or similar organic fluids on nanostructured surfaces are relatively rare, as evident in the reviews of the topic [16,17,20]. Heat transfer was worsened when Trisaksri and Wongwises [65] added titanium dioxide (TiO_2) nanoparticles to refrigerant R-141b for the pool boiling of a copper tube. Considering that their tube was sandblasted and thus had a relatively high roughness (R_a of 3.14 µm), it was likely that the nanoparticles deposited on the surface reduced the roughness and number of active nucleation sites. The heat transfer of plain surfaces was improved in some studies when nanostructures were used in the pool boiling of refrigerants [66] and Fluorinerts [48,67,68] and the flow boiling of Fluorinerts [69], with authors attributing this to increased nucleation site density caused by the particular nanocoatings used.

In some cases, the nanostructures only improved the heat transfer at higher heat fluxes, while at lower heat fluxes, the plain surfaces were comparable or better than the nanostructured surface [54,70]. Comparing this result with those discussed under the section detailing the influence of roughness on pool boiling, this points to the nanostructures changing the population distribution of the nucleation sites, with the nanostructured surfaces possibly having a large number of small nucleation sites that only activate at high heat fluxes.

Nanostructured surfaces are expected to share some of the heat transfer mechanisms discussed under the preceding microstructure section considering the often-porous nature and expected presence of capillary wicking. However, considering the difference in scale of nanostructures, where bubbles are not able to nucleate within the much smaller nanoporous layers but rather on top, the relative importance and presence of the six microstructured enhancement mechanisms listed in Section **2.2.6** are expected to differ from nanostructured surfaces.

The results of Wu et al. [48] illustrate this. As discussed in Section **2.2.4**, Wu et al. investigated the heat transfer of TiO_2- and SiO_2-coated surfaces and found that the improved wettability of the TiO_2 surface allowed for improved HTCs compared with the SiO_2 surface, suggested to be due to increased liquid-solid interaction and reduced dry patches underneath growing bubbles. The increased liquid-solid interaction explanation falls within the framework that Thome [55] gave for microstructures, with increased sensible heat transfer due to increased natural convection within the nanostructured porous layers and greater wetted surface area. The reduced dryout underneath the bubbles is a mechanism not within Thome's framework and thus a unique nanostructured surface mechanism, which has been confirmed to take place by Rahman et al. [64], already discussed in this section. The relative contribution of these various mechanisms for nanostructures must still be understood and quantified.

2.3 Falling film boiling heat transfer

Ribatski and Jacobi [1], Thome [5], Fernandez-Seara and Pardiñas [2] and Abed et al. [6] provide reviews on the subject of falling film evaporation in the refrigeration industry that provide relevant background to the topic in general.

2.3.1 Heat flux

A number of falling film boiling studies [11,12,14,22,71-73] with refrigerants on the outside of plain horizontal tubes showed that increases in heat flux increased the HTCs measured up until a point, whereafter the HTCs began to decrease. However, Moeykens, Huebsch and Pate [71] and Zhao et al. [22] showed that if the film Reynolds number was increased, the HTCs at lower heat fluxes remained constant, while the HTCs at higher heat fluxes increased, which suggests that some form of dryout is often the cause for lowered HTCs at high heat fluxes. Dryout of falling films is discussed in further detail in the upcoming Section **2.6**.

Jige, Miyata and Inoue [14] tested plain tubes under falling film evaporation conditions, which ranged from 2.5 to 40 kW/m^2, and so covered both convective and boiling falling film heat transfer modes. The tests were conducted in R-1234ze(E) and R-245fa across a range of film Reynolds numbers from 100 to 1 000 and at saturation temperatures of 10°C and 20°C. Below a heat flux of 5 kW/m^2 for R-1234ze(E) and 10 kW/m^2 for R-245fa, changes in heat flux had no influence on the HTC; and the HTCs were similar for both refrigerants. No bubbles were seen on the tubes under these conditions and thus were considered convective heat transfer conditions. Beyond these thresholds, as heat flux was increased, bubbles were seen on the surface of the tubes and the HTCs increased as heat flux was increased, showing that nucleate falling film boiling was becoming the dominant heat transfer mechanism and was the cause of the increased HTCs as heat flux was increased.

2.3.2 Roughness, material and wettability influence

The absolute magnitude of the heat transfer measured on plain copper tubes varied between falling film boiling studies, with the HTCs measured in R-134a at saturation temperatures close to 5°C by Roques and Thome [11] between three and six times higher than those measured by Moeykens, Huebsch and Pate [71], while the HTCs measured by Zhao et al. [22] fell closer to the data of Moeykens, Huebsch and Pate [71].

The wide spread of results between these studies of plain copper tubes may be influenced by the differences in saturation temperature between the studies, with the studies of Moeykens, Huebsch and Pate [71], Roques and Thome [11] and Zhao et al. [22] conducted at 2, 5 and 6°C respectively with R-134a. However, Zhao et al.'s [22] data shows that a 4°C increase in saturation temperature from 6 to 10°C will result in an increase in HTC of between 12 to 1 % across the heat flux range of 20 to 80 kW/m^2 in R-134a, which suggests that the large differences seen between studies is not alone due to saturation temperature differences. The study of Moeykens, Huebsch and Pate [71] did make use of a spray distributor, while Roques and Thome [11] and Zhao et al. [22] made use of gravity-fed distributors. This may also have contributed to some of the differences seen, although spray distributors are expected to increase the HTCs of the Moeykens, Huebsch and Pate [71] study compared to the others, not decrease them [2].

A significant contributing factor to the spread of results may in fact be due to differences in roughness, because the influence of surface roughness on falling film boiling has had little attention. Much of the work that was done on falling film boiling of refrigerant on plain tubes was done without the measurement of the surface roughness of the tubes, thus limiting the database of information available. For example, early work by Moeykens, Huebsch and Pate [71] and more recent work by Chien and co-authors [72-74], Jige et al. [14], Ubara et al. [56] and the group of Prof. Tao [8,9,12,22] on plain tubes did not measure the surface roughness of the tubes.

The arithmetic mean roughness, R_a, of the plain tubes used by Roques and Thome [11] was measured as 0.8 µm, which is relatively high when compared with the typically quoted roughness range of commercial tubes of 0.2 µm to 0.6 µm [18]. Both Moeykens et al. [71] and Zhao et al. [22] did not state the roughness of their tubes, but this factor may go some way towards explaining the differences in the HTC magnitudes, with the high roughness of Roques and Thome's tubes a likely reason for the higher HTCs.

However, no experimental data is available at present to determine the influence of roughness on falling film boiling HTCs and whether it will follow the same trend as seen in pool boiling.

All the studies described conducted tests on copper tubes and thus, similarly, there is a lack of data on whether falling film boiling of refrigerants on different material surfaces will influence HTCs in a similar manner as seen in pool boiling.

Lastly, there is a lack of information on the influence that wettability has on falling film boiling. Zheng et al. [75] conducted a study of convective heat transfer in falling films of water and found HTCs to be similar for plain, hydrophilic and superhydrophilic tubes if sufficient fluid was supplied to prevent dryout. However, under falling film boiling conditions, the influence of wettability has not been explicitly investigated yet.

2.3.3 Fluid influence

A number of studies by the group of Professor Tao and co-authors [8,12] showed that the falling film boiling HTCs on plain tubes tended to increase as refrigerants with higher reduced pressures were used.

Zhao et al. [8] tested R-134a and R-123 at a saturation temperature of 6°C for the falling film boiling of plain and microstructured tubes across a heat flux range of 20 to 60 kW/m^2 and a refrigerant film flow rate of 0 to 0.16 kg/m/s. The HTCs measured with the higher-pressure R-134a were approximately 2.5 times higher than those of the lower-pressure R-123.

Jin et al. [12] conducted a study of falling film boiling on plain tubes in R-134a, R-290 (propane) and R-600a (isobutane) at a saturation temperature of 6°C across heat fluxes of 10 to 150 kW/m^2 and film Reynolds numbers of 0 to 2 200. They found that R-290 produced the highest HTCs, followed by R-134a and then R-600. This follows the trend of the reduced pressure of these refrigerants at 6°C.

Studies of falling film boiling have also confirmed that as saturation pressure and temperature are increased, falling film boiling HTCs have increased [14,76,77] on plain and microstructured tubes, which also shows that higher reduced pressures result in higher HTCs for falling film boiling.

Another study by Jin et al. [9] found the falling film boiling HTCs of plain tubes were higher for R-410a than for R-32, which again follows the trend, because R-410a has a higher reduced pressure than R-32.

However, Jin et al. [9] recorded an exception to this rule when the HTCs of plain tubes decreased as the saturation temperature was increased from 6°C to 10°C. Considering that the R-32 and R-410a used in the study are both high-pressure refrigerants, these results are similar to those of the pool boiling results of Jung, An and Park [50] already discussed, where the high-pressure refrigerant R-125 had lower HTCs than refrigerants with lower reduced pressures. Therefore, the falling film results of Jin et al. [9] are likely a result of a similar mechanism to that suggested for the pool boiling results of Jung, An and Park [50], with high reduced pressure refrigerants likely already having high active nucleation site densities and subsequent further increases in reduced pressure not resulting in further HTC benefit, and possibly even worse HTC performance due to now non-optimal bubble dynamics or increased bubble-induced dryout in the case of falling film boiling specifically.

Jin et al. [9], as well as Christians and Thome [13], Jige et al. [14] and Zhao et al. [57], also found that when saturation temperatures were increased for falling film boiling on various microstructured tubes, the HTCs were barely influenced. Considering the previous discussion about pool boiling results of a similar nature, this may also be caused by microstructured tubes having already fully activated all nucleation sites and thus not benefiting from further increases in reduced pressure, or non-optimal bubble dynamics arising that do not interact well with the specific microstructures tested.

2.3.4 Microstructured surfaces

Microstructured surfaces showed a number of trends in falling film boiling similar to pool boiling. Increases in heat flux also had varying influences on HTCs across different microstructured surfaces, because HTCs increased [8,9,23,56,57], remained constant [13,59] or decreased [10,11,58] as heat flux was increased in falling film boiling.

A number of studies by Professor Tao and co-authors investigated microstructured tubes under falling film boiling conditions. Most recently, Jin et al. [10] investigated a microstructured tube and found that as heat flux was increased from 5 to 120 kW/m^2, HTCs increased at first, peaked at approximately 10 to 30 kW/m^2 and then decreased as heat fluxes were further increased. These tests were conducted in R-134a at a saturation temperature of 6°C and film Reynolds numbers of 800 and 1 600. The enhanced tube HTCs were approximately six times those of plain tubes at 5 kW/m^2, but equal to those of the plain tubes at 120 kW/m^2. Therefore, the microstructured tube may not have been able to benefit any further from increases in heat flux above 5 kW/m^2 as a result of already activated nucleation sites, and instead, non-optimal bubble dynamics may have arisen as heat flux increased and even internal dryout of the porous microstructured surface.

Ubara, Asano and Sugimoto [56] conducted falling film boiling studies on a plain and microstructured tube in R-134a at a saturation temperature of 20°C. Heat fluxes were varied between 10 and 85 kW/m^2 and film Reynolds numbers from 323 to 643. The microstructured tube was created by the thermal spray coating of a plain tube with melted copper, which created a porous layer approximately 0.1 mm thick. This created a very rough microstructure, with a laser microscope measuring an average roughness of 20.6 µm. This porous surface with many internal and external cavities had HTCs up to five times that of the plain tube. This high enhancement was recorded at the lower end of the heat flux range at 10 kW/m^2, which Ubara, Asano and Sugimoto pointed out likely indicated a high nucleation site density. As heat fluxes were increased, the HTCs of the microstructured tube were less sensitive to heat flux changes than for the plain surface, with the enhancement ratio of the microstructured tube dropping to approximately 2 at 85 kW/m^2. Again, the high active nucleation site density of the microstructured tube at low heat fluxes could mean that further increases in heat flux did not result in increases in nucleation site density to the same extent that occurred on the plain surface.

2.3.5 Nanostructured surfaces

No works of literature were found on falling film boiling on what could be classified as nanostructured surfaces. This presented an opportunity to see whether the various advantages of pool boiling on nanostructures discussed already could be applicable to falling film boiling of refrigerants. A significant advantage of nanostructured surfaces is their improved wettability, which could possibly reduce the influence of dryout on falling film boiling. The possible dryout of nanostructured surfaces is discussed in more detail in Section **2.6.4**.

2.4 Falling film heat transfer enhancement

The falling film heat transfer enhancement ratio, K_{ff}, is the ratio of falling film boiling HTC to pool boiling HTC and gives insight into the falling film boiling process. Unfortunately, many authors do not explicitly calculate it, such as Moeykens, Huebsch and Pate [71], Chien and Chen [73] and Zhao et al. [22], or it is often calculated with pool boiling correlations, which themselves often have a high degree of uncertainty that is thus incorporated into the K_{ff} ratios calculated.

2.4.1 Plain tubes

Falling film heat transfer enhancement ratios for plain copper tubes at saturation temperatures close to 5°C with R-134a are provided in **Figure 2-1.** Extracting data from the studies' published plots of the falling film boiling and pool boiling HTCs allowed the calculation of the enhancement ratios so that it could be compared with those of Roques and Thome [21], who did explicitly calculate them.

There is significant scatter between the authors. Roques and Thome [21] calculated enhancement ratios of 1.4, which were relatively insensitive to variations in heat flux from 20 to 60 kW/m^2. Both Zhao et al. [22] and Moeykens, Huebsch and Pate [71] had enhancement ratios that were both lower and more sensitive to changes in heat flux than those of Roques and Thome [21]. Moeykens, Huebsch and Pate [71] conducted their studies at relatively low film Reynolds numbers where some form of dryout could be expected to have deteriorated the heat transfer process, which could account for their lowered results. The reasons for the differences between the ratios of Zhao et al. [22] and Roques and Thome [21] are difficult to determine. As stated previously, Roques and Thome [21] conducted their tests on tubes with relatively high roughness compared with that of typical commercial tubes. It can thus be hypothesised that Zhao et al. [22] conducted their tests on smoother tubes, which could have caused the differences in their results. The results of Chien and Chen [73] are difficult to explain.

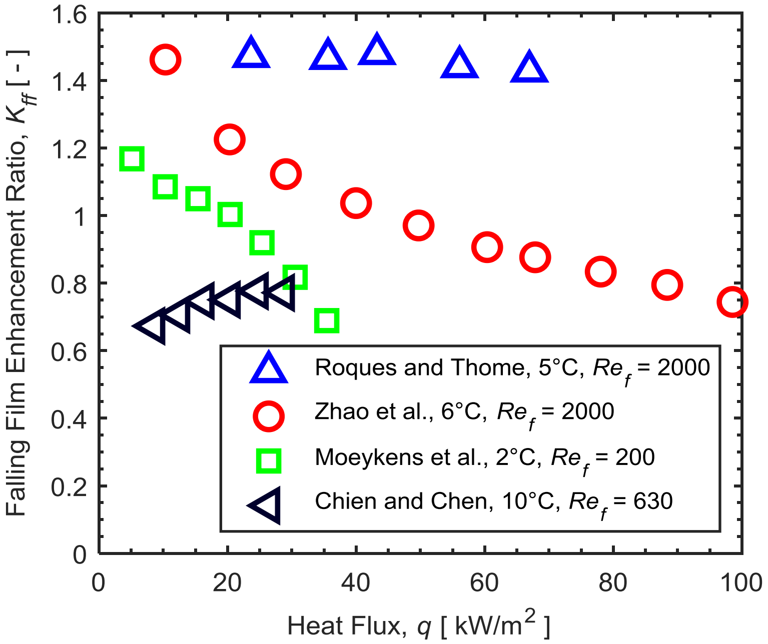

Figure 2-1. Comparison of literature values for K_{ff} of plain tubes in R-134a at saturation temperatures close to 5°C (Roques and Thome [21], Zhao et al. [22], Moeykens, Huebsch and Pate [71], Chien and Chen [73]).

Falling film boiling heat transfer has been shown to outperform the respective pool boiling heat transfer not only on the outside of horizontal tubes, but also in thin falling vertical films [78] and in thin stationary horizontal films [79]. In fact, Nishikawa et al. [79] found that as the liquid level was dropped in pool boiling experiments of water, ethanol and an aqueous solution of sodium oleate, the HTCs remained relatively constant until the level dropped below approximately 5 mm, whereafter the HTCs increased.

The nature of boiling in thin films, either stationary or moving, is clearly different from pool boiling. Mesler [78] and Cerza and Sernas [80] theorise that the enhancement is caused by bubbles becoming trapped in the thin films, with the increased microlayer evaporation through the bubble base enhancing heat transfer in particular. Mesler and Mailen [81] further hypothesised that the seeding of secondary nucleation sites from bubbles bursting while being trapped in the thin films also contributes to the thin film heat transfer enhancement.

It thus follows from literature that studies of falling film boiling with refrigerants on plain tubes are fairly limited and there is significant disagreement between results, particularly concerning the falling film heat transfer enhancement ratio for plain tubes. Few authors measure and quote their surface roughness and as such, it is difficult to infer the influence of surface roughness on falling film boiling HTCs and falling film heat transfer enhancement. Furthermore, all studies reviewed make use of copper tubes. At present, there is thus a research gap because no experimental studies have focused on quantifying the influence that surface roughness or surface material has on the falling film boiling of refrigerants and the falling film heat transfer enhancement ratio.

2.4.2 Microstructured tubes

Roques and Thome [21] measured K_{ff} ratios for microstructured tubes and a plain tube in the range of 1 to 1.5 in R-134a at a saturation temperature of 5°C and across a range of heat fluxes of 20 to 80 kW/m^2 at film Reynolds number above 1000.

Christians and Thome [13] recorded K_{ff} ratios as high as 2.5 in their study of the microstructured Turbo-B5 and Gewa-B5 tubes in R-236fa and R-134a at a saturation temperature of 5°C, across refrigerant film Reynolds numbers of 0 to 3000 and heat fluxes of 20 to 60 kW/m^2. The enhancement ratios were between 1.5 and 2.5 in R-236fa for both tubes, while only between 1 and 1.5 in R-134a for both tubes.

Christians and Thome [82] subsequently speculated that the capillary pumping of liquid by departing bubbles through the microstructured surface structures, discussed previously in Section **2.2.6**, was a key mechanism to understand their results. The commercial Turbo-B5 and Gewa-B5 tubes had geometric features, such as pore size, optimised for use in R-134a pool boiling. Therefore, the R-236fa pool boiling HTCs may have been suppressed due to non-optimal capillary pumping of liquid through the microstructured porous surface under pool boiling conditions, because the bubble departure properties will have been altered by the change in refrigerant and would not be suited to the geometry of the tubes. The falling film HTCs might not have been similarly suppressed because the bubbles were driven not only by buoyancy forces as in the pool boiling case, but also by entrainment in the flowing thin film, providing a large enough pressure differential to overcome the increased pressure drop within the capillary pores due to poorly optimised geometric features. This would have led to increased K_{ff} ratios under R-236fa. However, the K_{ff} ratios of R-134a were far more typical of microstructured tubes and plain surfaces because the pool boiling HTCs were not suppressed.

Ji et al. [23] found values of approximately similar magnitude to those of Roques and Thome [21] in their study of a re-entrant microstructured tube with K_{ff} ratios of between 1.2 and 0.95 measured across a heat flux range of 10 to 50 kW/m^2, where tubes were tested in R-134a at a saturation temperature of 11°C and at film Reynolds number of 2 000.

Ji et al. speculated that a mechanism almost opposite to that suggested by Christians and Thome [82] could be at play to explain their results, suggesting that under pool boiling conditions, the bubble buoyancy allowed for easier bubble detachment, while under falling film conditions, bubble detachment from nucleation sites was more difficult because it was only driven by liquid flow. They suggest that at low heat fluxes, this is not a major factor given the low nucleation site density, while at increased heat fluxes (40 kW/m^2 in Ji et al.'s study), this becomes a problem for falling film boiling and thus the enhancement ratio falls below 1.

These differing views illustrate that there is still debate concerning the mechanisms at play in falling film heat transfer enhancement and further research must be done on the topic.

2.5 Terminology for operational limits of falling film and pool boiling

It should be noted that the term CHF is not used nor measured consistently between pool boiling and falling film boiling studies. Falling film boiling studies have at times defined CHF as the point where wall superheats increased dramatically as a result of DNB where the falling liquid film separates from and no longer wets the boiling surface [83,84], while other studies defined CHF as where wall superheat dramatically increased as a result of dryout as film flow rates were reduced, with no liquid separation from the boiling surface [85,86]. Onset-of-dryout was another falling film boiling limit defined in some studies [11,12] which referred to the point where HTCs collapse as a result of dryout as film flow rates were decreased.

Pool boiling studies meanwhile typically use the term CHF to indicate the peak heat flux that can be reached as wall superheats are increased before the heat flux collapses due to DNB and the accompanying presence of an insulating vapour film and separation of the fluid from the surface [30,87], as dryout due to a lack of liquid mass flow is not a mechanism present in pool boiling.

In this study, as the CHF point for falling film boiling can be a result of either dryout or DNB, the term DNB CHF has been used to describe the peak heat flux recorded before the heat flux collapsed because of DNB in pool boiling or falling film boiling. Falling film boiling studies would thus experience a separation of the falling liquid film from the boiling surface and pool boiling studies would experience a similar separation of the bulk fluid from the boiling surface.

In falling film boiling the term critical dryout was defined as the point where wall superheat increased, and thus HTCs collapsed, as the film flow rate was decreased, with liquid boiling on the tube surface in parts and no liquid separating from the tube. The term critical dryout is thus the same as the term onset-of dryout already mentioned. Dryout CHF was defined as the minimum film flow rate that could support a particular set heat flux, or vice versa, and only occurred once the film flow rate was decreased beyond that of the critical dryout point. However, while the dryout CHF was recorded, it was not discussed in any detail in this study as the critical dryout point was used as the dryout operational limit. Critical dryout is the more conservative dryout limit and is typically used within more recent falling film boiling studies [8,9,11,12]. Precise descriptions of how these limits were measured are given in Section **3.7** as part of the data reduction.

2.6 Dryout of falling films

The refrigerant film flow rate of the falling film on the outside of the boiling tube has been shown to influence heat transfer in two distinctive regimes. At higher film flow rates, HTCs are relatively stable as film flow rates are varied, termed the plateau region. However, as refrigerant film flow rates drop a critical threshold is eventually reached where HTCs decrease dramatically due to a permanent breakdown in the thin film with large dry patches present as a result of insufficient liquid supply [11,22]. This critical dryout threshold is an operational limit of the falling film boiling process due to the rapid reduction in HTCs.

2.6.1 Mechanics of thin film breakdown

The film Reynolds number is defined as the ratio of inertial forces to viscous forces for thin flowing films and is used to determine whether the thin film flow is in the laminar or turbulent regime. It is defined for one side of a tube as

$$Re_f = \frac{2\dot{m}_r}{\mu_l L} \qquad \text{2-1}$$

The film Reynolds number is also typically used in calculations of film thickness and thin film convective HTCs [30].

Hartley and Murgatroyd [88] undertook a theoretical examination of the conditions necessary to maintain a dry patch on a flat vertical plate under a thin falling film of liquid. Considering conditions with no heat transfer, a force balance determined that a stagnation pressure force as a result of the flowing fluid would attempt to close dry patches and would have to balance the surface adhesion force between the liquid and plate that would tend to keep dry patches open, once a dry patch had already formed. This force balance was used to calculate the minimum wetting rate (MWR) required to prevent dry patches from remaining on surfaces.

Zuber and Staub [89] extended the analysis of Harley and Murgatroyd to include heat transfer. Two new forces that both act to open dry patches were added to the force balance, namely the vapour thrust force and the thermocapillary force. The vapour thrust force opens dry patches through the vaporisation of fluid at the interface of the liquid film and dry patch. The thermocapillary force opens the dry patch due to the Marangoni effect, where a section of liquid film may be superheated for a number of reasons, such as a local thinning of the liquid film. This temperature gradient results in an associated surface tension gradient across the liquid film which, in turn, results in a net mass transfer and net force. Given that in most typical heat transfer fluids, surface tension decreases as temperature rises, this will cause a surface tension gradient that increases away from the typically thinned film with localised superheating. The thermocapillary force thus typically opens dry patches in falling films. Zuber and Staub [89] used this theoretical underpinning to produce a prediction for the MWR for heated films.

These theoretical models have been extended since to accommodate further considerations, such as the work by Ruckenstein [90], who accounted for rivulets within the falling liquid film.

A further force to consider is the vapour shear force, with the flow of vapour over the thin falling film generating a shear stress. This force may open up dry patches if counter-current to the falling film, but may close up dry patches if flowing co-currently. Ribatski and Thome [91] found that co-current vapour flow of up to 1 m/s had no appreciable impact on HTCs measured in falling film boiling of R-134a, while counter-current vapour flow lowered HTCs by up to half at lower refrigerant film flow rates. Ji et al. [59] tested a microstructured tube in falling film boiling conditions of R-134a and they found that the influence of counter-current vapour flow was very complex, with changes in HTCs due to vapour flow of a few percent up to 120%. However, they argue that these effects can be ignored because the significant vapour influences are only measured at vapour flow speeds far higher than those present in industrial evaporators. Cross vapour flow is another consideration that has been investigated recently by Zhao and co-authors [57,92] with again complex interactions found, although Zhao et al. [57] did note that generally, the HTCs were weakened by the presence of cross vapour flow.

Dryout is also dependent on whether dry patches are already present, as the MWR can be as much as four times higher to rewet a surface that is initially dry compared with the MWR required to prevent an already wet surface from creating dry patches [93].

The creation of the dry patches has been thought to occur through a number of mechanisms. Cerza [94] suggests that there are two key mechanisms in falling film boiling, namely the evaporation of thinned regions of liquid film formed from the turbulent flow of the liquid and the dryout of the microlayer underneath bubbles, with a dry patch visible once the bubble bursts. Thin film boiling is thus expected to suffer more from dryout than convectively heated thin films, due to the presence of higher wall heat fluxes that evaporate the fluid more readily as well as the presence of bubbles and the subsequent opportunity for microlayer dryout.

2.6.2 Plateau region

The plateau region occurs at film flow rates above the critical dryout threshold where HTCs are less sensitive to changes in film flow rate than HTCs at film flow rates below the critical dryout threshold. HTCs have been found to remain completely insensitive to changes [11,12] or slightly decrease [8,9] or slightly increase [10] in the plateau region, but all changes are significantly less severe than the sensitivity of HTCs seen once critical dryout has occurred.

Compared with each other, plain tubes exhibit differences in sensitivity of HTCs within the plateau region across various studies. The falling film boiling HTCs shown by Jin et al. [12] and Roques and Thome [11] were found to be relatively insensitive to changes in film flow rate with variations of less than 5%. However, Zhao et al. [22] found a greater sensitivity of HTCs to changes in film flow rate within the plateau regime, with HTCs changing by approximately 10% to 25%. It is difficult to say whether possible differences in tube roughness caused these different HTC sensitivities to film flow rates or whether other factors, such as differences in the effectiveness of falling film distributors, were the cause.

The plateau region must not be confused with an always fully wetted region that occurs only above the MWR, because dry patches have been noted to occur while operating within the plateau region. However, these dry patches have been noted to be temporary [91].

Microstructured tubes often show plateau regions with HTCs that are particularly insensitive to changes in film flow rate [8,10,11,23]. There were also cases with microstructured tubes where reducing film flow rates had minimal effect on HTCs up until a point, whereafter HTCs increased. Shortly after this increase in HTCs, if the film flow rate was decreased any further, the HTCs collapsed due to critical dryout [8,10]. This created an HTC 'hump' just prior to the collapse of the HTCs due to critical dryout.

Microstructured tubes are considered to have improved wetting compared with plain tubes as a result of the interconnected channels and pores which reduce the onset of dry patches [8,91]. The improved wettability may be the cause of the HTC hump, because the microstructured tubes are able to support a layer of liquid that is so thin with no dry patches forming that the liquid film becomes superheated, decreasing the evaporative resistance to the point that it can meaningfully contribute to the overall HTC.

2.6.3 Critical dryout

Critical dryout occurs once stable dry patches form on the tube and severely decrease the HTCs [11]. Ueda et al. [85] provided an illustration of both critical dryout and DNB CHF limitations for the falling film boiling of water and refrigerants R-11 and R-113 on the outside of vertical tubes. Ueda et al. defined three types of critical limitations, the first two of which are termed in this study critical dryout and the third termed DNB CHF. Each limit was identified by a sharp rise in wall temperature and each typically occurring at different film flow rates. At the lowest film flow rates Type I critical dryout occurred, characterised by dryout as a result of a film flow rate below that of the MWR of the surface. Type I critical dryout was not significantly influenced by changes in boiling heat flux. Type II critical dryout occurred at typically higher film flow rates with dryout occurring at film flow rates above that of the MWR of the surface and was dependent on heat flux. Type I and II critical dryout both consisted of dry patches limiting the boiling heat transfer, with wetted patches still boiling. The third critical limitation was as a result of DNB CHF and is discussed in Section **2.7**. Ueda et al. [85] thus showed that falling film boiling could in cases be limited by either critical dryout or DNB depending on conditions

Roques and Thome [21] showed that as heat flux was increased, the film Reynolds number at which critical dryout occurred increased almost linearly for both a plain tube and three microstructured tubes tested in R-134a at 5°C.

Refrigerant properties influence the point of critical dryout. Christians and Thome [13] found that R-134a experienced critical dryout at higher film Reynolds numbers than R-236fa for two types of microstructured tubes at saturation temperatures of 5°C. Zhao et al. [8] found that critical dryout occurred at higher film Reynolds numbers for R-123 than for R-134a for plain and microstructured tubes.

2.6.4 Nanostructured surfaces

No works of literature have been found on the use of surfaces that can be categorised as nanostructured in falling film boiling conditions. Reduced dryout compared with plain surfaces was successfully achieved on microstructured tubes tested under falling film boiling conditions with refrigerants, with plateau regions more insensitive to flow rate changes [8,9,56] and critical dryout at lower flow rates [8,9] than for plain tubes. The improved wetting performance has been suggested to be through the ability of microstructured surfaces to better distribute the thin liquid films across the heat transfer surfaces [86] with interconnected internal pores distributing liquid [8] and nucleating bubbles further assisting by sucking liquid through the capillary pores to the nucleation sites [95]. Therefore, nanostructured surfaces with a high wettability and wickability may also reduce dryout in falling film boiling conditions in a similar fashion.

Horizontal tube falling film convective heat transfer studies of water have shown reduced critical dryout for superhydrophilic and hydrophilic tubes compared with that of a plain tube [75] and porous and hydrophilic tubes compared with that of a plain tube [96].

When testing superhydrophilic, hydrophilic and plain tubes with water, Zheng et al. [75] showed that under falling film convective heat transfer conditions, the HTCs were similar for all tubes tested as the film Reynolds number was decreased. Once the film Reynolds number dropped below a value of approximately 300, the HTCs for the plain tube decreased and the tube was seen to experience dryout, while the superhydrophilic and hydrophilic tube HTCs increased and were able to maintain a fully wetted surface under these low flow conditions. The resulting thin superheated fluid film was thought to reduce the evaporative thermal resistance and cause the increased HTCs. A study by Lee et al. [97] also showed that microporous tubes improved wetting through capillary-assisted wicking of water in a falling film convective heat transfer study and as the film Reynolds number was decreased, the microporous tube HTCs increased, while plain tube HTCs remained constant and then decreased due to dryout.

2.7 Critical heat flux due to departure from nucleate boiling

2.7.1 Plain surfaces in pool boiling

A number of mechanisms have been postulated to explain and predict the DNB event that results in a CHF point for plain surfaces in pool boiling, where the pool of liquid separates from the boiling surface due to an insulating vapour film. The hydrodynamic instability theory is perhaps the most well-known and postulates that the key mechanism controlling the DNB CHF process is the instabilities between the vapour departing the surface and the surrounding liquid. Once a breakdown in the vapour release from the surface occurs, a vapour blanket can form leading to DNB [30].

Zuber [98,99] first proposed the hydrodynamic instability mechanism and conducted an analysis for pool boiling on a flat plate and developed a correlation to predict it. This analysis was expanded by Lienhard and Dhir [100,101] to take into account a variety of other shapes such as horizontal cylinders.

A number of other DNB mechanisms have been proposed and are reviewed in Rohsenhow, Hartnett and Cho [30] for plain surfaces.

2.7.2 Nanostructures in pool boiling

DNB CHF has been shown to generally increase with the presence of nanostructures compared with plain surfaces when boiling water [16,20]. This improved DNB performance was attributed to mechanisms such as improved wettability of the surfaces

[17], increased contact line length of the bubble due to increased roughness [63] and improved wickability of the surfaces [47,70,102], all delaying the creation of a vapour blanket. Given the wide range of nanostructured surfaces produced, it is possible that the relevance of these mechanisms varies for each type of surface.

The LbL nanoparticle coating method implemented in this study was used to produce both hydrophilic and hydrophobic coatings for the pool boiling of water on nickel wires [46]. The DNB CHF was increased by both the hydrophobic and hydrophilic coating and increased with nanocoating layer thickness compared with that of a plain surface. Further studies on LbL surfaces by O'Hanley et al. [103] found no significant influence of the wettability of plain smooth surfaces on the DNB CHF, nor the surface roughness of plain or nanostructured surfaces in their study. However, the porosity and wettability of nanostructured surfaces were found to influence the DNB CHF, with hydrophobic porous structures decreasing the CHF and hydrophilic porous structures increasing the CHF. O'Hanley et al. [103] concluded that capillary wicking appeared to play a significant role in determining the CHF point. Tetreault-Friend et al. [104] found that there was an optimum layer thickness for maximum CHF enhancement by the porous LbL surfaces. They proposed that competition between capillary wicking and conduction heat transfer within the porous layer determined the optimal porous layer thickness and subsequent magnitude of CHF enhancement.

The CuO surface used in this study was found to increase the DNB CHF [63,64] when boiling water, with the authors suggesting that this was caused by the high surface roughness providing a pinning force to prevent dryout [63] or the high wickability of the surface supplying fresh liquid to boiling sites that prevented the onset of dryout and the subsequent formation of a vapour blanket [64].

The influence of nanostructured surfaces on the CHF point when boiling organic fluids has been mixed. The CHF was increased compared with that of plain surfaces in some studies of pool boiling of Fluorinerts [67,68] with Kumar et al. [68] having measured that the copper nanowires used in their study lowered the contact angle of FC-72 from 15° to less than 5°. They attributed the enhanced CHF to this improved wetting, combined with capillary wicking providing liquid replenishment to nucleation sites.

Liu et al. [70] found that the CHF stayed the same in the pool boiling of n-pentane on a nanoparticle-coated surface, while the CHF improved for combined nano/microstructured surfaces. High-speed videos showed that the nanoparticle-coated and plain surfaces had similar droplet-spreading abilities, while the nano/microstructured surfaces showed improved droplet spreading. This metric of droplet spreading used by Liu et al. [70] could be related to the wickability of the surface, considering that both liquid spreading and the capillary wicking of liquid involve adhesive forces between the liquid and the surfaces.

However, the DNB CHF was found to decrease compared with that of plain surfaces for studies of nanowire-coated surfaces in the flow boiling [69,105] and pool boiling [54] of Fluorinert FC-72 by values of between 20% and 30%, despite two of the studies reflecting improvements in CHF when boiling the nanowire-coated surfaces in water [69,105]. Shin et al. [105] and Zimmermann et al. [54] measured FC-72 contact angles that increased by between 5 and 7° when nanostructures were added to a plain surface, which the authors suggested was part of the reason for the reduced CHF of these surfaces in FC-72. However, Kim et al. [69] also recorded a reduction in the CHF through the addition of nanowires in FC-72 despite the nanowires lowering the contact angle by 3°, suggesting that wetting characteristics are not the only factor in CHF determination. Other factors attributed to influencing the lowered CHF seen in FC-72 were the reduced wicking ability of FC-72 compared with water due to its lower surface tension [69,105], as well as the possibility that nanowires hindered vapour removal from the surface [54,105]. CHF may thus be a concern when boiling organic fluids on nanostructures, despite the success of nanostructures in improving CHF performance when boiling water.

2.7.3 Falling film boiling

No studies could be found on CHF as a result of DNB for the falling film boiling on horizontal tubes. A number of falling film boiling studies that investigated DNB CHF have been conducted on flat horizontal plates [83,84,106] and vertical tubes [85] in refrigerants, water and Fluorinerts.

The DNB CHF in these falling film boiling studies was shown to increase as the fluid velocity was increased for flat plates with refrigerants [85] and Fluorinerts [83,106] as well as for inclined plates with water and refrigerants [84].

Ueda et al. [85] provided an illustration of both critical dryout and DNB CHF limitations for the falling film boiling of water and refrigerants R-11 and R-113 on the outside of vertical tubes. Critical dryout was noted where large stable dry patches were formed and has been already been addressed. DNB of the type seen in pool boiling where the fluid separated from the surface was also recorded with the fluid seen to lift from the surface with a thin liquid subfilm underneath. This subfilm, also noted in studies on vertical plates [83,84,106], was thought to be key to the process and it was theorised that falling film DNB CHF occurred when the subfilm layer dried out.

2.8 Summary and conclusions

This chapter reviewed a number of fundamental and state-of-the-art aspects of pool boiling and falling film boiling with a focus on the surface influences of roughness, material, microstructure and nanostructure. The limiting factors of DNB CHF of pool boiling and falling film boiling as well as dryout of falling film boiling were also reviewed.

The influence of surface properties on pool boiling was found to perhaps be one of the least well understood factors in determining heat transfer performance, with the complexity of characterising the surface and decoupling the various interlinked influences contributing to this problem. Further developments that allows for better quantification of roughness size and distribution influences are still required. The mean arithmetic roughness and thermal effusivity are typically used to capture the influence of roughness and material respectively on HTCs. The performance of nanostructures in the pool boiling of organic fluids was found to be another relatively under researched topic. However, research of the pool boiling of water on nanostructures and previous microstructure research showed that it is a complex process with a number of both single-phase and two-phase mechanisms that can enhance and, in some instances, diminish boiling heat transfer.

Falling film boiling heat transfer is a less well understood process than pool boiling heat transfer, with a wide spread between results for plain tubes. No research was found that has investigated the influence of roughness, material or nanostructure influence. Existing research on microstructures in falling film boiling conditions has shown that heat transfer can be enhanced under falling film boiling conditions, although the mechanisms involved are debated.

Falling film heat transfer enhancement, where the HTCs of falling film boiling are compared with those of pool boiling under the same conditions, is also not well understood, with a wide spread of results again found for plain tubes, possibly as a result of surface roughness not being measured by the various studies, and no research on the influence of roughness, material or wettability. Microstructured surfaces have shown that the enhancement mechanisms described under pool boiling are likely modified by the presence of the falling film, thus adding a further level of complexity to the process, which goes some ways towards explaining the differing opinions on the mechanisms likely at play.

Dryout of falling films is a well-documented concern for falling film boiling and one that requires further research to better understand its key influence, because there is still some spread in the results between studies. Refrigerant influence has been documented but not conclusively resolved. Nanostructures, while untested in falling film boiling, offer promise of reducing dryout in falling film boiling, given the results seen on microstructured surfaces and in nanostructured surfaces in convective heat transfer studies.

CHF due to DNB is typically suppressed by nanostructures in pool boiling studies of water. However, a few recent studies have indicated that it may be a concern when boiling organic fluids because lower CHFs have been found to occur than on corresponding plain surfaces. The DNB CHF of falling films has typically been investigated on vertical tubes and flat plates but not on horizontal tubes.

Therefore, it can be concluded that there is a large gap in knowledge of the influence of surface factors and nanostructure modification on pool boiling and more so for falling film boiling. This is the case for both the expected heat transfer behaviour as well as influences on dryout and CHF. Experimental investigations are required not only to understand the influence these factors have on the heat transfer mechanisms present in both pool boiling and falling film boiling so that an improved understanding can lead to better falling film and flooded evaporators, but also so that the published data set can be increased to allow for the eventual development of predictive correlations for these factors.

3. Experimental setup and data reduction

3.1 Introduction

Studies were conducted on an experimental system which was originally built at the Laboratoire de Transfert de Chaleur et de Masse (LTCM) located at the École Polytechnique Fédérale de Lausanne (EPFL) in Switzerland. The system was previously used for a number of studies under the leadership of Prof. Thome (EPFL), such as the falling film condensation work of Gstoehl [107], and the falling film boiling work on plain and microstructured tubes of Roques [108], Habert [109] and Christians [110]. The system was reassembled, recalibrated and fully recommissioned in South Africa at the University of Pretoria's Clean Energy Research Group (CERG). What follows is a description of the experimental equipment as well as the preparation and characterisation of the tubes used in this study. The complete test matrix and the methods of data reduction and processing are documented, followed lastly by the calculated uncertainty of the data.

3.2 Experimental setup

3.2.1 Refrigerant network and test chamber

The refrigerant conditioning network is schematically illustrated in **Figure 3-1.** Experiments were conducted within a test chamber (Item 1 in **Figure 3-1**) which consisted of a stainless steel rectangular shell with windows for visual access and removable tube sheets on each end so that tubes could be loaded to create a horizontal tube bank for investigation.

The tube were tested individually and loaded horizontally into the test chamber, which has a maximum pressure rating of 10 bar gauge. The tubes all had an external diameter of 19.05 mm and were placed in a tube-sheet with a pitch of 22.3 mm, resulting in an inter-tube gap of 3.25 mm.

Liquid refrigerant from the bottom of the system was fed by an oil free gear pump (Item 2) towards the test chamber. The flow rate of the refrigerant was controlled with a variable frequency drive combined with a bypass line around the pump that was used at low flow rates. The refrigerant subsequently passed through a vibration dampener and Coriolis mass flow meter (Item 3). Thereafter an electric element heater (Item 4) was used for fine tuning of the liquid refrigerant temperature to within 0.5°C of the saturation temperature on the way to the liquid distributor (Item 5) that spread the refrigerant evenly along the entire length of the tubes. Once refrigerant was fed over the tubes, any non-evaporated liquid returned to the bottom of the system under the action of gravity.

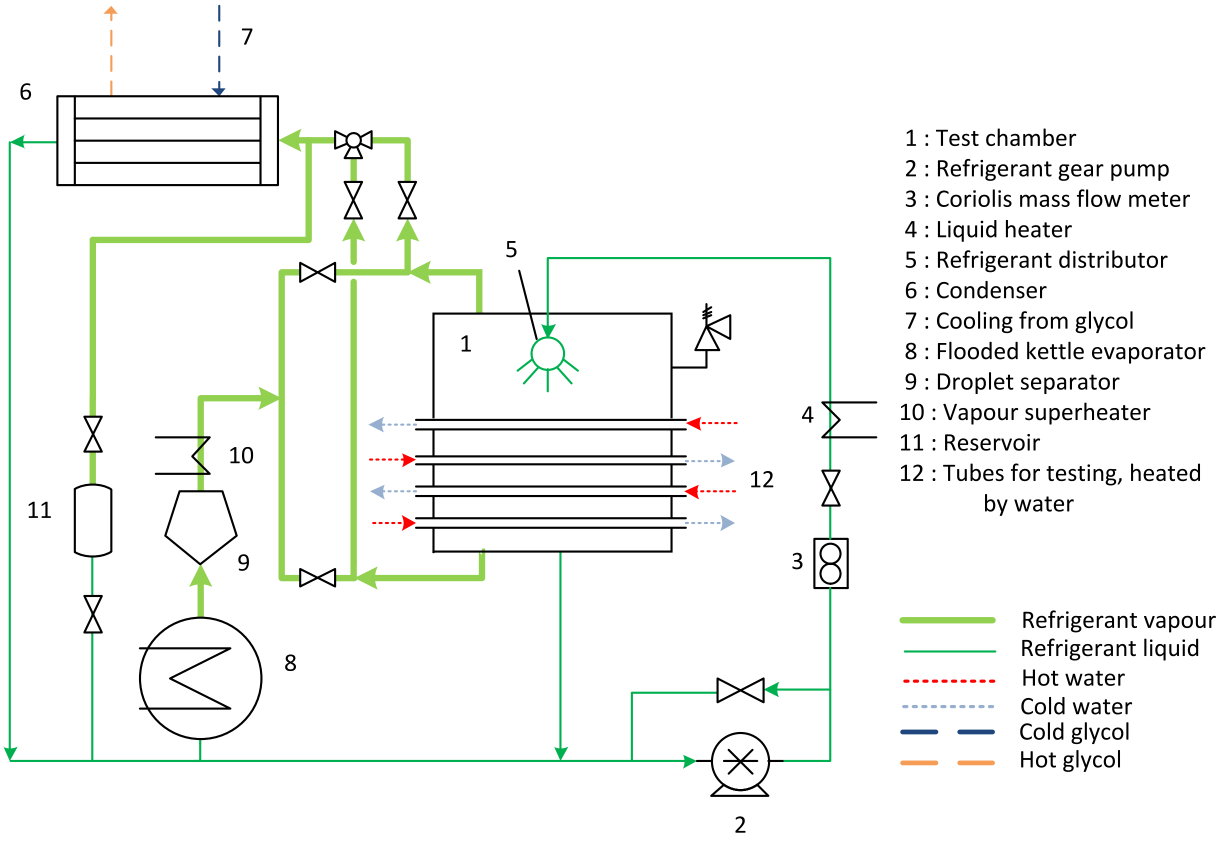

Figure 3-1. Schematic of refrigerant network.

Vapour created by refrigerant boiling on the tubes was driven upwards by buoyancy towards an overhead condenser (Item 6), which was cooled by chilled glycol (Item 7) supplied by a separate condensing glycol conditioning network. The subsequently condensed refrigerant returned under the action of gravity to the bottom section of the system.

The overall control of the saturation pressure of the refrigerant was achieved with an automatically controlled flooded electric kettle evaporator (Item 8), which served to balance the various heating and cooling loads the test chamber and overhead condenser applied to the refrigerant network. Refrigerant vapour created by the electric evaporator passed through a droplet separator (Item 9) and a fine-tuning electric heater (Item 10) before it reached the test chamber where it could be fed in either from the bottom or the top. A liquid reservoir (Item 11) together with a float level ensured the electric kettle evaporator did not run dry. The tested tubes were heated with water (Item 12) conditioned by a separate heating water conditioning network.

For this study vapour produced from falling film boiling in the test chamber was drawn downwards away from the boiling tubes so as not to obscure the falling film boiling process and so that the vapour flowed concurrently with the falling film. This vapour flow was considered to have minimal influence on the falling film process because Ribatski and Thome [91] found that co-current vapour flow of a velocity of approximately 1 m/s had little influence on falling film distribution or heat transfer and the maximum vapour velocity in the test chamber during this study was an order of magnitude smaller, calculated as 0.08 m/s.

Pool boiling (**Figure 3-2** (a)) or falling film boiling (**Figure 3-2** (b)) experiments were conducted in the test chamber. For pool boiling experiments the test chamber was closed off at the bottom and filled with refrigerant while for falling film studies the test chamber was opened up and liquid refrigerant was evenly distributed along the length of the tube.

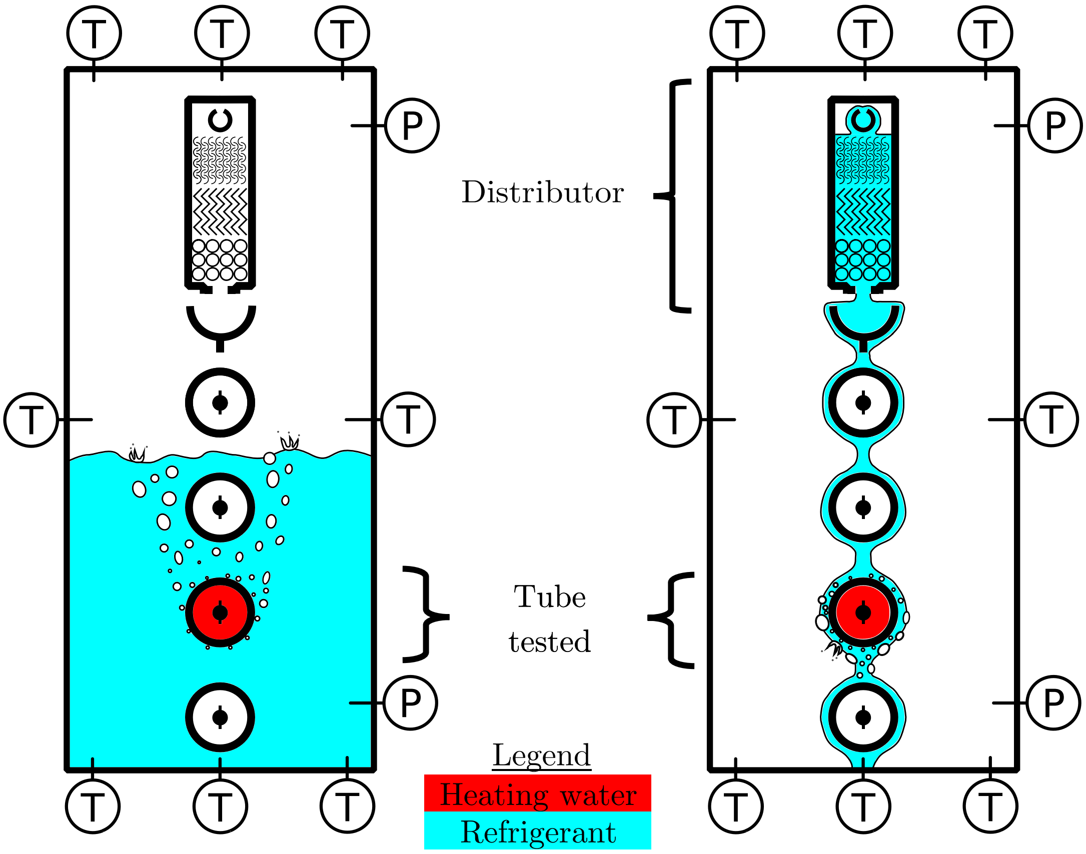

(a) Pool boiling mode (b) Falling film boiling mode

Figure 3-2. Schematics of test chamber operation modes and temperature and pressure measuring points.

While the test chamber can accommodate and a bank of up to three columns of ten rows of tubes and simultaneously test ten tubes at a time, in this paper only single tubes were tested at a time.

Pool boiling and falling film boiling studies of the same tubes at the same test conditions were conducted on successive days to minimize differences so as to further aide reproducibility between the respective data sets and reduce uncertainty in the calculation of the falling film heat transfer enhancement ratio.

Special care was taken to ensure an even liquid distribution to prevent the refrigerant distribution from influencing the results significantly. Liquid refrigerant was thus fed into the test chamber and distributed along the tube length via a liquid distributor. This distributor, shown in **Figure 3-2**, consists of a box with a 13 mm stainless steel tube at the top with a series of 3 mm holes along its upper length at 5 mm intervals. Refrigerant fed into this tube spills out the holes and then flows through layers of loosely packed polyurethane foam and compactly packed polyethylene foam respectively. Thereafter it flows through a distribution bottom plate with 268 holes along its length and then into a half tube. The liquid overflows from the half tube and then falls down from a sharp leading edge that has been machined into the bottom of the tube. This sharp edge ensures the refrigerant flows exactly from the centre of the half tube. Adjustment of the half tube ensured that liquid was fed onto the top most point of the tube below it. These efforts to distribute the liquid as evenly as possible along the length of the tube were considered largely successful based on visual inspection of the liquid distribution.

Previous gases were removed from the experimental setup by a vacuum process prior to filling with new refrigerants. A vacuum pump was connected to the refrigerant network until a pressure of 100 Pa absolute was achieved and maintained. Any non-condensable gases that did remain would collect in the overhead condenser. The success of this process was determined by the difference in saturation temperature calculated from the saturation pressures measured and actual temperatures measured within the test chamber. These were found to differ by no more than 0.2°C.

3.2.2 Heating water network

The heating water network conditioned the water that flowed inside and heated the tubes being tested in the test chamber. **Figure 3-3** illustrates this network.

Water was pumped by a multi-stage variable speed drive centrifugal pump (Item 1) through the network. The pump had a bypass line (Item 2) to further assist in fine tuning the flow rate.

The water was pumped through two heat exchangers to control its temperature. The first heat exchanger (Item 3) was supplied with the laboratory's 5°C utility water (Item 4) and cooled the heating water down to a base temperature set with the aid of a manual hand valve (Item 5). The second heat exchanger (Item 6) was supplied with the laboratory's 60°C utility water (Item 7). Both the 5°C and 60°C utility water were supplied at fixed temperatures from a refrigeration unit and heat pump respectively on the roof of the laboratory. The heating water was heated and controlled to the required set temperature through a computer-controlled valve (Item 8) on the outlet of the hot utility water. This system thus controlled the heating water's temperature as flow rates were changed and compensated for any fluctuations in the utility water temperature.

The heating water, now at its set temperature, then flowed through a Coriolis mass flow meter (Item 9), whereafter it could be split into various loops, facilitated by rotameters (Item 10) on each loop of the test chamber and allows for the testing of tube bundles when required, which was not needed in this study.

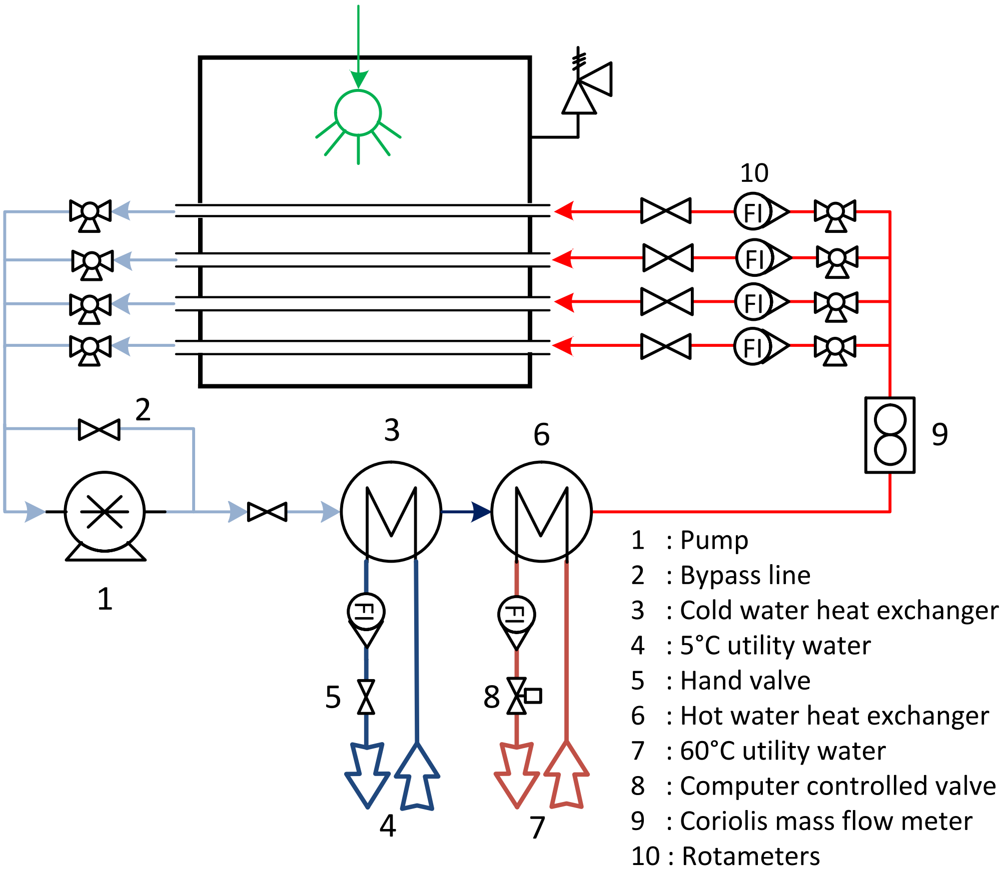

Figure 3-3. Schematic of heating water network.

3.2.3 Condensing glycol network

The condensing glycol network conditioned the water-glycol mix that was used as a cold source for the overhead condenser, condensing refrigerant vapour formed during the course of operation. **Figure 3-4** illustrates this network.

The glycol (a 50-50 water-propylene glycol mix) was pumped by a variable speed drive multi-stage centrifugal pump (Item 1) equipped with a bypass line (Item 2) for fine flow rate control.

The glycol network was operated in one of two modes, depending on the cooling load needed. It was either operated as an open system, directly coupled to the laboratory's central utility glycol system (Item 3) which supplied glycol at a fixed temperature of -20°C with the aid of a computer controlled refrigeration unit on the roof of the laboratory. Or the glycol network was operated as a closed system, where the glycol flowed through a heat exchanger (Item 4) that cooled it with the laboratory’s 5°C utility water (Item 5).

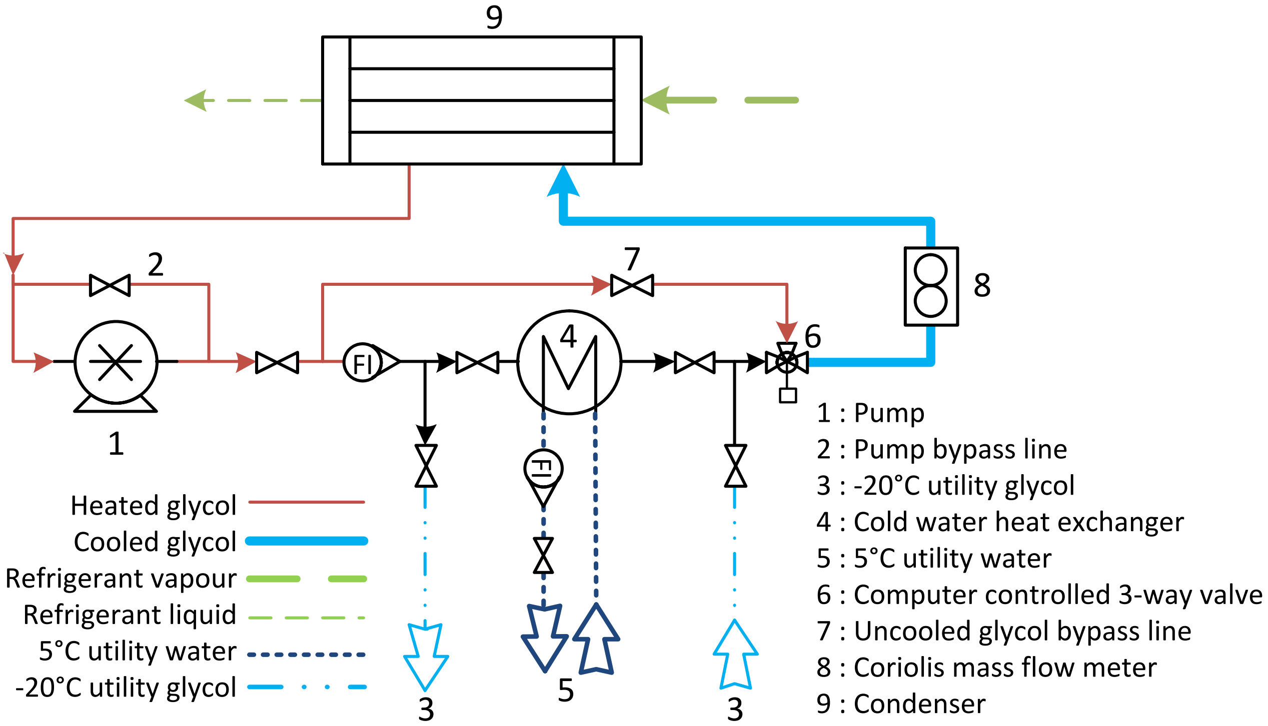

Figure 3-4. Schematic of condensing glycol network.

The glycol temperature was set at the outlet of a computer controlled three-way valve (Item 6) that mixed the cooled glycol with uncooled glycol flowing through a bypass line (Item 7). After the temperature had been set by the three-way valve, the water-glycol mix flowed through a Coriolis mass flow meter (Item 8) and then to the overhead condenser (Item 9) where it condensed the refrigerant vapour generated during operation of the system.

3.3 Instrumentation, data acquisition and control

The test chamber was instrumented at the top and bottom with two absolute pressure transducers and measured with eight K-type thermocouples along the height and width of the test chamber, illustrated in **Figure 3-2**. The temperature of the refrigerant liquid and vapour that entered and exited the test chamber was also measured with thermocouples.

During testing the saturation conditions were monitored and controlled using the pressure transducer measurements, with the saturation temperature subsequently calculated with REFPROP 8 [111] based on these pressure measurements. The thermocouple measurements within the test chamber were found to be on average within 0.2°C of the set saturation temperature across the test chamber which confirmed that there was an even temperature distribution within the test chamber and that no significant amount of non-condensable gases were present in the refrigerant network.

The temperature profile of the hot water inside the tube tested was measured with a custom developed probe, as illustrated in **Figure 3-5**. The probe consisted of a central 8 mm stainless steel tube with six 0.5 mm K-type thermocouples fed through the tube and protruding out into the water at three evenly spaced locations. At each location there were two thermocouples, one protruding upwards and another downwards. To ensure the heating water was well mixed within the tube, a wire of rectangular cross section was wrapped around the probe producing a helical mixing spiral.

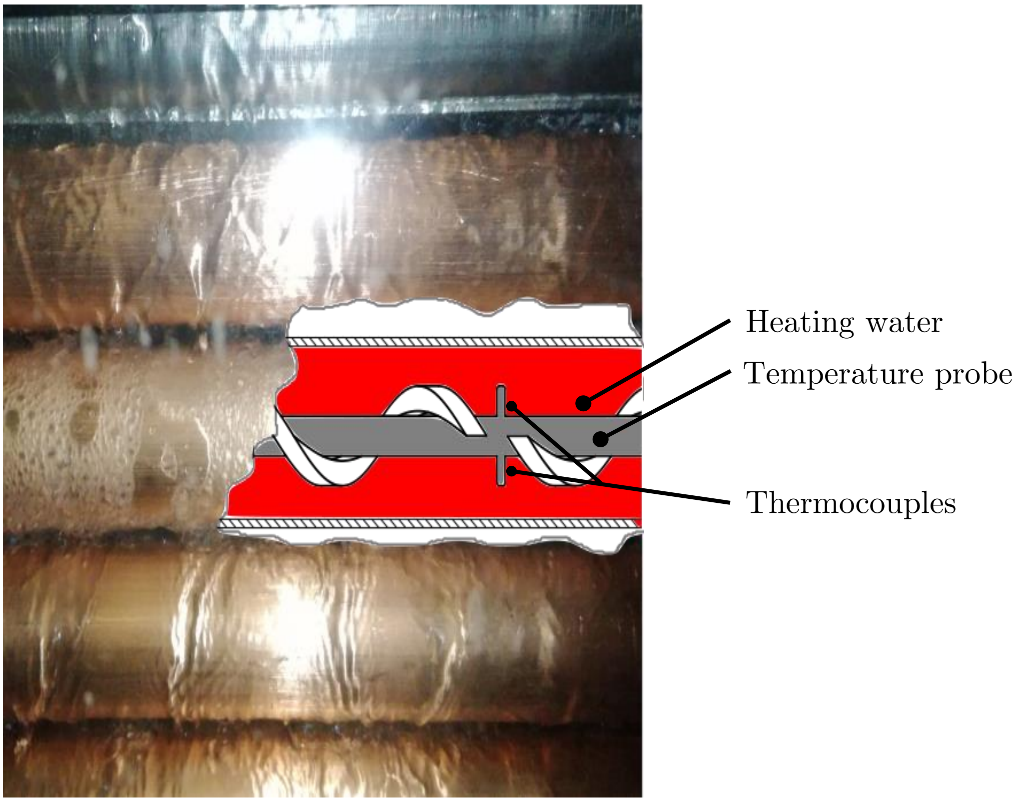

Figure 3-5. Photo of test chamber with cut away schematic of tube tested illustrating measurement probe.

The mass flow rates of the refrigerant, heating water and cooling glycol were measured with Coriolis mass flow meters.

All probes were calibrated against reference probes or made use of manufacturer calibration. The calibration process together with further detailed information on the probes mentioned here are documented in Appendix **A**.

The test chamber was fitted with windows on the front and back, which allowed for visual access. Boiling on the tubes was recorded with a Photron FASTCAM Mini UX100 high-speed video camera at 2 000 fps using a Tonica AT-X 100 mm 2.8 macro lens with the aid of front and back lighting by GS Vitec PT high-power white LEDs.

The data acquisition was performed with a National Instruments (NI) system controlled through LabVIEW software. Each data point captured and averaged 30 data points, which themselves were the average of 800 samples recorded at 100 Hz. Thermocouple measurements were fed into a NI TC-2095 terminal chamber, which performed cold junction compensation with the aid of a metallic plate to keep all the junctions at the same temperature and an in-built thermistor to determine the cold junction temperature.

Pressure transducer current outputs were measured and converted into voltage outputs by Sirax TV 808 isolating amplifiers before being fed into the NI TC-2095 terminal chamber. The terminal block was fed into a NI SCXI-1102 thermocouple input module. These modules contained a 2 Hz low pass filter to reduce electromagnetic noise. They were subsequently plugged into a NI SCXI-1000 chassis, which then communicated through a PCI-MIO-16XE-50 acquisition card to a designated measurement personal computer (PC) operating LabVIEW software.

The control of the experimental setup was achieved through a combination of manual valves and switches and automated control valves and heaters via a designated control PC that ran LabVIEW software. The control system data acquisition system was similar to the measurement acquisition system, with the addition of a number of purpose fit modules, such as current measurement with a NI SCXI-1308 terminal block, voltage measurement with a SCXI-1303 terminal block, while outputs were sent with a SCXI-1325 terminal block connected to a SCXI-1124 module.

3.4 Tubes tested

3.4.1 Plain tubes

The properties of the plain tubes tested for pool and falling film boiling are listed in **Table 3-1**. All tubes tested had an outer diameter of 19.05 mm and were internally heated by water for a heated length of 568 mm. As thermal effusivity is known to be an important wall material influence on pool boiling [18], tubes made from copper, mild steel and stainless steel were tested as they span a relative wide range of effusivities from 8 to 34 kWs$^{0.5}$/m^{2}K, as evident in **Table 3-1**.

Plain tubes were first polished with grit 1200 sandpaper to remove any initial roughness, whereafter some were roughened in a longitudinal direction to varying degrees of roughness. Four copper tubes were prepared by hand with sandpapers of various grits (Grits 1200, 600, 100 and 40). Due to increased material hardness, the mild steel and stainless steel tubes could not be polished or roughened by hand and instead an angle grinder fitted with sandpaper discs of grits 1200 and 100 were used.

It should be noted that going forward in this study tubes sanded with the grit 1200 sandpaper (either by hand or with the aid of the angle grinder) will often be referred to as 'polished' tubes, while tubes sanded with grit 100 or 40 sandpapers will often be referred to as 'roughened' tubes. This is because these two extremes of the roughness spectrum used within this study are useful benchmarks, particularly for understanding the nanostructured tubes' performance.

Table 3-1. Properties of different material tubes tested.

Property	**Copper**	**Stainless steel**	**Mild steel**	**Units**
Material grade	C 122	304	A 179	
Outer diameter	19.05*	19.05*	19.05*	mm
Inner diameter	16.65*	16.65*	14.83*	mm
Rockwell hardness B	60 **	92 †	72*	HRB
Thermal conductivity	340 **	16 †	47 ‡	W/m/K
Specific heat capacity	0.385 **	0.5 †	0.486 ‡	kJ/kg/K
Density	8 941 **	8 000 †	7 850 ‡	kg/m^3
Effusivity	34	8	13	kWs$^{0.5}$/m^2/K
Notes	Hard drawn seamless	Seamless	Cold drawn seamless	

*Taken from material data sheets,
**[112], †[113], ‡[114]

The plain tube roughness's were measured with a diamond tip profilometer (Mitutoyo SJ Surftest 210 profilometer) producing results adhering to ISO 4287:1997 and ISO 4288:1998 with a resolution of 0.002 µm. As per ISO 4288: 1998, the cut-off length was set to 0.8 mm as the roughness values, R_a, were lower than 2 µm. The roughness was measured both across and with the grain. Previous papers have not specified the direction of their roughness measurements with regards to the roughness grain [11,32]. To allow for comparison to previous papers it was assumed that previously stated roughnesses were measured against the grain as this is a standard approach when measuring machined surfaces [115]. Thus all roughnesses quoted going forward in this study are those across the grain. Values were cross checked with a diamond tip Alpha-Step 200 profilometer and the average disagreement was less than 0.05 µm.

The roughnesses of the tubes are shown in **Table 3-2** and are illustrated in **Figure 3-6**. The grit sandpapers chosen produced tubes that span and exceed the roughnesses often seen in industrial tubing. Gorenflo and Kenning [18] suggested that a range of 0.2 µm to 0.6 µm was typical for commercial tubing, while the roughnesses ranged from 0.11 to 1.91 µm in this study.

Table 3-2. Plain tube roughnesses.

Material	**Grit**	**Roughening method**	**Mean roughness across grain** R_a [µm]	**Mean roughness with the grain** R_a [µm]
Copper	G1200	Hand	0.12	0.11
	G600	Hand	0.35	0.35
	G100	Hand	0.74	0.47
	G40	Hand	1.37	0.85
Mild steel	G1200	Angle grinder	0.11	0.10
	G100	Angle grinder	1.91	0.70
Stainless steel	G1200	Angle grinder	0.09	0.10
	G100	Angle grinder	1.32	0.81

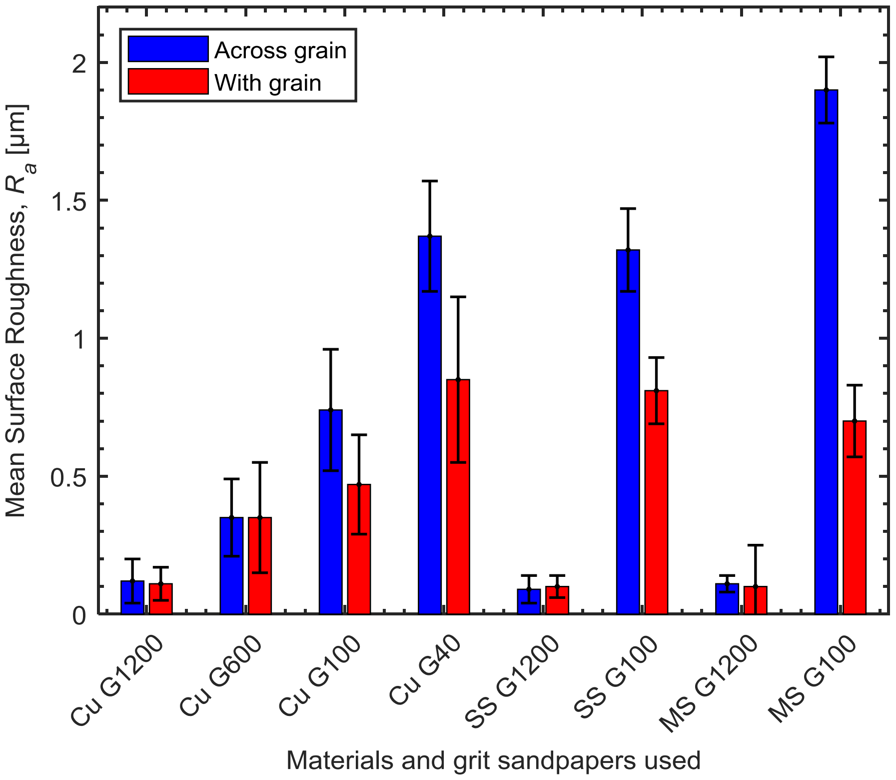

Figure 3-6. Mean surface roughnesses across and with the grain of various tubes tested (Cu = Copper tube; SS = Stainless steel tube; MS = Mild steel tube).

It should be noted that a number of previous works made use of the older mean surface roughness parameter R_p as defined by the now defunct German standard DIN 4762:1960 to characterise surface roughness. ISO 4287 has since superseded this standard and now defines R_p as the maximum profile peak height and R_a as the mean surface roughness. In this work the DIN 4762 average surface roughness definition will be denoted by $R_{p,old}$, while the new ISO 4287 surface roughness definition will be denoted by R_a. However $R_{p,old}$ and R_a are not equivalent. In order to make use older correlations based on the $R_{p,old}$ standard, Gorenflo et al. [42] noted that Schomann found the relationship $R_a = 0.4\ R_{p,old}$. This approach will be used in this work when using older correlations such as Cooper's [39].

The tubes were stored for three days after preparation to ensure a stable surface had formed and thereafter tested within three months to minimise the influence of long term surface degradation on the results.

3.4.2 Nanostructured tubes

Three different nanocoatings were applied to the outside of copper tubes. The tubes were first polished with grit 1200 sandpaper and cleaned with an ultrasonic probe in an acetone bath followed by a deionised water rinse.

The first nanocoating used a layer-by-layer (LbL) process developed by Rubner and Cohen [116] to apply LUDOX® TM-40 silica (SiO_2) nanoparticles with a diameter of approximately 20 nm to the surface of the tube. The tube was constantly rotated by an automated apparatus and dipped first into a cationic solution of poly (allylamine hydrochloride) followed by an anionic solution of silica nanoparticles with three deionised water rinses between each. Forrest et al. [46] gave a more detailed description of the process used in this study. This process was repeated 50 times to create a nominally 50 nanoparticle thick layer on the surface.

The second nanocoating process immersed a tube in an alkali oxidising solution heated to 95°C for 10 min, which created copper oxide (CuO) nanostructures on the surface of the tube. The solution was detailed in Nam and Ju [117] and listed as the Type I solution. The tube was manually rotated at 1 min intervals to ensure an even distribution of nanostructures.

The nanoFLUX© surface is a commercial process applied by Oxford nanoSystems. The nanoFLUX© coating is applied through a proprietary process by Oxford nanoSystems that produces a metallic dendritic structure on a surface which can be optimised to a specific size from 1 µm to 30 µm.

Scanning electron microscopy (SEM) images of the plain and nanostructured tube surfaces shown in **Figure 3-7** depict the various surface morphologies produced by the processes used in this study. The polished (**Figure 3-7** (a)) and roughened (**Figure 3-7** (b & c)) copper tubes had roughness that was characterised by longitudinal grooves of relatively uniform nature along the length of the tube in the direction of the sandpapering, with the grooves of the surfaces becoming larger as the roughness of the surface increased due to the use of coarser grit sandpapers.

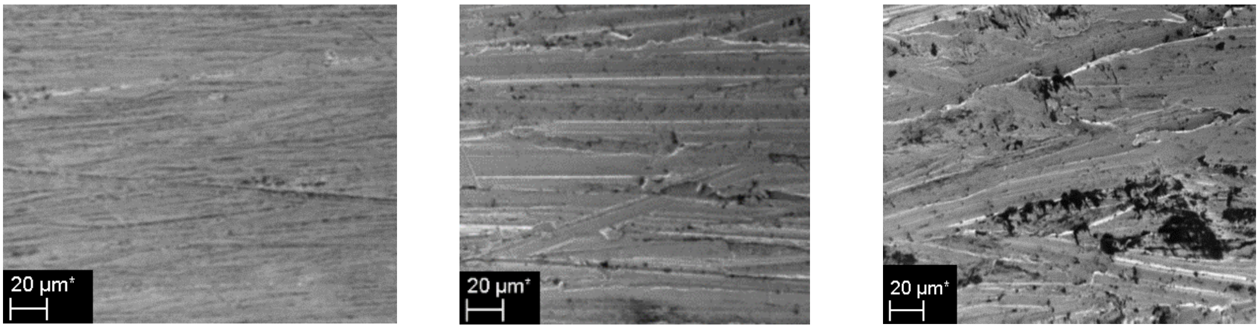

(a) Polished Cu, Grit 1200 (b) Roughened Cu, Grit 100 (c) Roughened Cu, Grit 40

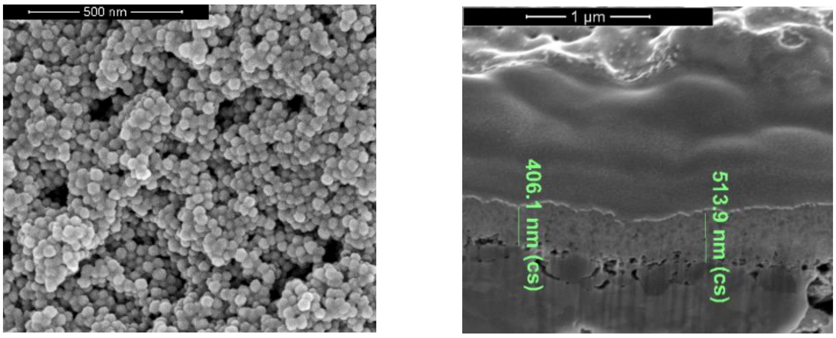

(d) LbL – top view (e) LbL – cross-section

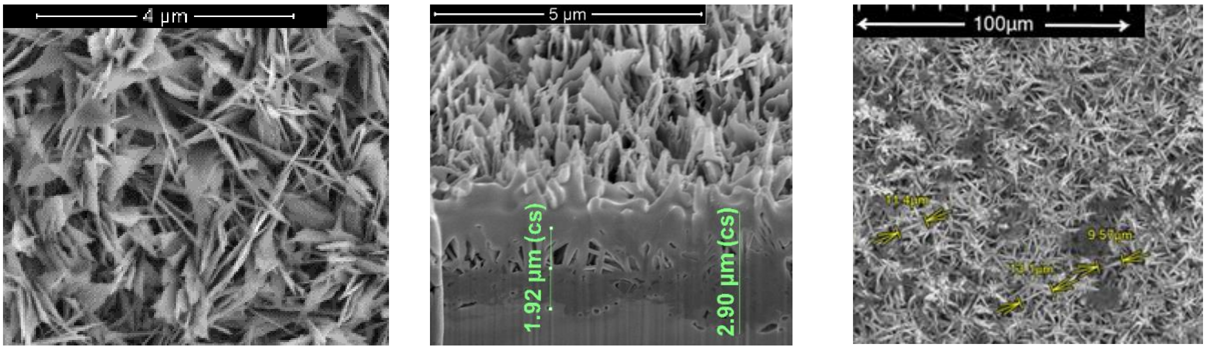

(f) CuO – top view (g) CuO – cross-section (h) nanoFLUX

Figure 3-7. SEM images of tube surfaces.

The LbL (**Figure 3-7** (d & e)) surface had very small surface structures compared with the other nanocoatings, with a layer thickness of approximately 0.4 to 0.5 µm. It should be noted in the images of the LbL coating that the surface was not very porous, and the nanoparticles appeared to clump together. The CuO (**Figure 3-7** (f & g)) and nanoFLUX surface (**Figure 3-7** (h)) both produced an intertwined fibrous mat of sharp needle-like or dendritic extrusions. The CuO coating was approximately 2 to 3 µm thick. The nanoFLUX extrusions are shown to be of a larger scale than those of the other surfaces. SEM images of samples taken around the circumference of the nanostructured tubes showed similar nanostructures, suggesting that even coatings were applied to all the tubes.

The roughness of the nanostructured surfaces could not be measured by the profilometer as the tip scratched the coatings. Atomic force microscopy (AFM) was used to measure the surface profiles, with the results of the polished and LbL surfaces shown in **Figure 3-8**. The AFM scans show the grooves on the polished surface and show that the nanoparticles of the LBL coating process appear to have, at times, clumped together to form local valleys and troughs. The AFM scans of the nanoFLUX and CuO surfaces failed to produce realistic images when compared with the SEM information due to the high aspect ratio of these surface structures.

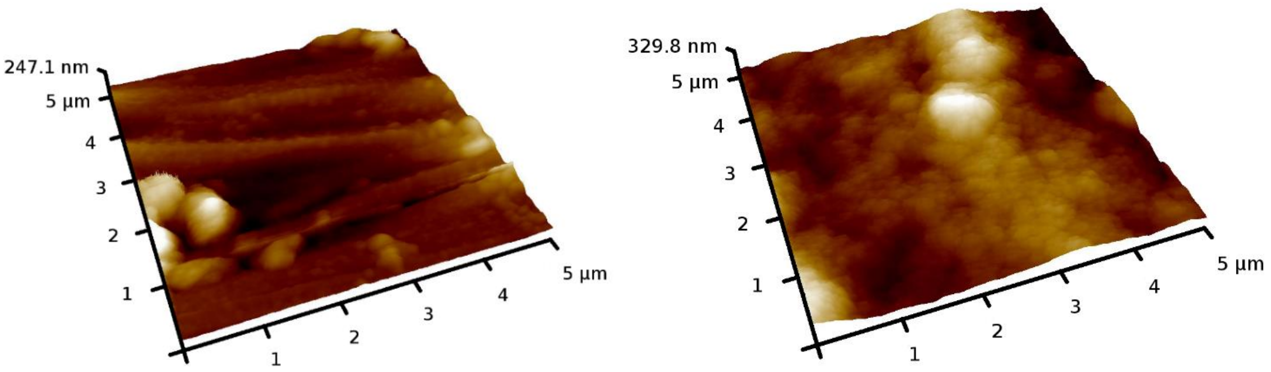

(a) Polished (b) LbL

Figure 3-8. AFM scans of tube surfaces.

The nanostructured coatings are assumed to have added minimal thermal resistance to the tubes. While the SiO_2 of the LBL coating and CuO coating have low thermal conductivities of 1.4 [118] and 33 W/m/K [119] respectively, compared to the 340 W/m/K [112] of the copper tube, the LbL and CuO coatings are very thin, with thicknesses of 0.45 µm and 2.5 µm respectively (estimated from **Figure 3-7)** compared to the 1.2 mm thickness of the copper tube. This means that the total thermal resistance of the copper tube wall is increased by less than 0.1% by the addition of the nanostructured coatings.

The durability of the nanostructured coatings was not quantified in this study. The CuO surface was noted to be easily scratched and so great care was taken during handling and installation of all tubes to ensure minimal physical damage. No evidence of longer term degradation was seen in this study, with no significant change seen in the HTCs of the nanostructured tubes over their 6 month testing period. However, the tubes were only actively tested for approximately 150 hours each and this is thus a poor indication of their long term durability.

3.4.3 Contact angle measurements

The wettability of the various surfaces tested was characterised by contact angle measurements. The CuO nanocoated surface showed significant changes to its wettability during the study. Immediately after coating the tube, the CuO surface was very hydrophilic, with contact angles measured with water in air of less than 5°. Once testing started, the surface showed very low HTCs, most likely due to the high wettability flooding potential nucleation sites. Over the initial two hours of testing, the HTCs increased and then stabilised for the remainder of the study. Subsequent testing of the contact angle of water in air of the CuO surface showed that the surface had become hydrophobic, with contact angles now greater than 90°. The change of the wettability of the CuO surface in water was likely through the adsorption of the organic refrigerant onto the surface as described previously [120,121]. The CuO surface also aged similarly if left out in the atmosphere for a few weeks, again likely through the adsorption of organic molecules from the atmosphere. Subsequently all data recorded in this study was after boiling the surfaces for a number of hours in refrigerant to ensure they were all in a stable 'aged' condition. The aged CuO surface was considered stable as it showed good repeatability of HTCs for the duration of testing for this study.

Contact angles of approximately 20° were measured on all aged surfaces with R-245fa in air at atmospheric temperatures of approximately 25°C with the aid of the images from a high-speed video camera analysed with a low-bond axisymmetric drop shape algorithm [122] implemented in the ImageJ software program [123]. The rapid evaporation of the fluid introduced significant noise. No statistically significant differences between the contact angles of the surfaces could therefore be detected with this measurement method. The refrigerant was thus able to wet all the surfaces and was likely in the Wenzel wetting state [124] at these test conditions. It should be noted that previous tests conducted with the CuO surface in water-boiling studies had been in a superhydrophilic state (contact angle of ~0°) [64]. In this study, the CuO surface was still well wetted by the refrigerant, but to a lesser extent (contact angle of ~20°).

The measured contact angles of all the surfaces in the aged condition for water in air are shown in **Table 3-3**. The CuO and nanoFLUX surfaces were hydrophobic to water with the needle-like fibrous structures on the surfaces likely trapping air beneath the droplet causing wetting in the Cassie-Baxter state [125].

The roughened surface was shown to have a higher contact angle than the polished copper surface. This however goes against the Wenzel correlation [124], which suggests that the rougher the surface, the lower the contact angle should be. However the results were relatively close to each other compared to the contact angles measured on the other surfaces, with may indicate that the testing did not have the precision required to detect the difference between the two surfaces.

Table 3-3. Contact angles of water on aged surfaces

Surface	**Average contact angle** (Average ± standard deviation) [°]
Polished copper	78 ± 4
Roughened copper	85 ± 3
LbL	52 ± 7
CuO	122 ± 24
nanoFLUX	161 ± 16

3.4.4 Surface wicking

The CuO and nanoFLUX surfaces were shown to wick liquid, with refrigerant dripped onto the CuO and nanoFLUX surfaces under isothermal conditions showing a wetted region adjacent to the droplet front. This was not seen on any of the other surfaces tested. It appears that the LbL surface in this study did not produce a wickable porous surface as in the previous studies in which it had been used, with the AFM scans shown in **Figure 3-8** suggesting that the clumping of the nanoparticles could have limited the porosity produced.

High speed video was taken of the surfaces under falling film boiling conditions to determine if wicking still took place on the CuO and nanoFLUX surfaces during boiling. **Figure 3-9** shows a zoomed-in progression of dry spots on the vertical sides of the polished copper and nanoFLUX tube in R-245fa at 20°C at 50 kW/m^2 and a film flow rate of 0.13 kg/m/s.

Wetting of the surfaces at these high film flow rates took place with a series of intermittent thick waves of liquid wetting the surface. The images of **Figure 3-9** were of dry spots that developed undisturbed between these waves. **Figure 3-9** (a) indicates that a dry spot was started on the polished tube by a bubble popping, just before the frame began. The dry spot increased in size as the wetting front receded and then merged with a neighbouring dry spot. As the two dry spots merged, necking could be seen between the two spots, as indicated by the arrows at $t = 11$ ms. No wicking front was visible in these images for the polished tube. A dry spot began on the nanoFLUX surface with a thinned region, indicated by arrows in **Figure 3-9** (b) at the 0 and 3.5 ms mark. As the wetting front receded, a small receding wicking front could be seen around the dry spot. A larger wicking front appeared once the dry spot merged with a neighbouring dry spot at the 17.5 ms mark, indicated by arrows. This wicking front was visible around most of the circumference of the dry spot, suggesting that the wicking front was able to overcome the influence of gravity (which is downwards in **Figure 3-9**).

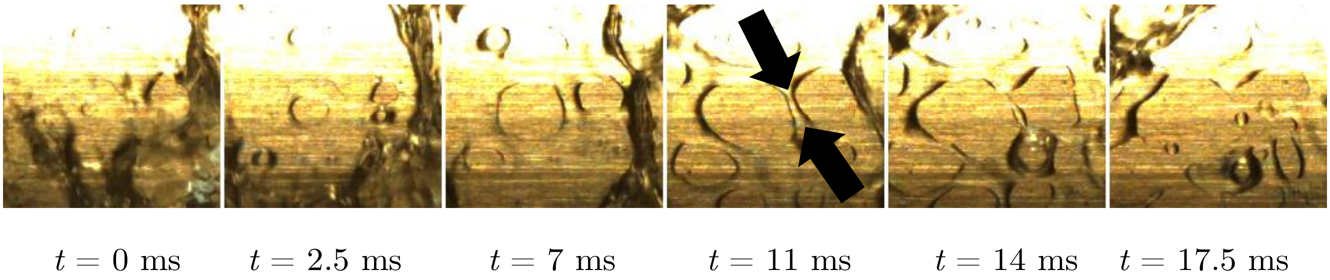

(a) Polished

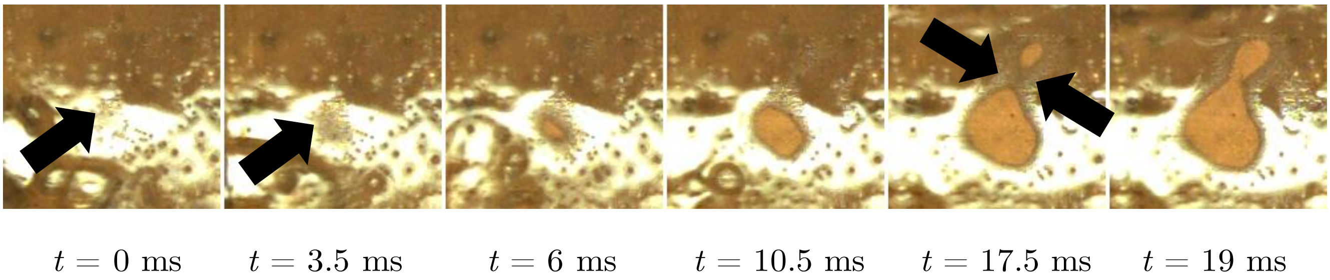

(b) nanoFLUX

Figure 3-9. Dry spot progression of polished and nanoFLUX tubes in R-245fa at 20°C at 50 kW/m^2 at 0.13 kg/m/s.

The CuO tube also displayed wicking fronts, as seen in **Figure 3-10**. However the CuO wicking front was smaller than that seen on the nanoFLUX surface, and was not always visible, with the wicking front only visible on some edges of the dry spots, highlighted with arrows in **Figure 3-10**. Thus the CuO surface likely had a lower wicking ability than that of the nanoFLUX tube, and under some conditions it is likely no wicking took place at all.

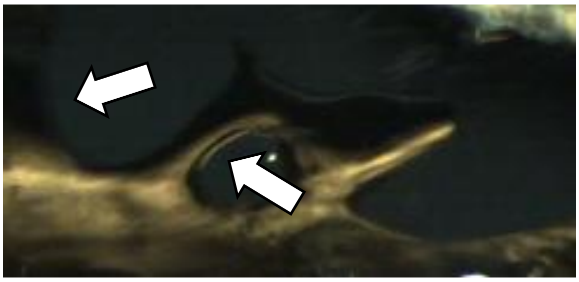

Figure 3-10. CuO wicking front in R-245fa at 20°C at 50 kW/m^2 at 0.13 kg/m/s.

3.5 Refrigerants tested

Refrigerants and saturation temperatures were chosen so that tests could be conducted across a wide range of reduced pressure values, while operating within the capabilities of the experimental facility, as reduced pressure is a key correlating parameter used within a number of widely used pool boiling correlations to account for fluid influences in pool boiling heat transfer based on the theorem of corresponding states [18,39]. Furthermore, refrigerants were chosen so that comparison to previous work was possible while also factoring in availability and cost.

R-134a was thus chosen as a higher-pressure refrigerant as it is widely available and it is one of the most common refrigerants that falling film boiling studies have been conducted with, as evident in the reviews of the topic [1,2,6]. R-245fa was chosen as a lower-pressure refrigerant so as to allow for tests to be conducted across a range of reduced pressure values.

Tests were conducted at three different reduced pressure values under saturated refrigerant conditions, namely a reduced pressure, p_r, of 0.034 in refrigerant R-245fa at a saturation temperature of 20°C and a p_r of 0.086 and 0.160 in refrigerant R-134a at saturation temperatures of 5 and 25°C, respectively.

The properties of the refrigerants tested were determined with REFPROP 8, a software application provided by the National Institute of Standards and Technology [111] and are shown in **Table 3-4**.

Table 3-4. Thermophysical properties of saturated refrigerants.

Property	**R-245fa at 20°C**	**R-134a at 5°C**	**R-134 at 25°C**	**Units**
Saturation pressure	122	350	665	kPa
Reduced pressure	0.034	0.086	0.160	-
Dynamic viscosity of liquid	0.434	0.250	0.195	mPa.s
Liquid density	1352	1278	1207	kg/m^3
Vapour density	7.15	17.1	32.4	kg/m^3
Latent heat of vapourisation	193	195	178	kJ/kg
Specific heat of liquid	1.31	1.36	1.42	kJ/kg/K
Surface tension of liquid	14.7	10.8	8.1	mN/m

3.6 Test matrix

The test matrix for those studies where the heat flux was varied for falling film boiling at the maximum film flow rate of approximately 0.13 kg/m/s are shown in **Table 3-5**. The same test matrix was also used for the pool boiling studies.

Table 3-5. Falling film boiling and pool boiling test matrix at a range of heat fluxes.

Material	**Surface condition**	**Refrigerant condition**	**Heat flux**	**Refrigerant film flow rate for falling film boiling studies**
Copper	R_a of 0.12 µm, Plain	R-245fa @ 20°C R-134a @ 5°C R134a @ 25°C	20 – 100 kW/m^2	~0.13 kg/m/s
	$R_a = 0.35$ µm, Plain	R-134a @ 5°C R134a @ 25°C		
	$R_a = 0.74$ µm, Plain			
	R_a of 1.37 µm, Plain	R-245fa @ 20°C R-134a @ 5°C R134a @ 25°C		
Mild steel	$R_a = 0.11$ µm, Plain	R-134a @ 5°C R134a @ 25°C		
	$R_a = 1.91$ µm, Plain	R-134a @ 5°C		
Stainless steel	$R_a = 0.09$ µm, Plain	R-134a @ 5°C R134a @ 25°C		
	$R_a = 1.32$ µm, Plain	R-134a @ 5°C		
Copper	LbL	R-245fa @ 20°C R-134a @ 5°C R134a @ 25°C	20 – 100 kW/m^2	
	CuO		20 – 100 kW/m^2 and CHF	
	nanoFLUX		20 – 100 kW/m^2 and CHF	

Heat fluxes were tested across a range of 20 to 100 kW/m^2. The lowest heat flux tested was 20 kW/m^2 because the analysis in Section **3.8** illustrated that uncertainties increased exponentially as this lower heat flux limit was approached and thus testing at heat fluxes below this limit on this equipment was not practically viable. The heat flux was increased beyond the upper limit of 100 kW/m^2 to test whether the CHF point due to DNB could be reached and data was only recorded in those cases where it did, which was only on the CuO and nanoFLUX tubes. The other surfaces could not reach the high heat fluxes needed for DNB to occur due to their low HTCs and experimental equipment limitations. Testing at both lower and higher heat fluxes are recommended for future studies, with lower heat fluxes allowing for the investigation of the onset of falling film boiling and higher heat fluxes allowing for the DNB CHF points of the plain tubes to be measured.

The maximum possible film flow rate per unit length, Γ_r, on a single side of a tube was approximately 0.13 kg/m/s across the range of conditions, with the maximum achieved film flow rate at each test condition being 0.14 kg/m/s for R-245fa at 20°C and 0.13 kg/m/s and 0.12 kg/m/s for R-134a at 5°C and 25°C respectively.

Table 3-6 shows the test matrix for those falling film boiling studies where the heat flux was kept constant at either 20, 50 or 80 kW/m^2 and the film flow rate was varied from a high of approximately 0.13 kg/m/s to the lowest possible film flow rate that could support the tested heat flux.

Table 3-6. Falling film boiling test matrix at a range of film flow rates.

Material	**Surface condition**	**Refrigerant condition**	**Film flow rate per unit length**	**Heat flux**
Copper	R_a of 0.12 μm, Plain	R-245fa @ 20°C R-134a @ 5°C R134a @ 25°C	0 - 0.13 kg/m/s	20 kW/m^2 50 kW/m^2 80 kW/m^2
	R_a = 0.74 μm, Plain	R-134a @ 5°C R134a @ 25°C		
	R_a of 1.37 μm, Plain	R-245fa @ 20°C		
Mild steel	R_a = 0.11 μm, Plain	R-134a @ 5°C		
Stainless steel	R_a = 0.09 μm, Plain	R-134a @ 5°C		
Copper	LbL	R-245fa @ 20°C R-134a @ 5°C R134a @ 25°C		
	CuO			
	nanoFLUX			

In total, tests were conducted under 67 different set points, consisting of 17 pool boiling set points, 17 falling film boiling set points with constant film flow rate and 33 falling film boiling set points with constant heat fluxes. These 67 set points encompassed 2655 separate data points, 1893 for falling film boiling and 762 for pool boiling.

The published database of pool boiling and falling film boiling HTCs on tubes was thus expanded significantly through this study.

3.7 Data reduction

3.7.1 Film Reynolds number

For the falling film experiments, the film flow rate of refrigerant on one side of the tube per unit length, Γ_r, was defined as the measured total mass flow rate of refrigerant fed to the refrigerant distributor on the top of the tube, $\dot{m}_r$, per one side of a tube of length L and was given by Eq. (1).

$$\Gamma_r = \frac{\dot{m}_r}{2L} \tag{3-1}$$

From this the film Reynolds number, Re_f, was defined as

$$Re_f = \frac{4\Gamma_r}{\mu_l} \tag{3-2}$$

The dynamic viscosity of the liquid refrigerant, μ_l, at the measured temperature, together with other refrigerant and water thermo-physical properties (e.g. specific heat, c_p, and thermal conductivity, k) were determined with the aid of REFPROP 8, a software application provided by the National Institute of Standards and Technology [111].

3.7.2 Local heat flux

In order to determine the local HTC at the midpoint of the length of the instrumented tube, the local heat flux was calculated at the midpoint of the tube length. As described by Christians [110], the local heat flux was calculated as

$$q = \frac{\dot{m}_w c_p}{\pi D_o} \frac{dT_w}{dx} \tag{3-3}$$

where $\dot{m}_w$ was the measured water mass flow rate and D_o the measured outside diameter of the tested tube. The temperature gradient, dT_w/dx was estimated at the midpoint of the tube's length using the gradient of a second order polynomial fit to the measured water temperature profile along the length of the tested tube.

3.7.3 Internal heat transfer coefficient - Wilson plot

As only the overall HTC of the tube in the test chamber could be measured due to the infeasibility of installing wall temperature sensors on the tube surface, the internal HTC of the tube tested was estimated with the aid of a Briggs and Young-type Wilson plot as implemented by Van Rooyen et al. [126]. h_i was assumed to take the form of the Gnielinski correlation [127], h_{gni}, with a lead coefficient, C_i, calculated from the Wilson plot to account for the presence of the temperature probe within the tube and correlation error as follows:

$$h_i = C_i h_{gni} \tag{3-4}$$

A more detailed description of the Wilson plot method employed as well as the results are detailed in Appendix **C**.

3.7.4 External heat transfer coefficient

The local external HTC, h_o, on the outside of the midpoint of the tube was determined as

$$h_o = \left(\frac{1}{U_o} - R_{wall} - \frac{1}{h_i}\frac{D_o}{D_i}\right)^{-1} \tag{3-5}$$

The total HTC, U_o, was calculated by

$$U_o = \frac{q}{T_w - T_{sat}} \tag{3-6}$$

where the water temperature, T_w, was estimated at the midpoint of the tube's length using a second order polynomial fit to the water temperature profile measured along the inside of the tube length and the refrigerant saturation temperature, T_{sat}, was estimated using REFPROP 8 based on the saturation pressure measured at the top of the test chamber.

The wall thermal resistance, R_{wall}, was determined by

$$R_{wall} = \frac{D_o ln\left(\frac{D_o}{D_i}\right)}{2k_{wall}} \tag{3-7}$$

3.7.5 Surface heat transfer enhancement ratio

The surface heat transfer enhancement ratio, $K_{surf,}$ of surfaces in pool boiling and falling film boiling is the ratio of the measured HTC relative to that of a polished copper tube under the same conditions and was calculated by

$$K_{surf} = \frac{h_o}{h_{o,pol}} \qquad \text{3-8}$$

where $h_{o,pol}$ is interpolated to the same heat flux as the numerator based on a fourth-degree polynomial fit to the measured polished tube HTCs.

3.7.6 Falling film heat transfer enhancement ratio

The falling film heat transfer enhancement ratio, K_{ff}, was calculated as the ratio of the external falling film boiling HTC, $h_{o,ff}$, to the respective external pool boiling HTC, $h_{o,pb}$, at the same heat flux and refrigerant set point.

$$K_{ff} = \frac{h_{o,ff}}{h_{o,pb}} \qquad \text{3-9}$$

The pool boiling HTC was interpolated with the aid of a fourth-degree polynomial fit to calculate the HTC at the specific heat flux the falling film HTC was measured.

3.7.7 Normalised HTC

A normalised HTC, h^+ , was calculated for studies where the film flow rate was varied at a constant heat flux as follows:

$$h^+ = \frac{h_o}{h_o\ (Re_f = 1250)} \qquad \text{3-10}$$

where the h_o at a film Reynolds number of 1250 was used as the normalising denominator, as this was the highest film Reynolds number achieved under all refrigerant conditions.

3.7.8 Critical dryout threshold

The critical dryout threshold is typically determined at a film Reynolds number rather than the film flow rate per unit length. The strategies used in previous studies to identify the film Reynolds number at which critical dryout occurs were found to be at times not particularly successful in this study and as such a new methodology was employed. In particular many previous strategies made use of the average HTC over the entire range of film Reynolds numbers tested as a key input into their criterion. These methods often struggled with data from this study where the HTC dropped throughout the film Reynolds number range or where a large amount of data was captured at film Reynolds numbers below the critical dryout threshold.

A gradient based approach was decided on in this study, as this would allow for the identification of the point of rapid HTC decrease while ignoring more gradual decreases observed in the data. Initially the use of the gradient of HTC versus film Reynolds number, dh_o/dRe_f, proved adequate to identify the critical dryout point, as published in the Bock et al. [27] study on plain tubes. However, subsequent results from the nanostructured tubes struggled with this approach due to the wider range of HTC magnitudes and gradient magnitudes present. A gradient based on the normalised HTC versus film Reynolds number subsequently proved more successful in identifying the critical dryout limit. The results from Bock et al. [27] were reprocessed using this new normalised HTC gradient and there was little change in the critical dryout limit of those results, as was intended.

The critical dryout limit was thus defined as the first point, as the film Reynolds number was decreased from the maximum to the minimum recorded, at which all subsequent normalised HTC gradient points met the criteria as follows:

$$\frac{dh^+}{dRe_f} > 0.0005 \qquad \text{3-11}$$

The threshold value of 0.0005 was determined through trail-and-error to find a single threshold value that correctly identified the critical dryout limit across all the tests conducted.

Figure 3-11 illustrates the implementation of this strategy on a copper tube with the HTC as a function of film Reynolds number. The gradient, dh^+/dRe_f, is also given in the figure as a function of film Reynolds number. As the film Reynolds number was decreased the gradient was relatively constant and low until dryout began and the gradient became very large. Applying the dryout criterion, the first data point as the film Reynolds number was decreased to have all subsequent data points have gradients of above 0.0005 occurs at a film Reynolds number of approximately 630 with a corresponding HTC of 15 kW/m^{2}K.

The new criteria succeeded in a wide variety of experiment conditions to successfully identify the critical dryout threshold. The critical dryout threshold defined by the method of Christians and Thome [13] is plotted for comparison in **Figure 3-11**. Their method in effect identified the threshold as the first data point that fell below 5% of the mean HTC of the data set. **Figure 3-11** illustrates that it selected a point that is within the dryout regime in this case rather than identifying the threshold point.

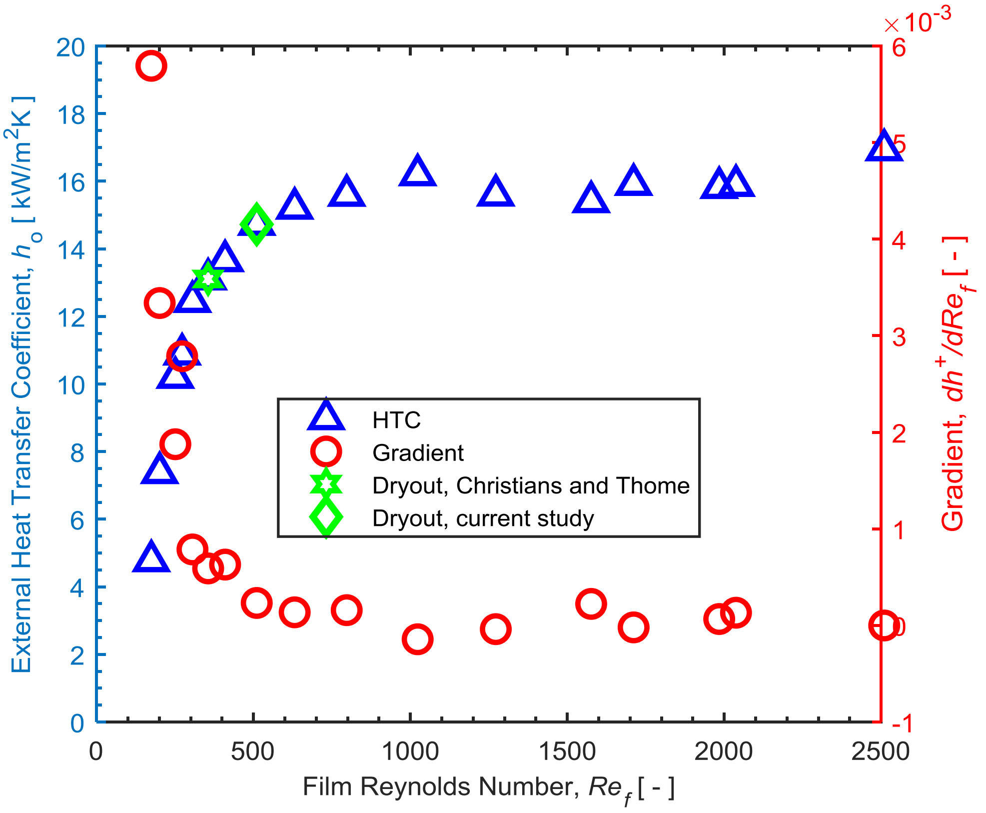

Figure 3-11. Critical dryout thresholding methods of the falling film boiling HTCs illustrating the method of Christians and Thome [13] and the current study (Copper tube, R_a of 0.74 µm, R-134a, 25°C, 50 kW/m^2).

3.7.9 Dryout CHF

The dryout CHF point was the last data point successfully recorded at a constant heat flux as the film flow rate was decreased and no liquid separation occurred.

3.7.10 DNB CHF point for pool boiling

The CHF point due to DNB for pool boiling was determined by incrementing the heat flux upwards until the heat flux collapsed due to liquid separation from the tube. The peak heat flux achieved during this process was considered the CHF.

3.7.11 DNB CHF point for falling film boiling

The DNB CHF point was determined in two ways, depending on the test conducted. In tests where the heat flux was increased and the film flow rate was kept constant at a maximum (typically 0.13 kg/m/s), the DNB CHF point was recorded as the peak heat flux obtained if separation between the liquid and the boiling surface occurred. In tests where the heat flux was kept constant and the film flow rate decreased, the DNB CHF point was the last data point successfully recorded at that heat flux before liquid separation was noted. If no liquid separation was noted but heat flux collapsed with dry patches observed, that was then a dryout CHF point.

3.7.12 Critical film Reynolds number

The critical film Reynolds number, $Re_{f,cr}$, was determined as the highest film Reynolds number at a particular heat flux at which either critical dryout, dryout CHF or DNB CHF occurred.

3.7.13 Average deviation

The average deviation between correlations and experimental data was defined as

$$Average\ deviation = \frac{1}{n}\sum_{i=1}^{n} \frac{|(Correlation\ value) - (Experimental\ value)|}{(Experimental\ value)} \times 100 \tag{3-12}$$

in order to facilitate the comparison of experimental data to correlations. The correlation values were calculated at each of the experimental data points.

3.7.14 Nucleation site density

The nucleation site density was calculated from high-speed video taken of the pool boiling surfaces at a heat flux of 20 kW/m^2 with R-245fa at a saturation temperature of 20°C. The nucleation sites were identified manually by zooming in on the high-speed video and forwarding and reversing the playback to identify where bubbles originated. The nucleation site density could not be determined at higher heat fluxes with R-245fa or with any R-134a tests because the greater bubble nucleation brought about by these conditions caused an increased number of passing bubbles that obscured the nucleation sites.

The nucleation site density could also not be determined for falling film boiling conditions as the majority of bubble nucleation took place on the top of the tube where the camera did not have adequate visual access to the tube. Furthermore nucleation sites on the sides of the tubes were generally obscured by the sliding bubbles that primarily originated from the top of the tube.

3.7.15 Boiling exponent *m*

The sensitivity of the pool boiling and falling film boiling HTCs to changes in heat flux was quantified by fitting the following power law relation to the data to determine the boiling exponent m.

$$h_o = aq^m \tag{3-13}$$

3.7.16 Evaporative limit i.t.o. film Reynolds number

The evaporative limit in terms of film Reynolds number, which is the minimum film Reynolds number that can support a particular heat flux assuming all supplied liquid is vaporised by the boiling process, was calculated as:

$$Re_{f,evap} = 4\pi D_o \frac{q}{h_{fg}\mu_l} \tag{3-14}$$

where h_{fg} was the latent heat of vapourisation of the refrigerant, estimated with REFPROP 8.

3.8 Uncertainty

The full description and derivation of how the uncertainties of the measured and calculated quantities were determined is given in Appendix **B**. Only a brief overview of the methods employed to determine the uncertainties will be presented here followed by the results of the uncertainty analysis.

The expanded standard uncertainties of the various sensors were determined as per the methodology employed in Dunn [128]. The bias was assumed to be equal to the uncertainty of the reference probes used and the precision was assumed to be equal to the uncertainty introduced by the calibration process and the calibration linear regression fit. The resulting expanded standard uncertainties of the probes are listed in **Table 3-7**, with a 95% confidence interval employed. The combined standard uncertainties of the various calculated quantities were determined through the law of propagation of uncertainty as detailed in JCGM 100:2008 [129].

The uncertainty of the roughness measurements was estimated through a Type A evaluation and an assumed normal distribution of roughnesses about the mean value measured (as per JCGM 100:2008 [129]) with a confidence interval of 95% employed. The individual roughness uncertainties are illustrated in with the overall average roughness uncertainty found to be 0.17 µm as listed in **Table 3-7**. illustrates that the absolute magnitude of the roughness uncertainties increased as the roughness increased and that the differences in roughness between tubes of a particular material are significant when compared to the uncertainties, suggesting a sufficiently spread sample of roughnesses has been chosen.

Table 3-7. Sensor uncertainties.

Sensor	**Symbol**	**Uncertainty**
Temperature	ΔT	0.1°C
Pressure	ΔP	1 kPa
Refrigerant film flow rate	$\Delta\dot{m}_r$	0.54%
Heating water mass flow rate	$\Delta\dot{m}_w$	0.19%
Surface roughness	ΔR_a	0.17 µm

The uncertainties calculated for two typical cases of a polished copper tube (R_a of 0.12 µm) under falling film boiling conditions are illustrated in **Figure 3-12** as a function of heat flux. The uncertainties vary across the range of heat fluxes tested, with the lowest uncertainties at the highest heat fluxes due to the larger temperature differences across the heating water and between the heating water and refrigerant. Measurements at heat fluxes lower than 20 kW/m^2 were not practical and were avoided due to the exponential rise in the uncertainty of the HTC as the heat flux was lowered. The falling film heat transfer enhancement uncertainty was significantly lower than the other calculated quantities as it was a ratio calculated from two dependant properties.

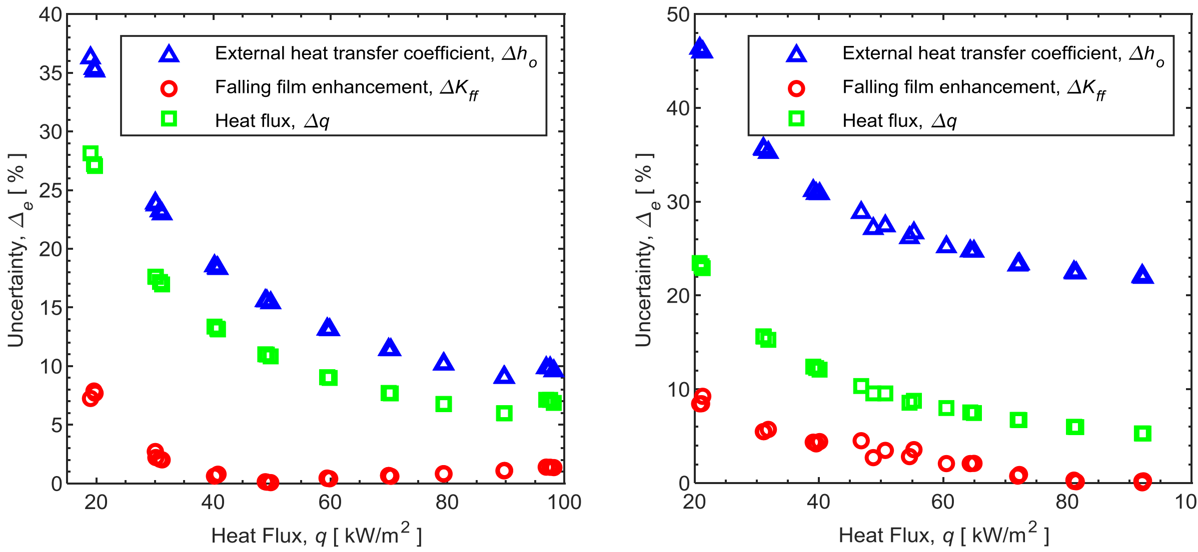

(a) R-245fa at 20°C (b) R-134a at 5°C

Figure 3-12. Uncertainties as a function of heat flux in for a polished copper tube (R_a of 0.12 µm) under falling film boiling conditions.

The overall average uncertainties of the calculated quantities as a function of heat flux across the entire range of tests are shown in **Table 3-8**. The average HTC uncertainty was 29 and 32% for pool and falling film boiling respectively, with a minimum of 19 and 23% at a heat flux of 100 kW/m^2 and a maximum of 43 and 47% at a heat flux of 20 kW/m^2 for pool and falling film boiling respectively. The uncertainty of the falling film heat transfer enhancement ratio varies from 7.1% at a heat flux of 20 kW/m^2 to 2.0% at a heat flux of 100 kW/m^2. These uncertainties are comparable to previous researchers who worked on this same piece of equipment [11,13] and other similar experimental setups [22].

Table 3-8. Summary of uncertainties of calculated quantities for pool boiling and falling film conditions.

Calculated quantity	**Overall average uncertainty**	**Average uncertainty at 20 kW/m²**	**Average uncertainty at 100 kW/m²**
q_{pb}	11%	23%	5.9%
q_{ff}	13%	26%	5.3%
h_{pb}	29%	43%	19%
h_{ff}	32%	47%	23%
K_{surf}	14%	13%	34%
K_{ff}	4.3%	7.1%	2.0%

3.9 Summary, conclusions and recommendations

An experimental system was commissioned and calibrated in order to conduct heat transfer studies on horizontal tubes under either pool boiling or falling film boiling of saturated refrigerants.

A number of plain tubes of different roughness and material were prepared for use in the study. Three nanostructured surfaces were also prepared on polished copper tubes for use in the study. Surface characterisation of the plain tubes showed that a range of roughnesses had been chosen that exceed those seen on typical commercial tubes, and material properties showed that the thermal effusivities of the copper, mild steel and stainless steel tubes chosen spanned a wide range.

Tests showed a significant aging effect on the CuO surface, with the organic refrigerant likely adsorbed onto the surface, which altered the wetting characteristics significantly. Subsequent surface characterisation of the aged nanostructured surfaces showed that the CuO and nanoFLUX surfaces operated in the Cassie-Baxter state when water in air contact angle tests were conducted, while the remaining surfaces had contact angles below 90°. Refrigerant in air contact angle measurements showed all surfaces were wetted by the refrigerant, although significant noise during the measuring process did not allow for any differences in refrigerant wetting between the surfaces to be distinguished. Isothermal tests as well as high speed video of falling film boiling showed that the CuO and nanoFLUX surfaces had the capability to wick liquid, while the other surfaces tested did not.

Experiments were conducted across heat fluxes from 20 to 100 kW/m^2, film flow rates from 0 to 0.13 kg/m/s and reduced pressures of 0.034 to 0.160. Testing at both lower and higher heat fluxes are recommended for future studies, with lower heat fluxes allowing for the investigation of onset of falling film boiling and higher heat fluxes allowing for the DNB CHF points of plain tubes to be measured.

The data reduction allowed for local external HTCs to be measured at the midpoint of the tubes tested. An uncertainty analysis showed that the HTC uncertainties varied across the heat flux range, with HTC uncertainties varying from a high of approximately 45% at 20 kW/m^2 to a low of approximately 20% at 100 kW/m^2 for pool boiling and falling film boiling, with an overall average HTC uncertainty of approximately 30%. The uncertainty of the falling film heat transfer enhancement ratio, K_{ff} , was significantly lower as it was a ratio calculated from two dependant properties, with uncertainties ranging between 7 to 2% across the heat flux range.

4. Validation

4.1 Introduction

The experimental setup and method of data reduction was validated through the comparison of the data gathered in this study to data gathered in previous studies and existing correlations. The data compared was the Wilson plots, a condensation heat transfer study conducted specifically for validation purposes and pool boiling and falling film boiling heat transfer studies on copper tubes.

4.2 Wilson plots

The Wilson plots conducted acted as an initial validation stage, as the internal heat transfer modifying coefficient, C_i, determined in this paper of 1.25 compared satisfactorily to previous researchers who worked with plain tubes on this same experimental setup when it was operational in Switzerland with values of 1.27 [108], 1.18 [109] and 1.29 [130] previously measured. Appendix **C** details the Wilson plot process and results in full.

4.3 Condensation

Condensation tests were used to validate the measurement system of the experimental apparatus as the literature for pool boiling and falling film studies often exhibit a wide spread of results as well as a lack of surface roughness information. Furthermore, the most successful modelling solutions for boiling are semi-empirical as the production of correlations for nucleate boiling is fraught with difficulty [30], which makes them unsuitable for stand-alone validation purposes.

Condensation tests were chosen specifically as the Nusselt solution for condensation on tubes without inundation [5] is a solution that has been shown by previous work to agree well with experimental data, with previous results lying within 5% of the solution [131]. Thus the Nusselt solution can serve as a reference for comparison and validation. The results for a single horizontal polished plain copper tube (R_a of 0.12 µm) with condensation on the outside of the tube at a saturation temperature of 30°C and no inundation are illustrated in **Figure 4-1**.

Condensation validation tests were conducted at the beginning of the study when R-134a was used and midway through the study when testing began with R-245fa. The experimental data compares well with the Nusselt solution in both cases. For R-134a, 93% of the data fell within 5% of the Nusselt solution and the average deviation between the data and the Nusselt solution was 2.3%, while for R-245fa 82% of the data fell within

5% of the Nusselt solution and the average deviation between the data and Nusselt solution was 3.2%.

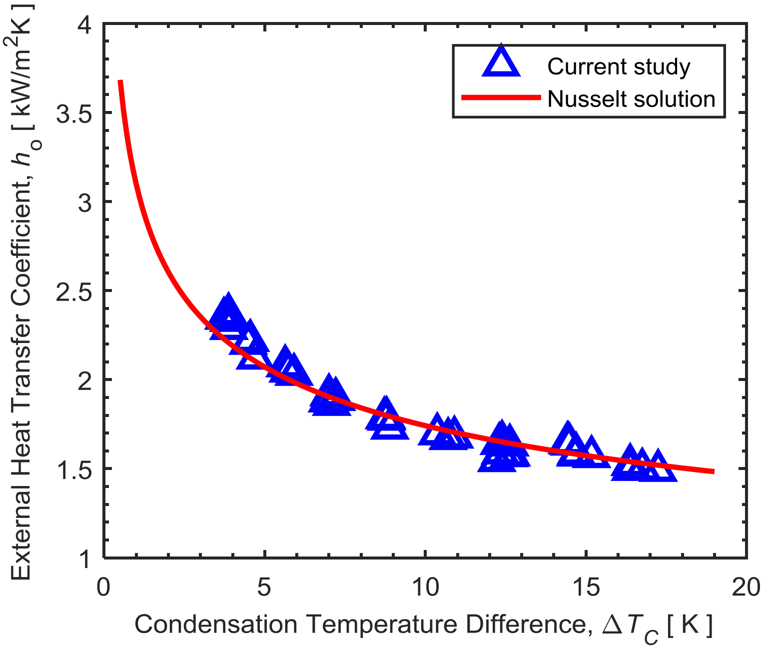

(a) R-134a

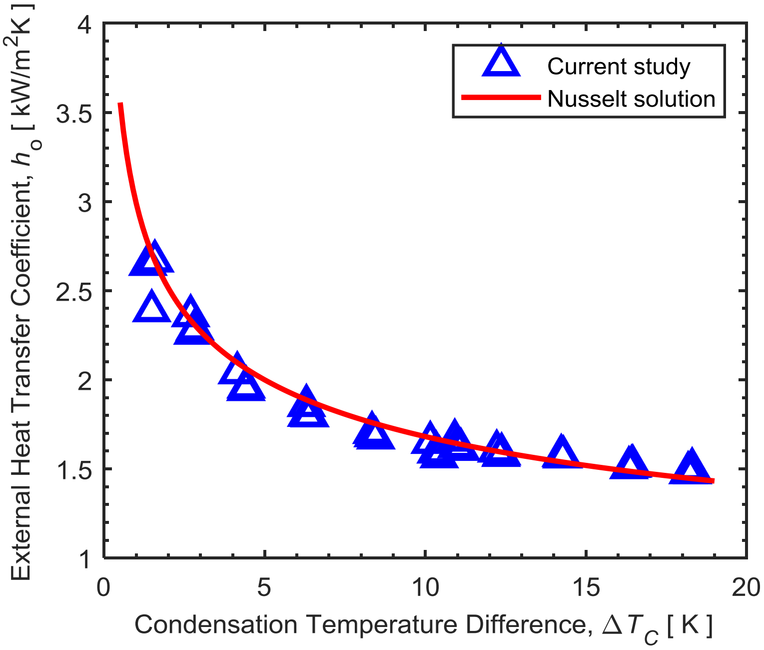

(b) R-245fa

Figure 4-1. Validation of condensation tests at a saturation temperature of 30°C.

4.4 Pool boiling

Pool boiling tests conducted on a single plain copper tube of roughness R_a of 0.74 µm at a saturation temperature of 5˚C with R-134a are presented in **Figure 4-2**. The HTCs are compared to the results of Roques and Thome [11] who conducted pool boiling tests under identical conditions with a similar roughness R_a of 0.8 µm, as well as the correlations of Cooper [39] and Gorenflo and Kenning [18]. The results matched closely to those of Roques and Thome [11] at the upper end of the heat flux range at 80 kW/m^2. However, the two datasets diverged at the lower end of the heat flux range, with a difference of 40% at a heat flux of 20 kW/m^2. Given that the uncertainty of the data increases towards 45% as heat fluxes lower towards 20 kW/m^2, this deviation is expected.

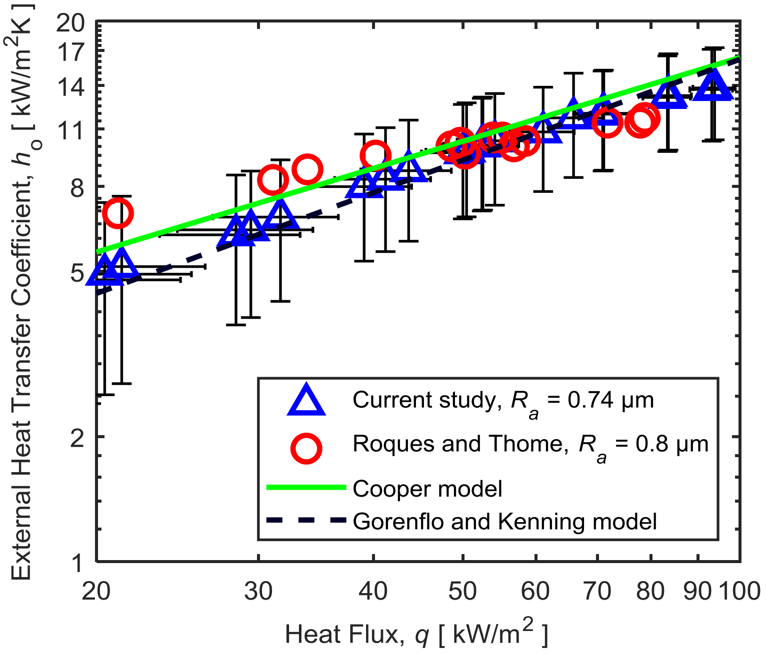

Figure 4-2. Validation of pool boiling of roughened copper tube in R-134a at 5°C.

The Cooper [39] and Gorenflo and Kenning [18] correlations compared well with the results. The average deviation between the data and Cooper correlation was 9.6%, with 95% of the data falling within 15% of the correlation. The average deviation between the data and Gorenflo and Kenning's correlation was 9.2%, with 95% of the data falling within 16% of the correlation.

4.5 Falling film boiling

Falling film boiling tests with a copper tube of roughness R_a of 0.74 µm were compared to the study by Roques and Thome [11] in **Figure 4-3**, with data collected at a saturation temperature of 5˚C with R-134a. Similar to the pool boiling data comparison, the data is more closely matched at higher heat fluxes, with a difference of approximately 20% at a heat flux of 60 kW/m², while the data diverges to a difference of approximately 70% at the lower heat flux of 20 kW/m². A possible reason for the differences between the datasets, despite being measured on the same equipment, could be the various improvements in calibration and roughness measurements that have occurred since the study by Roques and Thome [11], as well as the higher uncertainties at lower heat fluxes.

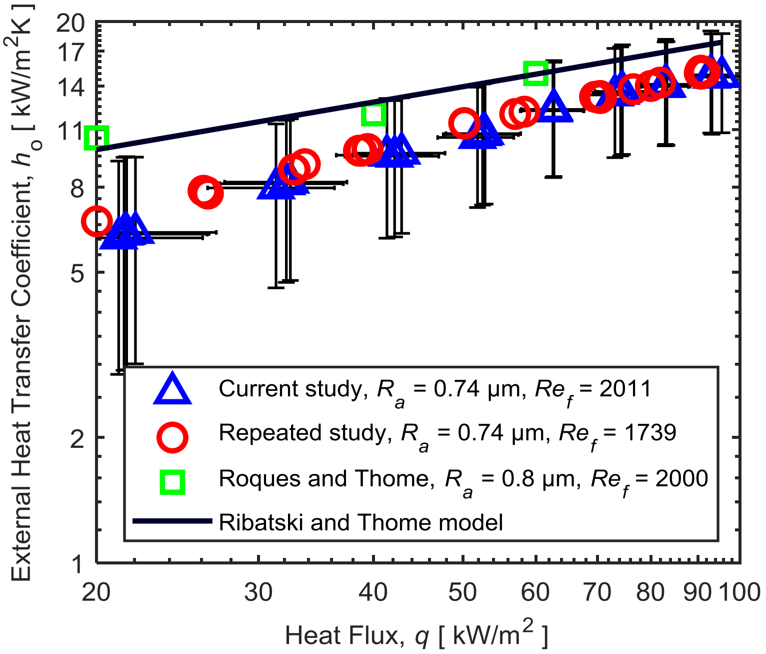

Figure 4-3. Validation of falling film boiling of roughened copper tube in R-134a at 5°C.

The average deviation between the data and the Ribatski and Thome [132] correlation was 34% with 48% lying within 30% of the correlation. The Ribatski and Thome correlation has close agreement with the Roques and Thome [11] data, which can be expected as it incorporated data from Roques and Thome [11] into its fitting process. Other falling film correlations were not considered as they do not take surface roughness into account.

The short term repeatability of the experiments are illustrated throughout the study, with data successively captured at the same tests point. For example in **Figure 4-3** three successive readings were taken at each set point, with the data points differing by less than 3% of each other. The longer term repeatability of the experiments is also illustrated in **Figure 4-3**, with two nearly identical studies conducted five months apart having produced data that highly overlapped, with an average deviation of 5.4% between the repeated data and a curve fit through the original data.

4.6 Summary and conclusion

The experimental equipment, calibration process and data reduction were validated through a number of different approaches. The Wilson plots produced modifying coefficients C_i similar to those measured previously on the same experimental equipment when previously operational in Switzerland. Condensation tests were conducted specifically to validate the equipment setup, as pool boiling and falling film boiling are known to display an often wide spread between different results. Measurements of condensation tests on a single polished copper tube were found to have an average deviation of less than 5% when compared to Nusselt's solution. Pool boiling and falling film boiling HTCs were taken with a roughened copper tube and compared to previous researchers who had also measured their surface roughness. Agreement was typically closer at higher heat fluxes, likely because of reduced uncertainty. Considering the spread typically seen between results of different boiling studies, these pool boiling and falling film results were considered satisfactory.

Considering the good agreement of the condensation tests with Nusselt's solution, the close agreement between the Wilson plot internal coefficients of this study and previous researchers and the fair agreement of the pool boiling and falling film boiling HTCs with previous researchers, the experimental equipment was considered to be suitable to produce valid results so as to meet the research aims of this study.

5. Falling film and pool boiling of plain tubes

Surface roughness and material influence

5.1 Introduction

This chapter details the influence surface roughness and surface material have on the pool boiling and falling film boiling HTCs of plain tubes in R-134a. The HTCs measured under pool boiling conditions are investigated first. Falling film boiling HTCs are then measured at the highest possible film flow rate the experimental equipment could achieve in order to record HTCs with as little dryout influence as possible, across a range of heat fluxes and refrigerant conditions. The influence of the surface roughness and material are compared under falling film boiling to pool boiling using the falling film heat transfer enhancement ratio. The film flow rate is then varied while the heat flux is kept constant for falling film boiling to understand the influence of dryout on the HTCs and to identify the critical dryout threshold. The results presented in this chapter were published in Bock, Meyer and Thome [27].

5.2 Pool boiling results

5.2.1 Influence of roughness on heat transfer

The HTCs measured under pool boiling conditions of R-134a for a range of different roughness copper tubes as a function of heat flux are shown in **Figure 5-1** for saturation temperatures of 5°C and 25°C. Errors bars were omitted on this figure and all subsequent figures to ensure data clarity. The HTCs for all the tubes increased "linearly" on the double log plot as the heat flux was increased. The increases in roughness R_a resulted in an increase in HTC due to an increase in active nucleation sites, as is well documented in previous studies [18,30].

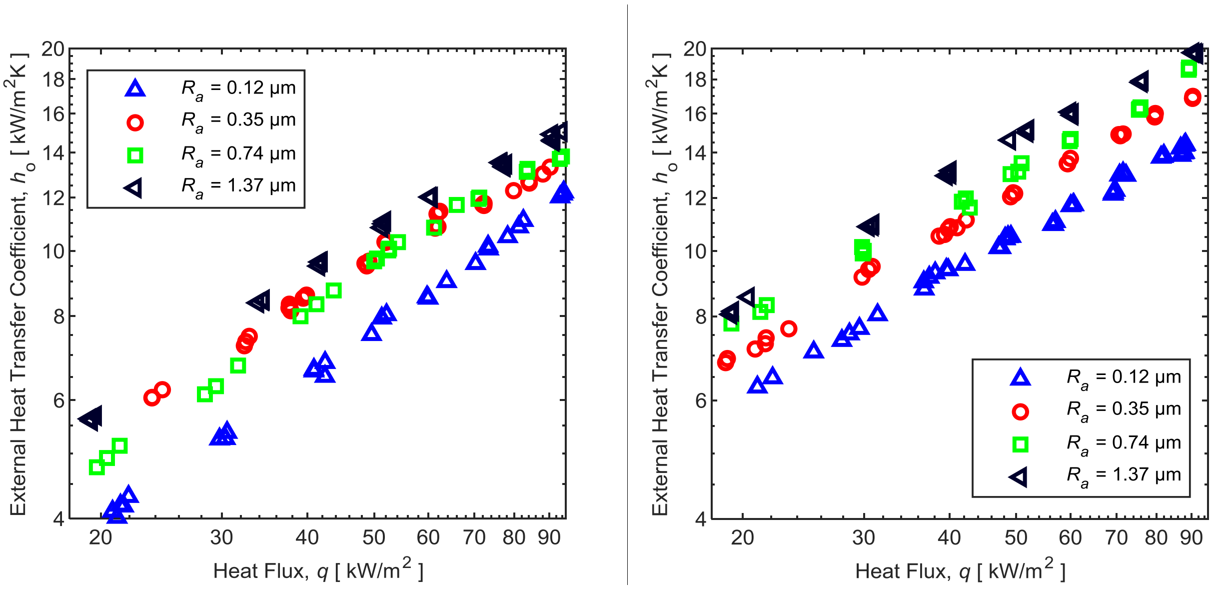

(a) 5°C (b) 25°C

Figure 5-1. Pool boiling HTCs as a function of heat flux of different roughness copper tubes in R-134a.

The influence of the roughness on the HTCs was characterised by the fit of the relation $h_o \propto {R_a}^b$ to the experimental data, with the results for the copper tubes under pool boiling conditions listed in **Table 5-1**. The pool boiling results were found to approximately adhere to Stephan's relation of $h_o \propto R_a^{0.133}$ [133] for copper tubes in refrigerant.

Table 5-1. Relationship between external HTC and surface roughness for copper tubes for pool boiling in R-134a.

Saturation temperature [°C]	**Dependence of external HTC on surface roughness**
5	$h_o \propto R_a^{0.11}$
25	$h_o \propto R_a^{0.13}$

It should be noted that the roughness heat transfer enhancement limit, where increased surface roughness no longer results in heat transfer improvements [19,34], was not reached in this study for pool boiling conditions.

The increase in saturation temperature from 5°C to 25°C increased the HTC by approximately 50% to 30% across the range of heat fluxes for all roughnesses. The increase is to be expected given the well-known influence of pressure on boiling heat transfer [18,30]. While surface roughness has been shown to have a stronger effect at lower pressures [31], this effect could not be distinguished in this study.

5.2.2 Influence of surface material on heat transfer

The HTC's as a function of heat flux of three different material tubes that were polished at saturation temperatures of 5°C and 25°C under pool boiling conditions of R-134a are presented in **Figure 5-2**. In general the HTC's increased linearly on the double log plot as the heat flux was increased. However, the HTCs of the mild steel tube were shown to be less sensitive to increases in heat flux than the copper and stainless steel tubes.

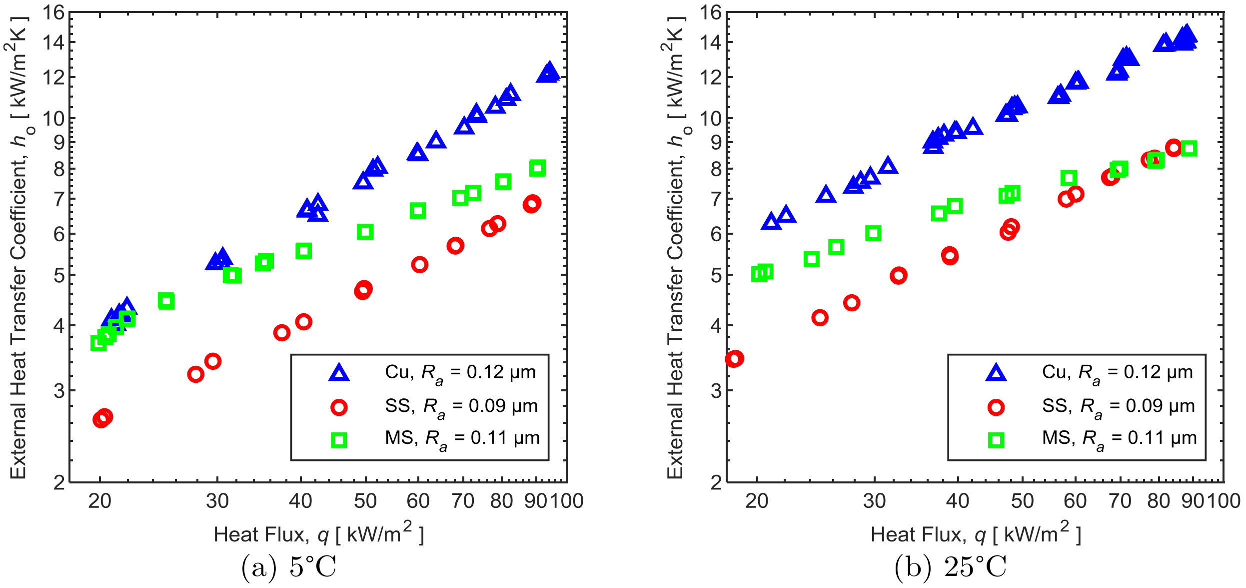

(a) 5°C (b) 25°C

Figure 5-2. Pool boiling HTCs as a function of heat flux with polished tubes of different materials in R-134a.

The copper tube is shown to have the highest HTCs, followed by the mild steel tube and then the stainless steel tube. This follows the trend of the thermal effusivity of the tubes, which is considered an influential property of surface materials on the heat transfer process in pool boiling [18].

The increase in saturation temperature again shows an increase in HTCs as the temperature is raised across all three materials. Copper and stainless steel increased by between 54% to 18% and 35% to 29% respectively with the increase in saturation temperature. Mild steel was shown to be less sensitive to the saturation temperature increase, increasing by between 32 to 10% across the heat flux range.

The HTCs of roughened tubes of different material as a function of heat flux are shown in **Figure 5-3**. The trends displayed are similar in form to that of the polished tubes illustrated in **Figure 5-2.** The mild steel is shown to be less sensitive to the increase in roughness than copper and stainless steel, despite having the highest roughness of the three tubes tested in **Figure 5-3.**

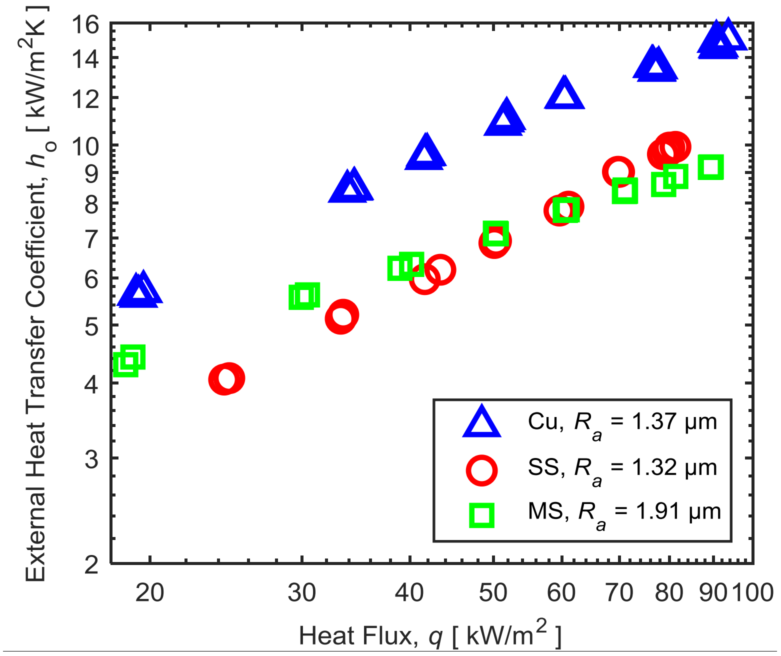

Figure 5-3. Pool boiling HTCs as a function of heat flux with roughened tubes of different material at 5°C in R-134a.

5.3 Falling film results

5.3.1 Influence of roughness on heat transfer

The HTCs as a function of heat flux for falling film boiling conditions are shown in **Figure 5-4**. A range of different roughness copper tubes were tested at saturation temperatures of 5°C and 25°C in R-134a with a film flow rate of approximately 0.13 kg/m/s.

The falling film HTCs are shown to mostly exhibit similar overall trends to the comparative pool boiling results in **Figure 5-1** with the HTCs seen to mostly increase linearly as the heat flux is increased on the log-log plot. The HTCs of the tubes displayed a similar sensitivity to increases in heat flux across the range of roughnesses tested. However as higher heat fluxes are reached, the falling film HTCs begin to tail off and become less sensitive to increases in heat flux. This is due to partial dryout resulting in a drop-off of heat transfer, despite the high film flow rate.

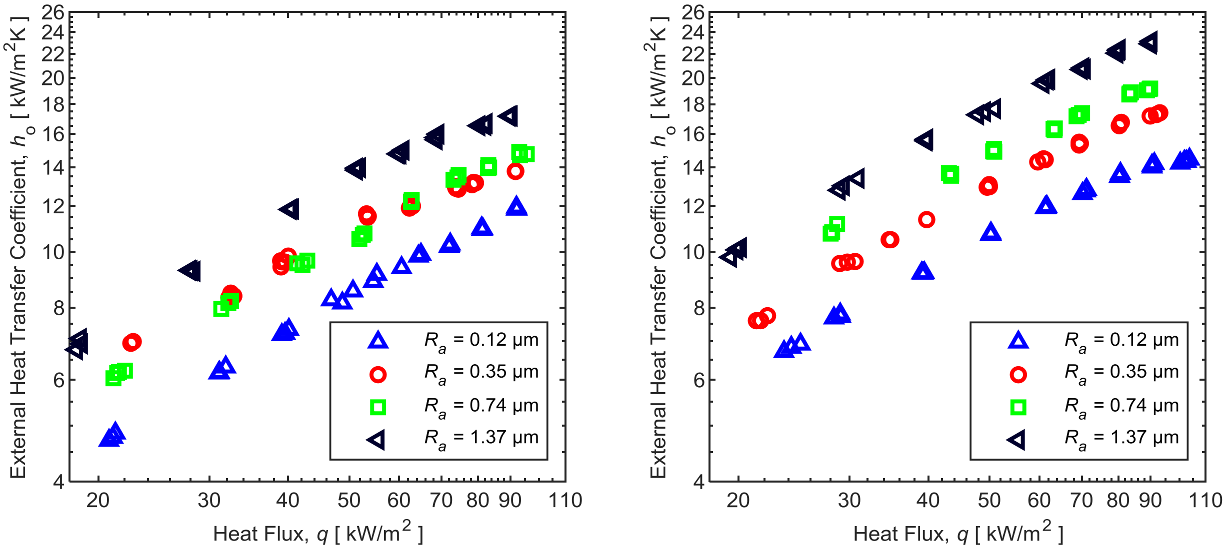

(a) 5°C (b) 25°C

Figure 5-4. Falling film boiling HTC's as function of heat flux with different roughness copper tubes at a film flow rate of ~0.13 kg/m/s in R134a.

The falling film HTCs however increased more as roughness was increased when compared to the respective pool boiling results. At 20 kW/m^2 when the roughness R_a was increased from 0.12 μm to 1.37 μm, the falling film HTCs increased by 75% compared to an increase of only 50% for the comparable pool boiling HTCs. The influence of the roughness on the HTCs for the falling film boiling studies for copper tubes are shown in **Table 5-2** and was found to adhere to the relationship $h_o \propto R_a{}^{0.17}$ at 5°C and $h_o \propto R_a{}^{0.21}$ at 25°C. These exponents are larger than the equivalent for pool boiling as listed in **Table 5-1,** which were 0.11 and 0.13, and Stephan's relation for pool boiling of copper tubes in refrigerant of $h_o \propto R_a{}^{0.133}$ [133] and further illustrate that falling film boiling HTCs are more sensitive to increases in roughness than pool boiling.

Table 5-2. Relationship between external HTC and surface roughness for copper tubes for falling film boiling in R-134a.

Saturation temperature [°C]	**Dependence of external HTC on surface roughness**
5	$h_o \propto R_a{}^{0.17}$
25	$h_o \propto R_a{}^{0.21}$

It should be noted that, similar to the pool boiling results, the falling film boiling results did not reach the roughness heat transfer enhancement limit, where increased surface roughness no longer results in heat transfer improvements [19,34]. This limit has not been confirmed to also occur in falling film boiling and thus testing at greater roughnesses than used in this study is recommended for future work.

The differing impacts of roughness on the two modes of boiling is further illustrated by the falling film heat transfer enhancement ratio, K_{ff}, shown as a function of heat flux for the range of different roughness copper tubes in **Figure 5-5** for R-134a for saturation temperatures of 5°C and 25°C with a film flow rate of approximately 0.13 kg/m/s. Falling film boiling mostly outperformed pool boiling, with enhancement ratios varying from 1 – 1.3. As discussed in Chapter **2**, this can be attributed to the enhancement mechanisms that have been suggested to be influential in the thin film boiling process, such as the role of trapped bubbles sliding in the falling film [78,80] and increased bubbles sliding in the falling film due to the secondary nucleation mechanism [81,134] resulting in increased microlayer evaporation.

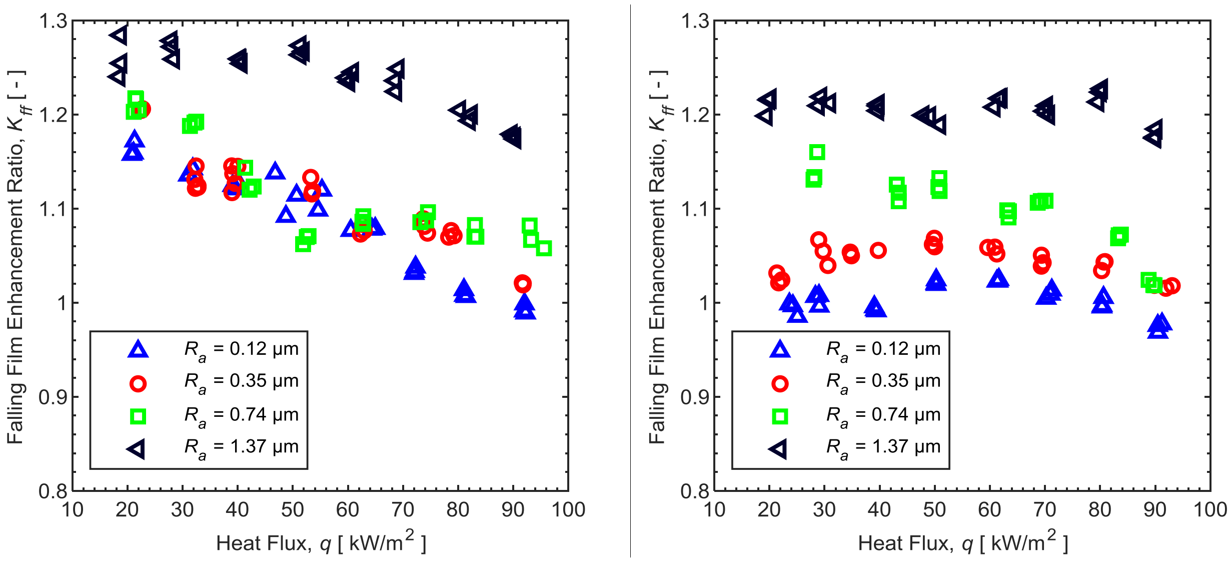

(a) 5°C (b) 25°C

Figure 5-5. K_{ff} as a function of heat flux with different roughness copper tubes at a film flow rate of ~0.13 kg/m/s in R-134a.

The enhancement was weakly influenced by heat flux, with the enhancement decreasing by approximately 10% as the heat flux increases from 20 to 90 kW/m^2 at 5°C, while at 25°C the enhancement ratio was insensitive to changes in heat flux across the range tested.

The falling film enhancements generally increased as the roughness of the tubes was increased for copper tubes, with the enhancement ratio ranging from 1 to 1.3 as the surface roughness was increased from 0.12 μm to 1.37 μm. The reason that rougher tubes benefit more from falling film conditions than their smoother counterparts is likely due to the greater bubble density on rougher tubes due to their greater nucleation site density. This greater bubble density would result in an increased enhancement of heat transfer compared to pool boiling due to an increased number of bubbles trapped in the thin film and the resulting increased microlayer evaporation. A visualisation study with a high speed camera is recommended to further investigate this hypothesis. Testing surfaces with greater roughnesses would also determine if the falling film enhancement due to roughness has an upper limit.

The falling film enhancement ratio appears weakly dependant on the saturation temperature, with the enhancement ratios increasing by between 0 to 15% as the saturation temperature was dropped from 25°C to 5°C. As a result additional tests were conducted on the low pressure refrigerant R-245fa in an attempt to better determine the refrigerant influence on the enhancement ratio. These results are documented in Chapter **7**, as important insight was gained into the fluid influence on the enhancement ratio through the comparison of the results of the nanostructured and plain tubes tested across the range of refrigerant conditions.

The trends regarding falling film heat transfer performance are noted to be less clear at 5°C than 25°C, most likely through experimental uncertainty. However, when comparing the results of the smoothest and roughest tubes to each other, the trends discussed are clearly applicable.

5.3.2 Influence of surface material on heat transfer

The falling film HTCs as a function of heat flux for different materials of polished tubes are shown in **Figure 5-6** at saturation temperatures of 5°C and 25°C in R-134a, while the HTCs as a function of heat flux are shown for roughened tubes at a saturation temperature of 5°C in R-134a in **Figure 5-7**. Both tests were operated with a film flow rate of approximately 0.13 kg/m/s.

The general trends again follow those of the comparable pool boiling results, with the HTCs increasing as the heat flux is increased, with mild steel being less sensitive to the increases in heat flux than copper or stainless steel. Again the magnitude of the HTCs follows the trend of the thermal effusivities, with copper outperforming mild steel which outperforms stainless steel. At lower heat fluxes the mild steel has comparable heat transfer to the copper tubes, but as the heat flux increases its lower heat flux sensitivity means that it has comparable heat transfer performance to stainless steel at higher heat fluxes.

The falling film heat transfer enhancement ratio K_{ff} as a function of heat flux for smoother and rougher tubes of different material in R-134a at a saturation temperature of 5°C and film flow rate of 0.13 kg/m/s are shown in **Figure 5-8** (a). The enhancement ratios were weakly sensitive to the heat flux, with the enhancement ratios decreasing by less than 10% as the heat flux was increased from 20 to 90 kW/m^2. All three materials tested showed an increase in enhancement ratio as the roughness was increased.

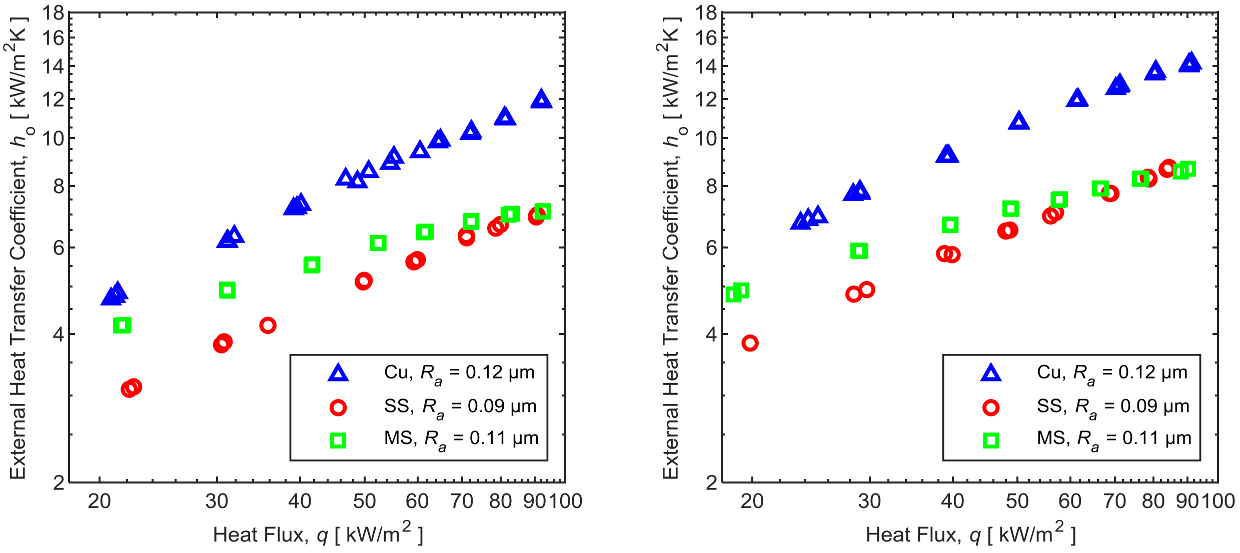

(a) 5°C

(b) 25°C

Figure 5-6. Falling film boiling HTCs as a function of heat flux with different material smoother tubes in R-134a at a film flow rate of ~0.13 kg/m/s.

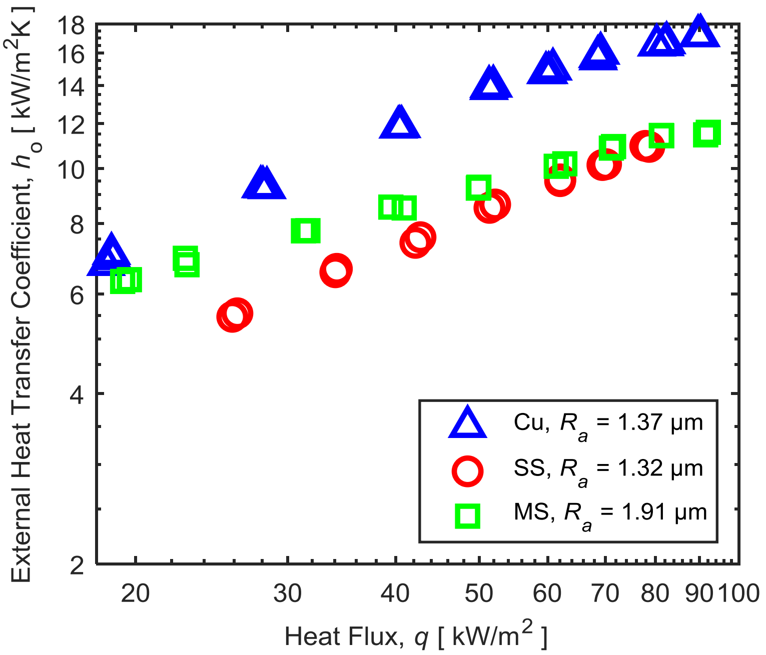

Figure 5-7. Falling film boiling HTCs as a function of heat flux with different material rougher tubes at a film flow rate of 0.13 kg/m/s in R-134a at 5°C.

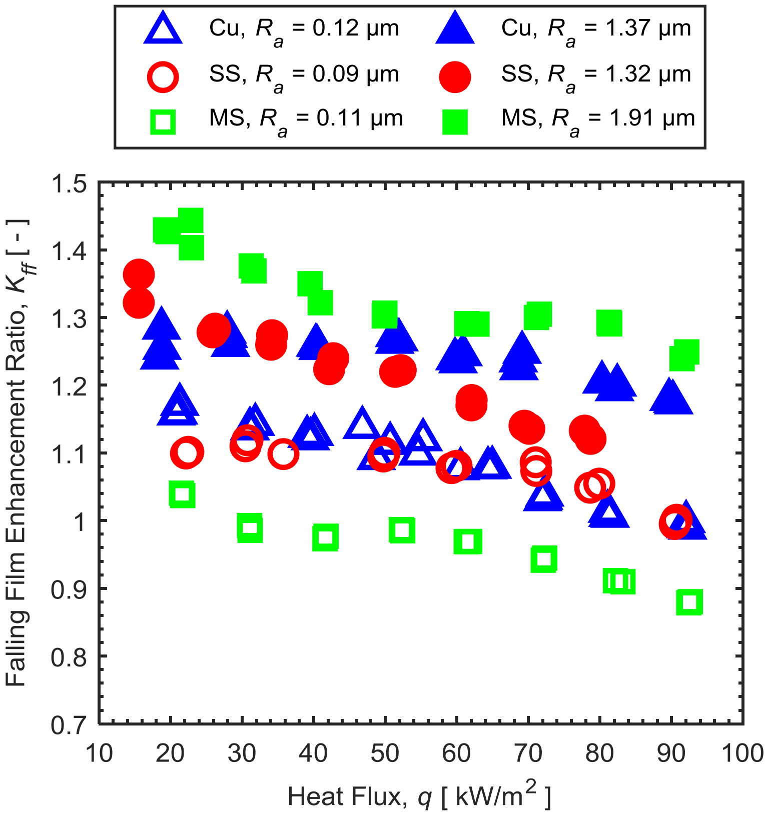

(a) 5°C

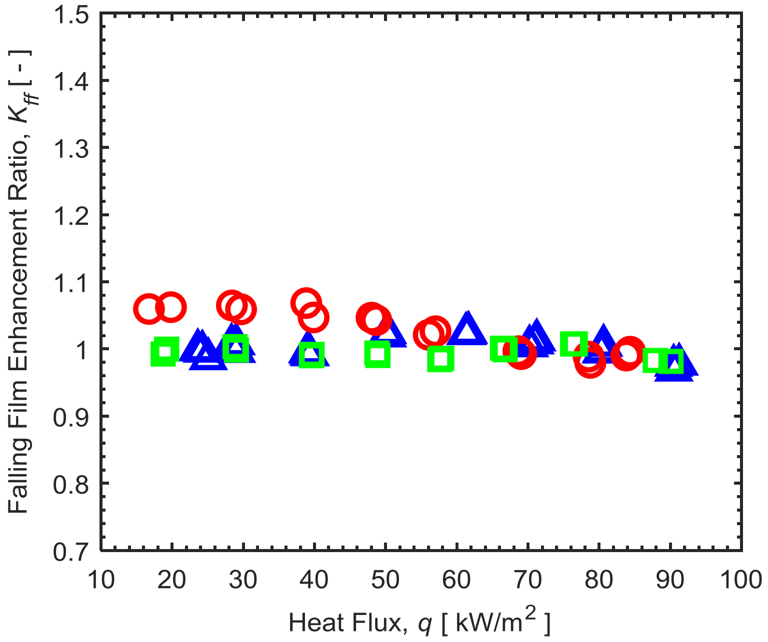

(b) 25°C

Figure 5-8. K_{ff} as function of heat flux with different material tubes at a film flow rate of ~0.13 kg/m/s in R-134a at a saturation temperature of (a) 5°C and (b) 25°C.

The K_{ff} ratio as a function of heat flux in R-134a at a saturation temperature of 25°C of the polished different material tubes are shown in **Figure 5-8** (b). There was very little falling film heat transfer enhancement under these conditions, with all materials exhibiting enhancement ratios close to one. The ratios were also relatively insensitive to changes in heat flux.

The difference in tube materials did not significantly influence the K_{ff} ratio, with both the smoother and rougher tube enhancement ratios of the various material tubes within approximately 10% of each other. It follows that the wall material did not significantly influence the various mechanisms suggested that cause the falling film heat transfer enhancement. This suggests that while the wall material influences the overall boiling process through the conduction of heat to the nucleation sites, it does not influence the any unique falling film heat transfer enhancement mechanism.

Compared to the comparable enhancement ratios at a saturation temperature of 5°C, the enhancement ratios decreased slightly for all materials at 25°C. This phenomena is investigate further in Chapter **7** with tests on nanostructured tubes and plain tubes in R-245fa providing valuable further insight into the influence refrigerant conditions play on the falling film heat transfer enhancement mechanism.

5.4 Dryout results

5.4.1 Influence of film flow rate on heat transfer

A typical plot of the HTC's as a function of film flow rate is shown in **Figure 5-9**. The results are for plain copper tubes that were polished (R_a of 0.12 µm) (**Figure 5-9** (a)) and roughened (R_a of 0.74 µm) (**Figure 5-9** (b)) and were tested at a saturation temperature of 5°C in R-134a at the heat fluxes of 20, 50 and 80 kW/m^2. Both tubes at all three heat fluxes followed similar general trends of relatively stable HTCs as the film flow rate was decreased from a maximum until a rapid drop off in heat transfer occurs, caused by critical dryout of the tubes.

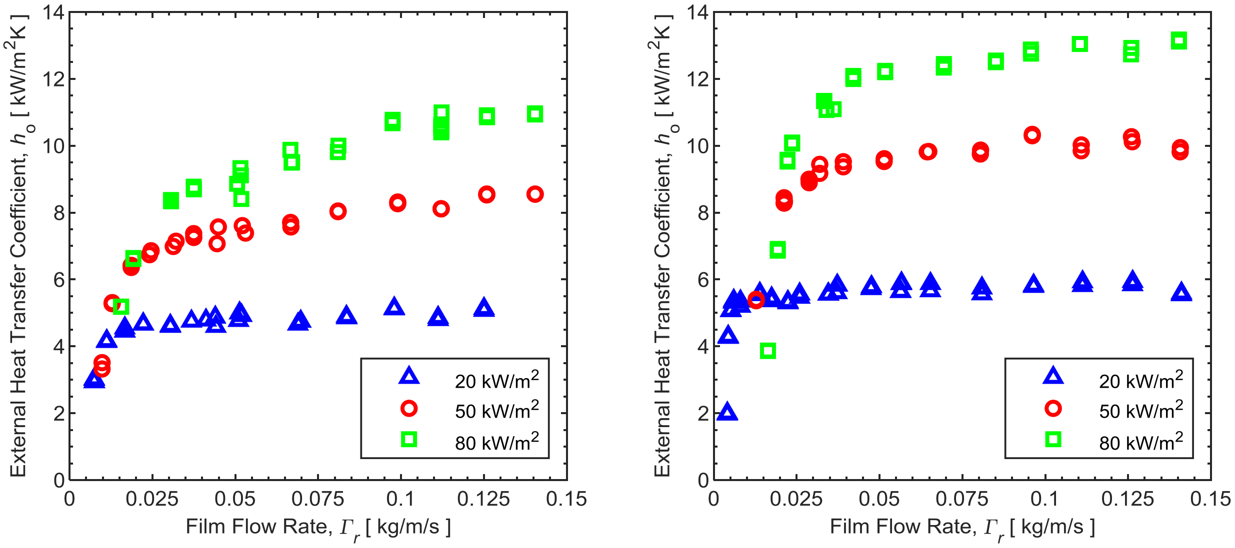

(a) R_a of 0.12 µm (b) R_a of 0.74 µm

Figure 5-9. Falling film boiling HTCs as a function of the film flow rate on plain copper tubes in R-134a at 5°C.

The cause of the rapid decrease in HTC resulting in critical dryout is relatively well understood, with the falling film breaking down and dry patches appearing on the tube at the low film flow rate conditions. This was visually confirmed during both this study and previous studies [91].

The rougher tube at all heat fluxes and the smoother tube at 20 kW/m^2 exhibit a region where the HTC is practically insensitive to film flow rate changes. The HTC is seen to change less than 5% for these tubes for film flow rates above 0.05 kg/m/s. Roques and Thome [11] and Ribatski and Thome [132] observed similar behaviour when they performed similar experiments on a plain tubes of roughness R_a of 0.8 µm with R-134a at a 5°C saturation temperature up to heat fluxes of 55 kW/m^2. Jin et al. [12] found a similar insensitive plateau region when testing with R134a, R290 and R600a with plain tubes of unspecified roughness.

However, the polished tube at higher heat fluxes of 50 and 80 kW/m^2 exhibits a plateau region with greater sensitivity to changes in film flow rate. The HTC drops by approximately 15% as the film flow rate is dropped from 0.13 to 0.05 kg/m/s. A falling film study by Zhao et al. [22] with R-134a at saturation temperatures of 6°C, 10°C and 16°C on plain copper tubes also exhibited a plateau region with higher sensitivity to changes in film flow rates.

A similar difference in plateau region sensitivity can be seen when Jin et al. [12] compared their heat transfer results for falling film boiling of plain tubes at 6°C to those of Zhao et al. [22] who tested under near identical conditions with the same experimental setup. Jin et al. [12] found their falling film plateau region to be very insensitive to changes in film flow rate, while the data of Zhao et al. [22] showed a greater plateau region sensitivity. Jin et al. [12] did not offer a possible explanation for the differences and noted that they were within experimental uncertainty limits. The surface roughness of the tubes was not recorded by either Jin et al. [12] or Zhao et al. [22].

A possible practical cause may be imperfections in the fluid distribution along the length of the tube. Despite every effort made in this study to ensure even fluid distribution along the length of the tubes, it was also noted through visual observation that even at high film flow rates (above 0.1 kg/m/s) dry patches would occasionally form and then immediately disappear on both polished and roughened tubes.

Thus there may have been maldistribution of the fluid for the polished tubes that led to localised areas along the length of the tube experiencing temporary instances of partial dryout, even at high film flow rates. This phenomena would worsen as the film flow rates decreased, thus causing a reduction in HTC.

A possible physical explanations is that the sensitivities are linked to the wettability of the tubes, with the rougher surface having an improved wettability over the smother tube. This improved wettability would reduce the intermittent dryout seen on the tubes even at high film flow rates. While the dry spots which formed within the plateau region were temporary, these dry spots would still temporarily reduce the heat transfer and thus have a negative effect on the time-averaged HTC. Surfaces with higher wettability could have a lower frequency of intermittent dry spots than surfaces with a lower wettability. The frequency of intermittent dry spots would be expected to increase as the film Reynolds number was decreased and thus have a progressively more negative effect on the HTCs of affected surfaces.

However, the rougher tube appears to have similar wettability to the polished tube based on results of the contact angle testing of water-in-air, shown in **Table 3-3** and the refrigerant contact angle tests. But these results do not reflect the condition of the surfaces under falling film boiling. In particular, as the polished tube operates at a higher wall superheat due to lower HTCs, the relatively hotter surface of the polished tube may have a lower wettability due to the greater thermocapillary force and vapour thrust force opening up dry patches. The hotter surface may also promote the creation of dry patches more readily through rapid evaporation of localised thinned areas compared to the colder surface of the roughened tubes.

Further detailed visualisation studies to better understand this phenomenon are recommended. Image analysis of the intermittent dry spots would be a recommended method of determining if the different tubes indeed had different frequencies of intermittent dryout so as to determine whether this sensitivity is indeed some form of dryout phenomenon as hypothesised here or rather caused by another physical process.

Furthermore tests at higher film flow rates may reveal whether all surfaces eventually form a plateau region that is completely insensitive to film flow rate changes.

5.4.2 Influence of surface roughness on critical dryout threshold

The critical dryout threshold, $Re_{f,cr}$, was determined for the non-dimensionalised film Reynolds number as a function of heat flux and is illustrated in **Figure 5-10** for a polished (R_a of 0.12 µm) and roughened (R_a of 0.74 µm) copper tube tested under falling film boiling of R-134a. Also plotted is the evaporative limit, which is the minimum film Reynolds number that can support the corresponding heat flux, assuming all heat is transferred from the tube to the refrigerant and the refrigerant evaporates as a result.

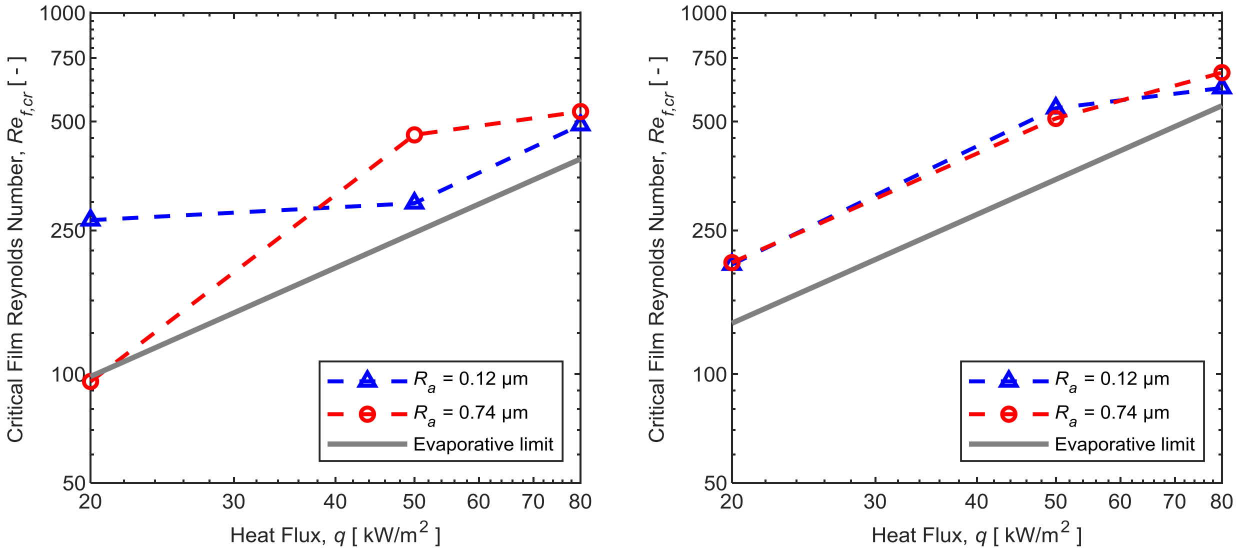

(a) 5°C (b) 25°C

Figure 5-10. Critical film Reynolds number, $Re_{f,cr}$, at which critical dryout took place as a function of heat flux for different roughness copper tubes in R-134a.

The general trend is that the critical dryout threshold increased as the heat flux increased and followed the trends seen in other studies [11,13,22]. The increase in critical dryout threshold approximately followed that of the increase in the evaporative limit across the two refrigerant conditions.

Changes in roughness and saturation temperature were not shown to have a discernible influence on the critical dryout threshold in **Figure 5-10**. Given the inherent difficulty in determining the critical dryout threshold and the relative coarseness of the methods used, influences of smaller magnitude may not be detectable with the methods used in this study. Chapter **7** details the additional testing of R-245fa in a further attempt to determine the influence refrigerant conditions have on critical dryout.

5.4.3 Influence of surface material on critical dryout threshold

The critical dryout threshold as a function of heat flux for different material tubes in R-134a at 5°C is shown in **Figure 5-11**. The critical dryout threshold shows a similar trend across all three materials, with the critical dryout threshold increasing as heat flux is increased proportionally to the increase in the evaporative limit. The wall material did not show a strong influence on the critical dryout threshold in this study.

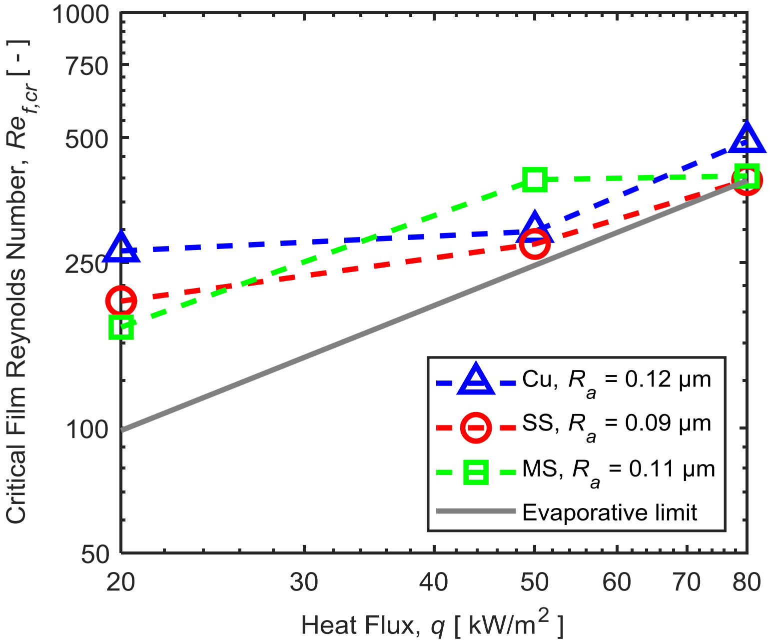

Figure 5-11. Critical film Reynolds number, $Re_{f,cr}$, at which critical dryout took place as a function of heat flux for different material polished tubes at a saturation temperature of 5°C in R-134a.

5.5 Summary, conclusions and recommendations

The purpose of this study was to experimentally measure the influence of surface roughness and surface material of plain tubes on falling film boiling heat transfer, dryout and enhancement ratios as well as on pool boiling heat transfer. Studies were conducted on plain tubes of varying roughness and material across a range of heat fluxes and film flow rates at two saturation temperatures in R-134a.

Plain tubes of different roughness and different material all displayed linearly increasing HTCs during both pool boiling and falling film boiling as the heat flux was increased on a log-log plot. Increases in roughness were found to increase the pool boiling HTCs of copper tubes and approximately adhere to Stephen's relation of $h_o \propto R_a{}^{0.133}$, with exponents measured in this study of 0.11 and 0.13. Surface material influenced the pool boiling HTCs with increasing thermal effusivity and thermal conductivity generally increasing HTCs measured.

Increased surface roughness was found to increase the HTCs of falling film boiling, as was the case for pool boiling. However the increase was greater than that experienced within the pool boiling studies, with the exponents of the fit $h_o \propto {R_a}^{\mathrm{b}}$ equal to 0.17 and 0.21, which were higher than the respective exponents measured under pool boiling conditions, which were 0.11 and 0.13. Thus falling film boiling heat transfer was found to be more sensitive to changes in roughness than pool boiling. This was thought to be as a result of the falling film heat transfer enhancement mechanism. Testing at greater roughnesses than used in this study is recommended for future work to determine if the heat transfer enhancement has an upper limit for falling film boiling similar to that seen in previous pool boiling studies.

Falling film boiling HTCs followed a similar trend to those of pool boiling HTCs when the different material tubes were tested. As the effusivity of the material was increased, the HTCs tended to increase in most cases.

The falling film heat transfer enhancement ratio increased as surface roughness increased for all material tubes tested, with the enhancement ratio ranging from 1 to 1.4 as the roughness ranged from 0.09 μm to 1.91 μm. It is hypothesized that the greater bubble density of rougher tubes increases the enhancement mechanisms proposed, such as greater microlayer evaporation of the sliding bubbles trapped within the falling film. The surface material was found to have no discernible influence on falling film enhancement. High speed falling film boiling visualisation is recommended as a future avenue of research to provide greater insight into the phenomena seen here. Testing surfaces with greater roughnesses would also determine if the falling film enhancement due to roughness has an upper limit.

The saturation temperature influenced the respective pool boiling and falling film HTCs, increasing them as the saturation temperature was increased. The falling film enhancement of the plain tubes was found to be weakly influenced by changes in saturation temperature of R-134a.

A plateau region was found in falling film boiling where the HTCs of the fully wetted tubes were fairly insensitive to changes in film flow rate. This insensitivity did vary across the tubes, with the HTCs of rougher tubes changing by approximately 5% as film flow rates varied from 0.13 to 0.05 kg/m/s, while the HTCs of smoother tubes varied by approximately 15%. Once the film flow rate dropped below a threshold, all tubes tested exhibited a significant drop in HTCs due to critical dryout. Tests at higher film flow rates may reveal whether all surfaces eventually form a plateau region that is completely insensitive to film flow rate changes.

The critical dryout threshold was shown to increase as heat flux was increased. The critical dryout threshold was not shown to be significantly influenced by surface roughness, surface material or saturation temperature. Further studies at larger ranges of surface roughness and saturation temperature are suggested to illicit if any influence is indeed present.

6. Pool boiling on nanostructured and plain tubes

6.1 Introduction

This chapter experimentally measures the HTCs in the pool boiling of R-134a and R-245fa over nanostructured and plain copper tubes. The nucleation site density of tubes is investigated to better understand the heat transfer mechanisms present. These results presented here also allowed for comparison to the falling film boiling results presented in Chapter **7** and the subsequent calculation of the falling film heat transfer enhancement ratios. The work presented in this chapter was published in Bock et al. [28].

6.2 Heat transfer coefficients

The measured external HTCs on the outside of tubes where pool boiling occurred as a function of the heat flux over nanostructured, polished (R_a of 0.12 µm) and roughened (R_a of 1.37 µm) copper tubes are illustrated in **Figure 6-1** for the three reduced pressures tested.

All tubes tested showed typical constant power law relationships with linearly increased HTCs as the heat flux was increased on a log-log plot. The polished and LbL tubes had the lowest HTCs overall. They had similar HTCs at the lowest reduced pressure of 0.034, but as the reduced pressure increased, the polished tube gradually outperformed the LbL tube. The roughened and CuO tubes generally had the second-highest and third-highest HTCs. However, at the higher reduced pressure values of 0.086 and 0.160, the CuO tube HTCs matched and at times surpassed the HTCs of the roughened tube at the upper end of the heat flux range tested. The nanoFLUX tube was associated with the highest HTCs at all reduced pressure values tested.

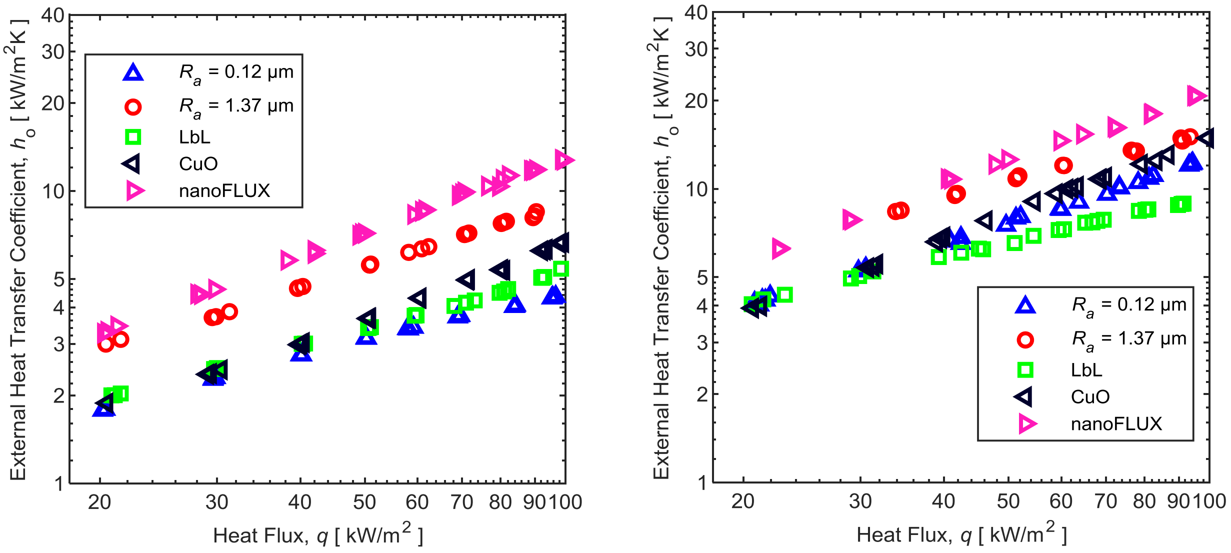

(a) R-245fa, 20°C, p_r of 0.034 (b) R-134a, 5°C, p_r of 0.086

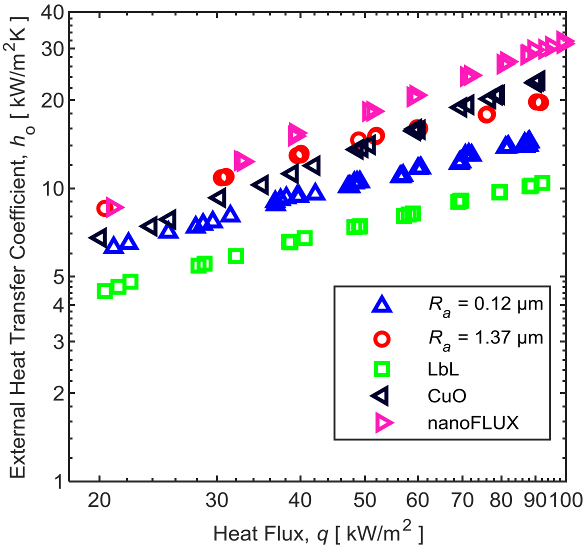

(c) R-134a, 25°C, p_r of 0.160

Figure 6-1. Pool boiling HTCs as a function of heat flux of nanostructured and plain tubes.

Figure 6-2 illustrates the heat transfer performance of the tubes relative to the polished plain copper tube (R_a *of 0.12* µm) at the three reduced pressure values tested. The roughened plain copper tube (R_a of 1.37 µm) outperformed the polished tube by between 60 and 100% at the lowest reduced pressure value, and by approximately 40% at the higher reduced pressure values. The LbL tube slightly outperformed the polished tube at the lowest reduced pressure value of 0.034 by between 5 and 20%. At the higher reduced pressure values, the LbL tube had down to 30% lower HTCs than the polished tube.

The CuO tube performed similarly to the polished tube at low heat fluxes, while at higher heat fluxes, the CuO HTCs were higher than the HTCs of the polished tube by up to 50%.

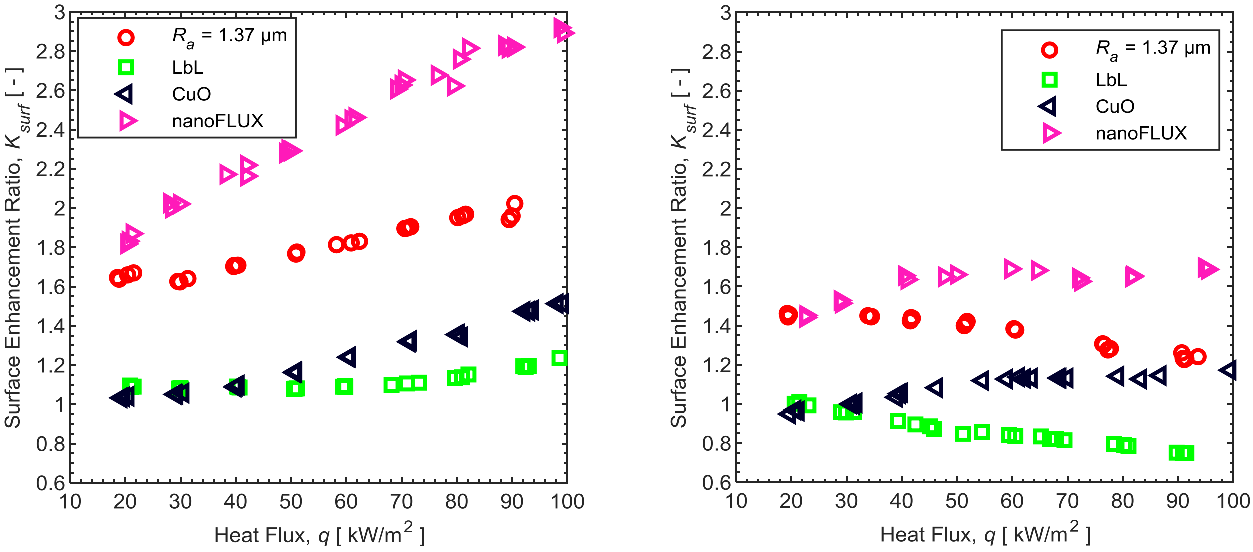

(a) R-245fa, 20°C, p_r of 0.034 (b) R-134a, 5°C, p_r of 0.086

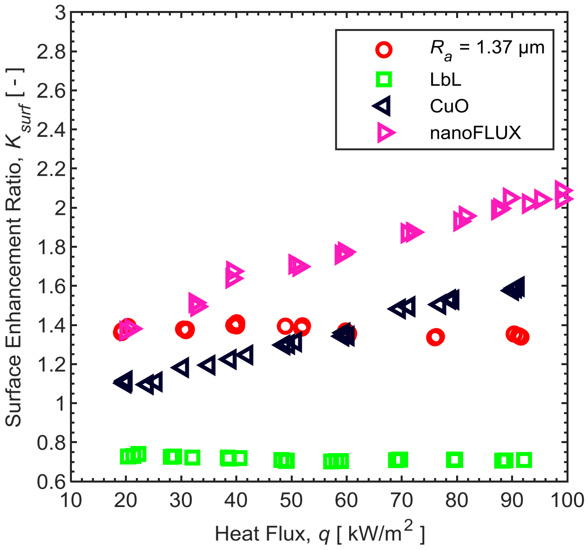

(c) R-134a, 25°C, p_r of 0.160

Figure 6-2. Pool boiling heat transfer performance relative to polished plain tube as a function of heat flux of nanostructured and plain tubes.

The nanoFLUX tube outperformed the polished tube over the heat flux range tested by between 80 and 200% at the lowest reduced pressure value and by approximately 40 to

100% at the higher reduced pressure values. The nanoFLUX tube generally outperformed the roughened tube by up to 50% across the range of test conditions, but the nanoFLUX and roughened tubes had similar HTCs at the lower ends of the heat flux range tested.

It can be noted in **Figure 6-2** that the sensitivity of the HTCs of the tubes to changes in heat flux varied relative to the polished tube and so was further quantified by determining the gradient of the data specifically by fitting the power law relation, $h_o = aq^m$, to the data in **Figure 6-1** to determine the exponent, m. The results are shown in **Figure 6-3**, where it can be seen that the roughened, polished and LbL tubes had lower boiling exponents which indicates that their HTCs were less sensitive to changes in heat flux, particularly at a reduced pressure of 0.16, while and the nanoFLUX and CuO tubes had the highest boiling exponents of approximately between 0.8 and 0.9 and thus had HTCs that where the most sensitive to changes in applied heat fluxes.

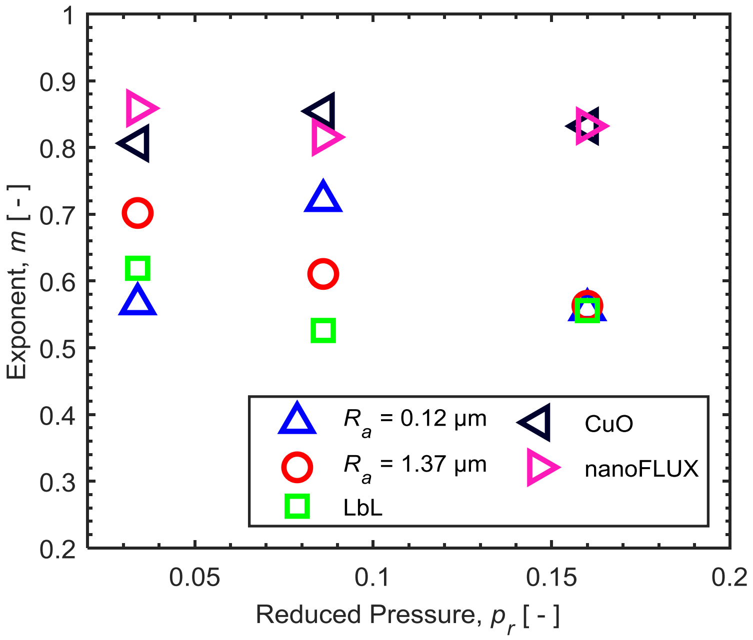

Figure 6-3. Boiling exponent, m, as a function of the reduced pressure for nanostructured and plain tubes in pool boiling.

Previous studies showed that heat flux sensitivity measured through the exponent, m, increased as the surface roughness decreased. This was thought to be because smoother surfaces had a greater number of smaller nucleation cavities that were only activated at higher heat fluxes [19], as increased heat fluxes result in increased wall superheats which reduce the diameter of vapour pockets that can become active nucleation sites [87]. Thus, the CuO and nanoFLUX tubes could similarly have a larger number of smaller cavities compared to the LbL, polished and roughened tubes that where only activated at higher heat fluxes and so increased the relative performance of the CuO and nanoFLUX tubes at higher heat fluxes compared to the other tubes.

The influence of the different refrigerant properties and saturation temperatures can be captured using reduced pressure. The HTCs, as a function of the reduced pressure, are illustrated in **Figure 6-4** at a heat flux of 50kW/m^2 on a log-log plot. Both plain and nanostructured tubes showed HTCs that increased as reduced pressure was increased, with similar sensitivities to changes in reduced pressure on the logarithmic plot, indicating a common power relationship for all the tubes involved. Similar trends were seen at higher and lower heat fluxes. This is in contrast to the findings of Zimmermann et al. [54], where the HTCs measured on a nanowire surface boiling in FC-72 were practically independent of changes in saturation pressure (and thus changes in reduced pressure).

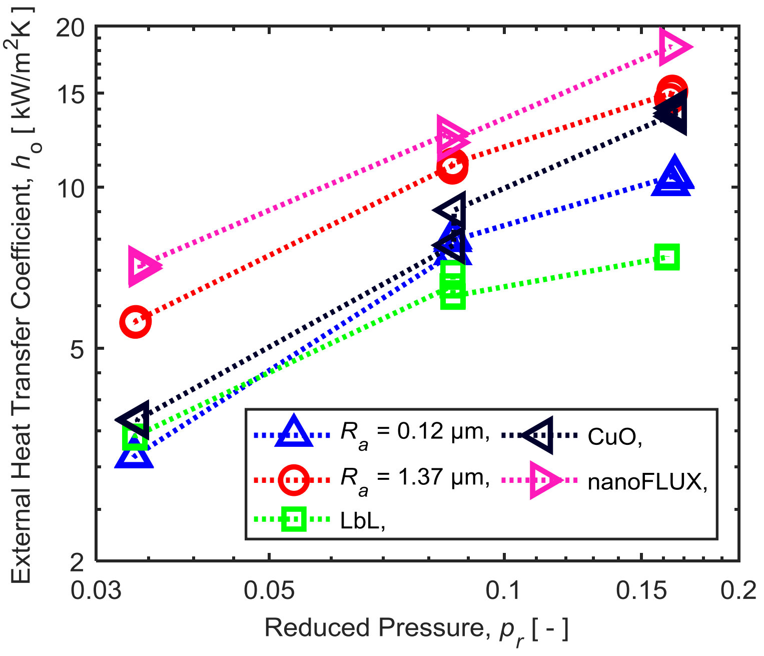

Figure 6-4. Influence of reduced pressure on pool boiling HTCs of nanostructured and plain tubes as a function of reduced pressure at 50 kW/m^2.

6.3 Nucleation site density

Images from a high-speed video camera taken with the aim of illustrating the differences in nucleation site density across the three nanostructured copper tubes as well as a polished (R_a of 0.12 µm) and roughened (R_a of 1.37 µm) plain copper tube are shown in **Figure 6-5**, while the nucleation site densities measured from such videos are listed in **Table 6-1**. These images were captured in R-245fa at a saturation temperature of 20°C at 20 kW/m^2.

Table 6-1. Nucleation site density of tubes in pool boiling of R-245fa at 20°C (p_r of 0.086) at 20 kW/m^2.

Tube	**Nucleation site density,** n [sites/m^2]	**Nucleation sites relative to polished tube,** n/n_{pol} [-]
Polished	1.4×10^5	1
Roughened	6.9×10^5	4.9
LbL	1.7×10^5	1.2
CuO	8.0×10^4	0.57
nanoFLUX	2.8×10^5	2.0

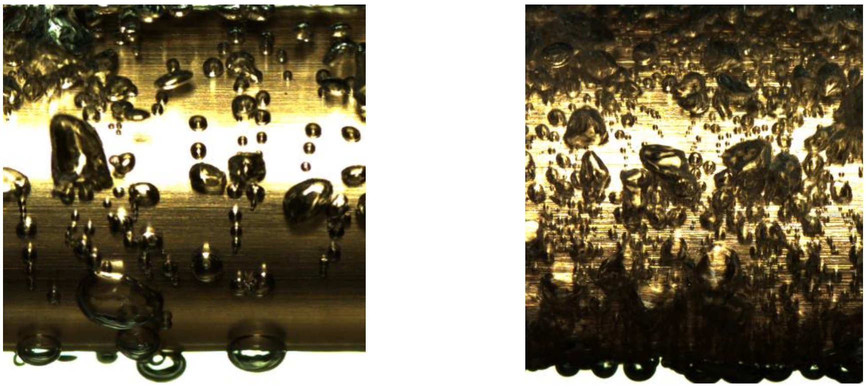

(a) Polished (b) Roughened

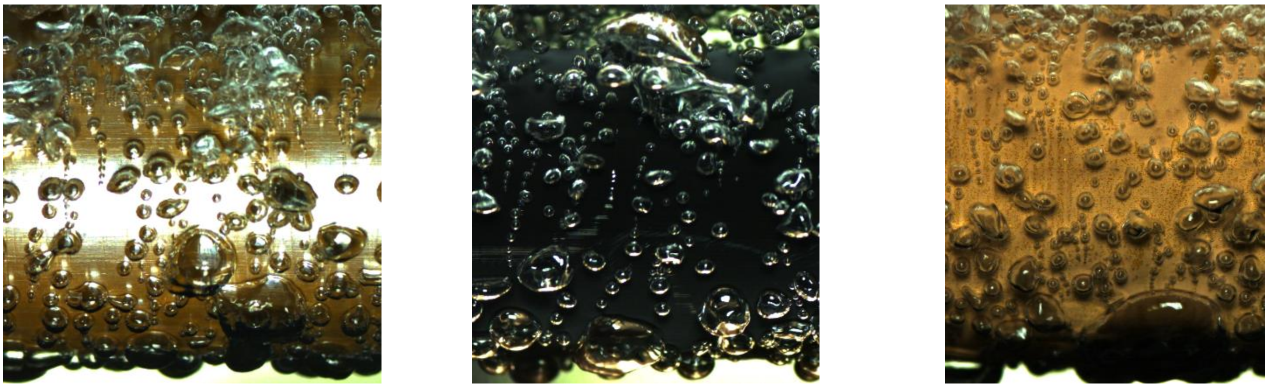

(c) LbL (d) CuO (e) nanoFLUX

Figure 6-5. Images of pool boiling tubes at 20kW/m^2 in R-245fa at 20°C (p_r of 0.086).

The roughened tube had five times the nucleation site density than that of the polished tube, and the LbL tube had a 20% greater nucleation site density than that of the polished tube. The improved HTCs of the roughened and LbL tubes at 20 kW/m^2 in R-245fa at 20°C relative to the polished tube can thus likely be accounted for by these greater nucleation site densities because bubble nucleation is known to improve heat transfer [30].

The nanoFLUX tube had a higher nucleation site density than the other nanostructured tubes, showing that part of its improved heat transfer performance over other nanostructured tubes was due to a rougher microstructure.

The CuO tube had approximately 60% of the nucleation sites of the polished tube, despite yielding slightly higher HTCs under these conditions. Similarly, the nanoFLUX tube had approximately 40% of the nucleation sites of the roughened tube, despite outperforming the HTCs of the roughened tube under these conditions by approximately 10%. Therefore, both the CuO and nanoFLUX tubes had fewer nucleation sites than the sandpapered tubes of similar or lower HTCs.

Physically speaking, this demonstrates that the outside boiling site density is *not* the heat transfer enhancement mechanism, and thus one needs to look inside the coating for an answer. As described in Thome [2], the single-phase heat transfer from the flow of liquid into and out of the porous coating through its nano-sized channels, pumped by the bubbles, may be the main heat transfer enhancement mechanism, where one can imagine the very high laminar flow HTCs for liquid passing through such small passages. For example, considering that simulations suggest Nusselt numbers for laminar flow convective heat transfer of water in nanochannels in the approximate range of 2 to 5 [135,136], an estimated pore size of 2 µm gives a range of HTCs of approximately 9 to 20 kW/m^{2}K for R-134a at 5°C. Furthermore, the CuO tube roughness ratio has been previously estimated to be in the range of 3 to 5 [63,102] and the nanoFLUX tube likely has an even higher roughness ratio based on the SEM images of the nanostructures. This illustrates how single phase heat transfer within the porous nanostructures as a result of capillary pumping could significantly contribute to the overall external HTC.

A further possible enhancement mechanism is the evaporation of liquid wicked underneath the nucleating bubbles. Rahman et al. [64] showed that the CuO coating had reduced dryout under the nucleating bubble footprint compared with an uncoated surface which contributed an additional flux pathway. The authors suggested that this was caused by the capillary flow of liquid underneath the bubbles induced by the nanostructures. This additional thin film evaporation would eject a much higher flow of vapour and bubbles from the outside surface. Analysis of the bubble frequency and size is thus recommended for future study as it would provide evidence as to whether the single phase or two phase enhancement mechanisms described here were the dominant enhancement.

These mechanisms rely on capillary pumping, which is plausible if one considers the SEM images from **Figure 3-7** and the AFM images from **Figure 3-8** which show that the CuO and nanoFLUX tubes created a porous structure, while the polished, roughened and LbL tubes did not. While refrigerants have a lower capillary action than water due to lower surface tensions, wicking was confirmed in Section **3.4.4** on both the CuO and nanoFLUX tubes. Both the CuO and nanoFLUX nanostructures are thus suggested to induce capillary flow within the porous layer while the non-wicking surfaces do not.

6.4 Departure from nucleate boiling critical heat flux

The DNB CHF was reached in three instances of pool boiling testing, as illustrated in **Figure 6-6**. These results are replotted in Appendix **D.2** in **Figure D-2** as HTCs versus heat flux for reference.

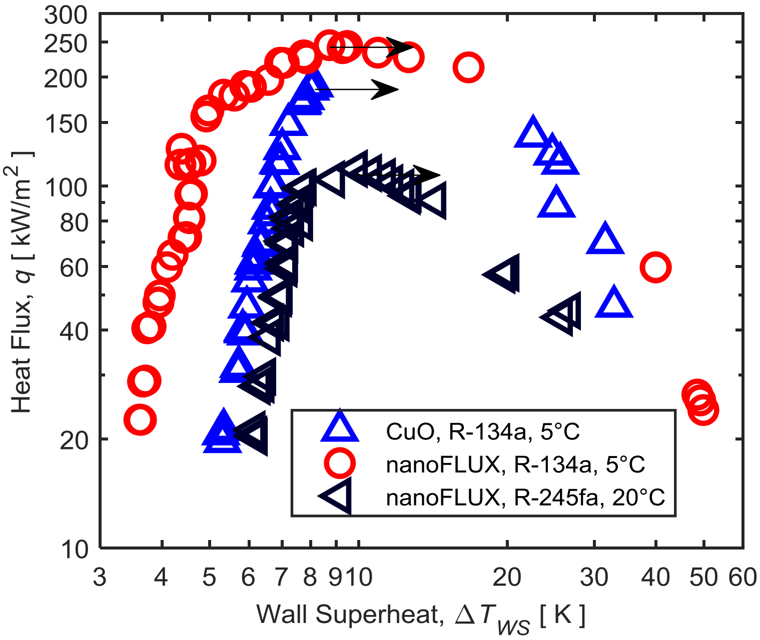

Figure 6-6. CHF seen in the pool boiling of nanoFLUX and CuO tubes with heat flux as a function of wall superheat. The CHF point is indicated with arrows.

As the wall superheat was raised, the heat flux reached a maximum, after which film boiling could be seen by visual observation to start at the heating water inlet end of the tube. Thereafter, as the wall superheat was increased further, film boiling spread along the length of the tube, resulting in a rapid decrease in the measured HTC. The experimental equipment employed was not designed with such high wall superheats in mind. Therefore, the fluxes necessary to reach the CHF of the other tubes could not be obtained due to their low HTCs. The CHFs recorded were expected to be lower than those of a plain cylindrical tube based on the prediction of Lienhard and Dhir [101], as shown in **Table 6-2**, with CHFs between 24 and 51% lower than the predicted CHF of a plain tube.

As discussed earlier, the CHF of a plain surface is generally improved by the addition of nanostructures that are wickable and wettable when boiling water, and researchers have recorded improvements for organic fluids in CHF in pool boiling conditions due to the presence of nanostructures [67,68,70]. However, some studies of pool boiling [54] and flow boiling [69,105] of organic fluids have found that the CHF decreased due to the presence of nanostructures, despite good wettability of the surface by the organic fluids (contact angles $< 25°$), as is the case in this study.

Table 6-2. Measured and predicted DNB CHFs for pool boiling.

Conditions	**Measured CHF, [kW/m²]**	**Predicted CHF of a plain tube [101], [kW/m²]**	**CHF relative to that predicted for a plain tube**
nanoFLUX tube, R-245fa at 20°C.	112	227	0.49
nanoFLUX tube, R-134a at 5°C.	245	324	0.76
CuO tube, R-134a at 5°C.	189	324	0.58

The reason for the lowered CHF may be that the wettability of organic fluids such as R-134a and R-245fa is significantly reduced at high heat fluxes through the trapping of vapour in suitable nanostructures (such as the nanoFLUX and CuO surfaces), causing the surface to switch to a Cassie-Baxter wetting state and so cause an early onset of CHF. **Table 3-3** shows that the water-in-air contact angles for the CuO and nanoFLUX surfaces can operate in the Cassie-Baxter state under suitable conditions. Unfortunately, previous authors who experienced early onset of CHF on nanostructured surfaces compared with that of plain surfaces when boiling organic fluids [54,69,105] did not take water contact angle tests on aged surfaces to indicate whether the surfaces could support wetting in the Cassie-Baxter state.

Such behaviour may be more likely for organic fluids than for water because organic fluids should not benefit as much from the nanostructure-induced wicking observed in water CHF studies. The lower wickability of organic fluids compared with that of water is not only evident from wicking studies [69,105], but from Washburn's equation [137], where the ratio of surface tension to viscosity is shown to be important to capillary flow, where water at 100°C (the most common test condition for water CHF studies) has a surface tension-to-viscosity ratio of almost five times that of R-134a at 5°C.

The lower latent heat of vaporisation, h_{fg}, of organic fluids, with R-134a having an h_{fg} of 1 947 kJ/kg at 5°C, while water has an h_{fg} of 2 256 kJ/kg at 100°C [111], may also play a part in organic fluids being more likely to switch to the Cassie-Baxter state at higher heat fluxes than for water, as it allows for quicker evaporation and dryout of the wicked liquid. The lower latent heat of vaporisation of organic fluids will also produce greater volumes of vapour than for water at the same heat flux, which may make it more susceptible to nanostructure vapour entrapment, although this will also cause greater evaporative-induced negative pressure that should, in turn, drive wicking [17].

If this reduced wetting hypothesis is accepted, the CHF trends in **Figure 6-6**, combined with data from previous studies [69,105], suggest that the sooner the wicking capabilities of the surface can be overcome as heat flux rises, the sooner the onset of CHF will occur. In this study, the nanoFLUX surface had larger nanostructures and larger wicking fronts than the CuO surface and also had a higher CHF than that of the CuO surface in R-134a at 5°C. A similar trend was found in the studies of Shin et al. [105] and Kim et al. [69], where longer nanowires had higher CHFs in the flow boiling of FC-72, although all were below the CHF value of the respective plain surface. These larger nanostructured surfaces were expected to induce more wicking, as shown in this study, wicking studies by Kim et al. [69], and considering that a greater pore radius drives greater capillary flow in terms of Washburn's equation [137].

Furthermore, the DNB CHF relative to a plain surface in this study was shown to be lower for R-245fa than for R-134a with the nanoFLUX surface. The R-245fa was expected to support less wicking than R-134a due to a lower surface tension-to-viscosity ratio (34 m/s for R-245fa at 20°C compared with 43 m/s for R-134a at 5°C). Therefore, this hypothesis suggests that, as heat flux is increased during boiling, the quicker the wicking abilities of the surface are overpowered, the quicker the surface can switch to a Cassie-Baxter state and the DNB be initiated.

6.5 Summary, conclusions and recommendations

The purpose of this chapter was to investigate experimentally the heat transfer characteristics of nanostructured and plain copper horizontal tubes in the saturated pool boiling of refrigerants. A smooth polished copper tube and a roughened copper tube were tested, together with three different nanostructured tubes that were applied to polished copper tubes. The HTCs of the saturated pool boiling of refrigerants at three reduced pressure values of 0.034 (R-245fa at 20°C), 0.086 (R-134a at 5°C) and 0.160 (R-134a at 25°C) were measured over a heat flux range from 20 to 100 kW/m^2, followed by a further increase in heat flux in an attempt to reach CHF.

The plain and nanostructured tubes displayed linearly increasing HTCs as the heat flux was increased on a log-log plot. The CuO and nanoFLUX tubes were more sensitive to changes in heat flux than the polished, roughened and LbL tubes, with improved heat transfer at higher heat fluxes than those of the other tubes. This finding could be due to a larger population of small nucleation sites. Both plain and nanostructured tubes displayed HTCs that increased similarly as reduced pressures were increased.

The LbL tube had up to 20% higher HTCs than those of the polished tube at the lowest reduced pressure and down to 20% lower HTCs at the highest reduced pressure tested.

The CuO tube performed similarly to the polished tube at low heat fluxes (20 kW/m^2), but outperformed the polished tube by approximately 60% at high heat fluxes (100 kW/m^2) in terms of HTCs.

Furthermore, it was found that the nanoFLUX nanostructured tube produced the highest HTCs, with measured HTCs between 40 and 200% higher than those of a polished copper tube, and between 0 and 50% higher than those of a roughened copper tube.

The nanoFLUX tube had a greater nucleation site density when boiling R-245fa at 20°C at 20 kW/m^2 compared to other nanostructured tubes, which suggested a rougher microstructure that contributed to its improved heat transfer. When boiling R-245fa at 20°C at 20 kW/m^2, the nanoFLUX and CuO tubes had fewer nucleation sites than those of sandpapered tubes of similar heat transfer performance and this suggests that the nanoFLUX and CuO surfaces had an additional unique heat transfer mechanism compared with sandpapered surfaces. This was possibly linked to capillary wicking of liquid inside the nanochannels of the porous coatings driven by the external bubble pumping, which contributed to enhanced single-phase liquid superheating by the flow of liquid through the nano-sized channels or reduced dryout and increased microlayer evaporation underneath the nucleating bubbles. Analysis of the bubble frequency and size is recommended for future studies to elucidate further the HTC enhancement mechanisms.

Finally, the measured CHF due to DNB of the CuO and nanoFLUX tubes was lower than that expected for a plain tube. It was suggested that the early onset of DNB for pool boiling over the CuO and nanoFLUX tubes may be due to vapour trapped in the fibrous nanostructure, resulting in reduced wetting in the Cassie-Baxter state.

7. Falling film boiling on nanostructured and plain tubes

7.1 Introduction

The heat transfer characteristics of falling film boiling over three nanostructured and two plain tubes in R-134a and R-245fa across a range of heat fluxes and film flow rates are detailed in this chapter. Cases where the CHF was reached as a result of DNB are investigated, followed by the dryout characteristics of the tubes as the film flow rates are decreased at fixed heat fluxes. The overall operational limits are then studied. The heat transfer characteristics are then investigated at the maximum film flow rate to record HTCs with as little dryout influence as possible. An attempt was made to consider the nucleation site density and its role on the heat transfer results. The HTCs measured during falling film boiling are then compared to the HTCs measured under pool boiling conditions documented in the previous chapter to calculate the falling film heat transfer enhancement ratio under the various conditions tested in this study to allow for a better understanding of the falling film boiling heat transfer process. The results presented in this chapter were published in Bock et al. [29].

7.2 Departure from nucleate boiling critical heat flux

DNB CHF occurred during testing of the CuO and nanoFLUX nanostructured tubes resulting in a peak heat flux being reached. Tests that achieved CHF at the maximum film flow of the experimental apparatus of approximately 0.13 kg/m/s are illustrated in **Figure 7-1** with the DNB CHF point indicated by an arrow. The results are replotted in Appendix **D.2** in **Figure D-4** as HTCs versus heat flux for reference. DNB was also recorded in some instances for the CuO and nanoFLUX tubes in tests where the film flow rate was reduced and these instances are indicated with arrows in **Figure 7-3**.

Increased wall superheat resulted in increased heat flux before the DNB CHF point was reached. As the DNB CHF point was approached, separation between the surface and liquid film was seen, initially at the heating water inlet end of the tube. The liquid separation progressively moved along the length of the tube as wall superheat was further increased resulting in heat flux peaking and then decreasing because of the decreased proportion of the tube in contact with the liquid. DNB eventually enveloped the entire tube and heat fluxes then collapsed to values below 10 kW/m^2, not shown in **Figure 7-1**. The heat fluxes of the plain and LbL tubes were set to the maximum limit that the experimental equipment could support but no DNB could be obtained.

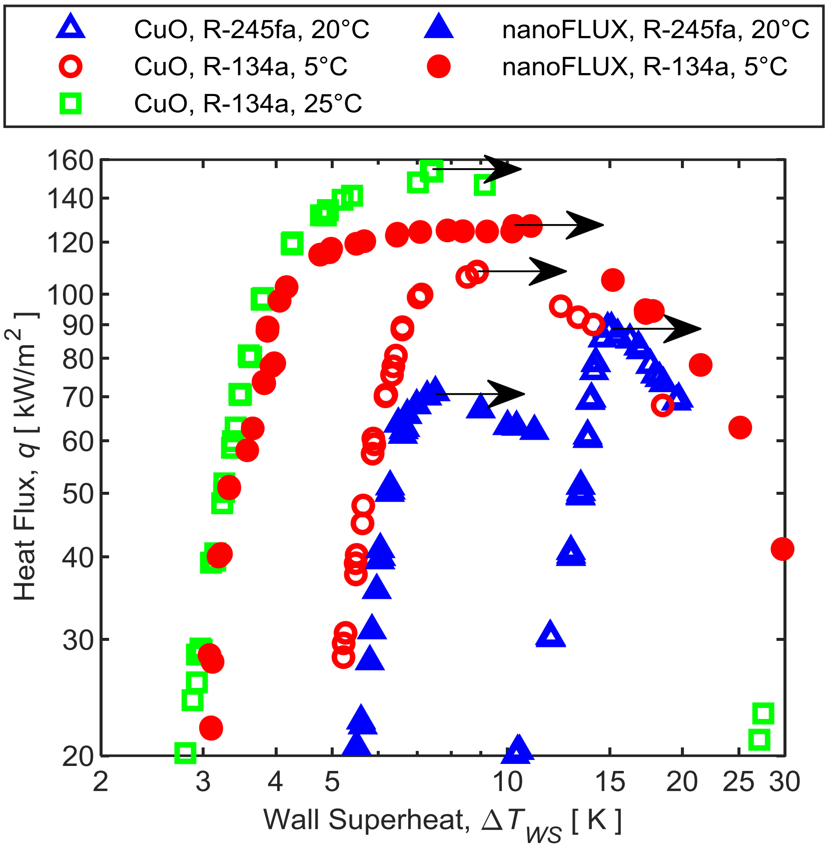

Figure 7-1. CHF seen in the falling film boiling of nanoFLUX and CuO tubes, with heat flux as a function of wall superheat with a film flow rate of ~0.13 kg/m/s. The CHF point is indicated with arrows.

Images from the high-speed video camera illustrating the DNB liquid separation process are shown in **Figure 7-2**, taken at the midpoint of the tube length. As the DNB CHF point was approached at a particular position on the tubes, the falling film began to separate from the tube. The separation started at the bottom of the tube and moved up the tube circumference until the fluid was completely separated from the tube. The tube was no longer wetted by the fluid and the falling liquid film bounced off the tube and deflected around it. It should be noted that the images in **Figure 7-2** were taken at the midpoint of the tube, while the liquid separation first began at the heating water inlet end of the tube. Thus, while the tube was fully wetted, as shown in **Figure 7-2** (a,i) and (b,i), the water inlet end of the tube was already experiencing film separation.

Studies of falling film boiling on plain flat plates and vertical tubes [83-85,106] noted that liquid separation began at the bottom end of the heater plate or vertical tube, similar to this study. However, the studies of flat plates and vertical tubes noted the presence of a thin subfilm of liquid beneath the main separated liquid film and theorised that this subfilm played a key role in the falling film DNB process. However, no subfilm was seen in this study, suggesting that this DNB took place through a different mechanism.

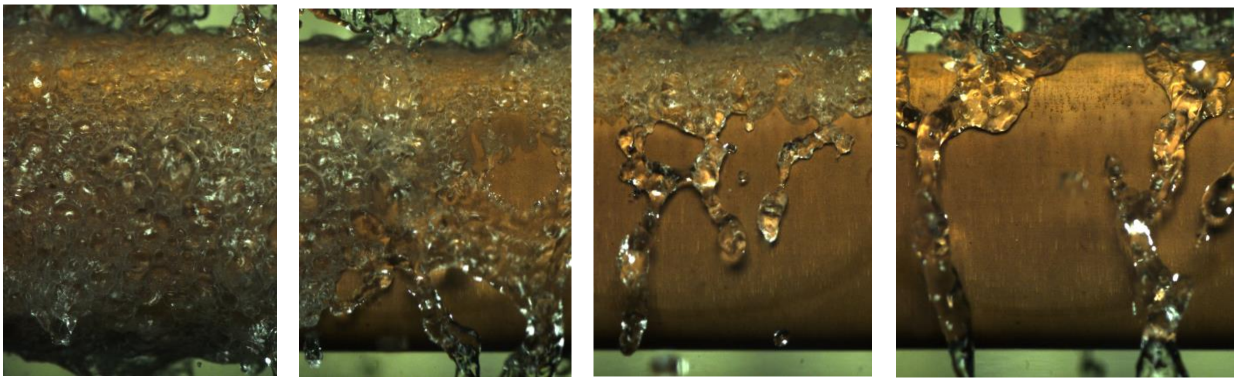

(i) $\Delta T_{ws} = 10°C$ (ii) $\Delta T_{ws} = 15°C$ (iii) $\Delta T_{ws} = 25°C$ (iv) $\Delta T_{ws} = 42°C$

(a) nanoFLUX tube in R-134a at 5°C at Γ_r of 0.13 kg/m/s.

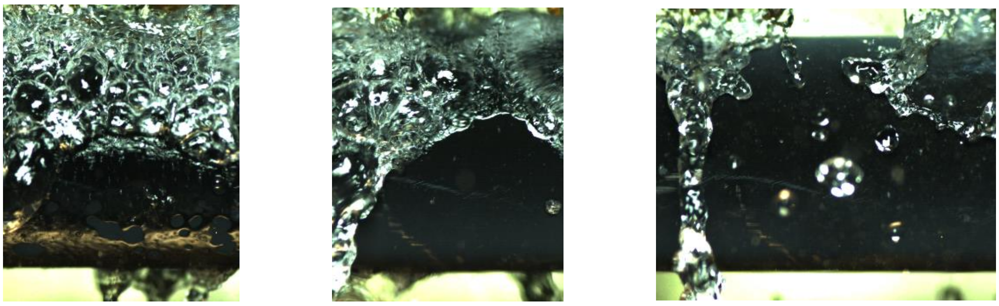

(i) $\Delta T_{ws} = 6.4°C$ (ii) $\Delta T_{ws} = 14°C$ (iii) $\Delta T_{ws} = 30°C$

(b) CuO tube in R-245fa at 20°C at Γ_r of 0.14 kg/m/s.

Figure 7-2. Images of falling film boiling liquid separation due to DNB at the midpoint of tube length.

The DNB CHF measured for the nanostructured tubes was lower than that of a plain tube also experiencing CHF as a result of DNB. For example, the polished copper (R_a of 0.12 µm) tube was able to reach 100 kW/m^2 in R-245fa at 20°C, above the 71 kW/m^2 DNB CHF of the nanoFLUX tube. Unfortunately, the DNB point of the plain and LbL tubes could not be reached as tests could not be conducted at higher fluxes due to the low HTCs of the plain and LbL tubes and the wall superheat limitations of the experimental equipment. The falling film DNB CHFs were also lower than those recorded under pool boiling conditions with the same tubes and identical refrigerant conditions, as indicated in **Table 7-1**. The falling film DNB CHFs were only about 50 to 60% of the respective pool boiling values.

Table 7-1. Measured falling film boiling DNB CHFs and comparison with pool boiling DNB CHFs.

Condition	**Tube**	DNB_{ff} [kW/m^2]	DNB_{pb} [kW/m^2]	$\frac{DNB_{ff}}{DNB_{pb}}$
R-245fa at 20°C	nanoFLUX	71	112	0.63
	CuO	89	N/A	N/A
R-134a at 5°C	nanoFLUX	127	245	0.52
	CuO	108	189	0.57
R-134a at 25°C	CuO	154	N/A	N/A

Figure 7-2 (a, ii) shows that the nanoFLUX and CuO tubes experienced this early DNB despite wicking still taking place on the upper section of the tube, while separation was occurring on the bottom half of the tube. The early onset of DNB was possibly caused by the same mechanism as proposed in the pool boiling section, namely once the wicking was overcome and the nanostructures dried out, a Cassie-Baxter state of wetting was initiated (a likelihood illustrated by the water contact angle data) and thus an early onset of DNB compared to plain tubes.

However this wicking hypothesis does not fully explain all the results seen in **Table 7-1.** In particular, the CuO tube had a higher CHF point due to DNB than the nanoFLUX tube under falling film boiling in R-245fa at 20°C, despite having a lower wicking ability as discussed in Section **3.4.4**. This suggests that the wicking ability of the tube is not the sole surface factor influencing the CHF due to DNB under falling film boiling of nanostructured surfaces. This may extend to pool boiling as the pool boiling CHF point of CuO in R-245fa could not be captured with the current experimental equipment to make a similar comparison.

7.3 Dryout

The influence of the film flow rate on the HTCs of the polished copper (R_a of 0.12 µm), roughened copper (R_a of 1.37 µm) and nanostructured tubes is shown in **Figure 7-3**. As the film flow rate was decreased, both plain and nanostructured tubes displayed a relatively insensitive HTC response, resulting in the typical plateau region. The sensitivity of the plateau region increased as the heat flux was increased for most tubes, particularly for the plain tubes. Dry patches were observed within these plateau regions with the aid of the high-speed camera. These patches were temporary and quickly covered by the flowing liquid film, as noted in previous studies [91]. The plateau region of the nanoFLUX region at 20 kW/m^2 was noted to be quite unstable, likely a result of the higher uncertainties under these conditions.

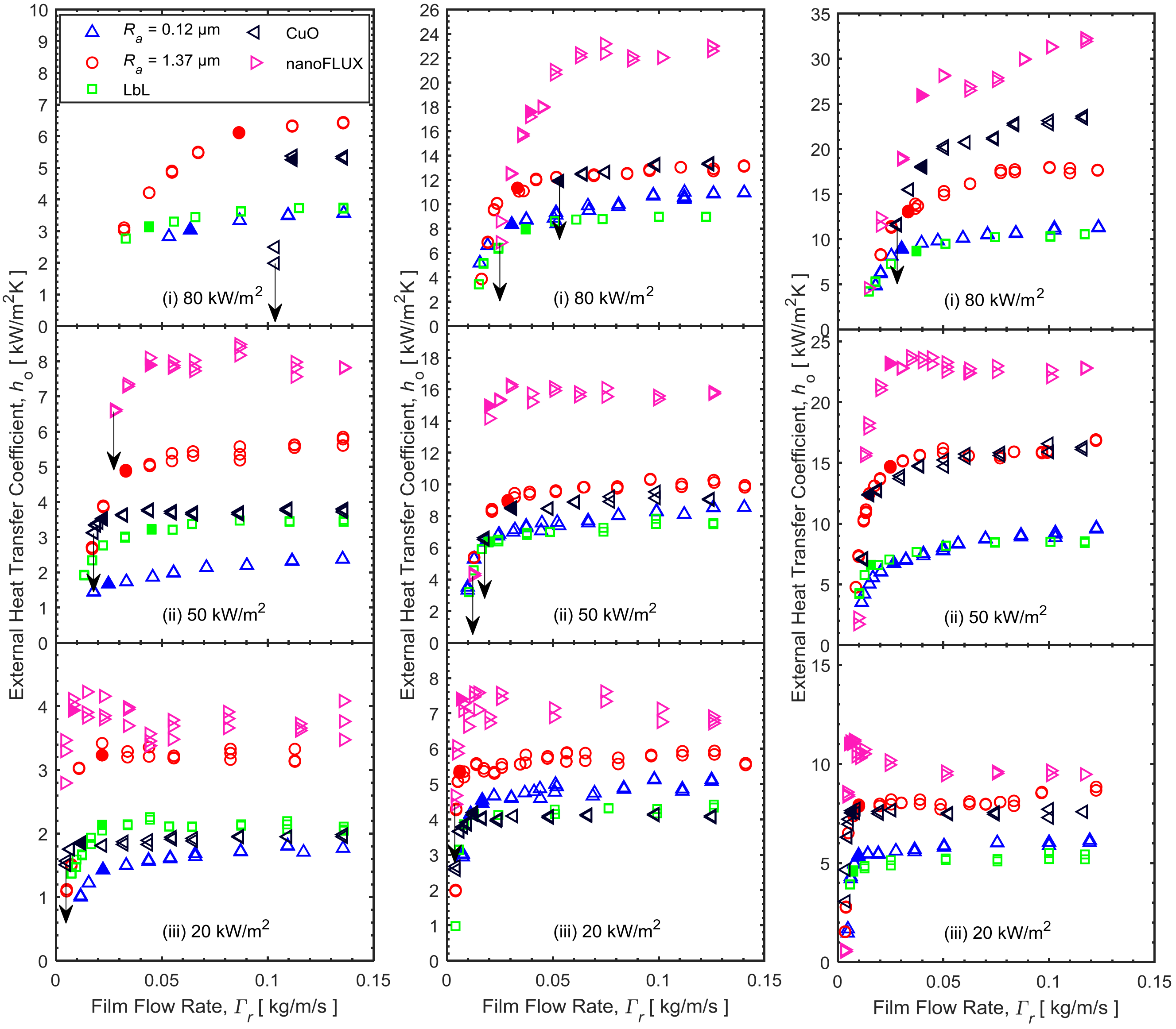

(a) R245fa, 20°C, p_r 0.034 (b) R134a, 5°C, p_r 0.086 (c) R134a, 25°C, p_r 0.160

Figure 7-3. Falling film boiling HTCs as a function of film flow rate for nanostructured and plain tubes. Critical dryout indicated by filled-in markers and DNB indicated by arrows.

The HTCs collapsed as the film flow rate was reduced further for both the plain and nanostructured tubes. This was caused by critical dryout, with the formation of large dry patches visible on the tube surfaces and insufficient liquid flow available to rewet the dry patches, while liquid boiled on the wetted portions of the tubes. The point of critical dryout is noted by filled-in markers in **Figure 7-3**. This critical dryout was seen to occur at higher film flow rates as the heat flux was increased for both plain and nanostructured tubes.

It should be noted that non-visible dryout of the nanostructure cavities may have also contributed to the decrease in HTCs as film flow rates were decreased and heat fluxes increased. However, at present, it is difficult to determine the magnitude of this contribution, if any. Future studies quantifying the visible dryout area may be able to determine if visible dryout is indeed the dominant factor for decreased HTCs or if underlying dryout of the nanostructure cavities contributes significantly as well.

DNB CHF was seen on the CuO and nanoFLUX tubes in a number of cases as the film flow rate was decreased, which resulted in the separation of the fluid from the tube surface and led to almost instantaneous decrease in HTC as the tube was no longer wetted and no boiling could take place. DNB CHF cases are noted in **Figure 7-3** with a downward arrow. However, a number of these cases occurred after the film flow rate was below the critical dryout point. In these cases, critical dryout was the limiting factor rather than DNB CHF because the HTCs had decreased significantly already. Lastly, as film flow rate was decreased, dryout CHF was reached on those cases where DNB CHF was not, with the minimum film flow rate data point recorded for each tube marking the dryout CHF point. The critical dryout point always occurred at a higher film flow rate that the dryout CHF and thus was the dryout operational limit in all cases.

The nanoFLUX tube displayed an increase in HTC as film flow rate was decreased in some cases, for example in R-134a at 25°C at 20 and 50 kW/m^2, as shown in **Figure 7-3** (c, ii) and (c, iii), resulting in an HTC 'hump'. This phenomenon of increased HTC at reduced falling film flow rates was captured before in the convective heat transfer of water falling films on microstructured tubes [138] and superhydrophilic and hydrophilic plain tubes [139]. This was also seen in the falling film boiling of refrigerants on microstructured tubes in R-134a [8,10]. A thinned superheated liquid layer, which resulted in a decrease in evaporative thermal resistance, was considered the likely cause [138,139].

Images of the boiling process during the increased HTC hump are shown in **Figure 7-4**. The HTC hump occurred in this case at a film flow rate of 0.02 kg/m/s, as shown in **Figure 7-4** (b), with a completely wetted surface with very little waves or rivulets compared with the higher film flow rate, as shown in **Figure 7-4** (a), supporting the idea of a stable thin layer being formed. Furthermore, the backlight below the tube where the vapour passed, as shown in **Figure 7-4** (b), was the darkest, which again suggested that significant evaporation of fluid was taking place, increasing the HTCs. The HTC dropped rapidly after the film flow rate was further decreased through the formation of stable dry patches visible in **Figure 7-4** (c). The nanoFLUX tube had to maintain a film layer so thin that it became superheated and the evaporative thermal resistance became so low that it could meaningfully contribute to the HTC thus causing the hump, because previous reductions in film thickness at higher film flow rates were not accompanied by increased HTCs.

The nanoFLUX tube's ability to maintain a thin film is likely linked to its wicking ability, as it was the only tube documented to have a HTC hump and has the greatest wicking ability of the tubes tested here.

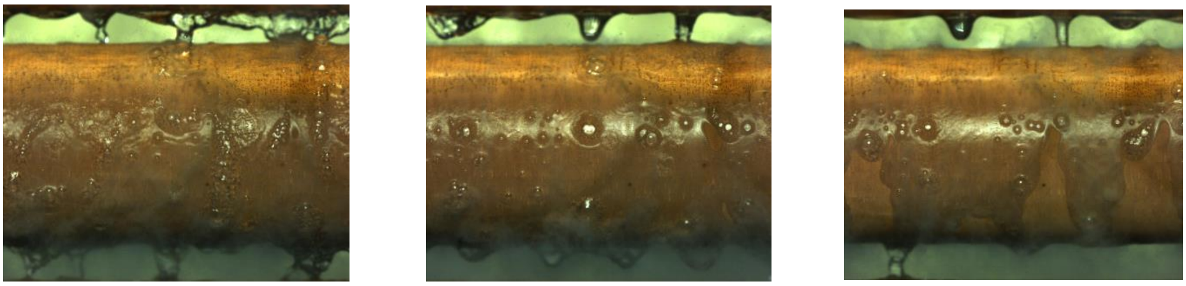

(a) Γ_r of 0.1 kg/m/s (b) Γ_r of 0.02 kg/m/s (c) Γ_r of 0.01 kg/m/s

Figure 7-4. Heat transfer hump for nanoFLUX tube in R-134a at 25°C at 20 kW/m^2.

In an effort to understand the influence of surface and refrigerant properties on dryout, a normalised HTC , h^+, and the dimensionless film Reynolds number, Re_f, were plotted for 50 kW/m^2 in **Figure 7-5** for plain tubes and **Figure 7-6** for nanostructured tubes. The equivalent plots at 20 kW/m^2 and 80 kW/m^2 are included in Appendix **D.5** for completeness. The plateau region of the polished copper tube was the most sensitive to film Reynolds number changes. The nanoFLUX tube and to a lesser degree the CuO tube had plateau regions that were very insensitive to film Reynolds number changes, which was likely due to the wicking abilities of these surfaces. The roughened and LbL tubes had plateau regions of intermediate film Reynolds number sensitivities.

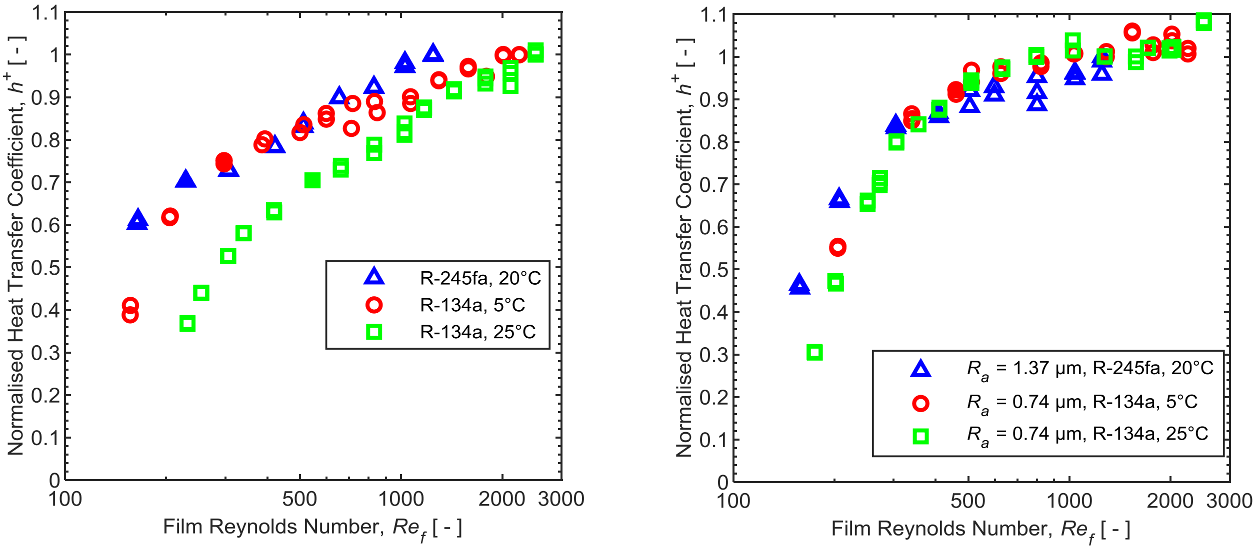

(a) Polished (R_a of 0.12 μm) copper (b) Roughened copper

Figure 7-5. Normalised HTC versus Re_f of plain tubes at 50 kW/m^2. Critical dryout point indicated with filled markers.

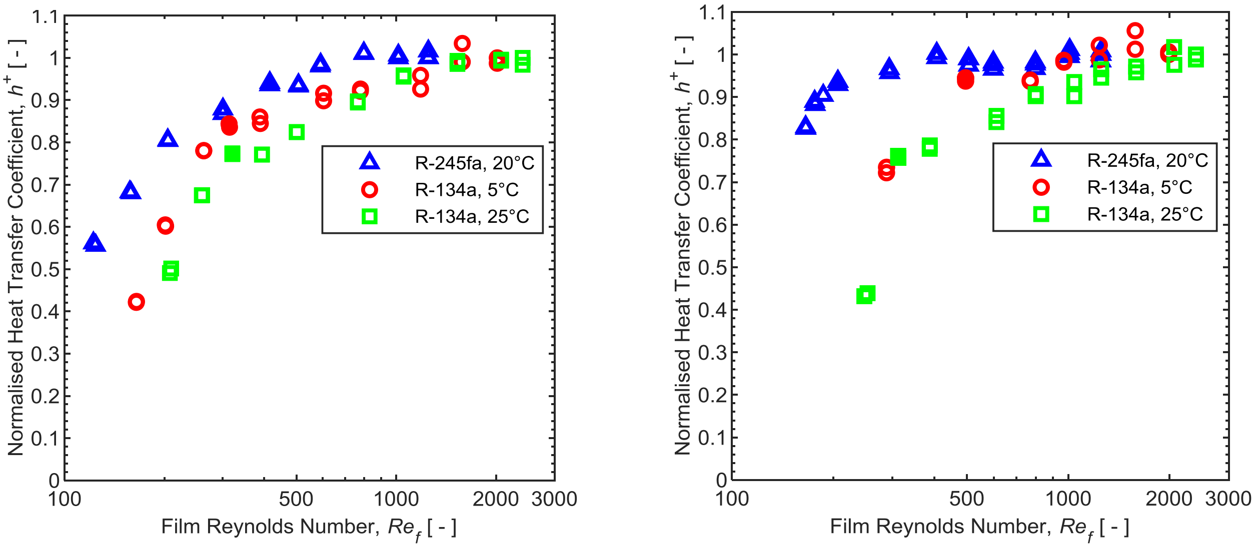

(a) LbL (b) CuO

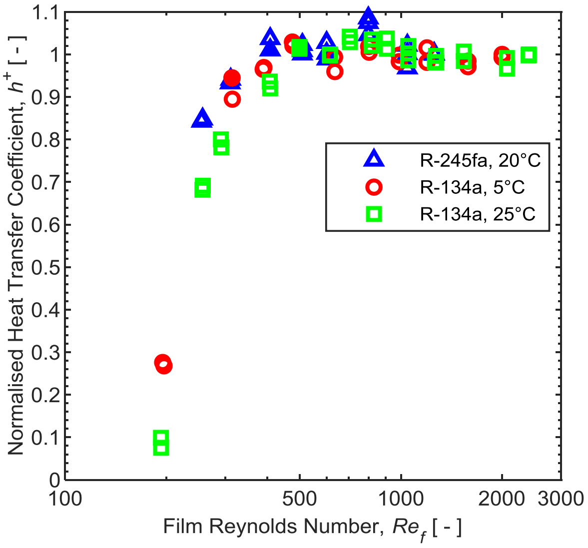

(c) nanoFLUX

Figure 7-6. Normalised HTC versus Re_f of nanostructured tubes at 50 kW/m^2. Critical dryout point indicated with filled markers.

The differing sensitivities of the plateau regions of the surfaces could again be because of differences in wettability and the resulting differences in the frequency of intermittent dryout within the plateau region, as discussed in Section **5.4.1**. Fluid maldistribution was suggested as another possible cause in Section **5.4.1**, but given the results of the nanostructured tubes it does suggest that surface factors, such as wettability, rather than experimental factors are the cause of the differing plateau region sensitivities.

Figure 7-5 and **Figure 7-6** show that at a given film Reynolds number, the normalised HTC was typically the lowest for R-134a at 25°C, followed by R-134a at 5°C and then R-245fa at 20°C across all tubes tested. Therefore, on a film Reynolds number basis, HTCs in R-134a at 25°C were most negatively affected by dryout, followed by R-134a at 5°C and then R-245fa at 20°C.

7.4 Operational limits

The operational limits of the tubes are illustrated in **Figure 7-7**, with the critical film Reynolds number as a result of critical dryout (open markers) or DNB CHF (filled markers) shown as a function of heat flux. The evaporative limit for each respective refrigerant condition was also plotted. These results are tabled in Appendix **D.6** in **Table D-1** to **Table D-5**.

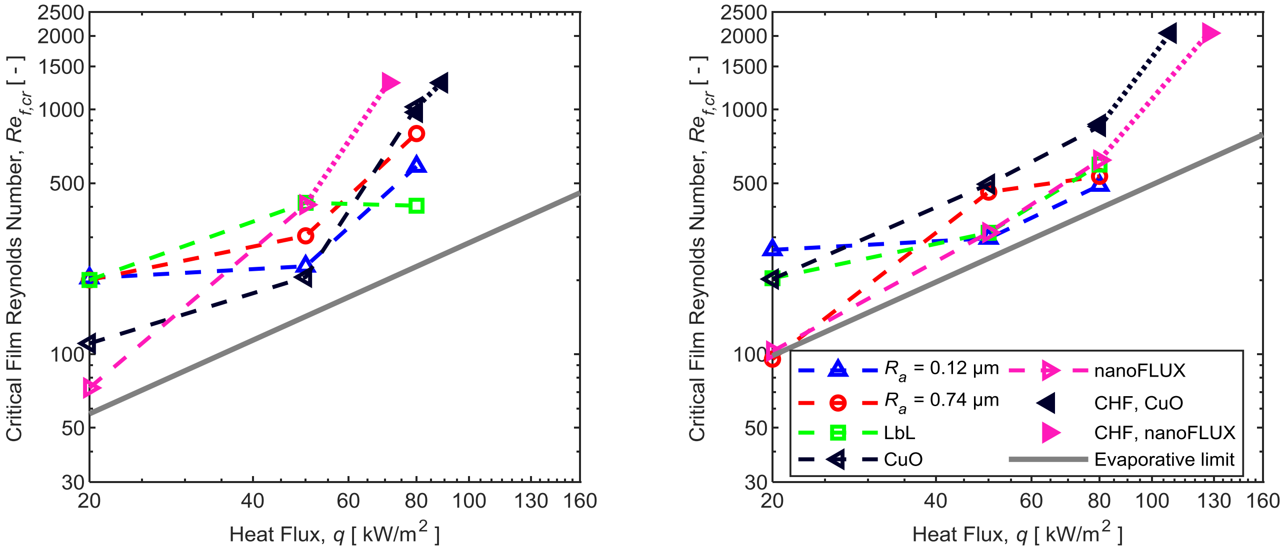

(a) R-245fa, 20°C, p_r of 0.034 (b) R-134a, 5°C, p_r of 0.086

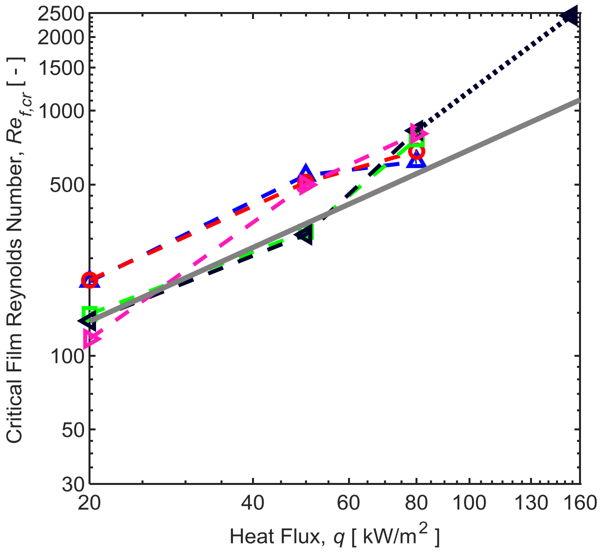

(c) R-134a, 25°C, p_r of 0.160

Figure 7-7. Critical film Reynolds number as a function of heat flux for nanostructured and plain tubes.

Lower heat fluxes resulted in lower film Reynolds numbers at which critical dryout or DNB occurred. Higher film flow rates suppressed critical dryout, with the liquid film rewetting dry spots that formed. Similarly, higher film flow rates suppressed DNB, with the falling liquid likely suppressing the dryout of the nanostructures and preventing the separation of the liquid film from the surface.

The critical film Reynolds numbers were the lowest for R-245fa at 20°C, while R-134a at 25°C had slightly higher critical dryout limits than for R-134a at 5°C. This agrees with the trends in **Figure 7-6** in terms of rate at which the normalised HTC, h^+, decreased as film Reynolds number was decreased, where R-134a at 25°C had the earliest normalised HTC drop, followed by R-134 at 5°C and then R-245fa at 20°C.

The polished (R_a of 0.12 µm) copper tube had some of the highest film Reynolds numbers at which critical dryout occurred at a heat flux of 20 kW/m^2, while the CuO and nanoFLUX tubes had some of the lowest. As the heat fluxes were increased above 20 kW/m^2, the critical film Reynolds number increased for the CuO and nanoFLUX tubes by the greatest amount of all the tubes such that they were the highest at 80 kW/m^2. At approximately this heat flux, DNB now became a concern and at times, the limiting factor for the CuO and nanoFLUX tubes.

The CuO and nanoFLUX tubes were thus shown to provide good dryout resistance at low heat fluxes (~20 kW/m^2) but at increased heat fluxes (~80 kW/m^2), these tubes had poor critical dryout resistance and poor DNB resistance. The worsened dryout and DNB performance of the CuO and nanoFLUX tubes were possibly through the dryout of the underlying nanostructures and subsequent operation in the Cassie-Baxter state of wetting, resulting in poor wetting and thus poor critical dryout and DNB performance.

However, the normalised HTC data of **Figure 7-6** should be kept in mind when considering the dryout limits shown in **Figure 7-7**. For example, the polished copper tube HTCs dropped by between 20 to 30% at a film Reynolds number of 500 at 50 kW/m^2 across the conditions tested, while the nanoFLUX tube still had HTCs within 3% of its maximum HTC. This merits consideration from designers of falling film evaporators, as both tubes have critical dryout limits below a film Reynolds number of 500, but the high sensitivity of tubes such as the polished tube means that significant HTC reduction can take place within the plateau region.

7.5 Heat transfer

7.5.1 Heat transfer coefficients

The HTCs measured during falling film boiling of the polished plain copper (R_a of 0.12 µm), roughened plain copper (R_a of 1.37 µm) and three nanostructured tubes are shown in **Figure 7-8** at a film flow rate of approximately 0.13 kg/m/s at three reduced pressures.

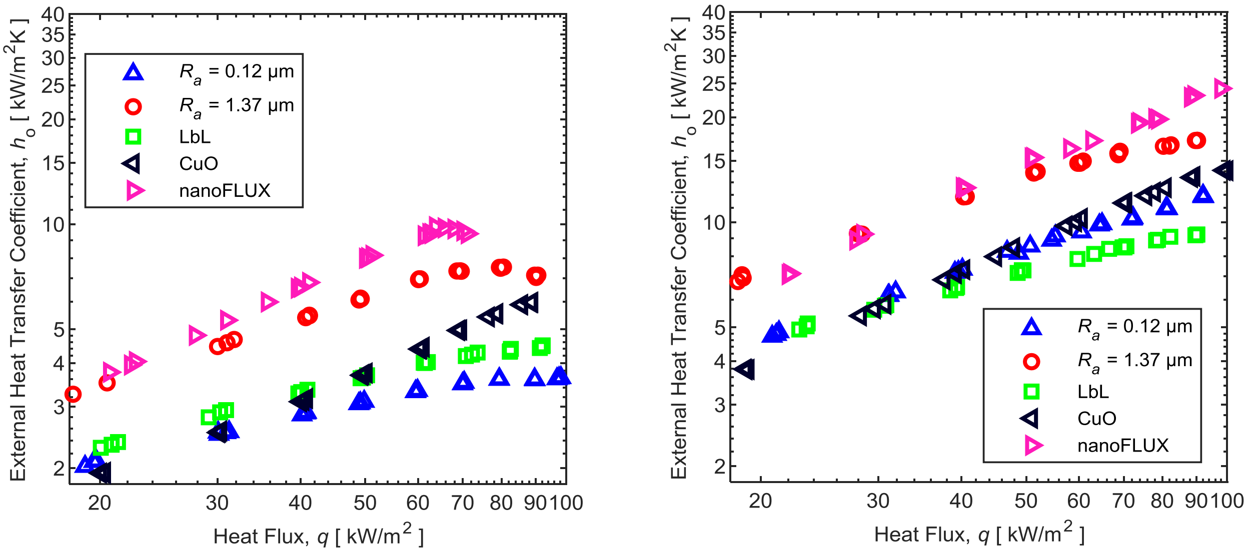

(a) R-245fa, 20°C, p_r of 0.034 (b) R-134a, 5°C, p_r of 0.086

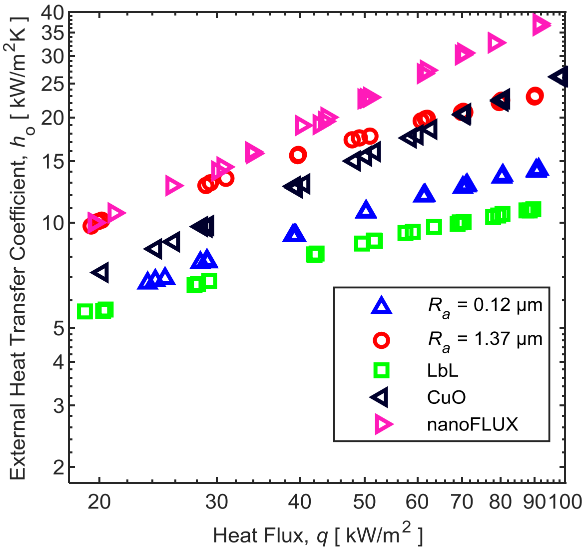

(c) R-134a, 25°C, p_r of 0.160

Figure 7-8. Falling film boiling HTCs as a function of heat flux of nanostructured and plain tubes at a film flow rate of ~0.13 kg/m/s.

All tubes showed a linear increase in HTCs as heat flux was increased on the log-log plot. However, at a reduced pressure of 0.034, the gradient of the HTCs of some tubes began to decrease as heat fluxes approached the upper end of the heat flux range tested. This was caused by dryout for the polished and roughened tubes and DNB for the nanoFLUX tube, as previously discussed. The polished and LbL tubes recorded the lowest HTCs across the three reduced pressures, the roughened and nanoFLUX tubes recorded the highest HTCs and the CuO tube HTCs were intermediate.

The polished copper tube (R_a of 0.12 µm) was used as a baseline to better illustrate the performance of the nanostructured tubes through the surface enhancement ratio in **Figure 7-9**.

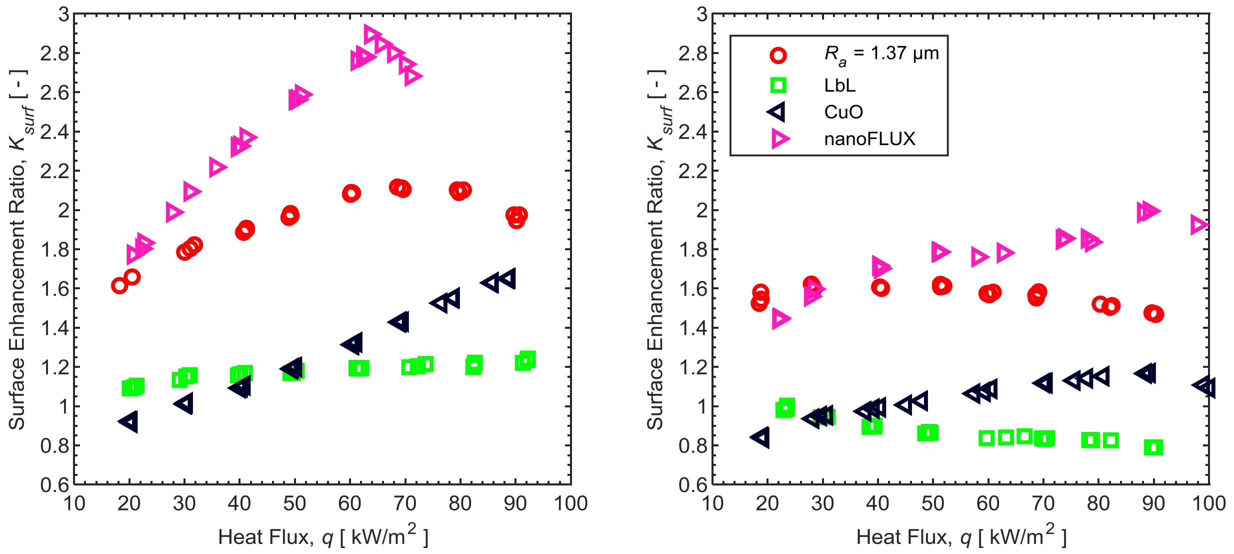

(a) R-245fa, 20°C, p_r of 0.034 (b) R-134a, 5°C, p_r of 0.086

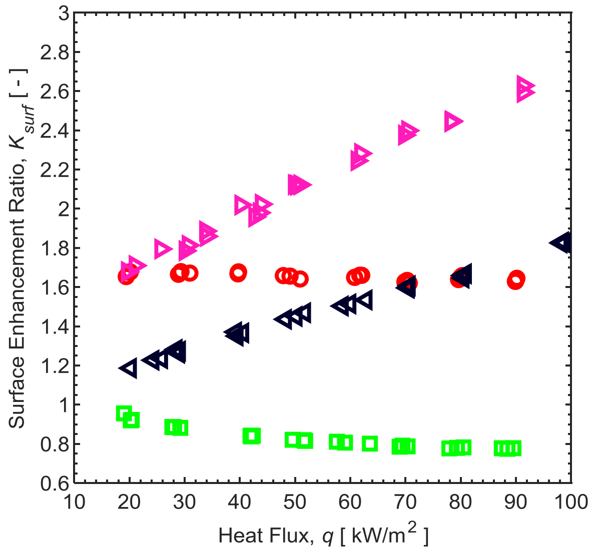

(c) R-134a, 25°C, p_r of 0.160

Figure 7-9. Falling film boiling HTC performance relative to smooth polished copper tube as a function of heat flux at a film flow rate of ~0.13 kg/m/s.

The roughened tube HTCs outperformed the polished tube HTCs by approximately 60% at the highest two reduced pressures and reached a maximum of 100% higher HTCs at the lowest reduced pressure. The LbL tube at a reduced pressure of 0.034 outperformed the polished tube by up to 20% but at the higher reduced pressures, the HTCs were 20% lower. The CuO tube HTCs were 20% lower than the polished tube HTCs at the lower range of the heat fluxes, but between 60 to 80% higher at the upper end of the heat flux range. The nanoFLUX tube had HTCs between 40 to 80% higher than those of the polished tube at the lower end of the heat flux range and up to 200% higher HTCs at the upper end of the heat flux range. Therefore, both the CuO and nanoFLUX tubes had increased sensitivity to heat flux changes compared with the polished tube.

This increased sensitivity was further investigated by fitting the relation $h_o = aq^m$ to the data of **Figure 7-8** with the results plotted in **Figure 7-10** (a). The heat flux sensitivities of the smooth, roughened and LbL tubes were similar, with an m of approximately between 0.4 to 0.6, while the CuO and nanoFLUX were more sensitive to heat flux changes with an m of approximately 0.8. This was similar to the pool boiling results, which suggested that the CuO and nanoFLUX tubes had a higher number of smaller nucleation cavities that were activated under both pool boiling and falling film boiling conditions as heat fluxes were increased compared with the other tubes.

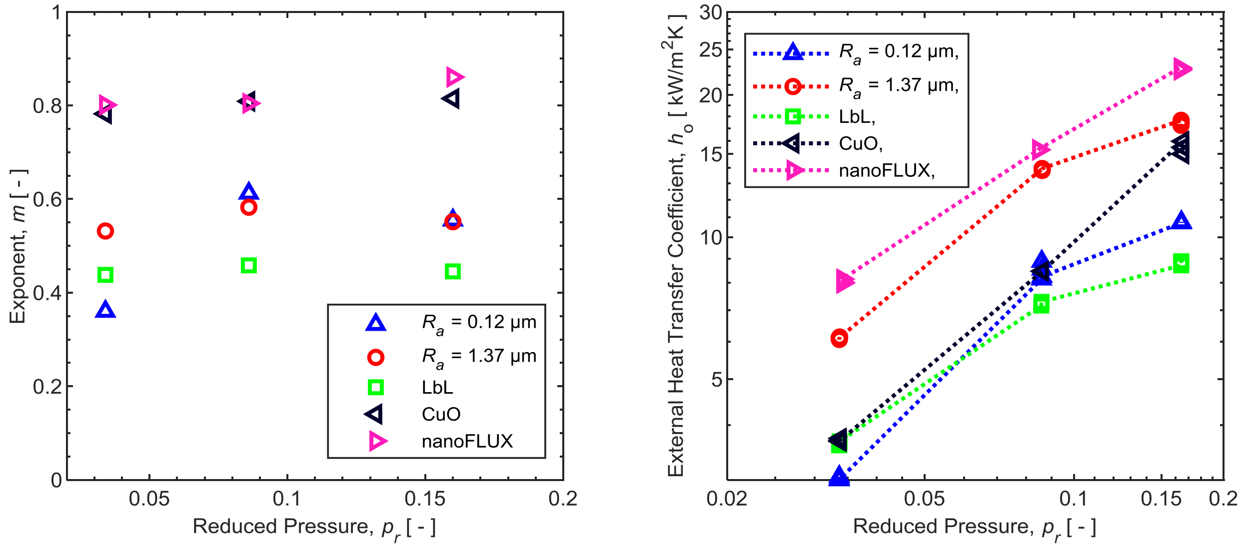

(a) Boiling exponent, m

(b) HTCs at 50 kW/m^2

Figure 7-10. Influence of reduced pressure on boiling exponent m and HTC.

In order to quantify the influence of fluid properties, the HTCs were plotted against the reduced pressure at 50 kW/m^2, as shown in **Figure 7-10** (b). The HTC of all tubes increased as the reduced pressure was increased, as in the corresponding pool boiling results. The CuO and nanoFLUX tubes showed a linear increase in HTC on the plot, while the polished, roughened and LbL tubes showed a reduction in the gradient as the reduced pressure reached its maximum. This may again be a result of a large population of small nucleation cavities on the nanoFLUX and CuO tubes that were activated as reduced pressure increased or as a result of dryout at the highest reduced pressure which lowered the HTCs of the nanoFLUX and CuO tubes the least.

7.5.2 Nucleation site density

In an attempt to quantify the nucleation site density of the surfaces, images from the high-speed camera were taken at the lowest HTCs and thus lowest expected nucleation site density in R-245fa at 20°C and these are shown in **Figure 7-11**. Nucleation sites could not be counted as was done for the pool boiling case in Section **6.3** because nucleation primarily occurred at the top of the tube with limited nucleation on the sides of the tube. The bubbles slid down the tube, which also obscured the sidewall nucleation sites more than was the case for pool boiling.

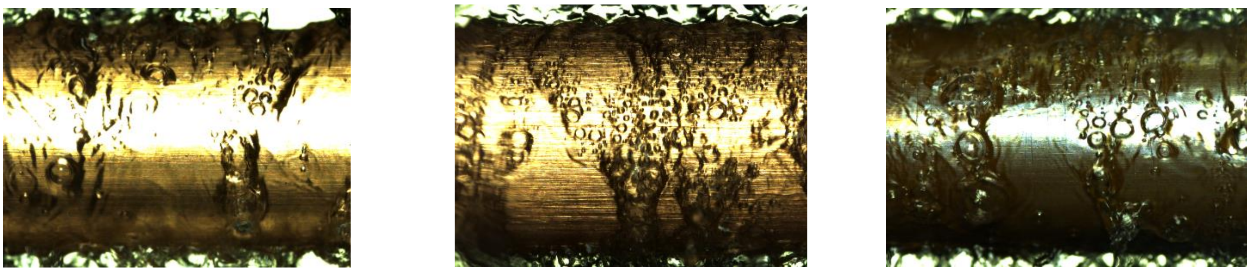

(a) Polished (R_a 0.12 µm) (b) Roughened (R_a 1.37 µm) (c) LbL

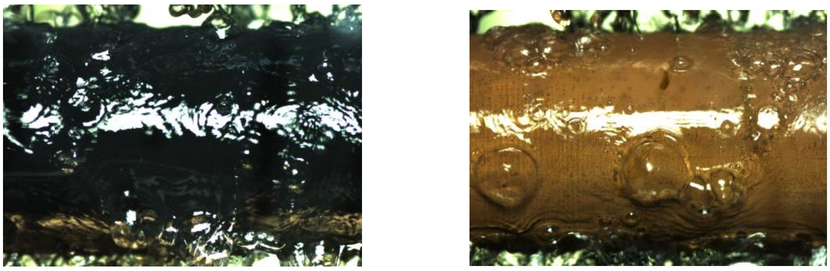

(d) CuO (e) nanoFLUX

Figure 7-11. Images of falling film boiling surfaces at 20 kW/m^2 in R-245fa at 20°C with a film flow rate of 0.14 kg/m/s.

However, it is clear from the images that the roughened tube had the most bubbles. This agrees with the findings of the pool boiling study where the roughened tube was found to have the most nucleation sites. The 60 to 100% higher HTCs of the roughened tube compared with those of the polished tube seen in **Figure 7-9** were thus likely due to increased nucleation site density, as the surfaces were otherwise structurally similar.

The LbL and CuO tubes had HTCs approximately 10% higher and lower than the polished tube respectively at 20 kW/m^2 in R-245fa at 20°C and it is not clear whether they had differing nucleation site densities based on **Figure 7-11** compared with those of the polished tube. The nanoFLUX tube appeared to have a lower nucleation site density than for the roughened tube in **Figure 7-11**, despite having HTCs approximately 10% higher than that of the roughened tube at 20 kW/m^2 in R-245fa at 20°C, with a similar trend seen in the pool boiling results. This suggested that the unique heat transfer mechanisms of the nanoFLUX tube (and possibly the CuO tube) seen within the pool boiling study was active under falling film conditions, namely the enhanced single-phase liquid superheating by the flow of liquid through the nano-sized channels or reduced dryout and increased microlayer evaporation underneath the nucleating bubbles. The nanoFLUX HTCs were likely also in part higher than the CuO tubes due to a rougher microstructure and higher nucleation site density based on the pool boiling nucleation site density findings.

However, this evidence was not conclusive and an approach to measuring nucleation site density under falling film conditions would need to be developed to confirm this.

7.5.3 Falling film heat transfer enhancement

The falling film heat transfer enhancement ratios, K_{ff}, where the falling film HTCs at a film flow rate of approximately 0.13 kg/m/s were compared with the pool boiling HTCs from Section **6.2** are shown in **Figure 7-12** as a function of heat flux.

The polished copper (R_a of 0.12 µm) tube had some of the lowest enhancement ratios, while the roughened copper (R_a of 1.37 µm) tube had some of the highest enhancement ratios. This is consistent with the theory that falling film enhancement is driven by increased microlayer evaporation from trapped and sliding bubbles [78,80]. The greater nucleation site density of the roughened tube compared to the polished tube would allow it to have more sliding bubbles and thus a greater enhancement ratio. The LbL tube had an intermediate enhancement ratio throughout.

The nanoFLUX tube also had some of the highest falling film enhancement ratios measured, while the CuO tube had some of the lowest enhancement ratios. Considering that both the CuO and nanoFLUX tubes had similar nanostructures, it was likely that the difference in falling film enhancement ratios could also be attributed to differences in microstructure roughness and the expected increased nucleation site density of the nanoFLUX tube, seen and measured in the pool boiling results, which would result in a greater number of sliding bubbles.

It should be noted that the falling film enhancement of the nanostructured tubes was similar in magnitude to that of the plain tubes. Therefore, the unique heat transfer mechanisms of the nanostructured tubes appear not to be enhanced under falling film conditions and rather any enhancement appears to be through a similar mechanism to that of the plain tubes.

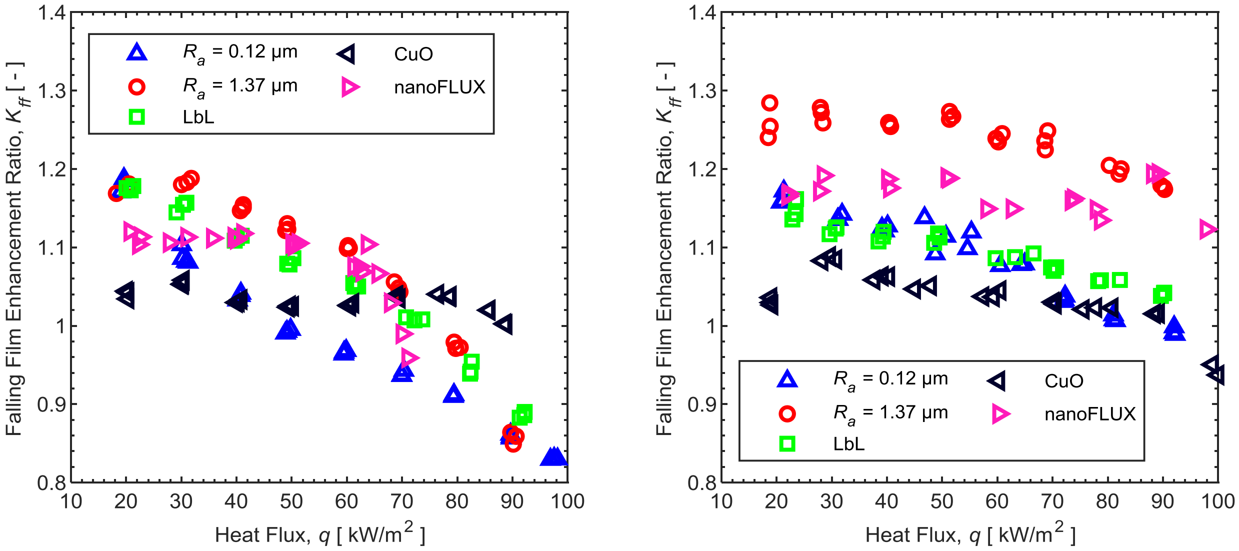

(a) R-245fa, 20°C, p_r of 0.034 (b) R-134a, 5°C, p_r of 0.086

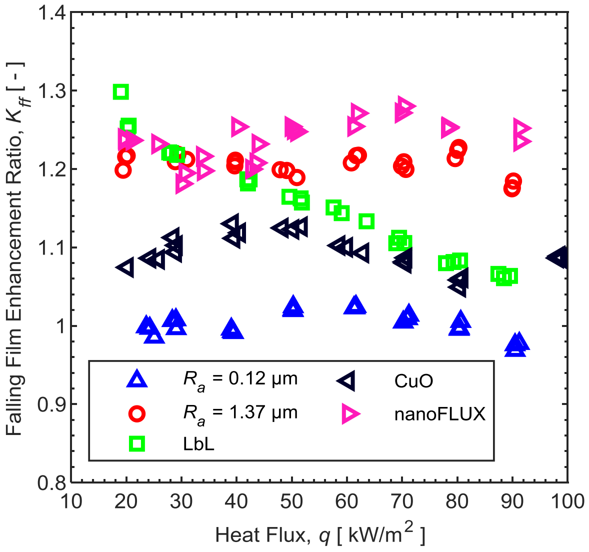

(c) R-134a, 25°C, p_r of 0.160

Figure 7-12. K_{ff} ratio as a function of heat flux of nanostructured and plain tubes.

The falling film heat transfer enhancement ratio of the polished, roughened and LbL tubes all displayed a sensitivity to heat flux, particularly in R-245fa at 20°C, while the nanoFLUX and CuO tube did not. This could be linked to dryout, because while these results showed that at a similar film Reynolds number the worst dryout performance was for R-134a at 25°C, when comparing at the same film flow rate of 0.13 kg/m/s as is the case in **Figure 7-12**, the worst dryout would occur in R-245fa at 20°C because the film Reynolds number of R-245fa was approximately half that of R-134a due to R-245fa having over double the dynamic viscosity of R-134a at 20°C.

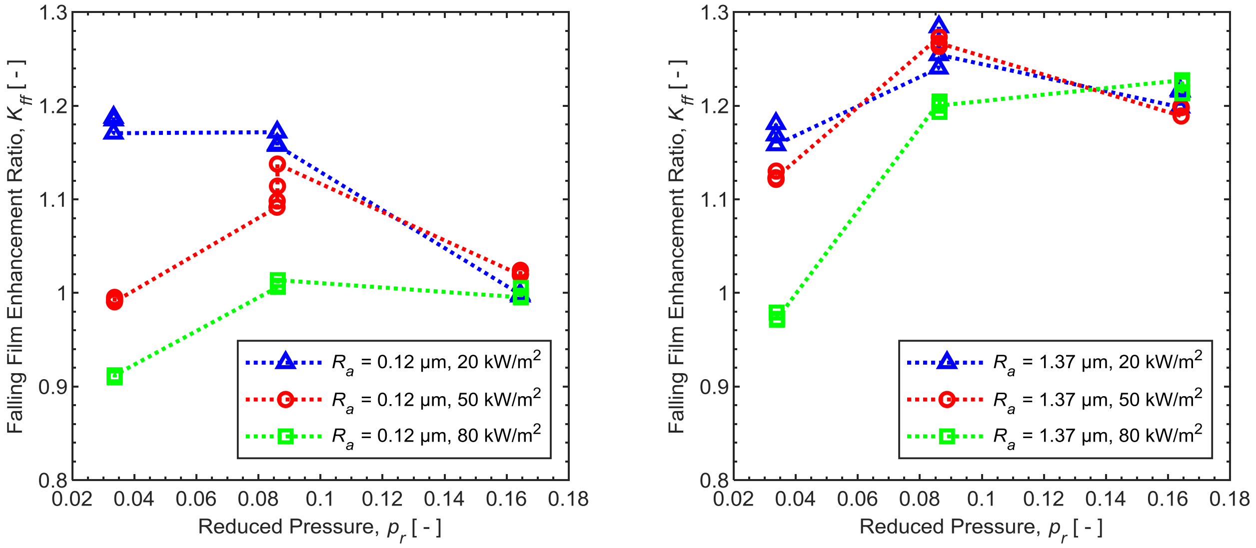

(a) Polished (b) Roughened

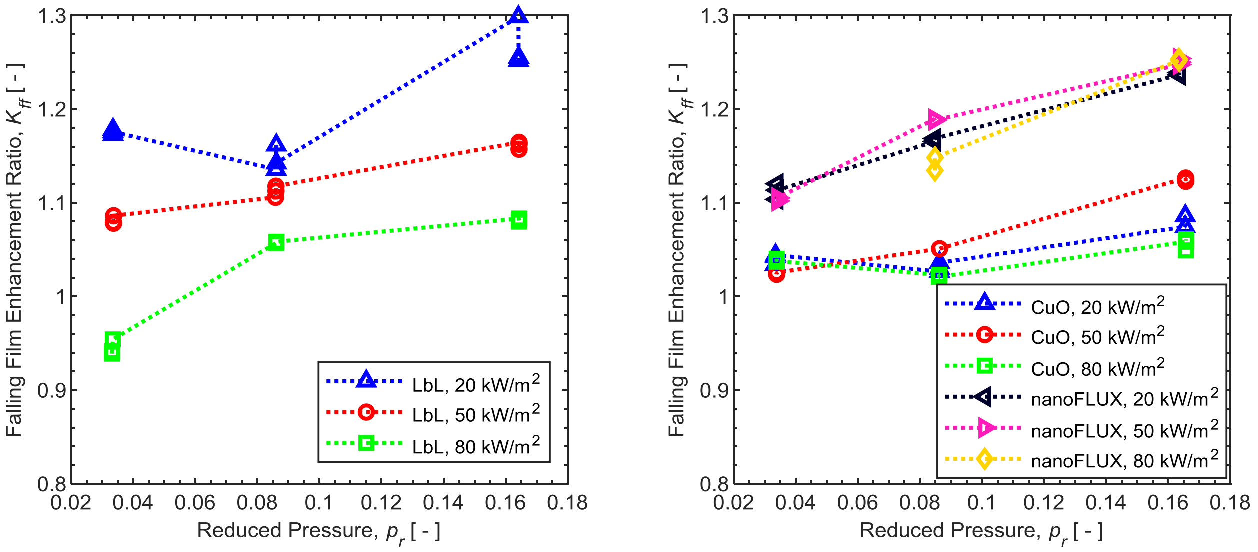

(c) LbL (d) nanoFLUX and CuO

Figure 7-13. K_{ff} as a function of reduced pressure of nanostructured and plain tubes with film flow rate of ~0.13 kg/m/s.

The influence of reduced pressure on the falling film heat transfer enhancement ratio is illustrated in **Figure 7-13** at three heat fluxes of 20, 50 and 80 kW/m^2. The falling film enhancement ratio of the polished copper (R_a of 0.12 μm) tube decreased as reduced pressure was increased at 20 kW/m^2, but increased at 80 kW/m^2. The roughened copper (R_a of 1.37 μm) tube showed a relatively stable enhancement ratio at heat fluxes of 20 and 50 kW/m^2, but an increasing enhancement ratio at 80 kW/m^2.

The LbL, CuO and nanoFLUX tubes showed a clear increase in falling film heat transfer enhancement ratios of approximately 10% as the reduced pressure was increased across the range of heat fluxes. This fits in with the already discussed theoretical framework, because increased reduced pressure leads to more activated nucleation sites and thus a greater number of sliding bubbles and increased microlayer evaporation than for pool boiling.

These findings, together with the findings Chapter **5**, where increased surface roughness showed an increase in falling film enhancement, all suggest that increases in bubble density are key to increasing the falling film enhancement ratio, as the increased number of trapped sliding bubbles increase the microlayer evaporation.

It is unclear why the polished copper tube had a reduction in enhancement ratio and the roughened copper tube enhancement ratio remained relatively constant as reduced pressure was increased at 20 kW/m^2. Dryout could be a factor, as the normalised HTCs in **Figure 7-6** show that the polished and roughened tubes had a sensitive HTC plateau possibly caused by intermittent dryout. Therefore, at a film flow rate higher than those tested in this study, the HTCs of the polished and roughened tubes could increase and thus also increase the falling film enhancement ratio resulting in trends similar to those displayed by the CuO and nanoFLUX tubes, which had less of a dryout influenced plateau region.

7.6 Summary, conclusions and recommendations

The HTCs on one polished copper (R_a of 0.12 µm), one roughened copper (R_a of 1.37 µm) and three nanostructured horizontal tubes were measured during saturated falling film boiling of refrigerants R-245fa at 20°C and R-134a at 5°C and 25°C. The refrigerant film flow rate on the outside of the tubes was varied from 0 kg/m/s to a maximum of approximately 0.13 kg/m/s.

Both plain and nanostructured tubes displayed the characteristic plateau region with HTCs being relatively insensitive to reductions in film flow rate, followed by critical dryout where the HTCs collapsed as visible dry patches became predominant. Future studies quantifying the visible dryout area may be able to determine if visible dryout is indeed the dominant factor for decreased HTCs or if underlying nanostructured dryout contributes as well.

The nanoFLUX tube, and the CuO tube to a lesser degree, produced a very insensitive plateau region as the film flow rate decreased, while the polished, roughened and LbL tubes all showed decreased HTCs within the plateau region up until the critical dryout point. These differences in plateau sensitivities are suggested to be due to differences in wettability of the surfaces under boiling conditions. In some cases, a HTC hump was observed for the nanoFLUX tubes, where up to a 20% increase in the HTC occurred just prior to the critical dryout limit as the film flow rate was decreased. This was thought to be due to maintaining a very thin superheated film of liquid that reduced the evaporative thermal resistance to a point where it could meaningfully contribute to the HTC.

Critical dryout occurred at higher film Reynolds numbers as the heat flux was increased for both plain and nanostructured tubes. The nanostructured CuO and nanoFLUX tubes had the lowest critical film Reynolds numbers at low heat fluxes (20 kW/m^2), but the highest critical film Reynolds numbers at higher heat fluxes (80 kW/m^2) due to the early onset of critical dryout or DNB at higher heat fluxes. The CuO and nanoFLUX tubes experienced early onset of DNB compared with the other tubes, with liquid separating and no longer wetting the surface of the tubes.

The mechanism that improved the dryout capabilities of the nanoFLUX and CuO tubes under lower heat flux conditions was likely their ability to wick liquid through their porous nanostructures. However, increased heat fluxes possibly led to dryout of the CuO and nanoFLUX nanostructures resulting in operation in the Cassie-Baxter state and thus reduced wettability with subsequent critical dryout and DNB CHF occurring. The worst dryout performance was seen when boiling R-134 at 25°C, followed by R-134a at 5°C and then R245fa at 20°C when compared on an equal film Reynolds number basis.

Both plain and nanostructured tubes had HTCs that increased linearly on a log-log plot as the heat flux was increased. Increases in reduced pressure also increased the HTCs for plain and nanostructured tubes. The CuO and nanoFLUX nanostructured tubes showed higher sensitivities to changes in the heat flux and reduced pressure than the other tubes, possibly as a result of a larger population of smaller nucleation sites.

Nanostructured tubes achieved both higher and lower falling film boiling HTCs than those associated with the plain tubes over the heat flux range from 20 to 100 kW/m^2 at the maximum film flow rate of approximately 0.13 kg/m/s. The roughened tube had HTCs between 60% and 100% higher than the polished tube, the LbL tube had HTCs between 20% lower and 20% higher than the polished tube, the CuO tube had HTCs between 20% lower and 80% higher than the polished tube, and the nanoFLUX tube had between 40 to 200% higher HTCs than the polished tube.

Based largely on findings from the pool boiling nucleation site density study, the heat transfer performance of the nanoFLUX, CuO and LbL tubes is likely explained by differences in nucleation site density, with the nanoFLUX tube having a rougher microstructure and higher nucleation site density than the CuO and LbL tubes. Furthermore it is likely that heat transfer mechanisms unique to the nanoFLUX and CuO nanostructures identified within the pool boiling study further played a role in their respective heat transfer performance, namely enhanced single-phase liquid superheating by the flow of liquid through the nano-sized channels or reduced dryout and increased microlayer evaporation underneath the nucleating bubbles.

The falling film heat transfer enhancement ratios of the nanostructured tubes tested in this study were of a similar order of magnitude to those of the plain tubes. Therefore, the unique heat transfer mechanisms of the nanostructured tubes appear not to be enhanced under falling film conditions.

The enhancement ratios of the LbL, CuO and nanoFLUX nanostructured tubes increased as the reduced pressure was increased, thought to be caused by increased bubble nucleation at higher reduced pressures resulting in greater microfilm evaporation from sliding bubbles trapped in the film. The falling film heat transfer enhancement ratios of the roughened and nanoFLUX tubes were higher than those of the polished and CuO tubes respectively, likely as a result of a greater number of active nucleation sites on the roughened and nanoFLUX tubes due to rougher microstructures. These findings suggest that bubble density is key to the falling film heat transfer enhancement mechanism. The polished and roughened tube falling film heat transfer enhancement ratios did not increase monotonically as the reduced pressure increased, possibly as a result of dryout considerations.

8. Summary, conclusions and recommendations

8.1 Summary

The purpose of this study was to improve the understanding of the influence of surface characteristics on heat transfer in falling film refrigerant evaporators through an experimental campaign to measure the heat transfer coefficients (HTCs) of plain tubes of different roughness and material as well different nanostructured tubes under falling film boiling conditions. Tubes were also tested under pool boiling conditions as these mechanisms are not particularly well understood for pool boiling as well, and comparisons to pool boiling heat transfer allows for the isolation of mechanisms unique to falling film boiling such as dryout and allow the use of the greater knowledge of pool boiling to further understand falling film boiling. However the pool boiling results themselves were unique and expanded our understanding of that complex process.

The study achieved this goal by measuring the HTCs across four different roughness copper tubes, polished and roughened mild steel and stainless steel tubes and three nanostructured tubes under both pool boiling and falling film boiling conditions across a range of heat fluxes and refrigerant conditions. The three nanostructured tubes tested were: (i) a layer-by-layer (LbL) tube, created through the deposition of approximately 50 layers of silica nanoparticles with a diameter of approximately 20 nm onto the surface of a copper tube, (ii) a tube with copper oxide (CuO) nanostructures over its surface, created by using a chemical bath to oxidise the surface of a copper tube, and (iii) a commercial nanoFLUX-coated copper tube. The critical heat flux (CHF) point as a result of departure from nucleate boiling (DNB) occurred on two of the nanostructured tubes under both pool boiling and falling film boiling conditions and was further investigated so as to understand the limitations of these surfaces. Furthermore, falling film boiling HTCs were recorded across a range of film flow rates at constant heat fluxes to understand the dryout characteristics of the surfaces tested and to measure the operational limits due to critical dryout. Lastly images taken by a high speed video camera aided in the understanding of some of the underlying mechanisms seen.

8.2 Conclusions

8.2.1 Pool boiling

All tubes of different roughness, different material and different nanostructure tested within this study displayed linearly increasing HTCs during pool boiling as the heat flux was increased on a log-log plot. The CuO and nanoFLUX tubes were more sensitive to changes in heat flux than a polished plain copper (R_a of 0.12 µm), roughened plain copper (R_a of 1.37 µm) and the LbL tube, with improved heat transfer of the CuO and nanoFLUX tubes at higher heat fluxes compared to the other tubes. This finding could be due to a larger population of small nucleation sites on the CuO and nanoFLUX surfaces. Both plain and nanostructured tubes displayed HTCs that increased similarly as reduced pressures were increased.

Increases in roughness of plain tubes and nanostructured tubes were found to increase the HTCs of tubes. Increases in roughness of plain copper tubes approximately adhered to Stephen's relation of $h_o \propto {R_a}^{0.1333}$, with exponents measured in this study of 0.11 and 0.13. Surface material influenced the pool boiling HTCs with increasing thermal effusivity and thermal conductivity generally increasing HTCs measured.

The LbL tube had up to 20% higher HTCs than those of the polished plain copper tube at the lowest reduced pressure and down to 20% lower HTCs at the highest reduced pressure tested during pool boiling. The CuO tube performed similarly to the polished tube at low heat fluxes (20 kW/m^2), but outperformed the polished tube by approximately 60% at high heat fluxes (100 kW/m^2) in terms of HTCs.

Furthermore, it was found that the nanoFLUX nanostructured tube produced the highest pool boiling HTCs measured during this entire study, with measured HTCs between 40 and 200% higher than those of a polished copper tube, and between 0 and 50% higher than those of a roughened copper tube.

The nanoFLUX tube had a greater nucleation site density when pool boiling R-245fa at 20°C at 20 kW/m^2 compared to other nanostructured tubes, which suggested a rougher microstructure that contributed to its improved heat transfer. When pool boiling R-245fa at 20°C at 20 kW/m^2, the nanoFLUX and CuO tubes had fewer nucleation sites than those of sandpapered tubes of similar heat transfer performance and this suggests that the nanoFLUX and CuO surfaces had an additional unique heat transfer mechanism compared with sandpapered surfaces. This was possibly linked to capillary wicking of liquid inside the nanochannels of the porous coatings driven by the external bubble pumping, which contributed to enhanced single-phase liquid superheating by the flow of liquid through the nano-sized channels or reduced dryout and increased microlayer evaporation underneath the nucleating bubbles.

The measured CHF as a result of DNB of the CuO and nanoFLUX tubes under pool boiling was lower than that expected for a plain tube. It was suggested that the early onset of DNB CHF for pool boiling over the CuO and nanoFLUX tubes may be due to vapour trapped in the fibrous nanostructure, resulting in reduced wetting in the Cassie-Baxter state.

8.2.2 Falling film boiling

All plain tubes of different material and roughness as well as nanostructured tubes displayed a characteristic plateau region with HTCs being relatively insensitive to reductions in film flow rate, followed by critical dryout where the HTCs collapsed as dry patches became predominant under falling film boiling conditions.

This insensitivity did however vary across the tubes, with the HTCs of rougher tubes changing by approximately 5% as film flow rates varied from 0.13 to 0.05 kg/m/s, while the HTCs of smoother tubes varied by approximately 15%. The nanoFLUX tube, and the CuO tube to a lesser degree, produced a very insensitive plateau region as the film flow rate decreased, while the LbL tube showed decreased HTCs within the plateau region up until the critical dryout point. These differences in plateau sensitivities are suggested to be due to differences in wettability of the surfaces under boiling conditions resulting in differences in frequency of intermittent dryout within the plateau region.

In some cases, a HTC hump was observed for the nanoFLUX tubes, where up to a 20% increase in the HTC occurred just prior to the critical dryout limit as the film flow rate was decreased. This was thought to be due to the nanoFLUX tube maintaining a very thin superheated film of liquid that reduced the evaporative thermal resistance to a point where it could meaningfully contribute to the HTC.

Critical dryout occurred at higher film Reynolds numbers as the heat flux was increased for both plain and nanostructured tubes. The critical dryout threshold was not shown to be significantly influenced by surface roughness or surface material. The nanostructured CuO and nanoFLUX tubes had the lowest critical film Reynolds numbers at low heat fluxes (20 kW/m^2), but the highest critical film Reynolds numbers at higher heat fluxes (80 kW/m^2) due to the early onset of critical dryout or departure from nucleate boiling (DNB) at higher heat fluxes. The CuO and nanoFLUX tubes experienced early onset of DNB during falling film boiling compared with the other tubes, with liquid separating and no longer wetting the surface of the tubes.

The mechanism that improved the dryout capabilities of the nanoFLUX and CuO tubes under lower heat flux conditions and within the plateau region was likely their ability to wick liquid through their porous nanostructures. However, increased heat fluxes possibly led to dryout of the CuO and nanoFLUX nanostructures resulting in operation in the Cassie-Baxter state and thus reduced wettability with subsequent critical dryout and DNB CHF occurring. The worst dryout performance was seen when boiling R-134 at 25°C, followed by R-134a at 5°C and then R245fa at 20°C when compared on an equal film Reynolds number basis.

Both plain and nanostructured tubes had HTCs that increased linearly on a log-log plot as the heat flux was increased in falling film boiling at constant film flow rates of ~0.13 kg/m/s. Increases in reduced pressure also increased the HTCs for all tubes tested in this study. The CuO and nanoFLUX nanostructured tubes showed higher sensitivities to changes in the heat flux and reduced pressure than the other tubes, again likely as a result of a larger population of small nucleation sites.

Falling film boiling HTCs followed similar trends to those of the pool boiling study when different material tubes were tested, with HTCs increasing as material effusivity was increased.

Nanostructured tubes achieved both higher and lower falling film boiling HTCs than plain tubes over the heat flux range from 20 to 100 kW/m^2 at the maximum film flow rate of approximately 0.13 kg/m/s. The roughened tube had HTCs between 60% and 100% higher than the polished tube, the LbL tube had HTCs between 20% lower and 20% higher than the polished tube, the CuO tube had HTCs between 20% lower and 80% higher than the polished tube, and the nanoFLUX tube had between 40 to 200% higher HTCs than the polished tubes.

Increased surface roughness on plain tubes of different materials was found to increase the HTCs of falling film boiling. Similarly the heat transfer performance of the nanoFLUX, CuO and LbL tubes is likely explained by differences in nucleation site density, with the nanoFLUX tube having a rougher microstructure and higher nucleation site density than the CuO and LbL tubes.

Furthermore it is likely that heat transfer mechanisms unique to the nanoFLUX and CuO nanostructures identified within the pool boiling study further played a role in their respective falling film boiling heat transfer performance, namely enhanced single-phase liquid superheating by the flow of liquid through the nano-sized channels or reduced dryout and increased microlayer evaporation underneath the nucleating bubbles.

However the increase in HTCs due to increased roughness on the plain tubes was greater than that experienced within the pool boiling studies, with the exponents of the fit $h_o \propto R_a{}^{\mathrm{b}}$ equal to 0.17 and 0.21, which were higher than the respective exponents measured under pool boiling conditions, which were 0.11 and 0.13. Thus falling film boiling heat transfer was found to be more sensitive to changes in roughness than pool boiling.

The falling film heat transfer enhancement ratio further illustrated this as it increased as surface roughness on plain tubes was increased for all material tubes tested, with the enhancement ratio ranging from 1 to 1.4 as the roughness ranged from 0.09 µm to 1.91 µm. The falling film heat transfer enhancement ratios of the nanoFLUX tube was higher than those of the CuO tube, also likely as a result of a rougher microstructure on the nanoFLUX tubes and the subsequent greater number of active nucleation sites. It is hypothesized that the greater bubble density of rougher tubes increased the enhancement mechanisms proposed, such as greater microlayer evaporation of trapped bubbles sliding within the falling film.

The surface material was found to have no discernible influence on falling film enhancement. The falling film heat transfer enhancement ratios of the nanostructured tubes tested in this study were of a similar order of magnitude to those of the plain tubes. Therefore, the unique heat transfer mechanisms of the nanostructured tubes appear not to be enhanced under falling film conditions.

The enhancement ratios of the LbL, CuO and nanoFLUX nanostructured tubes increased as the reduced pressure was increased, thought to be caused by increased bubble nucleation at higher reduced pressures resulting in greater microfilm evaporation from trapped sliding bubbles. The polished and roughened tube falling film heat transfer enhancement ratios did not increase monotonically as the reduced pressure increased, possibly as a result of dryout considerations.

Thus this study has shown that increases in bubble density are key to increasing the falling film enhancement ratio, with the microlayer evaporation under sliding bubbles trapped in the falling film a likely cause.

8.3 Recommendations

Recommendations for further work stemming from the findings of this study are as follows:

- The study conducted was not exhaustive and a number of parameters investigated can be investigated in greater detail and over a greater range. In particular higher film flow rates can be tested to see if all surfaces will eventually form a HTC plateau region that is very insensitive to film flow rate changes, as this was not found in this study. Higher heat fluxes can be tested to see what the measured CHF as a result of DNB on the plain tubes are, to replace the predictions used in this study, while lower heat fluxes would allow for the investigation of the onset of falling film boiling. A larger range of reduced pressures than used in this study may provide further insight into the refrigerant influence on the heat transfer process of pool and falling film boiling.

- Testing at lower heat fluxes was limited in this study by the HTC uncertainties as a result of the measurement technology used. Newer or differing technologies that allow for greater temperature measurement accuracy so that lower heat fluxes can be practically measured would be of great value to future studies.
- Further studies with a greater roughnesses would provide further insight into a number of phenomena seen in this study. Literature suggests that as roughness is increased a limit is reached where further increases in HTC are no longer achieved. This limit was not reached in this study and has not yet been confirmed to take place under falling film boiling conditions. Greater roughnesses would also confirm whether the lack of influence roughness was seen to have on critical dryout in this study is indeed the case and also confirm whether the falling film heat transfer enhancement caused by increased roughness has an upper limit.
- Further research or technology development that allows for better quantification of roughness size and distribution influences is still required, both for pool boiling and falling film boiling.
- High speed video analysis of falling film boiling within the plateau region may provide further evidence whether the mechanisms suggested in this study, such as intermittent dryout, are indeed the cause of the differences in plateau region HTC sensitivity to film flow rate changes. Future studies quantifying the visible dryout area may also be able to determine if visible dryout is indeed the dominant factor for decreased HTCs or if underlying dryout of the nanostructure cavities contribute as well.
- A study of bubble frequency and volume is required to determine whether increased microlayer evaporation is the reason for the enhanced heat transfer exhibited by the nanostructured tubes, or whether the single phase mechanisms suggested are the more likely reason.
- The theory that the nanostructured surface dries out at high heat fluxes and switches to the Cassie-Baxter state resulting in reduced wetting and thus the early onset of DNB could be investigated further through detailed contact angle tests of refrigerants under saturated refrigerant conditions and heated surface conditions.
- Studies to investigate those scenarios where nanostructured surfaces can be used to extend falling film boiling or further enhance pool boiling are suggested, such as low flux falling film boiling on complex geometries or pool boiling of microstructured surfaces that suffer from dryout within the cavities of the re-entrant cavities.
- Nanostructures tested within this study did not result in dramatic improvements in active nucleation site density. As all surfaces in this study were polished first before coating, the nucleation site density of nanostructures may thus be

significantly influenced by the underlying microstructure of the coated surface. Thus investigating the influence the underlying microstructure has on nanostructure heat transfer merits investigation as an optimum combination may be found.

- A model to predict falling film boiling HTCs should incorporate the work documented in this study.
- The hypotheses developed in this study may be interrogated further not only experimentally, but through the use of numerical simulation on a micro- and nanoscale to provide more insight into the likelihood of the processes hypothesized to occur in this study.

References

[1] G. Ribatski and A. M. Jacobi, "Falling-film evaporation on horizontal tubes - A critical review," *International Journal of Refrigeration,* vol. 28, no. 5, pp. 635-653, 2005.

[2] J. Fernandez-Seara and Á. Á. Pardiñas, "Refrigerant falling film evaporation review: Description, fluid dynamics and heat transfer," *Applied Thermal Engineering,* vol. 64, no. 1, pp. 155-171, 2014.

[3] UNEP, "Amendment to the montreal protocol on substances that deplete the ozone layer," *United Nations Environmental Program,* vol. Art IV (1), 2016.

[4] X. Wu, C. Dang, S. Xu, and E. Hihara, "State of the art on the flammability of hydrofluoroolefin (HFO) refrigerants," *International Journal of Refrigeration,* vol. 108, pp. 209-223, 2019.

[5] J. R. Thome, "Engineering data book 3," *Wolverine Tube Inc,* 2004.

[6] A. M. Abed, M. A. Alghoul, M. H. Yazdi, A. N. Al-Shamani, and K. Sopian, "The role of enhancement techniques on heat and mass transfer characteristics of shell and tube spray evaporator: A detailed review," *Applied Thermal Engineering,* vol. 75, pp. 923-940, 2015.

[7] Sulzer Chemtech, "Film evaporation technology," Accessed on: 30 June 2020 Available: https://www.sulzer.com/-/media/files/products/separation-technology/evaporation/film_evaporation_technology.ashx

[8] C.-Y. Zhao, P.-H. Jin, W.-T. Ji, Y.-L. He, and W.-Q. Tao, "Experimental investigations of R134a and R123 falling film evaporation on enhanced horizontal tubes," *International Journal of Refrigeration,* vol. 75, pp. 190-203, 2017.

[9] P.-H. Jin, C.-Y. Zhao, W.-T. Ji, and W.-Q. Tao, "Experimental investigation of R410A and R32 falling film evaporation on horizontal enhanced tubes," *Applied Thermal Engineering,* vol. 137, pp. 739-748, 2018.

[10] P.-H. Jin, Z. Zhang, I. Mostafa, C.-Y. Zhao, W.-T. Ji, and W.-Q. Tao, "Experimental study of falling film evaporation in tube bundles of doubly-enhanced, horizontal tubes," *Applied Thermal Engineering,* vol. 170, p. 115006, 2020.

[11] J. F. Roques and J. R. Thome, "Falling films on arrays of horizontal tubes with R134a, part 1: Boiling heat transfer results for four types of tubes," *Heat Transfer Engineering,* vol. 28, no. 5, pp. 398-414, 2007.

[12] P.-H. Jin, Z. Zhang, I. Mostafa, C.-Y. Zhao, W.-T. Ji, and W.-Q. Tao, "Heat transfer correlations of refrigerant falling film evaporation on a single horizontal smooth tube," *International Journal of Heat and Mass Transfer,* vol. 133, pp. 96-106, 2019.

[13] M. Christians and J. R. Thome, "Falling film evaporation on enhanced tubes, part 1: Experimental results for pool boiling, onset-of-dryout and falling film evaporation," *International Journal of Refrigeration,* vol. 35, no. 2, pp. 300-312, 2012.

[14] D. Jige, H. Miyata, and N. Inoue, "Falling film evaporation of R1234ze(E) and R245fa on a horizontal smooth tube," *Experimental Thermal and Fluid Science,* vol. 105, pp. 58-66, 2019.

[15] S. A. Moeykens and M. B. Pate, "Spray evaporation heat transfer of R134a on plain tubes," in *American Society of Heating, Refrigerating, and Air Conditioning Engineers (ASHRAE) annual meeting*, Orlando, FL (United States), 1994, vol. 100, pp. 173-184: American Society of Heating, Refrigerating and Air-Conditioning Engineers, Inc., .

[16] D. E. Kim, D. I. Yu, D. W. Jerng, M. H. Kim, and H. S. Ahn, "Review of boiling heat transfer enhancement on micro/nanostructured surfaces," *Experimental Thermal and Fluid Science,* vol. 66, pp. 173-196, 2015.

[17] X. Li, I. Cole, and J. Tu, "A review of nucleate boiling on nanoengineered surfaces: The nanostructures, phenomena and mechanisms," *International Journal of Heat and Mass Transfer,* vol. 141, pp. 20-33, 2019.

[18] D. Gorenflo and D. B. R. Kenning, "Pool boiling (chapter H2)," in *VDI Heat Atlas*, VDI-Gesellschaft Verfahrenstechnik und Chemieingenieurwesen (GVC), Ed. 2nd ed. Berlin, Heidelberg: Springer-Verlag, 2010, pp. 757-792.

[19] J. Jabardo, "An overview of surface roughness effects on nucleate boiling heat transfer," *The Open Conservation Biology Journal,* vol. 2, no. 1, 2010.

[20] C. S. Sujith Kumar, G. Udaya Kumar, M. R. Mata Arenales, C.-C. Hsu, S. Suresh, and P.-H. Chen, "Elucidating the mechanisms behind the boiling heat transfer enhancement using nano-structured surface coatings," *Applied Thermal Engineering,* vol. 137, pp. 868-891, 2018.

[21] J. F. Roques and J. R. Thome, "Falling films on arrays of horizontal tubes with R134a, part 2: Flow visualization, onset of dryout, and heat transfer predictions," *Heat Transfer Engineering,* vol. 28, no. 5, pp. 415-434, 2007.

[22] C.-Y. Zhao, W.-T. Ji, P.-H. Jin, and W.-Q. Tao, "Heat transfer correlation of the falling film evaporation on a single horizontal smooth tube," *Applied Thermal Engineering,* vol. 103, no. Supplement C, pp. 177-186, 2016.

[23] W.-T. Ji, E.-T. Zhao, C.-Y. Zhao, H. Zhang, and W.-Q. Tao, "Falling film evaporation and nucleate pool boiling heat transfer of R134a on the same enhanced tube," *Applied Thermal Engineering,* vol. 147, pp. 113-121, 2019.

[24] J. Barber, D. Brutin, and L. Tadrist, "A review on boiling heat transfer enhancement with nanofluids," *Nanoscale Research Letters,* vol. 6, no. 1, p. 280, 2011.

[25] C. G. Jothi Prakash and R. Prasanth, "Enhanced boiling heat transfer by nano structured surfaces and nanofluids," *Renewable and Sustainable Energy Reviews,* vol. 82, pp. 4028-4043, 2018.

[26] M. Shojaeian and A. Koşar, "Pool boiling and flow boiling on micro- and nanostructured surfaces," *Experimental Thermal and Fluid Science,* vol. 63, pp. 45-73, 2015.

[27] B. D. Bock, J. P. Meyer, and J. R. Thome, "Falling film boiling and pool boiling on plain circular tubes: Influence of surface roughness, surface material and saturation temperature on heat transfer and dryout," *Experimental Thermal and Fluid Science,* vol. 109, p. 109870, 2019.

[28] B. D. Bock, M. Bucci, C. N. Markides, J. R. Thome, and J. P. Meyer, "Pool boiling of refrigerants over nanostructured and roughened tubes," *International Journal of Heat and Mass Transfer,* vol. 162, p. 120387, 2020.

[29] B. D. Bock, M. Bucci, C. N. Markides, J. R. Thome, and J. P. Meyer, "Falling film boiling of refrigerants over nanostructured and roughened tubes: Heat transfer, dryout and critical heat flux," *International Journal of Heat and Mass Transfer,* vol. 163, p. 120452, 2020.

[30] W. M. Rohsenow, J. P. Hartnett, and Y. I. Cho, *Handbook of heat transfer*, 3rd ed. McGraw-Hill New York, 1998.

[31] G. Ribatski and J. M. S. Jabardo, "Experimental study of nucleate boiling of halocarbon refrigerants on cylindrical surfaces," *International Journal of Heat and Mass Transfer,* vol. 46, no. 23, pp. 4439-4451, 2003.

[32] J. M. S. Jabardo, G. Ribatski, and E. Stelute, "Roughness and surface material effects on nucleate boiling heat transfer from cylindrical surfaces to refrigerants R134a and R123," *Experimental Thermal and Fluid Science,* vol. 33, no. 4, pp. 579-590, 2009.

[33] B. J. Jones, J. P. McHale, and S. V. Garimella, "The Influence of surface roughness on nucleate pool boiling heat transfer," *Journal of Heat Transfer,* vol. 131, no. 12, pp. 121009-121009-14, 2009.

[34] I. L. Pioro, W. Rohsenow, and S. S. Doerffer, "Nucleate pool-boiling heat transfer. I: Review of parametric effects of boiling surface," *International Journal of Heat and Mass Transfer,* vol. 47, no. 23, pp. 5033-5044, 2004.

[35] A. Luke, "Pool boiling heat transfer from horizontal tubes with different surface roughness," *International Journal of Refrigeration,* vol. 20, no. 8, pp. 561-574, 1997.

[36] J. Kim, S. Jun, R. Laksnarain, and S. M. You, "Effect of surface roughness on pool boiling heat transfer at a heated surface having moderate wettability," *International Journal of Heat and Mass Transfer,* vol. 101, no. Supplement C, pp. 992-1002, 2016.

[37] H. Jo, H. S. Ahn, S. Kang, and M. H. Kim, "A study of nucleate boiling heat transfer on hydrophilic, hydrophobic and heterogeneous wetting surfaces," *International Journal of Heat and Mass Transfer,* vol. 54, no. 25, pp. 5643-5652, 2011.

[38] M. Yamada, B. Shen, T. Imamura, S. Hidaka, M. Kohno, K. Takahashi, and Y. Takata, "Enhancement of boiling heat transfer under sub-atmospheric pressures using biphilic surfaces," *International Journal of Heat and Mass Transfer,* vol. 115, pp. 753-762, 2017.

[39] M. Cooper, "Saturation nucleate pool boiling: A simple correlation," in *Institute of Chemical Engineering Symposium Series*, 1984, vol. 86, no. 2, pp. 785-793, 1984.

[40] I. I. Gogonin, "The effects of heat-release wall properties on boiling heat transfer," *Journal of Engineering Thermophysics,* vol. 16, no. 2, pp. 78-87, 2007.

[41] S. Kotthoff and D. Gorenflo, "Heat transfer and bubble formation on horizontal copper tubes with different diameters and roughness structures," *Heat and Mass Transfer,* vol. 45, no. 7, pp. 893-908, 2009.

[42] D. Gorenflo, E. Baumhögger, G. Herres, and S. Kotthoff, "Prediction methods for pool boiling heat transfer: A state-of-the-art review," *International Journal of Refrigeration,* vol. 43, no. Supplement C, pp. 203-226, 2014.

[43] A. Luke, "Preparation and analysis of different roughness structures for evaporator tubes," *Heat and Mass Transfer,* vol. 45, no. 7, pp. 909-917, 2009.

[44] C. Bombardieri and C. Manfletti, "Influence of wall material on nucleate pool boiling of liquid nitrogen," *International Journal of Heat and Mass Transfer,* vol. 94, pp. 1-8, 2016.

[45] C. H. Wang and V. K. Dhir, "Effect of surface wettability on active nucleation site density during pool boiling of water on a vertical surface," *Journal of Heat Transfer,* vol. 115, no. 3, pp. 659-669, 1993.

[46] E. Forrest, E. Williamson, J. Buongiorno, L.-W. Hu, M. Rubner, and R. Cohen, "Augmentation of nucleate boiling heat transfer and critical heat flux using nanoparticle thin-film coatings," *International Journal of Heat and Mass Transfer,* vol. 53, no. 1, pp. 58-67, 2010.

[47] J. Kim, S. Jun, J. Lee, J. Godinez, and S. M. You, "Effect of surface roughness on pool boiling heat transfer of water on a superhydrophilic aluminum surface," *Journal of Heat Transfer,* vol. 139, no. 10, 2017.

[48] W. Wu, H. Bostanci, L. C. Chow, Y. Hong, M. Su, and J. P. Kizito, "Nucleate boiling heat transfer enhancement for water and FC-72 on titanium oxide and silicon oxide surfaces," *International Journal of Heat and Mass Transfer,* vol. 53, no. 9, pp. 1773-1777, 2010.

[49] R. L. Webb and C. Pais, "Nucleate pool boiling data for five refrigerants on plain, integral-fin and enhanced tube geometries," *International Journal of Heat and Mass Transfer,* vol. 35, no. 8, pp. 1893-1904, 1992.

[50] D. Jung, K. An, and J. Park, "Nucleate boiling heat transfer coefficients of HCFC22, HFC134a, HFC125, and HFC32 on various enhanced tubes," *International Journal of Refrigeration,* vol. 27, no. 2, pp. 202-206, 2004.

[51] Y. Lee, D.-G. Kang, J.-H. Kim, and D. Jung, "Nucleate boiling heat transfer coefficients of hfo1234yf on various enhanced surfaces," *International Journal of Refrigeration,* vol. 38, pp. 198-205, 2014.

[52] E. Van Rooyen and J. R. Thome, "Pool boiling data and prediction method for enhanced boiling tubes with R134a, R236fa and R1234ze(e)," *International Journal of Refrigeration,* vol. 36, no. 2, pp. 447-455, 2013.

[53] D. Gorenflo, U. Chandra, S. Kotthoff, and A. Luke, "Influence of thermophysical properties on pool boiling heat transfer of refrigerants," *International Journal of Refrigeration,* vol. 27, no. 5, pp. 492-502, 2004.

[54] M. Zimmermann, M. Heinz, A. Sielaff, T. Gambaryan-Roisman, and P. Stephan, "Influence of system pressure on pool boiling regimes on a microstructured surface compared to a smooth surface," *Experimental Heat Transfer,* pp. 1-17, 2019.

[55] J. R. Thome, *Enhanced boiling heat transfer.* Taylor & Francis, 1990.

[56] T. Ubara, H. Asano, and K. Sugimoto, "Heat transfer enhancement of falling film evaporation on a horizontal tube by thermal spray coating," *Applied Sciences,* vol. 10, no. 5, p. 1632, 2020.

[57] C.-Y. Zhao, W.-T. Ji, P.-H. Jin, A.-G. Li, J.-F. Fan, S. Yoshioka, and W.-Q. Tao, "Falling film evaporation in a triangular tube bundle under the influence of cross vapor stream," *International Journal of Refrigeration,* vol. 112, pp. 44-55, 2020.

[58] C.-Y. Zhao, W.-T. Ji, P.-H. Jin, Y.-J. Zhong, and W.-Q. Tao, "Experimental study of the local and average falling film evaporation coefficients in a horizontal enhanced tube bundle using R134a," *Applied Thermal Engineering,* vol. 129, pp. 502-511, 2018.

[59] W.-T. Ji, C.-Y. Zhao, D.-C. Zhang, S. Yoshioka, Y.-L. He, and W.-Q. Tao, "Effect of vapor flow on the falling film evaporation of R134a outside a horizontal tube bundle," *International Journal of Heat and Mass Transfer,* vol. 92, pp. 1171-1181, 2016.

[60] W. Nakayama, T. Daikoku, H. Kuwahara, and T. Nakajima, "Dynamic model of enhanced boiling heat transfer on porous surfaces—Part I: Experimental investigation," *Journal of Heat Transfer,* vol. 102, no. 3, pp. 445-450, 1980.

[61] W. Nakayama, T. Daikoku, H. Kuwahara, and T. Nakajima, "Dynamic model of enhanced boiling heat transfer on porous surfaces—part ii: Analytical modeling," *Journal of Heat Transfer,* vol. 102, no. 3, pp. 451-456, 1980.

[62] W. Nakayama, T. Daikoku, and T. Nakajima, "Effects of pore diameters and system pressure on saturated pool nucleate boiling heat transfer from porous surfaces," *Journal of Heat Transfer,* vol. 104, no. 2, pp. 286-291, 1982.

[63] K.-H. Chu, Y. S. Joung, R. Enright, C. R. Buie, and E. N. Wang, "Hierarchically structured surfaces for boiling critical heat flux enhancement," *Applied Physics Letters,* vol. 102, no. 15, p. 151602, 2013.

[64] M. M. Rahman, A. Kossolapov, J. H. Seong, J. Buongiorno, and M. Bucci, "Investigation of pool boiling heat transfer and CHF enhancement on nano-engineered surfaces using advanced diagnostics," in *International Conference on Boiling and Condensation Heat Transfer*, Nagasaki, Japan, 2018.

[65] V. Trisaksri and S. Wongwises, "Nucleate pool boiling heat transfer of TiO2–R141b nanofluids," *International Journal of Heat and Mass Transfer,* vol. 52, no. 5, pp. 1582-1588, 2009.

[66] M. Ray, S. Deb, and S. Bhaumik, "Pool boiling heat transfer of refrigerant R-134a on TiO2 nano wire arrays surface," *Applied Thermal Engineering,* vol. 107, pp. 1294-1303, 2016.

[67] Y. Im, Y. Joshi, C. Dietz, and S. S. Lee, "Enhanced boiling of a dielectric liquid on copper nanowire surfaces," *International Journal of Micro-Nano Scale Transport,* vol. 1, no. 1, pp. 79-96, 2010.

[68] G. Udaya Kumar, S. Suresh, M. R. Thansekhar, and P. Dinesh Babu, "Effect of diameter of metal nanowires on pool boiling heat transfer with FC-72," *Applied Surface Science,* vol. 423, pp. 509-520, 2017.

[69] B. S. Kim, G. Choi, D. I. Shim, K. M. Kim, and H. H. Cho, "Surface roughening for hemi-wicking and its impact on convective boiling heat transfer," *International Journal of Heat and Mass Transfer,* vol. 102, pp. 1100-1107, 2016.

[70] B. Liu, Z. Cao, Y. Zhang, Z. Wu, A. Pham, W. Wang, Z. Yan, J. Wei, and B. Sundén, "Pool boiling heat transfer of n-pentane on micro/nanostructured surfaces," *International Journal of Thermal Sciences,* vol. 130, pp. 386-394, 2018.

[71] S. A. Moeykens, W. W. Huebsch, and M. B. Pate, "Heat transfer of R134a in single-tube spray evaporation including lubricant effects and enhanced surface results," in *American Society of Heating, Refrigerating and Air-Conditioning Engineers (ASHRAE) winter meeting and exhibition*, Chicago, IL (United States), 1995: American Society of Heating, Refrigerating and Air-Conditioning Engineers, Inc.,.

[72] L.-H. Chien and Y.-L. Tsai, "An experimental study of pool boiling and falling film vaporization on horizontal tubes in R245fa," *Applied Thermal Engineering,* vol. 31, no. 17–18, pp. 4044-4054, 2011.

[73] L. H. Chien and R. H. Chen, "An experimental study of falling film evaporation on horizontal tubes using R-134a," *Journal of Mechanics,* vol. 28, no. 2, pp. 319-327, 2012.

[74] L.-H. Chien, Y.-L. Tsai, and C.-H. Chang, "A study of pool boiling and falling-film vaporization with R-245fa/oil mixtures on horizontal tubes," *International Journal of Heat and Mass Transfer,* vol. 133, pp. 940-950, 2019.

[75] Y. Zheng, X. Ma, Y. Li, R. Jiang, K. Wang, Z. Lan, and Q. Liang, "Experimental study of falling film evaporation heat transfer on superhydrophilic horizontal-tubes at low spray density," *Applied Thermal Engineering,* vol. 111, pp. 1548-1556, 2017.

[76] S. A. Moeykens, "Heat transfer and fluid flow in spray evaporators with application to reducing refrigerant inventory," PhD, Iowa State University, Iowa, United States of America, 1994.

[77] M. Habert and J. R. Thome, "Falling-film evaporation on tube bundle with plain and enhanced tubes—part 1: Experimental results," *Experimental Heat Transfer,* vol. 23, no. 4, pp. 259-280, 2010.

[78] R. Mesler, "A mechanism supported by extensive experimental evidence to explain high heat fluxes observed during nucleate boiling," *AIChE Journal,* vol. 22, no. 2, pp. 246-252, 1976.

[79] K. Nishikawa, H. Kusuda, K. Yamasaki, and K. Tanaka, "Nucleate boiling at low liquid levels," *Bulletin of JSME,* vol. 10, no. 38, pp. 328-338, 1967.

[80] M. Cerza and V. Sernas, "A bubble growth model for nucleate boiling in thin, falling, superheated, laminar, water films," *International Journal of Heat and Mass Transfer,* vol. 28, no. 7, pp. 1307-1316, 1985.

[81] R. Mesler and G. Mailen, "Nucleate boiling in thin liquid films," *AIChE Journal,* vol. 23, no. 6, pp. 954-957, 1977.

[82] M. Christians and J. R. Thome, "Falling film evaporation on enhanced tubes, part 2: Prediction methods and visualization," *International Journal of Refrigeration,* vol. 35, no. 2, pp. 313-324, 2012.

[83] I. A. Mudawwar, T. A. Incropera, and F. P. Incropera, "Boiling heat transfer and critical heat flux in liquid films falling on vertically-mounted heat sources," *International Journal of Heat and Mass Transfer,* vol. 30, no. 10, pp. 2083-2095, 1987.

[84] R. P. Baines, M. A. El Masri, and W. M. Rohsenow, "Critical heat flux in flowing liquid films," *International Journal of Heat and Mass Transfer,* vol. 27, no. 9, pp. 1623-1629, 1984.

[85] T. Ueda, M. Inoue, and S. Nagatome, "Critical heat flux and droplet entrainment rate in boiling of falling liquid films," *International Journal of Heat and Mass Transfer,* vol. 24, no. 7, pp. 1257-1266, 1981.

[86] N. I. Pecherkin, A. N. Pavlenko, and O. A. Volodin, "Heat transfer and critical heat flux at evaporation and boiling in refrigerant mixture films falling down the tube with structured surfaces," *International Journal of Heat and Mass Transfer,* vol. 90, pp. 149-158, 2015.

[87] J. H. I. Lienhard and J. H. V. Lienhard, *A heat transfer textbook*, 4th ed. Cambridge, Massachusetts: Phlogiston Press, 2012.

[88] D. Hartley and W. Murgatroyd, "Criteria for the break-up of thin liquid layers flowing isothermally over solid surfaces," *International Journal of Heat and Mass Transfer,* vol. 7, no. 9, pp. 1003-1015, 1964.

[89] N. Zuber and F. W. Staub, "Stability of dry patches forming in liquid films flowing over heated surfaces," *International Journal of Heat and Mass Transfer,* vol. 9, no. 9, pp. 897-905, 1966.

[90] E. Ruckenstein, "On the break-up of thin liquid layers flowing along a surface," *International Journal of Heat and Mass Transfer,* vol. 14, no. 1, pp. 165-169, 1971.

[91] G. Ribatski and J. R. Thome, "A visual study of R134a falling film evaporation on enhanced and plain tubes," presented at the 5th International Symposium on Multiphase Flow, Heat Mass Transfer and Energy Conversion, Xi'an, China, 3-6 July, 2005, 2005. Available: http://infoscience.epfl.ch/record/52919

[92] C.-Y. Zhao, W.-T. Ji, P.-H. Jin, and W.-Q. Tao, "Cross vapor stream effect on falling film evaporation in horizontal tube bundle using R134a," *Heat Transfer Engineering,* pp. 1-14, 2017.

[93] D. Moalem Maron, G. Ingel, and N. Brauner, "Wettability and break-up of thin films on inclined surfaces with continuous and intermittent feed," *Desalination,* vol. 42, no. 1, pp. 87-96, 1982.

[94] M. Cerza, "Nucleate boiling in thin falling liquid films," in *Pool and External Flow Boiling Conference, Santa Barbara*, 1992, pp. 459-466.

[95] O. Volodin, N. Pecherkin, A. Pavlenko, and N. Zubkov, "Surface microstructures for boiling and evaporation enhancement in falling films of low-viscosity fluids," *International Journal of Heat and Mass Transfer,* vol. 155, p. 119722, 2020.

[96] B. Köroğlu, K. S. Lee, and C. Park, "Nano/micro-scale surface modifications using copper oxidation for enhancement of surface wetting and falling-film heat transfer," *International Journal of Heat and Mass Transfer,* vol. 62, pp. 794-804, 2013.

[97] S. Lee, B. Köroğlu, and C. Park, "Experimental investigation of capillary-assisted solution wetting and heat transfer using a micro-scale, porous-layer coating on horizontal-tube, falling-film heat exchanger," *International Journal of Refrigeration,* vol. 35, no. 4, pp. 1176-1187, 2012.

[98] N. Zuber, "Hydrodynamic aspects of boiling heat transfer," PhD, Univ. of California, Los Angeles, CA (United States), 1959.

[99] N. Zuber, "The hydrodynamic crisis in pool boiling of saturated and subcooled liquids," *International Developments in Heat Transfer, ASME,* vol. 27, pp. 230-236, 1961.

[100] J. H. Lienhard and V. K. Dhir, "Hydrodynamic prediction of peak pool-boiling heat fluxes from finite bodies," *Journal of Heat Transfer,* vol. 95, no. 2, pp. 152-158, 1973.

[101] J. Lienhard and V. K. Dhir, "Extended hydrodynamic theory of the peak and minimum pool boiling heat fluxes," *NASA Report CR-2270,* 1973.

[102] M. M. Rahman, E. Ölçeroğlu, and M. McCarthy, "Role of wickability on the critical heat flux of structured superhydrophilic surfaces," *Langmuir,* vol. 30, no. 37, pp. 11225-11234, 2014.

[103] H. O'Hanley, C. Coyle, J. Buongiorno, T. McKrell, L.-W. Hu, M. Rubner, and R. Cohen, "Separate effects of surface roughness, wettability, and porosity on the boiling critical heat flux," *Applied Physics Letters,* vol. 103, no. 2, p. 024102, 2013.

[104] M. Tetreault-Friend, R. Azizian, M. Bucci, T. McKrell, J. Buongiorno, M. Rubner, and R. Cohen, "Critical heat flux maxima resulting from the controlled morphology of nanoporous hydrophilic surface layers," *Applied Physics Letters,* vol. 108, no. 24, p. 243102, 2016.

[105] S. Shin, G. Choi, B. S. Kim, and H. H. Cho, "Flow boiling heat transfer on nanowire-coated surfaces with highly wetting liquid," *Energy,* vol. 76, pp. 428-435, 2014.

[106] T. A. Grimley, I. Mudawwar, and F. P. Incropera, "CHF enhancement in flowing fluorocarbon liquid films using structured surfaces and flow deflectors," *International Journal of Heat and Mass Transfer,* vol. 31, no. 1, pp. 55-65, 1988.

[107] D. Gstoehl, "Heat transfer and flow visualization of falling film condensation on tube arrays with plain and enhanced surfaces," PhD, École Polytechnique Fédérale de Lausanne, Lausanne, Switzerland, 2004.

[108] J.-F. Roques, "Falling film evaporation on a single tube and on a tube bundle," PhD, École Polytechnique Fédérale de Lausanne, Lausanne, Switzerland, 2004.

[109] M. Habert, "Falling film evaporation on a tube bundle with plain and enhanced tubes," PhD, École Polytechnique Fédérale de Lausanne, Lausanne, Switzerland, 2009.

[110] M. Christians, "Heat transfer and visualization of falling film evaporation on a tube bundle," Ph.D., École Polytechnique Fédérale de Lausanne, Lausanne, Switzerland, 2010.

[111] E. W. Lemmon, M. L. Huber, and M. O. McLinden, "NIST reference fluid thermodynamic and transport properties—REFPROP," *NIST Standard Reference Database,* vol. 23, p. v7, 2002.

[112] C. D. A. Inc. (2018, 28 August 2018). *Copper developement association : C12200.* Available: https://alloys.copper.org/alloy/C12200

[113] AZO. (2001, 28 Aug 2018). *Stainless steel - Grade 304 (UNS S30400).* Available: https://www.azom.com/article.aspx?ArticleID=965

[114] E. P. R. Institute, "Carbon steel handbook," Palo Alto, California, 2007.

[115] Mitutoyo, "Quick guide to surface roughness measurement," Mitutoyo America CorporationBulletin No. 2229, 2016.

[116] F. Ç. Cebeci, Z. Wu, L. Zhai, R. E. Cohen, and M. F. Rubner, "Nanoporosity-driven superhydrophilicity: A means to create multifunctional antifogging coatings," *Langmuir,* vol. 22, no. 6, pp. 2856-2862, 2006.

[117] Y. Nam and Y. S. Ju, "A comparative study of the morphology and wetting characteristics of micro/nanostructured Cu surfaces for phase change heat transfer applications," *Journal of Adhesion Science and Technology,* vol. 27, no. 20, pp. 2163-2176, 2013.

[118] A. Materials. (2020, 20 01 2021). *Silica - Silicon Dioxide (SiO2).* Available: https://www.azom.com/properties.aspx?ArticleID=1114

[119] M. Liu, M. C. Lin, and C. Wang, "Enhancements of thermal conductivities with Cu, CuO, and carbon nanotube nanofluids and application of MWNT/water nanofluid on a water chiller system," *Nanoscale Research Letters,* vol. 6, no. 1, p. 297, 2011.

[120] J. Drelich, E. Chibowski, D. D. Meng, and K. Terpilowski, "Hydrophilic and superhydrophilic surfaces and materials," *Soft Matter,* 10.1039/C1SM05849E vol. 7, no. 21, pp. 9804-9828, 2011.

[121] X. Yan, Z. Huang, S. Sett, J. Oh, H. Cha, L. Li, L. Feng, Y. Wu, C. Zhao, D. Orejon, F. Chen, and N. Miljkovic, "Atmosphere-mediated superhydrophobicity of rationally designed micro/nanostructured surfaces," *ACS Nano,* vol. 13, no. 4, pp. 4160-4173, 2019.

[122] A. F. Stalder, T. Melchior, M. Müller, D. Sage, T. Blu, and M. Unser, "Low-bond axisymmetric drop shape analysis for surface tension and contact angle measurements of sessile drops," *Colloids and Surfaces A: Physicochemical and Engineering Aspects,* vol. 364, no. 1, pp. 72-81, 2010.

[123] W. S. Rasband, "ImageJ," ed: Bethesda, MD, 1997.

[124] R. N. Wenzel, "Resistance of solid surfaces to wetting by water," *Industrial & Engineering Chemistry,* vol. 28, no. 8, pp. 988-994, 1936.

[125] A. B. D. Cassie and S. Baxter, "Wettability of porous surfaces," *Transactions of the Faraday Society,* 10.1039/TF9444000546 vol. 40, pp. 546-551, 1944.

[126] E. Van Rooyen, M. Christians, and J. R. Thome, "Modified Wilson plots for enhanced heat transfer experiments: Current status and future perspectives," *Heat Transfer Engineering,* vol. 33, no. 4-5, pp. 342-355, 2012.

[127] V. Gnielinski, "New equations for heat and mass-transfer in turbulent pipe and channel flow," *International Chemical Engineering,* vol. 16, no. 2, pp. 359-368, 1976.

[128] P. F. Dunn, *Measurement and data analysis for engineering and science*, 2nd ed. CRC press, 2010.

[129] I. BIPM, I. IFCC, I. ISO, and O. IUPAP, "Evaluation of measurement data—guide to the expression of uncertainty in measurement, JCGM 100: 2008 GUM 1995 with minor corrections.," *Joint Committee for Guides in Metrology,* 2008.

[130] F. Agostini, "Boiling on a tube bundle: Heat transfer, pressure drop and flow patterns," PhD, École Polytechnique Fédérale de Lausanne, 2008.

[131] D. Gstoehl and J. R. Thome, "Film condensation of R134a on tube arrays with plain and enhanced surfaces: Part 1— Experimental heat transfer coefficients," *Journal of Heat Transfer,* vol. 128, no. 1, pp. 21-32, 2006.

[132] G. Ribatski and J. R. Thome, "Experimental study on the onset of local dryout in an evaporating falling film on horizontal plain tubes," *Experimental Thermal and Fluid Science,* vol. 31, no. 6, pp. 483-493, 2007.

[133] K. Stephan, "Beitrag zur thermodynamik des wärmeüberganges beim sieden," PhD, Verlag nicht ermittelbar, 1963.

[134] R. Mesler, "Research on nucleate boiling," *Chemical Engineering Education,* vol. 16, no. 4, pp. 152-156, 1982.

[135] S. Ge, Y. Gu, and M. Chen, "A molecular dynamics simulation on the convective heat transfer in nanochannels," *Molecular Physics,* vol. 113, no. 7, pp. 703-710, 2015.

[136] W. A. Khan and M. M. Yovanovich, "Analytical modeling of fluid flow and heat transfer in microchannel/nanochannel heat sinks," *Journal of Thermophysics and Heat Transfer,* vol. 22, no. 3, pp. 352-359, 2008.

[137] E. W. Washburn, "The dynamics of capillary flow," *Physical Review,* vol. 17, no. 3, pp. 273-283, 1921.

[138] M.-C. Chyu and A. Bergles, "Horizontal-tube falling-film evaporation with structured surfaces," *Journal of Heat Transfer,* vol. 111, no. 2, pp. 518-524, 1989.

[139] M. C. Chyu, J. Zheng, and Z. Ayub, "Bundle effect of ammonia/lubricant mixture boiling on a horizontal bundle with enhanced tubing and inlet quality," *International Journal of Refrigeration,* vol. 32, no. 8, pp. 1876-1885, 2009.

Appendices

A. Calibration

A.1 Introduction

This chapter details the methodology behind the calibration of the sensors, as well further information on the sensors themselves used in this study.

A.2 Calibration approach

The sensors were calibrated internally by comparing the reference sensor measurements, R_{ref}, against the uncalibrated sensor measurements, R_{sensor}, and calculating the linear regression gradient, a, and intercept, c.

$$R_{ref} = aR_{sensor} + c \tag{A-1}$$

These coefficients were then used to correct the sensor readings to determine the calibrated sensor readings, R_{cal}, by

$$R_{cal} = aR_{sensor} + c \tag{A-2}$$

A.3 Thermocouple calibration

All thermocouples used were Type K and were in stainless steel sheaths. Thermocouples were calibrated by comparison to a Lauda DigiCal DCS 2 digital thermometer with a platinum resistance thermometer (Type PT 100) reference probe with a manufacturer calibrated uncertainty of 0.03°C. Thermocouples were divided into two groups, namely the general use thermocouples placed throughout the experimental rig and the temperature probe thermocouples used to measure the water temperature profile within the tube tested and these two groups were calibrated separately.

The general use thermocouples were calibrated with the thermocouples removed from the rig but still connected to the NI measuring system and placed within a Lauda Proline Thermal bath together with the PT 100 reference probe. The thermal bath temperature was ramped up and down over a range of 5 to 55°C to cover the range of temperatures seen in service.

The water probe thermocouples were placed within their own calibration rig as illustrated in **Figure A-1** and water was circulated from a thermal bath to the calibration rig. Two reference probes were placed on the inlet and outlet of the system.

Once a temperature difference of less than 0.1°C was recorded between the two reference probes a further 45 minute stabilisation time was given before readings were taken at each temperature set point. It was noted that with this stabilisation time no hysteresis was visible with errors being independent of direction of approach and random in nature. The temperature was ramped from 3°C to 33°C and back down again. This was repeated once a year and the calibration coefficients changed insignificantly.

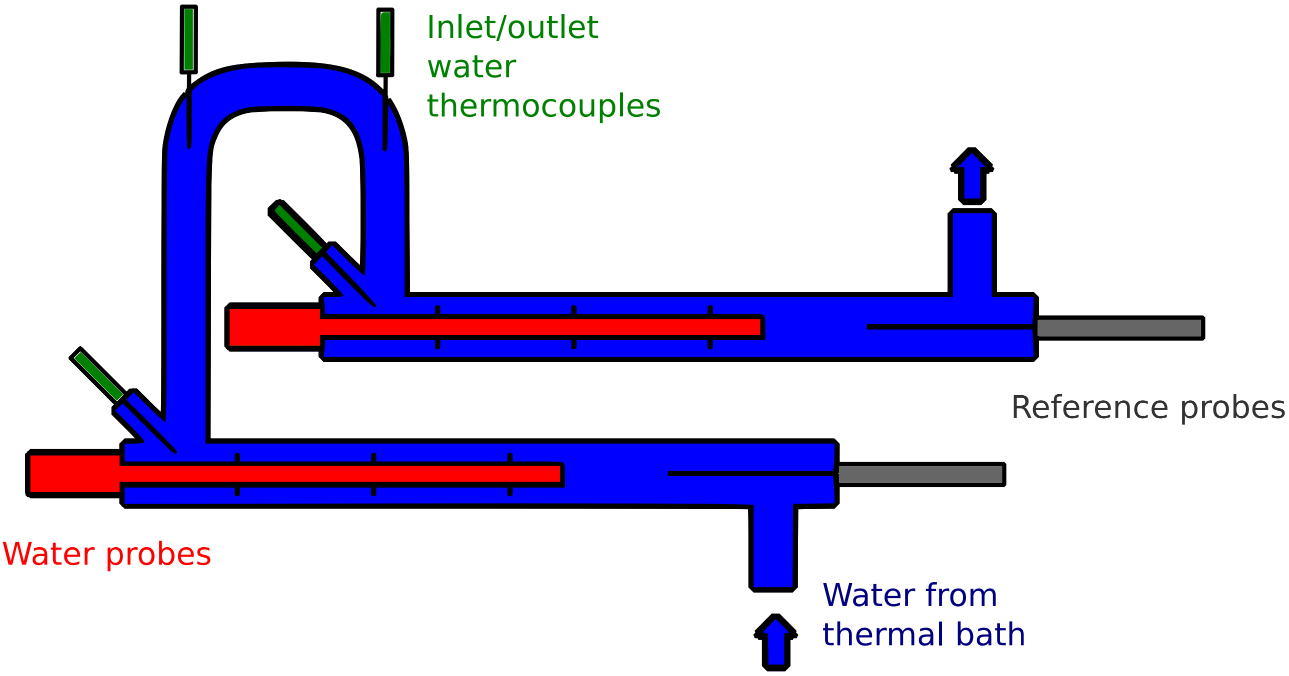

Figure A-1. Schematic of thermocouple calibration rig.

A.4 Pressure transducer calibration

Two classes of pressure transducer were used on the rig. Throughout the rig Haenni type ED 510 pressure transducers were used with an originally quoted full scale error of 0.4%. The readings of these pressure transducers were not used for any measured quantities but only for control. The test chamber used Endress+Hauser PMC 731 pressure transducers with an originally quoted full scale error of 0.1% and a range of 0 to 10 bar (abs). These transducers measured the saturation pressure which was used to determine the measured saturation temperature.

The transducers where calibrated using Wika's CPH 6400 hand held pressure indicator with a CPT 6400 pressure transducer which has a 0.025% full scale uncertainty with an assumed 95% confidence interval. Its full operating a range was 0 - 10 bar (abs), which results thus in a 0.25 kPa uncertainty. Air was the medium used for calibration, with the pressure generated by Wika's pneumatic CPP 30 hand pump.

In a manner similar to the thermocouple calibration, the transducers were calibrated by ramping pressure up and then down over the transducers' operating range, typically 1 to 10 bar absolute.

A.5 Mass flow meters

The mass flow meters used were Krohne Corimass MFM 4085 G+ mass flow meters, which make use of the Coriolis Effect to measure the mass flow. The lower flow rate of the refrigerant was measured using the 10 G model, while the higher flow of the water and glycol systems made use of the 100 G model. The refrigerant flow meter had its range set from 0 to 0.22 kg/s, while the water and glycol flow meters had their range set from 0 to 1.6 kg/s.

The flow meters were factory calibrated. To account for any noise introduced by the NI DAQ system used, the flow meter readings measured by the DAQ and displayed in the NI LabVIEW software were compared against the calibrated output of the flow meter's display unit and corrected with a calibration curve such that the values of the LabVIEW and display units of the mass flow meters were the same.

A.6 Summary and conclusions

The temperature and pressure sensors were calibrated over a range of values suitable to their service and calibration coefficients generated for each, while the mass flow meters were factory calibrated and integrated within the LabVIEW system through a calibration process of the signal transfer system.

A.7 Nomenclature

a	Linear regression gradient
c	Linear regression intercept
R	Measurement reading

Subscripts

cal	Calibrated sensor
ref	Reference sensor
sensor	Uncalibrated sensor

A.8 List of Acronyms

DAQ	Data acquisition system
NI	National Instruments

B. Uncertainty

B.1 Introduction

This chapter details the derivation and calculation of the uncertainties of the probe measurements as well as the uncertainties of the final calculated quantities used in this study.

B.2 Propagation of uncertainty

The uncertainty of calculated quantities, Δy, was determined by combining the uncertainties of input quantities, Δx, through the "Law of Propagation of Uncertainty" as described in JCGM 100:2008 [129] as follows

$$\Delta y^2 = \sum_{i=1}^{N} \left(\frac{\partial y}{\partial x_i} \right)^2 \Delta x_i{}^2 \qquad \text{B-1}$$

in cases where the input quantities were assumed to be independent. This applied to the majority of calculated quantities in this study and those that were assumed to not be independent are dealt with individually.

B.3 Calculation of standard uncertainties of sensors

The uncertainty of factory calibrated or externally calibrated sensors, such as the mass flow meters, was given by the calibration certificates.

The uncertainties of the various sensors that were calibrated internally as part of this study, such as thermocouples and pressure sensors, were calculated as per the methodology employed by Dunn [128], where the standard uncertainty, Δ_s, of the various sensors was given by

$$\Delta_s = \sqrt{\Delta_P{}^2 + \Delta_B{}^2} \qquad \text{B-2}$$

where Δ_B is the uncertainty due to bias and Δ_P is the uncertainty due to precision.

The bias, Δ_B, results from systematic influences that can be, through careful assumption, quantified to some extent and accounted for through offsets of some sort, such as the error of the reference probe used [128]. The bias was assumed to be equal to the uncertainty of the reference probes used in the calibration already discussed.

The precision, Δ_P, accounts for random uncontrollable influences on the measurements [128]. The precision was assumed to be equal to the error introduced by the linear regression fit of the calibration curve, Δ_{cal}, so as to account for noise measured on the sensors and the error of the linear regression itself.

B.4 Calibration uncertainty

The standard error of forecast [128] was used to estimate the uncertainty that the linear regression introduces to the calibrated output, Δ_{cal}, through the calibration equation $R_{cal} = aR_{sensor} + c$. The standard error of forecast determines the error of a linear regression of a set of data points (X, Y), which in this case were the original data points from the calibration process that produced $R_{ref} = aR_{sensor} + c$. However, the standard error of forecast assumes no error in the X variable. The calibration data points were thus reversed such that the X variable was the reference sensor measurements, R_{ref}, which can be assumed to have zero error as the bias was used to capture the uncertainty of the reference sensor, and the Y variable was the sensor measurement, R_{sensor}, such that

$$R_{sensor} = \frac{1}{a}R_{ref} + \frac{c}{a} \tag{B-3}$$

The standard error of forecast was then used to estimate the uncertainty that the linear regression in Equation **B-3** introduces through

$$\Delta_{sensor}(x) = S_{yx}\sqrt{\frac{1}{M} + \frac{1}{n'} + \frac{(x - \bar{X})^2}{S_{xx}}} \tag{B-4}$$

where $\Delta_{sensor}(x)$ is the uncertainty of the sensor due to the linear regression, $\bar{X}$ is the average of the X values of the dataset, M is the number of data observations per data point, n' is the number of data replications per data point and S_{yx} and S_{xx} are given by

$$S_{yx} = \sqrt{\frac{\sum_{i=1}^{n}\left(Y_i - y(X_i)\right)^2}{\{n - 2\}}} \tag{B-5}$$

and

$$S_{xx} = \sum_{i=1}^{n} (X_i - \bar{X})^2 \qquad \text{B-6}$$

where n is the total number of data points and $y(X_i)$ is the output of the linear regression shown in Equation **B-3** at the point X_i.

The final uncertainty of the calibrated sensor readings, Δ_{cal}, as a result of the linear regression was propagated back from the uncertainty of the sensor, Δ_{sensor}, using the law of propagation of uncertainty as follows

$$\Delta_{cal} = \frac{\Delta_{sensor}}{a} \qquad \text{B-7}$$

The precision, Δ_{P}, was then assumed to be equal to this uncertainty of the calibrated sensor reading, Δ_{cal}.

B.5 Coverage factor

The standard uncertainties discussed up until now have a confidence interval of 68% and an assumed normal Gaussian probability distribution. As the dataset used was for a finite number of samples, the student's t-distribution must be used to account that a finite sample size was used [128]. A typical standard confidence level used in industry for uncertainty is 95% and was thus adopted in this study.

The expanded uncertainty of each sensor, Δ_{e}, was calculated by multiplying the precision, Δ_{P}, by a coverage factor k_t given by the student's t-distribution to give a 95% confidence interval [128]. The bias, Δ_{B}, was provided from the manufacturer's calibration of the reference sensors and already had a 95% confidence interval applied and so no coverage factor was applied to it. Thus the standard uncertainty, Δ_{s}, was modified to give the expanded uncertainty as follows:

$$\Delta_e = \sqrt{(k_t \times \Delta_P)^2 + \Delta_B^2} \qquad \text{B-8}$$

B.6 Results of expanded uncertainty of sensors

The calculated calibrated thermocouple expanded uncertainty ranged from a maximum of 0.064°C to a minimum of 0.059°C over the temperature range of calibration. The conservative estimate of 0.1°C was thus used as the thermocouple uncertainty.

The expanded uncertainty of the calibrated test chamber pressure transducers was calculated to be less than the original manufacturer's quoted uncertainty of 0.1% of full range and similarly the uncertainty of the other pressure transducers used through the rig was found to be less than the original manufacturer's quoted uncertainty of 0.4% of full range.

The uncertainty was however conservatively assumed to be equal to the original manufacturers quoted uncertainty, namely 0.1% for the high accuracy test chamber transducers and 0.4% for the remaining pressure transducers.

The Coriolis mass flow meters' uncertainty, $\Delta\dot{m}$, was quoted by the manufactures [140] as:

$$\Delta\dot{m} = 0.0015\left(\dot{m} + \frac{A}{\dot{m}}\right) \quad \text{B-9}$$

where A is $8.\dot{3}\times 10^{-4}$ for the 10 G model used for the liquid refrigerant film flow rate measurement and $8.\dot{3}\times 10^{-3}$ for the 100 G model used for the remaining flow measurements [140].

After calibration the mass flow measured off the calibrated display units of the mass flow meters was the same as that recorded by LabVIEW and thus Equation **B-9** was used as the mass flow meters' uncertainty.

The average expanded uncertainty of the refrigerant and water/glycol flow meters over the conditions tested was 0.54% and 0.19%. A summary of the final sensor uncertainties used are in **Table B-1.**

Table B-1. Expanded sensor uncertainties.

Sensor	**Symbol**	**Uncertainty**
Temperature	ΔT	0.1°C
Pressure	ΔP	1 kPa
Refrigerant mass flow rate	$\Delta\dot{m}_r$	0.54%
Heating water mass flow rate	$\Delta\dot{m}_w$	0.19%

B.7 Estimation of uncertainty of other quantities

The uncertainties of a number of miscellaneous quantities are detailed in **Table B-2**.

Table B-2. Miscellaneous uncertainties.

Quantity	**Symbol**	**Uncertainty**
Length of tube	ΔL	1.11 mm
Diameter of tube (inside and outside)	ΔD	0.011 mm
Thermal conductivity of tube wall	Δk_{wall}	0.01%
Surface roughness	ΔR_a	0.17 µm

These uncertainties were estimated in the following manner:

B.7.1 Length of tube

A tape measure was used to measure the tube length. The smallest increment 0.5 mm was assumed as the precision and 1 mm was assumed as the bias.

B.7.2 Diameters of tube

Micrometers were used to measure the inside and outside diameters of tubes, with precision estimated as the smallest increment of 0.005 mm and the bias estimated as 0.01 mm.

B.7.3 Thermal conductivity of tube

The thermal conductivity was obtained from data sheets provided by the tube manufacturers which contained no mention of uncertainties. As such, a study by Abu-Eishah [141] was used to estimate the uncertainty, as Abu-Eishah conducted a detailed analysis of the uncertainty of a number of metals, copper included. Those calculated uncertainties were assumed for this study.

B.7.4 Roughness

The uncertainty of the roughness measurements was estimated through a Type A evaluation and an assumed normal distribution of roughnesses about the mean value measured (as per JCGM 100:2008 [129]) with a confidence interval of 95% employed as no uncertainty of the profilometer used was available. The standard uncertainties of the roughness measurements of the various surfaces had a coverage factor applied to determine the expanded uncertainties.

The individual roughness uncertainties are illustrated in **Figure B-1** with the overall average roughness uncertainty found to be 0.17 µm.

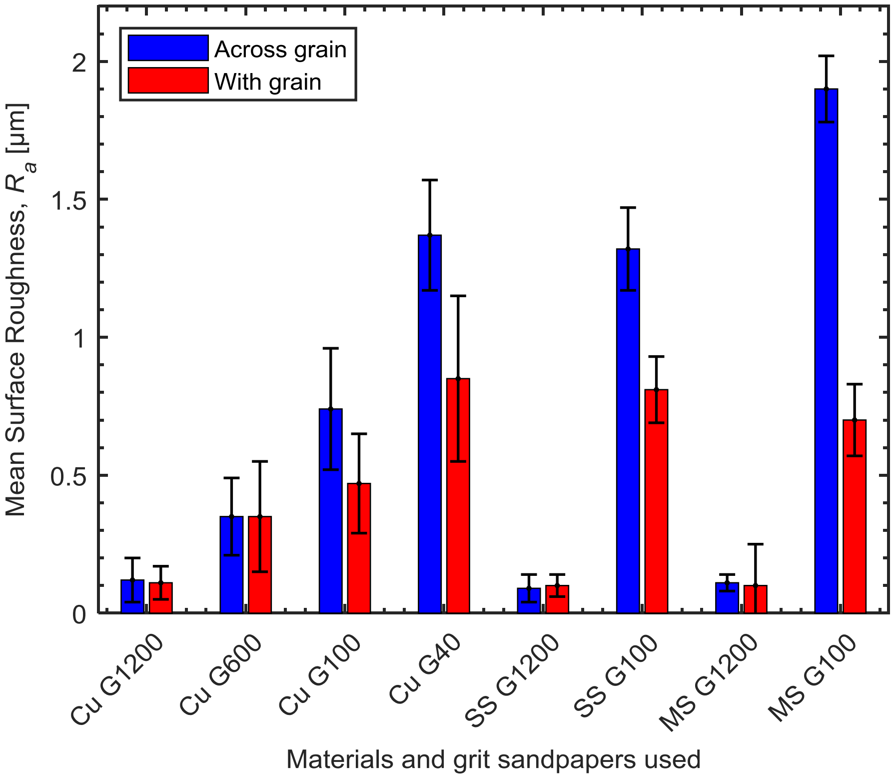

Figure B-1. Mean surface roughnesses across and with the roughness grain of various tubes tested.

Figure B-1 illustrated that the absolute magnitude of the roughness uncertainties increased as the roughness increased and that the differences in roughness between samples of a particular material were significant when compared to the uncertainties, suggesting a sufficiently spread sample of roughnesses has been chosen.

All thermo-physical properties were determined with the aid of the National Institute of Standards and Technology's REFPROP software [111]. The uncertainties of the various properties were based on investigation by Christians [110], who compiled these uncertainties by contacting the National Institute of Standards and Technology directly and consulting REFPROP's documentation. The uncertainties of the various thermo-physical properties are listed in **Table B-3**.

Table B-3. REFPROP estimated uncertainties.

Refrigerant property uncertainty		**Water property uncertainty**	
Property	**Uncertainty**	**Property**	**Uncertainty**
Enthalpy	0.5%	Enthalpy	0.05%
Thermal conductivity	3.9%	Thermal conductivity	1.8%
Dynamic viscosity	1.09%	Dynamic viscosity	1%
Density	0.1%	Density	0.001%
Surface tension	0.5%	Surface tension	0.1%
Specific heat	1%	Specific heat	0.1%

B.8 Calculation of uncertainties for quantities with uncorrelated inputs

The expanded uncertainties of the various calculated quantities where the inputs were assumed uncorrelated were calculated with the "Law of Propagation of Uncertainty", given in Equation **B-1**.

B.8.1 Mass flow rate per unit length

The mass flow rate per unit length of refrigerant, $\mathit{\Gamma}_r$, was given by

$$\mathit{\Gamma}_r = \frac{\dot{m}_r}{2L} \tag{B-10}$$

and thus the uncertainty was calculated as

$$\Delta \mathit{\Gamma}_r^2 = \frac{1}{4L^2}\Delta\dot{m}_r^2 + \frac{\dot{m}_r^2}{4L^4}\Delta L^2 \tag{B-11}$$

B.8.2 External heat transfer coefficient

The local external HTC was given by

$$h_o = \left(\frac{1}{U_o} - R_{wall} - \frac{1}{h_i}\frac{D_o}{D_i}\right)^{-1} \tag{B-12}$$

and as such the uncertainty was calculated as

$$\Delta h_o^2 = \left(\frac{\partial h_o}{\partial U_o}\Delta U_o\right)^2 + \left(\frac{\partial h_o}{\partial R_{wall}}\Delta R_{wall}\right)^2 + \left(\frac{\partial h_o}{\partial h_i}\Delta h_i\right)^2 + \left(\frac{\partial h_o}{\partial D_i}\Delta D_i\right)^2 + \left(\frac{\partial h_o}{\partial D_o}\Delta D_o\right)^2 \tag{B-13}$$

where the partial derivatives of the various components were

$$\frac{\partial h_o}{\partial U_o} = \frac{1}{\left(\frac{1}{U_o} - R_{wall} - \frac{1}{h_i}\frac{D_o}{D_i}\right)^2 {U_o}^2} \tag{B-14}$$

$$\frac{\partial h_o}{\partial R_w} = \frac{1}{\left(\frac{1}{U_o} - R_{wall} - \frac{1}{h_i}\frac{D_o}{D_i}\right)^2} \tag{B-15}$$

$$\frac{\partial h_o}{\partial h_i} = \frac{-\frac{D_o}{D_i}}{\left(\frac{1}{U_o} - R_{wall} - \frac{1}{h_i}\frac{D_o}{D_i}\right)^2 {h_i}^2} \tag{B-16}$$

$$\frac{\partial h_o}{\partial D_o} = \frac{1}{\left(\frac{1}{U_o} - R_{wall} - \frac{1}{h_i}\frac{D_o}{D_i}\right)^2 h_i D_i} \tag{B-17}$$

$$\frac{\partial h_o}{\partial D_i} = \frac{-D_o}{\left(\frac{1}{U_o} - R_{wall} - \frac{1}{h_i}\frac{D_o}{D_i}\right)^2 h_i D_i^2} \tag{B-18}$$

B.8.3 Local heat flux

The local heat flux was calculated based on the gradient of the 2nd order polynomial fit of the temperature profile along the tube. Due to difficulty in calculating the uncertainties of this method directly, the uncertainty of the overall heat flux is calculated. The overall heat flux is given by Equation **B-19** and was shown by Gstoehl [107] to be equivalent to the average of the local heat fluxes along the length of the tube.

$$q_o = \frac{\dot{m}_w c_p}{\pi D_o} \frac{T_o - T_i}{L} \tag{B-19}$$

The subsequent uncertainty of the heat flux was thus given by

$$\Delta q_o^2 = \left(\frac{\partial q_o}{\partial \dot{m}_{wat}} \Delta \dot{m}_w\right)^2 + \left(\frac{\partial q_o}{\partial c_p} \Delta c_p\right)^2 + \left(\frac{\partial q_o}{\partial T_o} \Delta T_o\right)^2 + \left(\frac{\partial q_o}{\partial T_i} \Delta T_i\right)^2 + \left(\frac{\partial q_o}{\partial D_o} \Delta D_o\right)^2 + \left(\frac{\partial q_o}{\partial L} \Delta L\right)^2 \tag{B-20}$$

The partial derivatives were given by

$$\frac{\partial q_o}{\partial \dot{m}_{wat}} = \frac{c_p (T_o - T_i)}{\pi D_o L} \tag{B-21}$$

$$\frac{\partial q_o}{\partial c_p} = \frac{\dot{m}_w (T_o - T_i)}{\pi D_o L} \tag{B-22}$$

$$\frac{\partial q_o}{\partial T_o} = \frac{c_p \dot{m}_w}{\pi D_{oL}} \tag{B-23}$$

$$\frac{\partial q_o}{\partial T_i} = -\frac{c_p \dot{m}_w}{\pi D_{oL}} \tag{B-24}$$

$$\frac{\partial q_o}{\partial D_o} = \frac{-c_p \dot{m}_w (T_o - T_i)}{\pi D_o^2 L} \tag{B-25}$$

$$\frac{\partial q_o}{\partial L} = \frac{-c_p \dot{m}_w (T_o - T_i)}{\pi D_o L^2} \tag{B-26}$$

B.8.4 Internal heat transfer coefficient

The internal HTC was calculated using the Gnielinski correlation [127] modified by the coefficient C_i which is determined through a Wilson plot.

$$h_i = C_i \frac{(f/8)(Re_w - 1000)Pr_w}{1 + 12.7(f/8)^{0.5}\left({Pr_w}^{2/3} - 1\right)}\left(\frac{k_w}{D_h}\right) \qquad \text{B-27}$$

The uncertainty of the internal HTC is thus calculated as

$$\Delta h_i^2 = \left(\frac{\partial h_i}{\partial C_i}\Delta C_i\right)^2 + \left(\frac{\partial h_i}{\partial f}\Delta f\right)^2 + \left(\frac{\partial h_i}{\partial Re_w}\Delta Re_w\right)^2 + \left(\frac{\partial h_i}{\partial Pr_w}\Delta Pr_w\right)^2 + \left(\frac{\partial h_i}{\partial k_w}\Delta k_w\right)^2 + \left(\frac{\partial h_i}{\partial D_h}\Delta D_h\right)^2 \qquad \text{B-28}$$

The partial derivatives of the various components were

$$\frac{\partial h_i}{\partial C_i} = \frac{(f/8)(Re_w - 1000)Pr_w}{1 + 12.7(f/8)^{0.5}\left({Pr_w}^{2/3} - 1\right)}\left(\frac{k_w}{D_h}\right) \qquad \text{B-29}$$

$$\frac{\partial h_i}{\partial f} = C_i \frac{(1/8)(Re_w - 1000)Pr_w}{1 + 12.7(f/8)^{0.5}\left({Pr_w}^{2/3} - 1\right)}\left(\frac{k_i}{D_h}\right) - \frac{12.7}{2} C_i \frac{(f/8)(Re_w - 1000)Pr_w}{\left(1 + 12.7(f/8)^{0.5}\left({Pr_w}^{2/3} - 1\right)^2\right)}\left(\frac{k_w}{D_h}\right) \qquad \text{B-30}$$

$$\frac{\partial h_i}{\partial Pr} = C_i \frac{(f/8)(Re_w - 1000)}{1 + 12.7(f/8)^{0.5}\left({Pr_w}^{2/3} - 1\right)}\left(\frac{k_w}{D_h}\right) - \frac{25.4}{3} C_i \frac{(f/8)^{\frac{3}{2}}(Re_w - 1000){Pr_w}^{-1/3}}{\left(1 + 12.7(f/8)^{0.5}\left({Pr_w}^{2/3} - 1\right)^2\right)}\left(\frac{k_w}{D_h}\right) \qquad \text{B-31}$$

$$\frac{\partial h_i}{\partial Re_w} = C_i \frac{(f/8)Pr_w}{1 + 12.7(f/8)^{0.5}\left({Pr_w}^{2/3} - 1\right)}\left(\frac{k_w}{D_h}\right) \qquad \text{B-32}$$

$$\frac{\partial h_i}{\partial k_w} = C_i \frac{(f/8)(Re_w - 1000)Pr_w}{1 + 12.7(f/8)^{0.5}\left({Pr_w}^{2/3} - 1\right)}\left(\frac{1}{D_h}\right) \qquad \text{B-33}$$

$$\frac{\partial h_i}{\partial D_h} = C_i \frac{(f/8)(Re_w - 1000)Pr_w}{1 + 12.7(f/8)^{0.5}\left({Pr_w}^{2/3} - 1\right)}\left(\frac{-k}{{D_h}^2}\right) \qquad \text{B-34}$$

B.9 Calculation of uncertainties for quantities with correlated inputs

The ratios of HTCs used in this study, such as the falling film heat transfer enhancement ratio, K_{ff}, and the surface enhancement ratio, K_{surf}, consist of the ratio of correlated inputs with the same inherent uncertainties, namely the ratios of HTCs measured in this study. Thus the "Law of Propagation of Uncertainty" for correlated inputs must be used to determine the uncertainty of these quantities, which is given by JCGM 100:2008 [129] as

$$\Delta y^2 = \sum_{i=1}^{N}\left(\frac{\partial y}{\partial x_i}\right)^2 \Delta {x_i}^2 + 2\sum_{i=1}^{N-1}\sum_{j=i+1}^{N}\left(\frac{\partial y}{\partial x_i}\right)\left(\frac{\partial y}{\partial x_j}\right)\Delta x_i\,\Delta x_j\, r(x_i, x_j) \qquad \text{B-35}$$

where $r(x_i,x_j)$ is the estimated correlation coefficient.

These ratios can be generically described by $K = h_{num}/h_{den}$. The uncertainty of the numerator, Δh_{num}, and denominator, Δh_{den}, of the ratio can be approximated to be equal as they are both of HTCs measured on the same apparatus with the same sensors under the same refrigerant conditions. This allowed the uncertainty of the HTC ratios K to be reduced to the following [142].

$$\Delta K^2 = \frac{\Delta h^2}{h^2}(1 - K)^2 K^2 \qquad \text{B-36}$$

For example the resulting uncertainty of the falling film heat transfer enhancement ratio, K_{ff} was given by

$$\Delta {K_{ff}}^2 = \left(\frac{\Delta h_{ff}}{h_{ff}}\right)^2 \left(1 - K_{ff}\right)^2 {K_{ff}}^2 \qquad \text{B-37}$$

B.10 Summary and conclusions

The expanded standard uncertainties of the various sensors was determined with the bias assumed to be equal to the uncertainty of the reference probes used and the precision assumed to be equal to the uncertainty introduced by the calibration process and the calibration linear regression fit. The resulting uncertainty of the temperature probes within the heating water was 0.1 K, the saturation pressure sensors was 1 kPa and the refrigerant mass flow rate was 0.5%. The combined standard uncertainties of the various calculated quantities were derived through the law of propagation of uncertainty.

B.11 Nomenclature

A	Mass flow meter uncertainty coefficient
a	Gradient of linear fit
c	Y-intercept of linear fit
C	Wilson plot modifier coefficient
c_p	Specific heat capacity
D	Diameter
f	Friction factor
h	Heat transfer coefficient
K	Heat transfer enhancement ratio
k_t	Coverage factor of t-student distribution
k	Thermal conductivity
L	Length of tube
M	Number of data observations
$\dot{m}$	Mass flow rate
n'	Number of data replications per data point
n	Total number of data points
P	Pressure
Pr_w	Prandtl number of heating water
q	Heat flux
R_a	Arithmetic mean roughness
R	Measurement probe reading
R_{wall}	Thermal resistance of tube wall
Re_w	Reynolds number of heating water
$r(x_i,x_j)$	Estimated correlation coefficient
S_{xx}	Sum of the squares of x
S_{yx}	Standard error of best fit
T	Temperature
U	Overall heat transfer coefficient
X	Set of input data points

x	Input
Y	Set of output data points
y	Output

Greek symbols

Δ	Uncertainty
Γ	Film mass flow rate per unit length

Subscripts

b	Bias
cal	Calibrated reading
den	Denominator
e	Expanded
ff	Falling film
h	Hydraulic
i	Inner
num	Numerator
o	Outer
p	Precision
r	Refrigerant
ref	Reference probe reading
s	standard
sensor	Measuring sensor reading
w	Water
wall	Tube wall

B.12 List of Acronyms

HTC	Heat transfer coefficient
NI	National Instruments

B.13 References

[107] D. Gstoehl, "Heat transfer and flow visualization of falling film condensation on tube arrays with plain and enhanced surfaces," PhD, École Polytechnique Fédérale de Lausanne, Lausanne, Switzerland, 2004.

[110] M. Christians, "Heat transfer and visualization of falling film evaporation on a tube bundle," Ph.D., École Polytechnique Fédérale de Lausanne, Lausanne, Switzerland, 2010.

[111] E. W. Lemmon, M. L. Huber, and M. O. McLinden, "NIST reference fluid thermodynamic and transport properties—REFPROP," *NIST Standard Reference Database,* vol. 23, p. v7, 2002.

[127] V. Gnielinski, "New equations for heat and mass-transfer in turbulent pipe and channel flow," *International Chemical Engineering,* vol. 16, no. 2, pp. 359-368, 1976.

[128] P. F. Dunn, *Measurement and data analysis for engineering and science*, 2nd ed. CRC press, 2010.

[129] I. BIPM, I. IFCC, I. ISO, and O. IUPAP, "Evaluation of measurement data—guide to the expression of uncertainty in measurement, JCGM 100: 2008 GUM 1995 with minor corrections.," *Joint Committee for Guides in Metrology,* 2008.

[140] Krohne, "Corimass G+ class," 1998, Available: cdn.krohne.com/dlc/MA_CORIMASS_G_e_72.pdf.

[141] S. Abu-Eishah, "Correlations for the thermal conductivity of metals as a function of temperature," *International Journal of Thermophysics,* vol. 22, no. 6, pp. 1855-1868, 2001.

[142] D. B. Hibbert, "The measurement uncertainty of ratios which share uncertainty components in numerator and denominator," *Accreditation and Quality Assurance,* vol. 8, no. 5, pp. 195-199, 2003.

C. Wilson plot

C.1 Introduction

The Wilson plot method is used to indirectly determine heat transfer coefficients (HTCs) in scenarios where direct measurement of wall temperatures is not feasible. The measurement of HTCs on the outside of tubes under boiling conditions suffers from this challenge, as physical sensors such as thermocouples cannot be placed on the outside surface as this would interfere with the very boiling process being characterized, and proves impractical to measure on the inside surface, as the long tubes make probe attachment difficult.

The Wilson plot method has thus been employed in this study to determine the internal and external HTCs of the tubes. As the external HTC is under investigation in this study, the Wilson plot method was conducted in a manner so as to characterise the internal HTC under all conditions it would experience over the course of the experimental program. The characterized internal HTC was then used for subsequent studies to calculate the outside HTCs.

C.2 Theoretical implementation

Initially described by Wilson [143], the methodology employed in this study to characterise the internal HTC follows that of Briggs and Young [144] as modified by Van Rooyen, Christians and Thome [126].

The heat transfer between the fluids inside and outside a tube is governed by the thermal resistance network of the inside surface, tube wall and outside surface respectively. This can be expressed as follows

$$R_{tot} = R_i + R_{wall} + R_o \qquad \text{C-1}$$

which can be expanded as

$$\frac{1}{U_o A_o} = \frac{1}{h_i A_i} + R_{wall} + \frac{1}{h_o A_o} \qquad \text{C-2}$$

In this study the fourth term in the above equation is the focus, namely the thermal resistance of the outside of the tube (or more specifically, the h_o).

The first term of Equation **C-2** describes the overall thermal resistance of the tube and in the case of this study, where water heats a tube with saturated refrigerant boiling on the outside, it can be determined by measuring the overall HTC, shown in Equation **C-3**.

$$U_o = \frac{q_{tot}}{T_w - T_{sat}} \tag{C-3}$$

The thermal resistance of the wall, R_{wall}, can be determined as follows:

$$R_{wall} = \frac{D_o \ln\left|\frac{D_o}{D_i}\right|}{2k_{wall}} \tag{C-4}$$

Equation **C-2** thus has two terms that are unknown, namely the inside and outside tube thermal resistances. The Wilson plot method can be used when these two thermal resistances cannot be separated by direct measurement.

The internal HTC was assumed to take the form of the Gnielinski correlation [127] modified by the coefficient C_i which was determined by the Wilson plot

$$h_i = C_i h_{gni} \tag{C-5}$$

where the Gnielinski correlation is given by

$$h_{gni} = \frac{(f/8)(Re_w - 1000)Pr_w}{1 + 12.7(f/8)^{0.5}\left({Pr_w}^{2/3} - 1\right)}\left(\frac{k_w}{D_h}\right) \tag{C-6}$$

The friction factor, f, was estimated from Petukhov's equation [145] for a smooth tube

$$f = (0.79 \log Re_w - 1.64)^{-2} \tag{C-7}$$

based on the Reynolds number of the water flowing through the inside of the tube, Re_w, as follows

$$Re_w = \frac{4\dot{m}_w}{\pi\left(D_i + D_{probe}\right)\mu_w} \tag{C-8}$$

In Equation **C-6** the measured hydraulic diameter D_h was given by $D_i - D_{probe}$.

The Prandlt number Pr_w was calculated as follows

$$Pr_w = \frac{c_{p,w}\mu_w}{k_w} \qquad \text{C-9}$$

The Wilson plots were conducted under pool boiling conditions and as such the external HTC was assumed to take the form of the boiling correlation

$$h_o = C_o q^m \qquad \text{C-10}$$

Equation **C-2** was thus rewritten as

$$\left(\frac{1}{U_o} - R_{wall}A_o\right){q_o}^m = \frac{1}{C_i}\frac{A_o}{A_i}\frac{{q_o}^m}{h_{gni}} + \frac{1}{C_o} \qquad \text{C-11}$$

The Briggs and Young Wilson plot implementation allows for the solving of leading coefficients C_i and C_o as well as the boiling exponent m in a two-step process.

The first step solves for the leading coefficients C_i and C_o through linear regression with an initial assumed value for the exponent m. The formulation to achieve this is as follows

$$y_1 = a_1 x_1 + c_1 \qquad \text{C-12}$$

where

$$\begin{gathered} y_1 = \left(\frac{1}{U_o} - R_{wall}A_o\right){q_o}^m \\ x_1 = \frac{A_o}{A_i}\frac{{q_o}^m}{h_{gni}} \\ a_1 = \frac{1}{C_i} \\ c_1 = \frac{1}{C_o} \end{gathered} \qquad \text{C-13}$$

The second step solves for the boiling exponent m using the results of the first step for C_i and C_o. Equation **C-11** was rewritten such that

$$\left(\frac{1}{U_o} - R_{wall}A_o - \frac{1}{C_i}\frac{1}{h_{gni}}\frac{A_o}{A_i}\right)^{-1} = C_o q_o{}^{m} \qquad \text{C-14}$$

The formulation to solve for m via linear regression was

$$y_2 = a_2 x_2 + c_2 \qquad \text{C-15}$$

where

$$y_2 = \left(\frac{1}{U_o} - R_{wall}A_o - \frac{1}{C_i}\frac{1}{h_{gni}}\frac{A_o}{A_i}\right)^{-1}$$

$$x_2 = \ln|q_o| \qquad \text{C-16}$$

$$a_2 = m$$

$$c_2 = \ln|C_o|$$

This two-step process is repeated until it converges on a solution for C_i, C_o and m. This Briggs and Young approach was further modified as suggested by Van Rooyen, Christians and Thome [126] to incorporate the weighted least squares method of York et al. [146] that incorporated the uncertainty of each point in the determination of the linear regression coefficients.

C.3 Experimental implementation

The Wilson plot study was conducted by operating the experimental rig in the pool boiling mode, as described in Chapter **3**. Pool boiling conditions were used for the outside of the tube as suggested by Gstoehl and Thome [131] as the conditions were easy to maintain, the outer thermal resistances were low and the heat transfer was easily represented by a proportional relationship.

The pool boiling occurred at constant conditions with saturation temperatures of 10°C and 25°C at constant heat fluxes of 20, 50 and 100 kW/m^2 respectively. The heating water inside the tubes was varied between Reynolds numbers of 10 000 to 18 000 in increments of 2 000.

C.4 Results

An illustrative plot of typical Wilson Plots at different heat fluxes tested are shown in **Figure C-1**. The Wilson plots were shown to be linear and a good fit was achieved by the weighted linear regression use, with the square of the correlation coefficient, R^2, greater than 0.99.

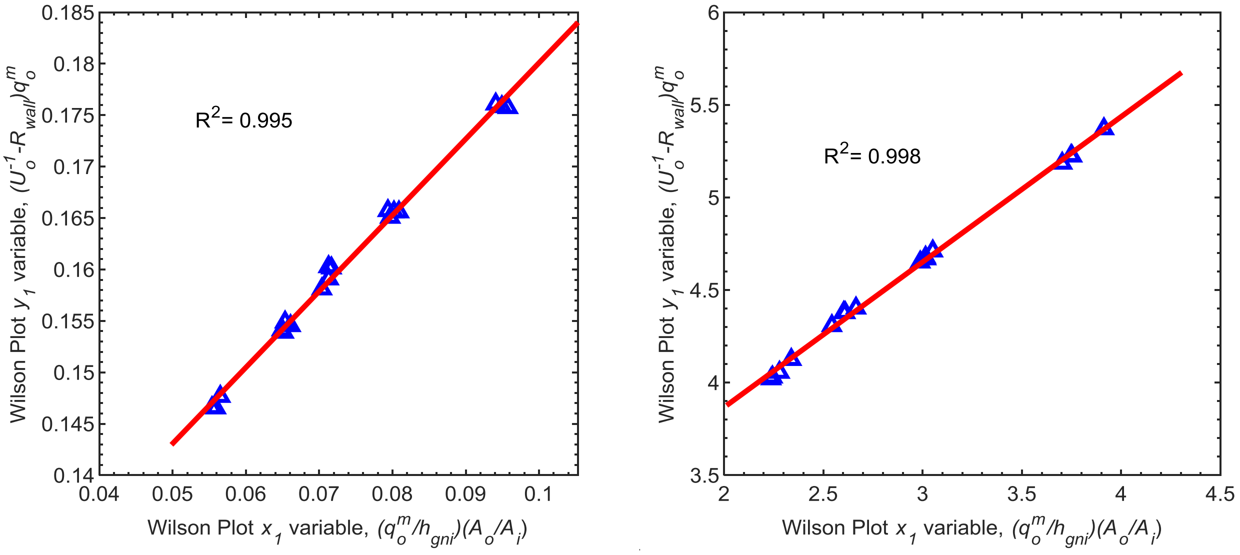

(a) 20 kW/m^2 (b) 50 kW/m^2

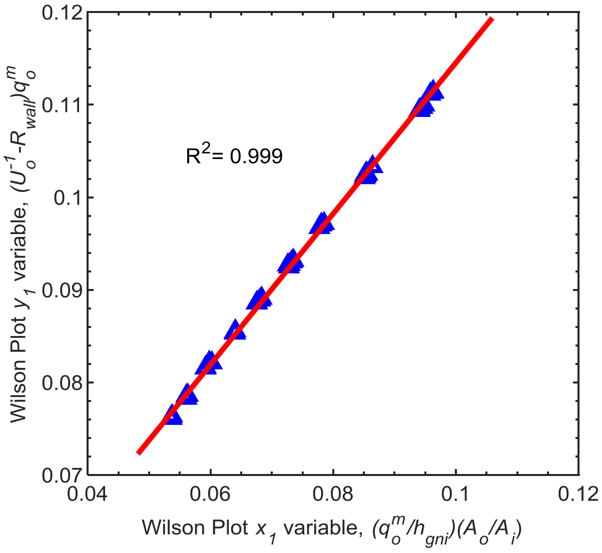

(c) 100 kW/m^2

Figure C-1. Wilson plot linear regression fits at 20°C for polished copper tubes.

A summary of the results of the Wilson plots for plain copper tubes are shown in **Table C-1**. The average internal coefficient, C_i, measured was 1.25 and the average boiling exponent, m, measured was 0.72. These results compare well with previous Wilson plot studies conducted on this experimental apparatus, as the internal coefficients, C_i, of Roques [108], Habert [109] and Agostini [130] were measured as 1.27, 1.18 and 1.29 respectively. As can be seen, the plots follow theory in that the fluxes play no discernible role in the Wilson plot outcome.

Table C-1. Wilson plot results of copper tubes.

Heat flux, q, [kW/m^2]	**Saturation temperature,** T_{sat} [°C]	**Internal coefficient,** C_i	**Boiling exponent,** m
100	20	1.22	0.72
100	20	1.22	0.52
50	20	1.27	0.92
50	20	1.24	0.68
50	20	1.29	0.66
50	20	1.24	0.63
20	20	1.34	0.62
20	20	1.20	0.81
20	10	1.22	0.89
Average		1.25	0.72

It should be noted that Roques [108], Agostini [130] and Habert [109] implemented their Wilson plot study in a different manner as the approach here. However when their approach was used, an average internal coefficient, C_i, of 1.24 was calculated, showing that in fact the differences in implementation had a minimal influence on the coefficient.

Figure C-2 compared the measured overall HTC with the overall HTC calculated with the Wilson plot internal leading coefficient, $C_{i,}$ of 1.25. As can be seen, the Wilson plot process had not distorted the overall HTC measured.

The stainless steel tube had the same internal diameter of the copper tube and Wilson plot testing found thus that it too had an internal coefficient of 1.25. The mild steel tube had a smaller internal diameter and the internal coefficient was as a result found to have a slightly higher value of 1.4.

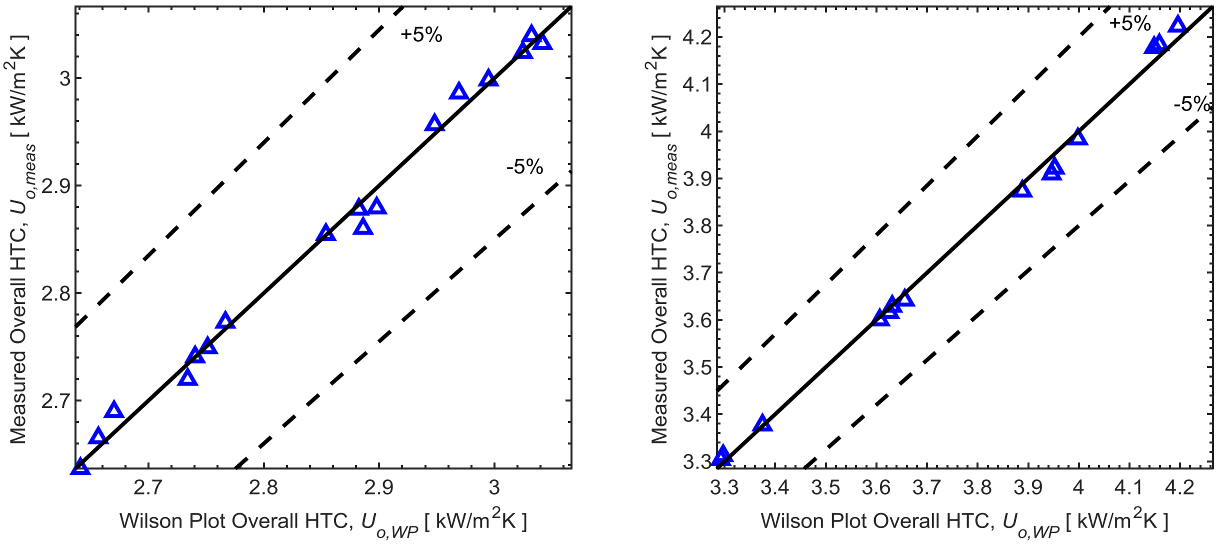

(a) 20 kW/m^2 (b) 50 kW/m^2

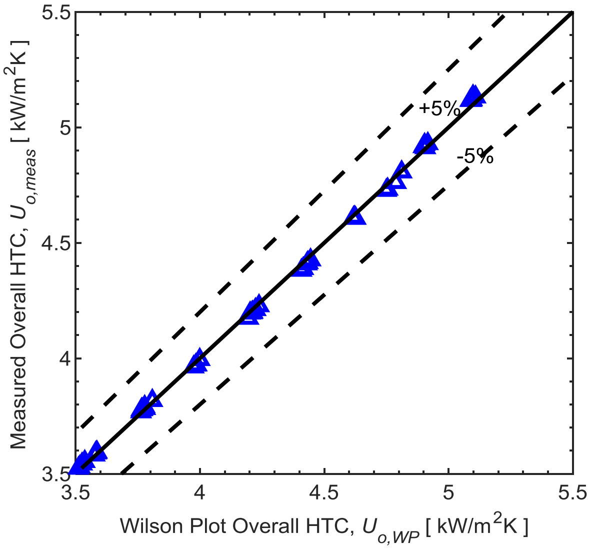

(c) 100 kW/m^2

Figure C-2. Comparison of measured overall HTC to the calculated overall HTC based on the Wilson plot calculation.

C.5 Summary and conclusions

The Wilson plot analysis was conducted for the tubes used within this study to determine the internal heat transfer multiplier coefficient, C_i, using the Briggs and Young approach [144] as modified by Van Rooyen, Christians and Thome [126]. The Wilson plot results produced good linear fits. A value of 1.25 for C_i will be used in this study for all copper tubes (which includes nanostructured tubes) and stainless steel tubes, while 1.4 will be used for mild steel tubes.

C.6 Nomenclature

a	Linear regression gradient
A	Area
C	Wilson plot modifier coefficient
c_p	Specific heat capacity
c	Linear regression intercept
D	Diameter
f	Friction factor
h	Heat transfer coefficient
k	Thermal conductivity
m	Boiling exponent
Pr_w	Prandtl number of heating water
q	Heat flux
R	Thermal resistance
R^2	Correlation coefficient
Re_w	Reynolds number of heating water
T	Temperature
U	Overall heat transfer coefficient
x	Wilson plot x-coordinate
y	Wilson plot y-coordinate

Greek symbols

μ	Dynamic viscosity

Subscripts

gni	Gnielinski correlation
h	Hydraulic
i	Inner
meas	Experimentally measured
o	Outer
probe	Heating water temperature probe
sat	Saturated refrigerant
tot	Total
w	Water
WP	Wilson plot
wall	Tube wall

C.7 List of Acronyms

HTC	Heat transfer coefficient

C.8 References

[108] J.-F. Roques, "Falling film evaporation on a single tube and on a tube bundle," PhD, École Polytechnique Fédérale de Lausanne, Lausanne, Switzerland, 2004.

[109] M. Habert, "Falling film evaporation on a tube bundle with plain and enhanced tubes," PhD, École Polytechnique Fédérale de Lausanne, Lausanne, Switzerland, 2009.

[126] E. Van Rooyen, M. Christians, and J. R. Thome, "Modified Wilson plots for enhanced heat transfer experiments: Current status and future perspectives," *Heat Transfer Engineering,* vol. 33, no. 4-5, pp. 342-355, 2012.

[127] V. Gnielinski, "New equations for heat and mass-transfer in turbulent pipe and channel flow," *International Chemical Engineering,* vol. 16, no. 2, pp. 359-368, 1976.

[130] F. Agostini, "Boiling on a tube bundle: Heat transfer, pressure drop and flow patterns," PhD, École Polytechnique Fédérale de Lausanne, 2008.

[131] D. Gstoehl and J. R. Thome, "Film condensation of R134a on tube arrays with plain and enhanced surfaces: Part 1— Experimental heat transfer coefficients," *Journal of Heat Transfer,* vol. 128, no. 1, pp. 21-32, 2006.

[143] E. E. Wilson, "A basis for rational design of heat transfer apparatus," *Trans. ASME,* vol. 37, no. 47, pp. 47-82, 1915.

[144] D. E. Briggs and E. H. Young, "Modified wilson plot techniques for obtaining heat transfer correlations for shell and tube heat exchangers," in *Chemical Engineering Progress Symposium Series*, 1969, vol. 65, no. 92, pp. 35-45: AIChE, New York, NY, 1969.

[145] B. S. Petukhov, "Heat transfer and friction in turbulent pipe flow with variable physical properties," in *Advances in Heat Transfer*, vol. 6, J. P. Hartnett and T. F. Irvine, Eds.: Elsevier, 1970, pp. 503-564.

[146] D. York, N. M. Evensen, M. L. Martınez, and J. D. B. Delgado, "Unified equations for the slope, intercept, and standard errors of the best straight line," *American Journal of Physics,* vol. 72, no. 3, pp. 367-375, 2004.

D. Additional results

D.1 Pool boiling: Influence of surface material

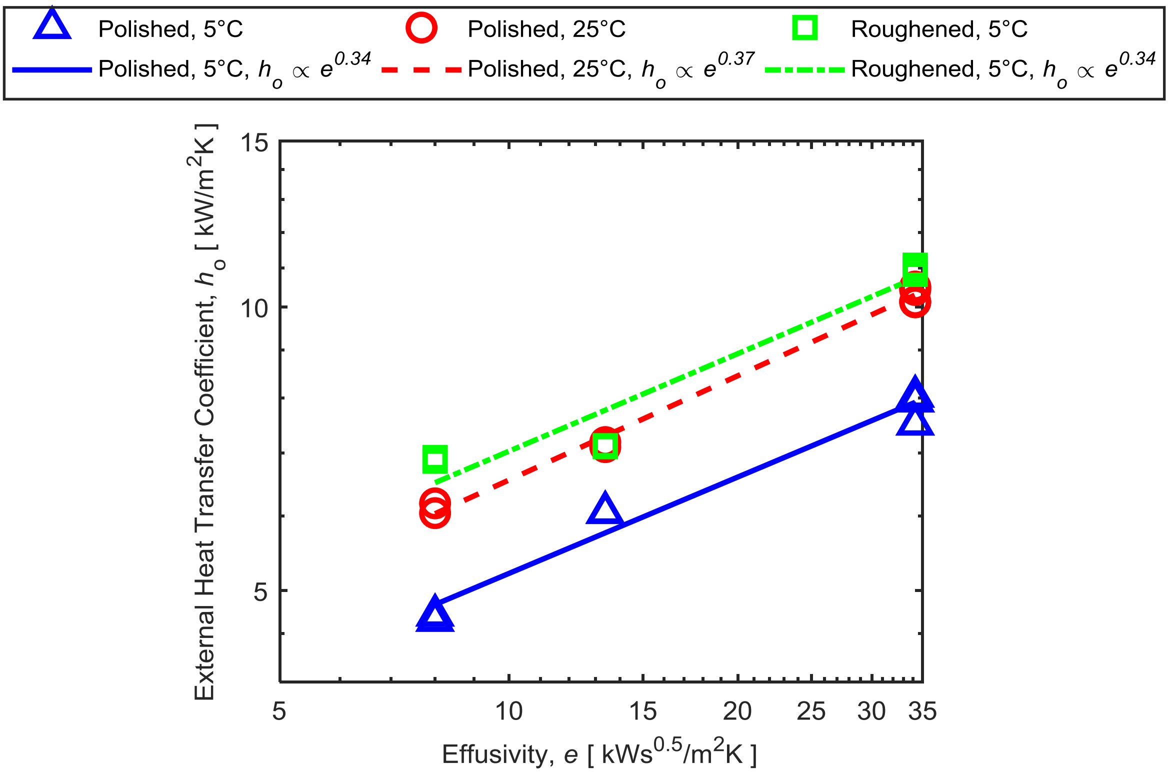

Figure D-1. Influence of effusivity on pool boiling in R-134a at 50 kW/m^2.

D.2 Pool boiling: Departure from nucleate boiling critical heat flux of nanostructured tubes

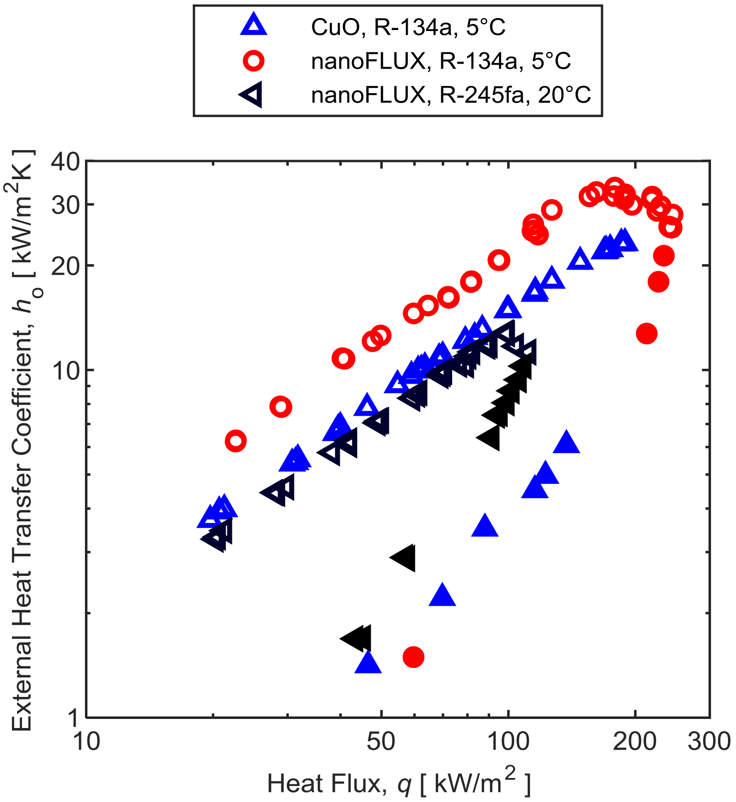

Figure D-2. CHF seen in the pool boiling of nanostructured tubes with HTC as a function of heat flux. The filled in markers indicate data points taken after DNB had been reached and wall superheat was subsequently increased further.

D.3 Falling film boiling: Influence of surface material

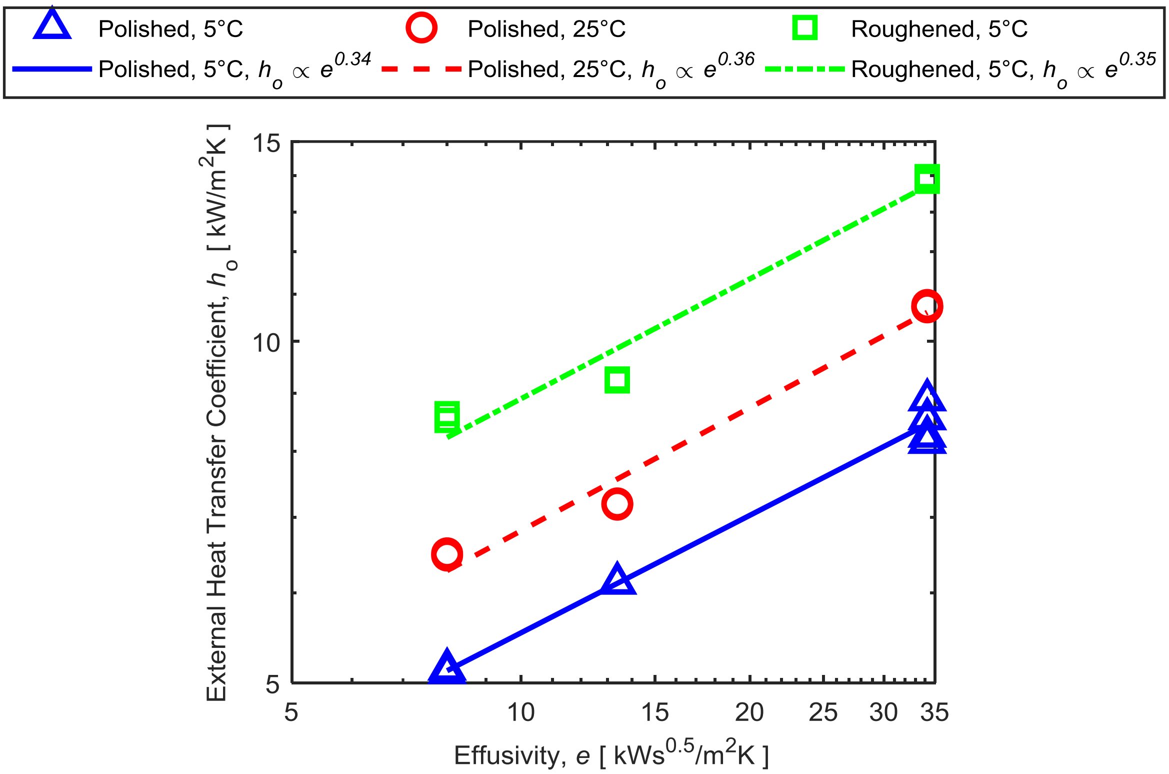

Figure D-3. Influence of effusivity on falling film boiling in R-134a at 50 kW/m^2.

D.4 Falling film boiling: Departure from nucleate boiling critical heat flux of nanostructured tubes

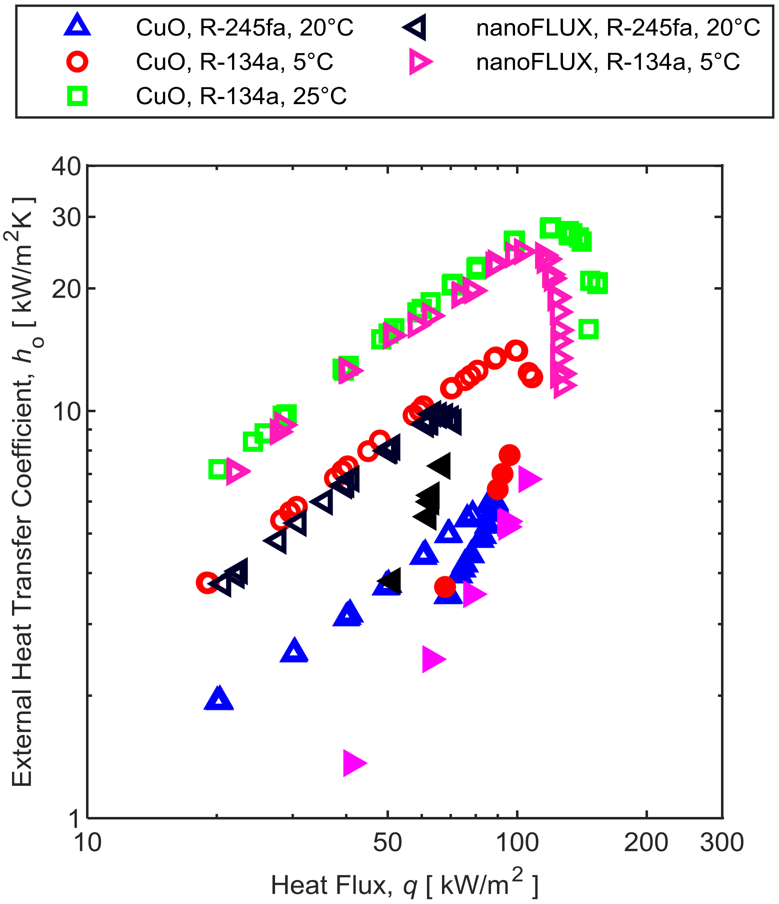

Figure D-4. CHF seen in the falling film boiling of nanostructured tubes with HTC as a function of heat flux. The filled in markers indicate data points taken after DNB had been reached and wall superheat was subsequently increased further.

D.5 Plateau dryout of falling films: Influence of refrigerant

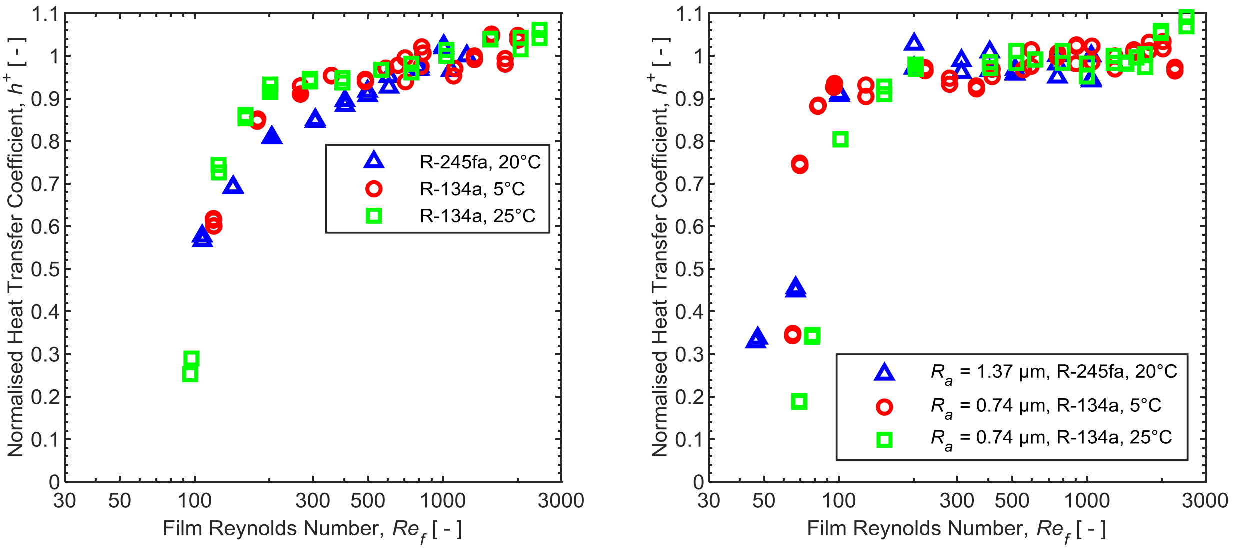

(a) Polished (R_a of 0.12 μm)

(d) Roughened

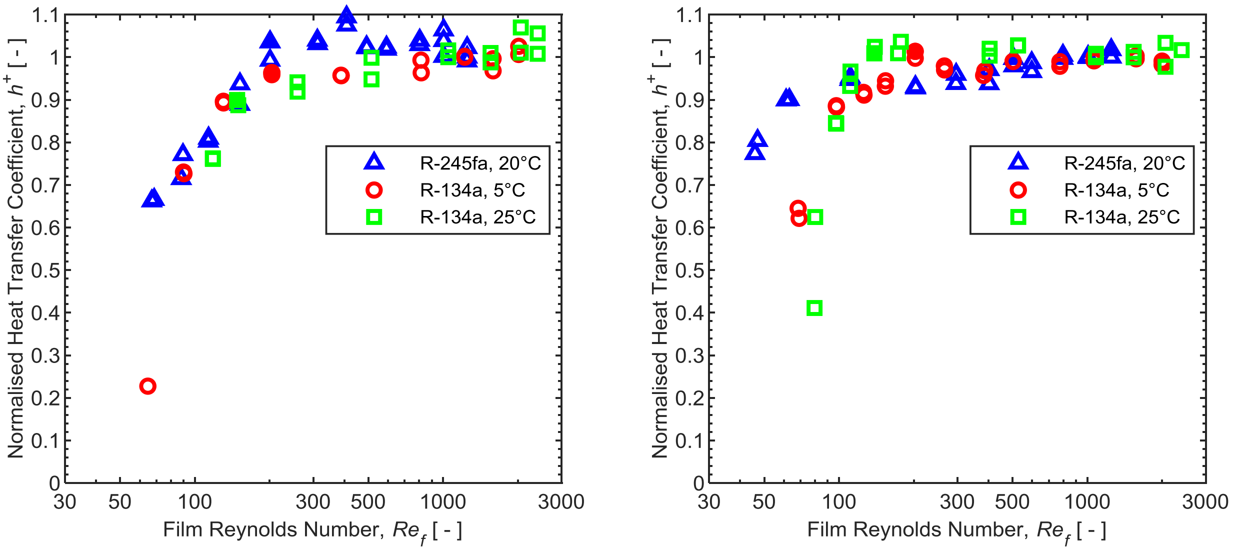

(c) LbL

(d) CuO

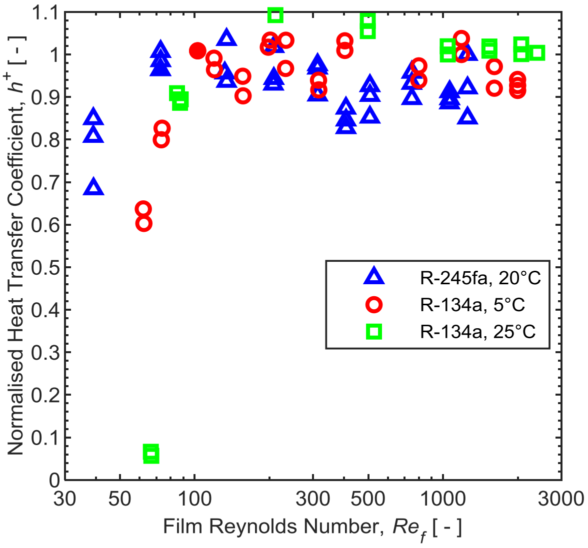

(e) nanoFLUX

Figure D-5. Normalised HTC versus Re_f at 20 kW/m². Critical dryout point indicated with filled markers.

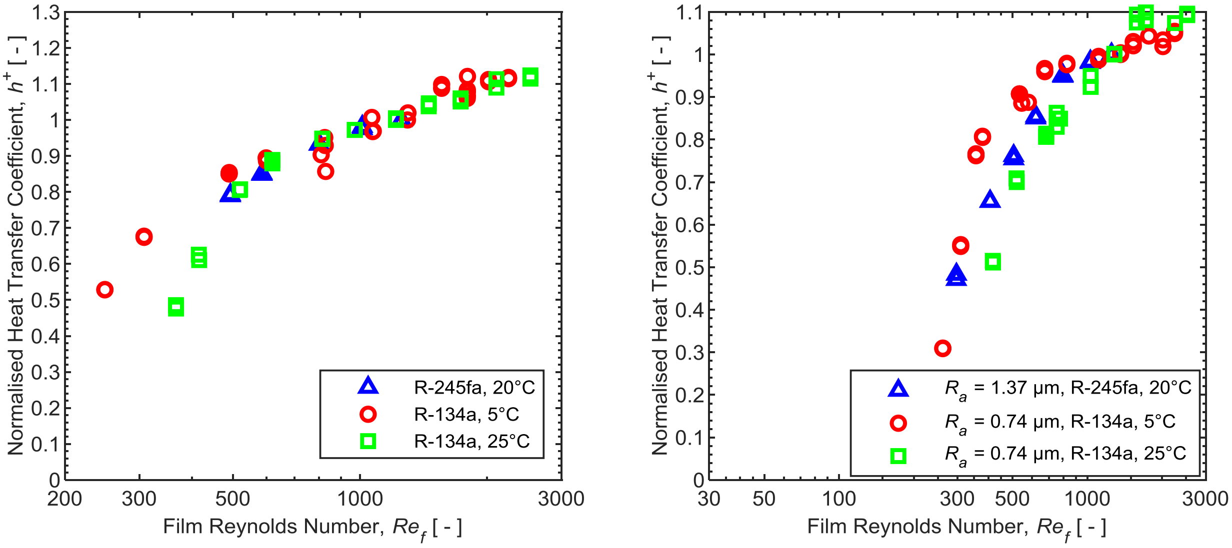

(a) Polished copper (R_a of 0.12 μm)

(d) Roughened copper (R_a of 1.37 μm)

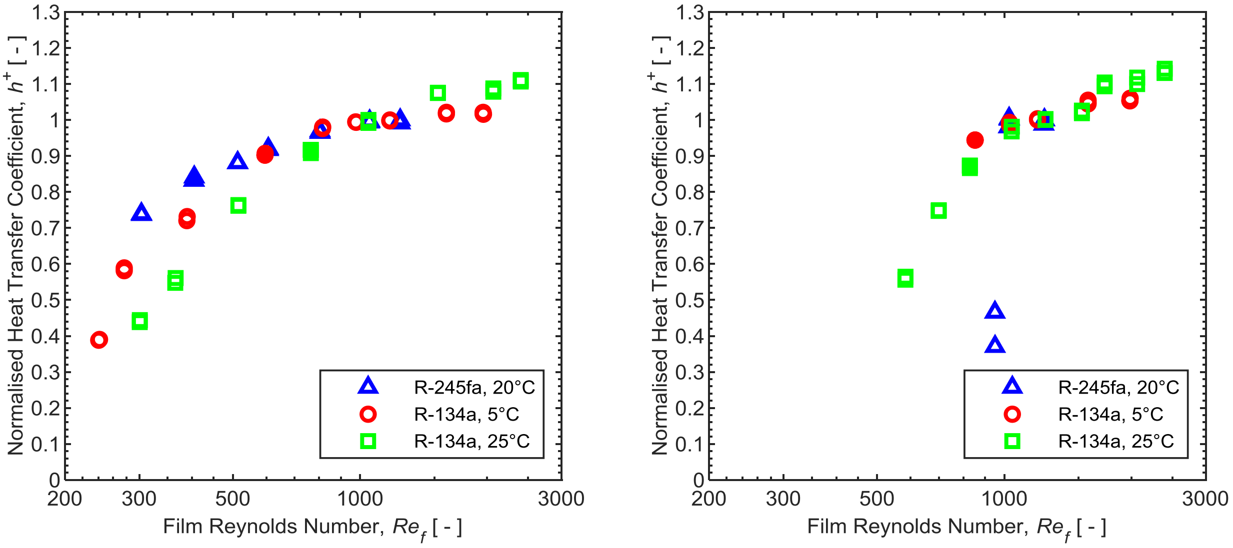

(c) LbL (d) CuO

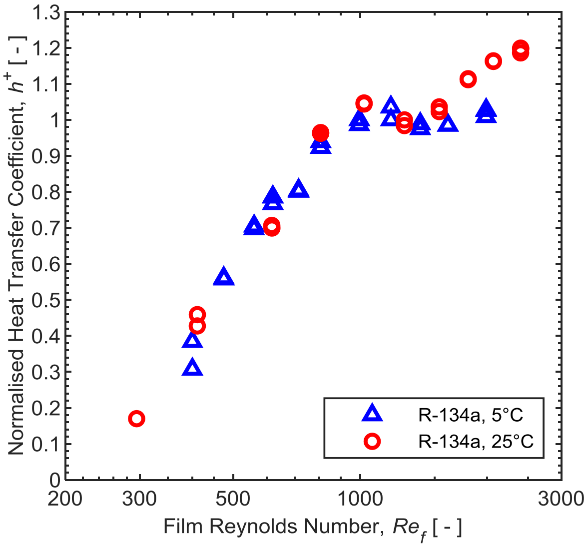

(e) nanoFLUX

Figure D-6. Normalised HTC versus Re_f at 80 kW/m^2. Critical dryout point indicated with filled markers.

D.6 Falling film boiling operational limits: Tabled results

Table D-1. Critical film Reynolds number of the polished tube ($R_a = 0.12$ µm) as a result of critical dryout.

Refrigerant	**Heat flux** q [kW/m^2]	**Critical film Reynolds number** $Re_{f,cr}$ [-]
R-245fa at 20°C	20	205
	50	228
	80	585
R-134a at 5°C	20	267
	50	297
	80	489
R-134a at 25°C	20	201
	50	545
	80	619

Table D-2. Critical film Reynolds number of the roughened tube ($R_a = 1.37$ µm) as a result of critical dryout.

Refrigerant	**Heat flux** q [kW/m^2]	**Critical film Reynolds number** $Re_{f,cr}$ [-]
R-245fa at 20°C	20	201
	50	304
	80	797
R-134a at 5°C	20	95
	50	459
	80	533
R-134a at 25°C	20	204
	50	510
	80	683

Table D-3. Critical film Reynolds number of the LbL tube as a result of critical dryout.

Refrigerant	**Heat flux** q [kW/m^2]	**Critical film Reynolds number** $Re_{f,cr}$ [-]
R-245fa at 20°C	20	201
	50	415
	80	404
R-134a at 5°C	20	204
	50	313
	80	595
R-134a at 25°C	20	148
	50	321
	80	764

Table D-4. Critical film Reynolds number of the CuO tube.

Refrigerant	**Heat flux** q [kW/m^2]	**Critical film Reynolds number** $Re_{f,cr}$ [-]	**Reason**
R-245fa at 20°C	20	111	Critical dryout
	50	206	Critical dryout
	80	1025	Critical dryout
	89	1285	DNB
R-134a at 5°C	20	203	Critical dryout
	50	495	Critical dryout
	80	852	Critical dryout
	108	2050	DNB
R-134a at 25°C	20	139	Critical dryout
	50	312	Critical dryout
	80	829	Critical dryout
	154	2441	DNB

Table D-5. Critical film Reynolds number of the nanoFLUX tube.

Refrigerant	**Heat flux** q [kW/m^2]	**Critical film Reynolds number** $Re_{f,cr}$ [-]	**Reason**
R-245fa at 20°C	20	73	Critical dryout
	50	408	Critical dryout
	71	1285	DNB
R-134a at 5°C	20	103	Critical dryout
	50	314	Critical dryout
	80	621	Critical dryout
	127	2050	DNB
R-134a at 25°C	20	117	Critical dryout
	50	498	Critical dryout
	80	806	Critical dryout